RHODES UNIVERSITY

Where leaders learn

Controls of lateral and vertical variations in the geochemistry of the Hotazel Fe-Mn Formation at Nchwaning and Gloria mines, Kalahari Manganese Field, South Africa.

Stephen Baysah Dorbor Jr.

Thesis submitted in fulfilment of the requirements for degree of

MASTER OF SCIENCE

in the Department of Geology, Rhodes University.

Submitted in 2023

Supervised by: Prof. Harilaos Tsikos

RHODES GEOLOGY

Declaration

I declare that this thesis, titled "Controls of the lateral and vertical variations in BIFs and Mn ores at the Nchwaning and Gloria mines, Kalahari Manganese Field, South Africa" is my own work, and information from other publications is adequately referenced. This thesis is submitted in fulfilment for the Masters of Science degree in the Department of Geology, Rhodes University.

Stephen Baysah Dorbor Jr

Name of candidate

Signature

Signed on the 14th day February 2023.

Acknowledgements

The journey to completing this research thesis was not an all-smooth one but I am so grateful that it was all worth it. Firstly, I want to thank God for giving me the strength and courage to continue pushing my dreams after saving me from a horrific car accident.

My family has been my biggest support system through out my years at Rhodes University and I love them so much. You might be in Liberia but your continuous love and support makes me wake up every day to keep pushing. Thanks a lot for the support because this would not be successful without the love from you all.

I would like to thank my supervisor Prof. Harilaos Tsikos, aka Hari, for his immense support, guidance and patience throughout the duration of this MSc project. Thanks for having your door open at all times. Your knowledge and calm demeanour helped me move through this study with great courage and confidence. It is without a doubt that your supervision is the best a student can ask for and I hope you continue to help students reach their dreams. I would also like to thank members of the PRIMOR group at the Rhodes University, especially Dr. Xolane Mhlanga, who all contributed in some ways to the completion of this thesis, even over some beers.

Many thanks go to ASSMANG for funding this project. It was a very great time sampling the drill cores at the Black Rock mine and I humbly appreciate everyone who assisted with information, especially Benjamin Ruzive who helped with the drill cores details, mine logistics and access to the core shed. My sincere and deepest gratititude to Ms. Christelle van der Merwe of Assmang for her tireless contribution in ensuring the smooth completion of this thesis.

I would be ungrateful if I do not appreciate the great job done by the staff in the geology department. Ashley Goddard has always been a part of my academic journey from the day I arrived at Rhodes University and her support is so much appreciated. The technical staffs who helped with sample preparation, I humbly appreciate your hard work and tireless effort in making this project a successful one.

Abstract

The Paleoproterozoic Kalahari manganese field (KMF) in the Northern Cape Province, South Africa, hosts a large resource of manganese ores that has been of great interest over many decades. The Kalahari Manganese deposit (KMD), which is the largest of five erosional relics of the Hotazel Formation in the KMF, hosts three beds of Mn ores with alternating layers of banded iron formation (BIF) and hematite lutite. These three rock types are all evaluated for their mineralogy and geochemistry in this study, with emphasis on lateral and vertical distributions across the Gloria and Nchwaning Mines in the northernmost KMF, an area of high-grade, hydrothermally altered Mn mineralisation.

The Mn ores of the Hotazel formation are traditionally categorised into two types. The carbonate-rich low Mn grade (Mn≤40 wt. %) ores (Mamatwan-type) domninates the largest part of the KMD, while carbonate-free, high Mn grade (Mn≥ 45 wt.%) ore (Wessels-type) occurs in the northernmost KMD. The Wessels-type ores are considered as the hydrothermally altered product of Mamatwan-type ores, and as indicated above, are the focus of this study. Five drill cores containing Wessels-type ores from the Nchwaning and Gloria area of the northern KMD were analysed to help understand the petrographic and particularly the geochemical variations in the Hotazel Fe-Mn Formation, both laterally for a given Mn layer of the three, and vertically across Mn layers as captured in specific drillcores.

Petrographic and whole-rock geochemical results obtained from the three rock types of the Hotazel Formation show variations in their mineralogical and geochemical compositions, especially in the high-grade Mn ores themselves. Most of the samples of the BIFs layers are dominated by hematite and chert occurring in banded fashion, which is typical of a normal carbonate-free altered BIF discussed in this thesis. The BIFs can also be locally enriched in hematite (ferruginised), occurring as massive hematite ores usually at the top of the stratigraphic profiles. The presence of aegirine-rich assemblages is also noted occurring in some of the BIF and hematite lutite sections immediately above and below the Mn ore beds.

The high-grade Mn ore beds vary greatly in mineralogy and texture of the ores laterally and even within a single drill core. In an extreme case, a single drillcore sampled from the Gloria mine (GL57) contains high-grade Wessels-type ore in the upper Mn bed and low-grade, Mamatwan-type ore in the lower Mn layer. Geochemically, the Mn ore bodies also show substantial geochemical variability, although a net increase in the Mn grade downward is

usually characterised by a corresponding depletion in mainly bulk Ca, Si and carbonate. However, the Fe content appears to be consistently higher in the upper ore bodies of the drillcores than the lower ones, and the increase in the concentration of the Fe-oxide expectedly causes a relative decrease in the bulk Mn-oxide concentration, usually expressed as an antithetic relationship between the two elements. In terms of trace element distributions, this appears to be more significant in the Mn ores than the other two rock types affected by the same alteration process, probably due to the presence of Mn phases such as hausmannite and braunite serving as good hosts to several trace elements. Cu, Zn, Pb and to a lesser extent Mo are trace metals that appear to show elevated concentration levels (net enrichments) in high-grade Mn ore by comparison to the presumed Mamatwan-type protolith. Ba is an additional element of clear enrichment, manifested mainly as the mineral barite.

The Northern KMD has a complex post-depositional history, which includes the intrusion of NE-SW-trending dykes, formation of the Mapedi/Gamagara erosional unconformity, normal faulting associated with the Wessels event and major thrust faults in the western part of the northern KMD. These structural events all have the potential to have contributed to the alteration and subsequent enrichment of the Mn ores in the Nchwaning and Gloria area. As such, the mineralogical, textural, and geochemical variations observed here can tentatively be attributed to the different structural features in the northern KMD. Classic interpretations suggest that normal N-S-trending fault structures have acted as fluid conduits for hydrothermal fluids, which led to the metasomatic alteration of the Mn ore body laterally. Drill cores proximal to and evidently affected by fault-controlled alteration in the SE and SW-portions of the Nchwaning area, have comparable mineralogical and geochemical characteristics for both ore bodies (upper and lower) with subdued alteration effects from the unconformed contact above. Fluids associated with the Mapedi/Gamagara unconformity, would have percolated down-stratigraphy causing oxidative ferruginisation, which led to the formation of massive hematite ores in the top BIF layers and ferruginised Mn ores in the Mn ore beds. This alteration effect appears more prominent in a drill core from the northern part of the study area where the unconformity contact appears more proximal to the upper Mn bed. Drill cores located in the western part of the Nchwaning area seem to also capture evidence of fluid alteration with enrichment in Na recorded in the local abundance of the mineral aegirine. Finally, the dyke structures appear to have acted as impermeable fluid barriers to both lateral and possibly down-dip fluid-flow.

Table of Contents

1) CHAPTER 1. INTRODUCTION

1.1. General

Manganese is an important element because of its utility in a variety of industrial applications. Manganese is commonly used in the iron and steel industries as a strengthening agent but is also important in chemical industries for use in dry cell batteries, and as oxidizing and colouring agents. Sedimentary manganese ore found in the Northern Cape Province of South Africa makes up approximately 77% of the known land-based manganese resource in the world (Fig. 1.1), which is approximately 4 billion metric tons of Mn (Cairncross and Beukes, 2013). This giant deposit hosted within the Kalahari Manganese Field (KMF) is located approximately 60 km north-west of the town of Kuruman in the Northern Cape Province, South Africa. The manganese ore of the KMF is interbedded with iron-formation of the Hotazel Formation (Fm) in the early Paleoproterozoic Transvaal Supergroup. There are three Mn ore beds within the Hotazel Formation and two (upper and lower) of these layers are economically viable.

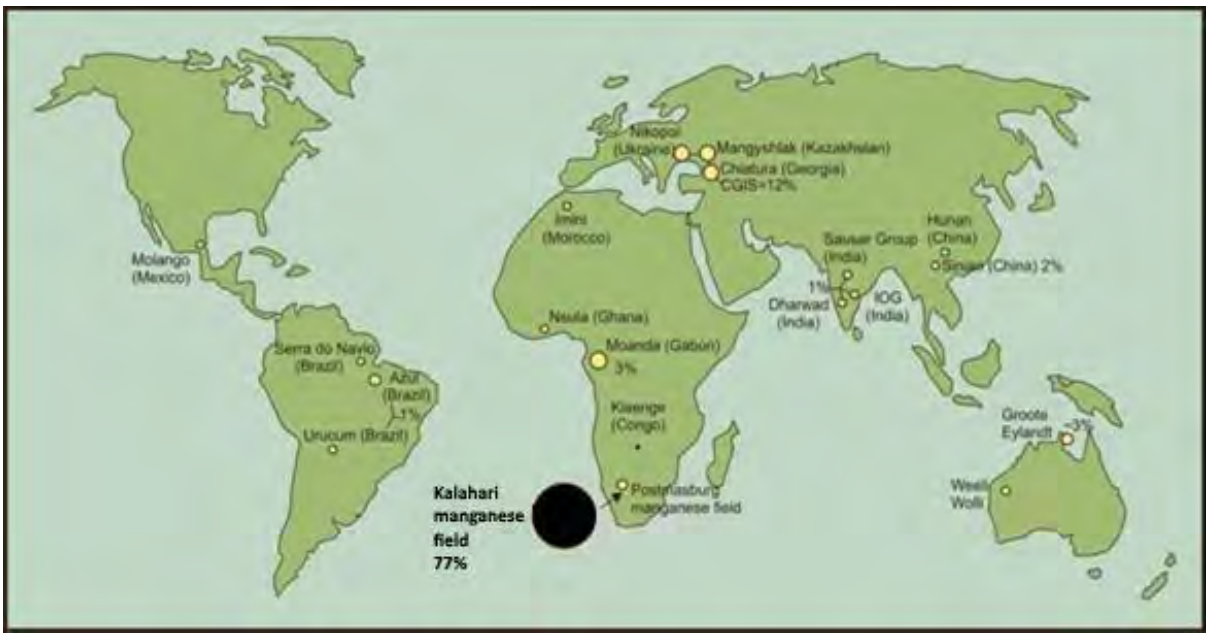

Figure 1. 1: Map showing the location of the KMF in the world. The map also shows all manganese ore reserves in the world and their known land-based Mn resource (modified after Cairncross and Beukes, 2013).

Sedimentary Mn ores of the KMF are divided into two types based on the grade. They are the low-grade Mamatwan-type ore in the south-east and the high-grade Wessels-type ore in the north-west area. The Wessels ore is suggested to be the result of metasomatic alteration of the low-grade Mamatwan-type ore (Gutzmer and Beukes, 1995).

1.2. The Kalahari Manganese Field

The KMF hosts two types of manganese ore that are mined from the Mn layers across the Hotazel Formation. The first one is the low-grade, primary sedimentary Mamatwan-type ore located within the south-eastern part of the KMF. The second one is the secondary, high-grade Wessels-type ore located in the northern part of the KMF (Gutzmer and Beukes, 1996). The Mamatwan-type ore dominates the southern and central parts of the KMF and represents the primary sedimentary manganese ore formed after deposition into the basin and subsequent diagenesis. Over the largest area of the KMD, these ores have undergone little or no alteration by fluids to cause significant change to its mineralogy. They are usually dark brown to black ores depending on the relative braunite to hematite content and contain abundant ovoids/lenses of carbonate minerals (Mn calcite, kutnahorite). The ore contains generally between 20 and 38 wt.% Mn which occurs mainly in the manganese minerals braunite and less so in the kutnohorite and manganocalcite fractions (Gutzmer, 1996; Tsikos et al., 2003).

The northern part of the KMF hosts most of the active Mn mines due to the abundant high-grade Wessels-type ore that is in this section. The Wessels-type ore contains above 45 to as high as 60 wt.% Mn in some cases, which makes it far more economically attractive than the Mamatwan-type ore. High-grade ores are significantly darker in colour and more crystalline, containing lesser carbonate than the low-grade Mamatwan type-ore (Gutzmer and Beukes, 1996). The ore contains mainly the manganese minerals braunite, braunite II, hausmannite and lesser bixbyite in some areas, while the pre-existing carbonates appear to be completely dissolved leaving behind secondary porosity, or locally replaced by Mn oxides (e.g. haysmannite). The Wessels-type ore has thus been characterised as the product of hydrothermally altered low-grade Mamatwan-type ore, with loss of carbonate and silica as the main drivers of manganese enrichment (Gutzmer, 1996; Gutzmer and Beukes, 1997).

Many structural features dominate the northern part of the KMF, and the general dip

direction of the strata is westerly at ~5-10°. Faulting is prominent throughout the Nchwaning mine area and is thought to have played a major role in the alteration of the primary sedimentary rocks of the Hotazel Formation. In the Gloria area, closely-spaced normal faults are also seen in a NE-SW strike direction, with two major faults in the Gloria area occuring in the central and northwestern part of the farm (Chetty, 2008).

In the west of the Nchwaning area are low angle thrust faults which result in duplicated stratigraphic "wedges" of the Hotazel Fm, underlying Ongeluk volcanics and overlying Mapedi/Gamagara strata (Fig. 1. 2). This thrusting is attributed to the Kheis orogenic event and its duration; the mafic rocks of the basal Ongeluk Fm are seen to be thrust over the Fe-Mn Hotazel Formation, causing brecciated andesites to be in contact with the shale of the Mapedi Formation (Puchner, 2002) . East of the thrust are a series on N-S faults that form the large graben feature in the central part of the Nchwaning area (Fig. 1. 2). The graben structure has displaced the Hotazel formation in this area much deeper, like what is seen in drill core N92I where the Hotazel Fm is intersected more than 600 meters below the surface.

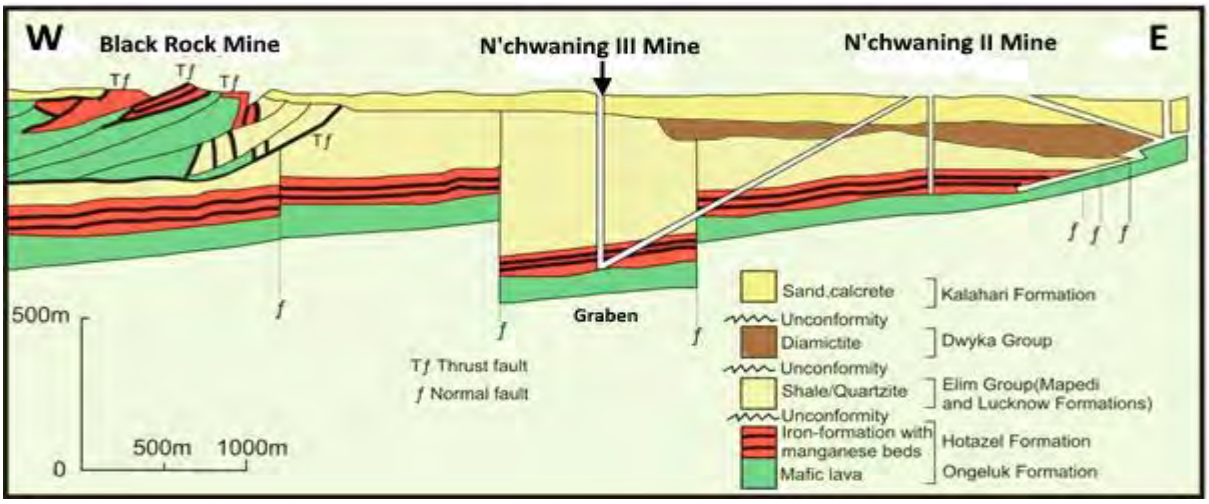

Figure 1. 2: Cross-section of the Nchwaning mines to the east and the Black rock mine to the west, illustrating the different structures. The Blackridge thrust fault forms duplicated wedges in the west and the N-S faults form the graben structure central of the area (after (Cairncross and Beukes, 2013)

1.3. Review of Post-depositional History

The northern part of the KMD has evidently undergone several deformational and alteration events following primary sediment deposition (Beukes et al., 1995; Chetty, 2008; Gutzmer,

1996). These deformational events led to the many structures we see associated with the Hotazel Formation, and these structures are likely to have been important to the alteration events that affected the rocks of the Hotazel Formation (Gutzmer and Beukes, 1995, 1996). At least three alterations events are thought to have followed the deposition of the sedimentary Mn ores, which led to the subsequent enrichment of these ores.

The oldest alteration event, known as the Wessels alteration event, involved the interaction of hydrothermal fluids at temperatures of around 350 to 400°C with the primary sedimentary rocks in the Nchwaning and Wessels mining areas. This alteration event has been linked to the Kibaran orogenic event and it is limited to only the northern section of the KMF (Thomas et al., 1994). This process involved the percolation/movements of these hydrothermal fluids along N-S-striking faults in the northern section of the KMF that acted as fluid conduits. Kleyenstüber (1984) had earlier suggested that alteration event in the same area may not be limited to the N-S-striking normal faults but should also include the minor E-W-oriented thrust faults as conduits for fluids that caused the alteration of the low-grade ores.

The effect of this fluid-rock interaction involved intense leaching of silica and dissolution of carbonates from these primary rocks that subsequently resulted in the enrichment and upgrading of the manganese ores (Gutzmer and Beukes, 1995, 1996, 1997). The mass loss from these major chemical constituents of the primary sedimentary Mn ore bed caused subsequent compaction of the ore beds to about two-thirds of their original thickness.

The loss of major element components (Si, Ca, CO_2) from the original protolith accompanied by the oxidation of the initial Mn^{2+} to Mn^{3+} resulted in major mineralogical changes as well as mineralogical variations. Gutzmer and Beukes (1995) proposed that variation in mineral assemblages of the altered ores was a function of distance from faults, and as such, the extent of the alteration was the greatest closer to the fault and gradually reduces towards the centre of the faulted blocks. Based on metasomatic zoning observed and reported from around the feeder faults, Gutzmer (1996) identified two styles of alteration associated with the Wessels event namely ferruginous and siliceous as illustrated in Fig. 1. 3.

The ferruginous style of alteration is characterised by the presence of massive braunite ore around a zone of intense ferruginisation adjacent to the feeder fault. Further away from the fault, towards the fault centre is less massive braunite ore that gradually grades into zones of coarse crystalline hausmannite-rich ore, followed by massive hausmannite-rich ore, and

medium-grained hausmannite-rich ore. With greater distance from the fault, the ore grades into zones of bixbyite-braunite II-hausmannite assemblages and then into braunite II - braunite-rich ore, that usually contains traces of the original low-grade Mamatwan-type ore.

The siliceous type of alteration is characterised by the presence of a high-grade ore zone directly adjacent to the fault. Curiously, although this alteration has been termed “siliceous” the ore itself consists predominantly of coarse-grained crystalline hausmannite, while the silicate andradite appears to characterise the zones immediately adjacent to the faults. With distance away from the fault, there is a decrease in grain size and abundance of hausmannite in the ores.

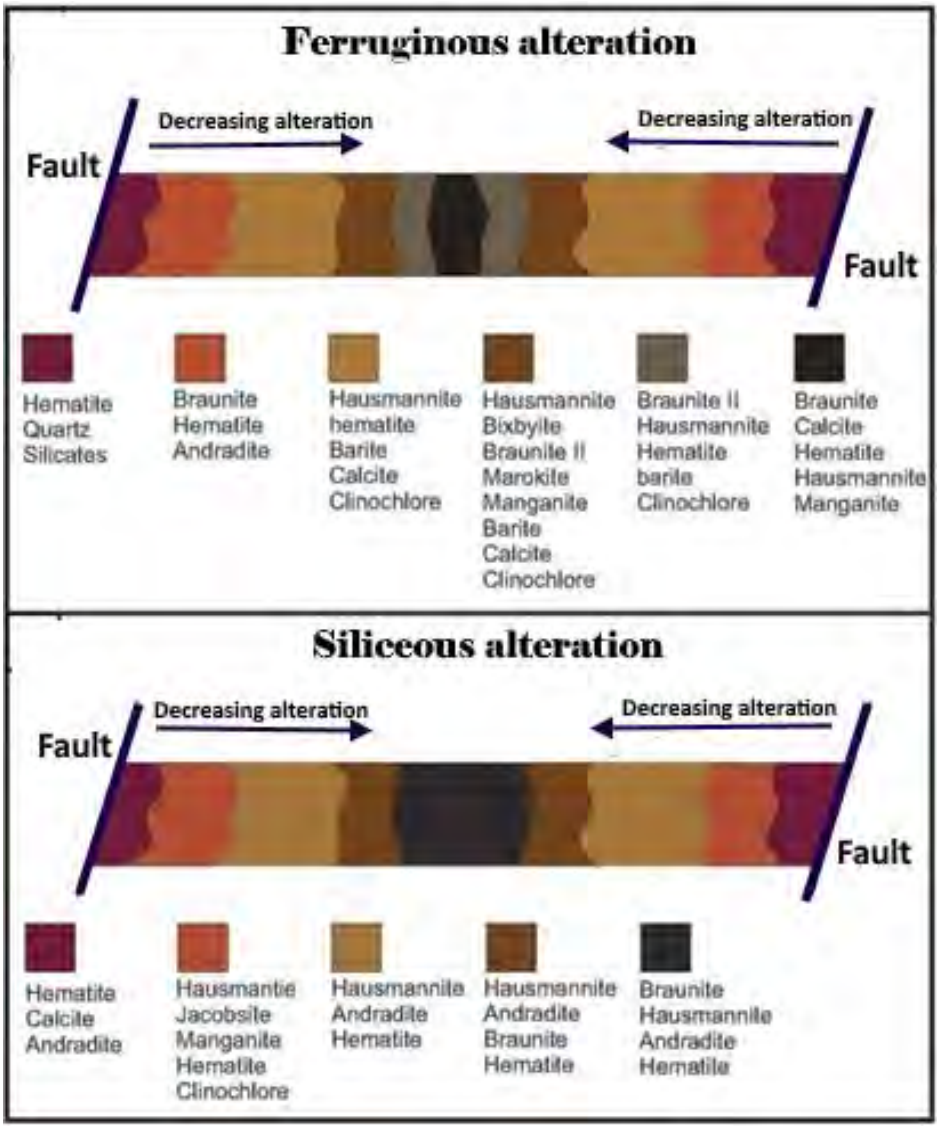

Figure 1. 3: Illustration of the two styles of alteration showing zones of mineral assemblages along faults which acted as fluid conduits during Wessels-type alteration (modified after (Gutzmer and Beukes, 1996)

The second of the three hydrothermal alteration events that affected the rocks of the Hotazel Formation occurred at 0.6 Ga. This alteration event is not connected to the Kibaran deformational event and is limited to the central and southern part of the KMF where the Mamatwan mine area is located. This event is associated with joints and minor faults in the KMF and is characterised mainly by the development of carbonates, sulphide and hematite association at the expense of carbonate-rich braunite ores. This process results in the formation of jacobsite, pyrite and quartz-rich assemblages, which formed at the expense of braunite and hematite alteration. The alteration of braunite to jacobsite (± hausmannite) represents the lowest degree of alteration, while the highest degree of alteration is evident by the formation of pyrite at the expense of hematite (Gutzmer and Beukes, 1996). This involves the leaching of the oxides thus causing the much darker ore to exhibit a much lighter colour in some areas. The alteration of carbonate-rich braunite-lutite along the fractures, faults and joints caused Mn and Fe-oxides to leach, thus resulting in the red discolouration within the Mn ore (Gutzmer and Beukes, 1996).

The third alteration event of the Hotazel rocks occurred post-formation of the Kalahari unconformity. Meteoric fluids along the unconformity infiltrated the rocks of the Hotazel Formation and altered the Mn ores and adjacent iron formation. The alteration process leached out carbonates and oxidised Mn^{2+}/Mn^{3+}-bearing minerals to Mn^{4+} oxy-hydroxide (Gutzmer and Beukes, 1996). This oxidation process resulted in the formation of todorokite, cryptomelane, pyrolusite and goethite at the expense of the minerals (braunite, hausmannite and kutnohorite) in the primary Mn ore (Du Plooy, 2002). These ores are occur closer to the Hotazel-Kalahari unconformity and are characterised by Mn ores having a bulk Mn concentration higher than 40 wt.% mainly as a result of CO_2 driven off during the oxidative process (Blignaut, 2017). This style of alteration is epitomised at the Smartt mine in the southeastern-most part of the KMD, north of the Mamatwan Mn mine (Gutzmer and Beukes, 1996). The Smartt event is associated with the occurrence of altered, brecciated ore in the fault zones of the Smartt mining area due to the influx of low-temperature fluids along N-E-trending, normal faults. The infiltration of these fluids led to the oxidation of carbonate minerals and the subsequent upgrading of braunite lutite adjacent to feeder structures (Gutzmer and Beukes, 1996). Alteration of the Mn beds is characterised by the development of Mn^{4+} minerals, such as todorokite and manganomelane at the expense of Mn carbonates, braunite and hausmannite in the primary low-grade ore (Gutzmer et al., 2012; Gutzmer and Beukes, 1996).

1.4. Previous Work

The KMF has been an area of research, over many years, due to its economic significance as well as the geology of the area. Enriched Mn ore of the KMF only outcrops at the Black Rock hill and this was first mapped by Rogers (1907). The very first full description of the Mn ore beds at the Black rock outcrop was completed in 1940. Boardman (1941) carried out major exploration drilling and some geophysical analysis on the outcrop, described the manganese mineralisation, and linked the origin of the deposit to metasomatic processes related to the Hotazel iron-formation. This work gained a lot of interest and led to the start of mining activities in the area. In subsequent years, the northern KMF also begun to become famous for hosting a large range of umusual mineral specimens and diverse mineral assemblages with over 135 minerals documented by researchers who worked on this deposit (Cairncross and Beukes, 2013).

Frankel (1958) carried out work at the Smartt mine and proposed a supergene origin for the Mn ore. De Villiers (1970)conducted the first comprehensive work on the mineralogy of the manganese ore and suggested a chemical sedimentary origin for the manganese ores of the KMF. Further subsequent work by many authors (Cairncross et al., 2000; Gutzmer and Beukes, 1996; Kleyenstüber, 1984; Tsikos and Moore, 2005; De Villiers, 1983) with focus on analysing in more detail the mineral paragenesis across the KMF, showed a wide range of mineral occurrences across the three rock types indicated earlier in this thesi. Minerals that have evidently formed in high-temperature conditions, as compared to the low-T primary assemblages, have been observed and interpreted as the combined result of multiple episodes of fluid infiltration taking place in the Kalahari area (e.g. Cairncross et al., 2000; Tsikos and Moore, 2005). Additional research into the alkali mineral paragenesis conducted by Tsikos and Moore (2005) with emphasis on Na-bearing mineral species such as sugilite and aegirine, have pointed to episodes of fluid infiltration that must have beem of an alkali-rich nature, most likely in the form of NaCl-enriched brines.

The bulk of mineralogical and geochemical studies of the Mn ore of the Hotazel Formation has focused on the conversion of primary sedimentary ore enriched into high-grade Mn ores due to the Wessels alteration event (Beukes et al., 1995; Gutzmer and Beukes, 1995,1996; Tsikos et al., 2003; Chetty and Gutzmer, 2012; Gutzmer et al., 2012). Gutzmer and Beukes (1996) first proposed the Wessels alteration event involved the movement of hydrothermal fluids through major N-S striking faults that acted as fluid feeders. This event is thought to be

the oldest of fluid alteration events and the major driver of high-grade Mn ore formation in the KMD through ferruginisation, oxidation, leaching and largely residual enrichment of Mn ores in the northern section of the KMF (Beukes et al., 1995; Gutzmer and Beukes, 1997; Tsikos et al., 2003). Subsequent to the Wessels event are the younger fluid alteration events (e.g. Smartt) that were also mentioned in the previous section (Gutzmer and Beukes, 1996).

Subsequent to the advent of the Wessels event (Gutzmer and Beukes, 1995,1996), Tsikos et al. (2003) focused more on the geochemistry and petrography of the iron-formations in the KMF. The authors used bulk and isotope geochemistry to highlight stratigraphic variations in the iron-formations of the Hotazel Formation before and after the Wessels alteration event. These studies explain that the effect of alteration was not the same on the rocks down section, as one would expect for a single fault related alteration event operating laterally in the rocks. Tsikos et al., (2003) concluded that the supergene alteration event associated with the Mapedi/Gamagara unconformity was a major factor that led to the alteration of the BIFs and residual enrichment of the manganese ores in the northern part of the KMF. The downward movement of low-temperature fluids along the unconformity led to intense ferruginisation in the BIFs and could move as far as 60 m from the unconformity also affecting the Mn ores (Tsikos, 1999).

Finally, Chetty (2008) conducted a detailed evaluation of the geometallurgy of the two beds, and subsequently published a study on the redistribution of REE within both ore beds(Chetty and Gutzmer, 2012). More recently, in her PhD thesis, Blignaut (2017) carried out a detailed analysis on high-grade ores from the Nchwaning and Gloria area for a better understanding of the petrographic and geochemical variations within both ore beds. The author makes detailed references to the geochemical variation between drill cores from different localities with respect to the relevant structures associated with the KMF. The element B is highlighted in this study as being of key importance to the research due to its detrimental effect on the geometallurgy of the ore. Boron concentrations greater than 400 ppm are considered highly undesirable and detrimental to the steel quality because B partions into the silicomangnese, during processing, thus making the steel brittle after addition of the silicomanganese (Blignaut, 2017). The study of Blignaut (2017) concludes that the distribution of Mn ore in the high-grade Nchwaning area is the result of a compex combination of fluid processes that exploited faults, thrusts and the Gamagara/Mapedi unconformity, and that B distribution shows no specific pattern of distribution to constrain its exact origin and controls.

1.5. Project outlines and objectives

This thesis is based on the investigation of five (5) drill cores from the Nchwaning and Gloria mines located in the Black Rock major deposit of the KMF, Northern Cape. All drill cores have been provided by the company ASSMANG operating in the area, and the exact study area and borehole location are shown in Figure 1. 4.

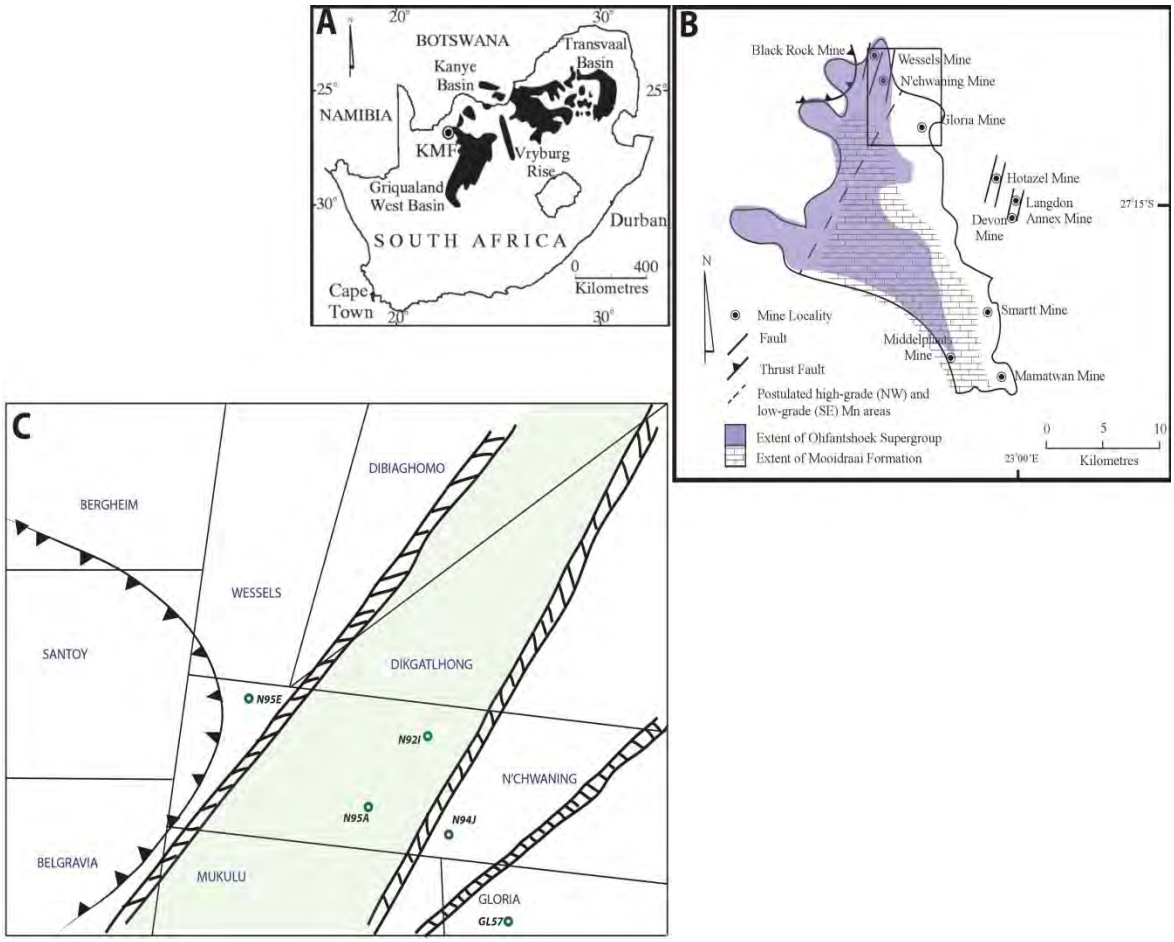

Figure 1. 4: a) Geological map of the Griqualand West sequence of the Transvaal Supergroup showing the geographical location of the KMF. b) Geological map of the KMF showing the Northern part of the KMF. c) Enlarged image of the Northern KMD showing Gloria and Nchwaning farms (highlighted in light-green) with structures and the location of the drill cores used in the study (after Cairncross and Beukes, 2013.

Up until recently, only the lowermost of the three Mn layers was being mined, but this has now changed with the local development of the topmost Mn layer as well at Nchwaning and adjacent Wessels mines. Previous research work has shown that the Mn ores in the KMF vary both mineralogically and geochemically across space, and this has led to important questions about the exact mode of origin of different mineralogical types of Mn ore. These questions

revolve mainly around the issue of the controls for these variations both laterally and vertically. This project, therefore, has focussed on the detailed investigation of five drill cores across the Nchwaning and Gloria areas where both Mn ore layers and the interbedded iron formation and hematite-lutiute transitions are of interest. This approach is a step further to the work done recently by Blignaut (2017) where only the Mn ores from Nchwaning mine were analysed but not the interbedded iron formations. Therefore, samples used in this project were collected from all rock types within the Hotazel Formation to gather detailed information that will hopefull shed some more light on the causes and controls of variations in geochemistry in space and the implications that they have for further modelling, exploration and mining. Therefore, the main objectives of this study include:

- Report the mineralogical distribution of the Hotazel ores and host iron formations from all five drillcores, and highlight their variability spatially,
- Present and evaluate the geochemical results from the same drillcore in light of the observed mineralogical variability,
- Evaluating and identifying the possible controls for these variations where possible; and,
- Compare and contrast the results of this thesis with existing ore-forming models.

Throughout this thesis, the approach of the author is to always compare the mineralogy of a typical Mamatwan-type ore to what is observed in the five drill cores of the high-grade ores targeted in this study. The specific context for comparison is geochemical results from typical low-grade Mn ore (upper and lower beds) from the nearby Gloria mine, in which the overall stratigraphic layout of the Hotazel Formation appears directly comparable to the one see in the high-grade Nchwaning farm area (see also Tsikos et al., 2003). The Gloria stratigraphy and geochemistry is thus used throughout this thesis as the comparative context for the evaluation of all new results.

In the first part (Chapter 3), the bulk mineralogy and textures of the sampled drillcores are concisely discussed. Emphasis is given mainly to the two Mn-ore bodies of each intersection borehole and possible variations are assessed. This creates the framework for the evaluation of the geochemical data presented in Chapter 4, in the form of major, minor, trace and rare-earth elements (REE) data for all samples. These results are illustrated using geochemical profiles, isocon diagrams as well as REE plots. Mass balance considerations for alteration are

presented in Chapter 5, while Chapter 6 discusses and evaluates the results of this thesis in light of existing models.

1.6. Sample selection and borehole characteristics

Five (5) borehole intersections were selected and sampled from the Assmang mine in the Black Rock area, South Africa (Fig. 1. 5). The selections were based on a combination of two factors: namely the composition of the contained ores in each drillcore with respect to different major element ratio maps obtained from the mine, as well as their locality with respect to significant structural features (e.g. faults, dykes). The maps showing the elemental ratios in both ore bodies for each of the drill cores are included in the APPENDIX at the end of this thesis. The drillcore selection was specifically guided by lateral and vertical variations seen in two-dimensional space for element ratios involving Mn against Ca, Si and Fe. Compositional ratio maps were therefore used courtesy of the mine geologists of ASSMANG at Nchwaning mine (especially Mr B. Ruzive and L. Ngqalela). It should be stressed that such compositional maps were prepared for both the upper and the lower Mn layers, as the latteral distribution of ratio data for each layer is clearly different.

From the five boreholes intersection used for this research, four (N92I, N95A, N95E, and N94J) are from the Nchwaning mine while the other one (GL57) is from the Gloria mine, located south-southeast of the Nchwaning mine. In total, a hundred and thirty-seven (137) samples were selected from the five boreholes with a significant number of samples taken from each lithological units, thus sampling the entire Hotazel Formation from the top BIF to lower BIF layers. A brief description for each of these boreholes given below shows their major general characteristics.

The borehole labelled N95E is located at the north-westernmost edge of the Nchwaning area between two major structures (fault and dyke) although it is closer (~ 100 m) to an N-S fault structure than it is to the dyke. This drill core was selected due to its high Mn/Si ratio in the lower ore body but a significantly low Mn/Si ratio in the top ore body. N95E has the minimum overall thickness (~ 33 m) of the five. The vertical distance from the start of the top BIF to the top Mn ore bed is ~7 m (mainly as transitional hematite lutite), and the drill core is overlain unconformably by shales of the Mapedi Formation. The Top BIF layer is only 3 m thick and the thickness of the top Mn ore bed is much smaller (~4 m) than that of the lower ore body (8 m).

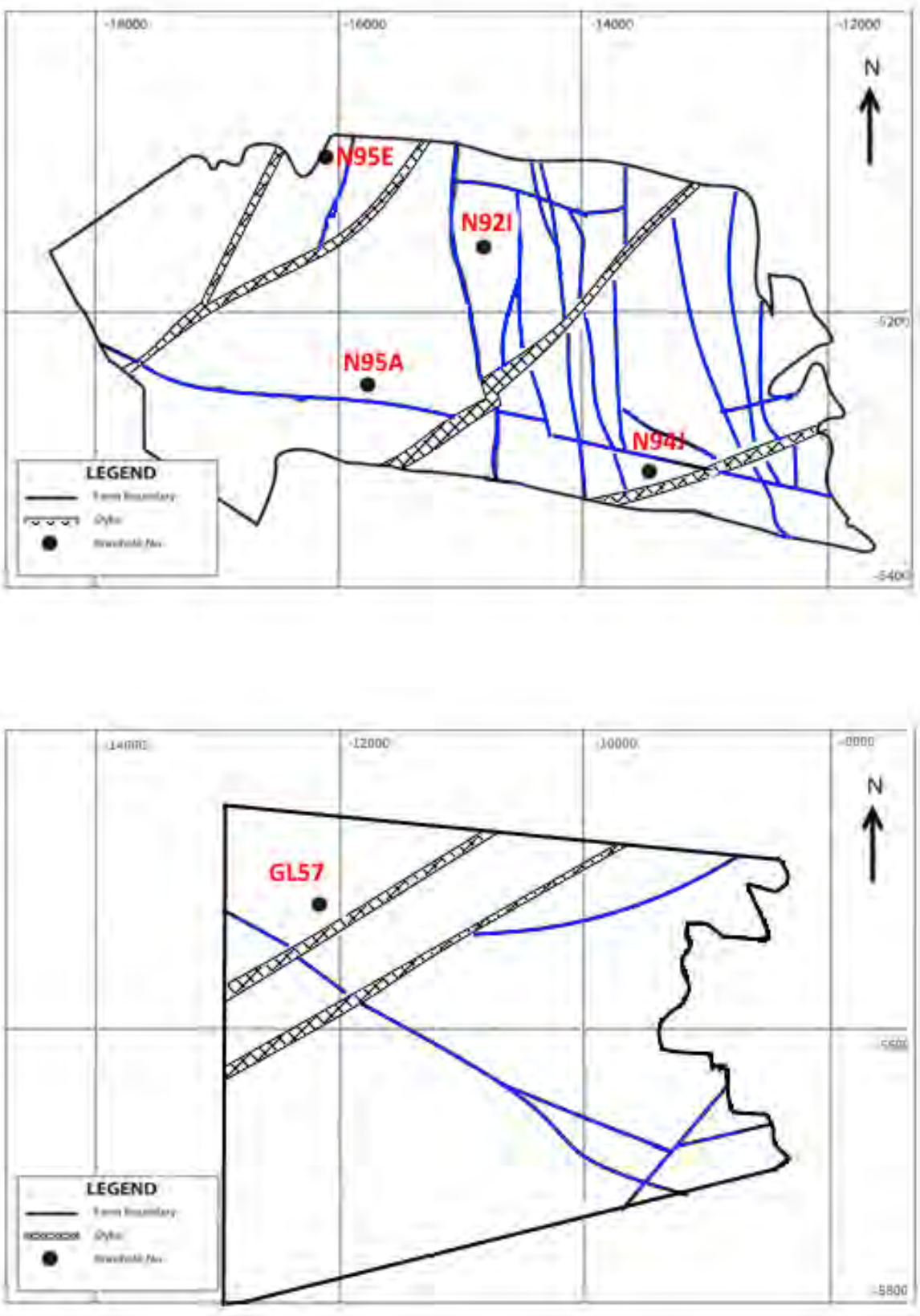

Figure 1. 5: Maps of Nchwaning and Gloria mining areas in the northern KMF, showing faults (blue lines), dykes (cross-hatched lines) as well as the location of the individual cores.

Drillcore N95A is located in the south-western part of the Nchwaning area away from the major graben structure but has an E-W trending minor fault structure close to it. It was selected due to the relatively high Mn/Fe ratio in both ore bodies. The borehole intersection is 50m thick and the distance from the top BIF layer until the first Mn ore bed is approximately 19m. The top Mn ore layer here appears to be a little bit thicker (~7m) than the lower ore body which is about 6m thick.

The borehole labelled N92I is located in the central part of the Nchwaning farm (see fig. 1.5). This borehole was selected due to its high Mn/Si ratio in the top ore body as well as its locality, it is located adjacent to the major graben fault structure in the central part of the Nchwaning mine area. The borehole intersection here is ~52 m thick, the top Mn ore bed is significantly thicker (10 m) than the lower ore body (4 m), and the distance from the top of the stratigraphy to the top ore body is about 10 m long.

Borehole N94J is from the south-eastern region of the Nchwaning area, and it is closer (~ 200 m) to the eastern NE-SW-trending dyke that runs across the Nchwaning area, and also to a major N-S striking fault structure. This borehole was selected due to the very high Mn/Ca ratio in the top ore body and a relatively lower such ratio in the lower ore body, which is usually also a good empeirical indicator for very good quality high-grade ores. N94J is the longest borehole among the four from the Nchwaning area. It is about 80 m thick and it has 24 m of BIF and hematite lutite above the top Mn ore body.

Finally, borehole GL57 is the only drillcore intersection that was selected to be sampled from the Gloria area. The interesting feature of this drillcore that sparked immediate interest and led to the present study, is that this borehole is characterised by high Mn ore grade (Wessels-type ore) in the top ore body and low-grade (Mamatwan-type) Mn ore in the lower ore body. In other words, a single borehole captures the two contrasting Mn ore types in the same intersection. The extent of the core drilled is about 105 m and lies closest (shallowest) in relation to the present surface (185 m). The distance from the top of the section to the start of the top Mn ore bed is 47 m long, which includes about 37 m of BIF and 10m of hematite lutite. The lower ore body in this borehole is significantly thicker (~15 m) than the top ore body which is about eight (8) meters thick. Finally, it must be noted that this is also the only drillcore intersection out of those selected for this study, in which the rocks unconformably overlying the Hotazel Formation are not the Mapedi/Gamagara sequence, but Paleozoic glacial tillite of the Dwyke Formation.

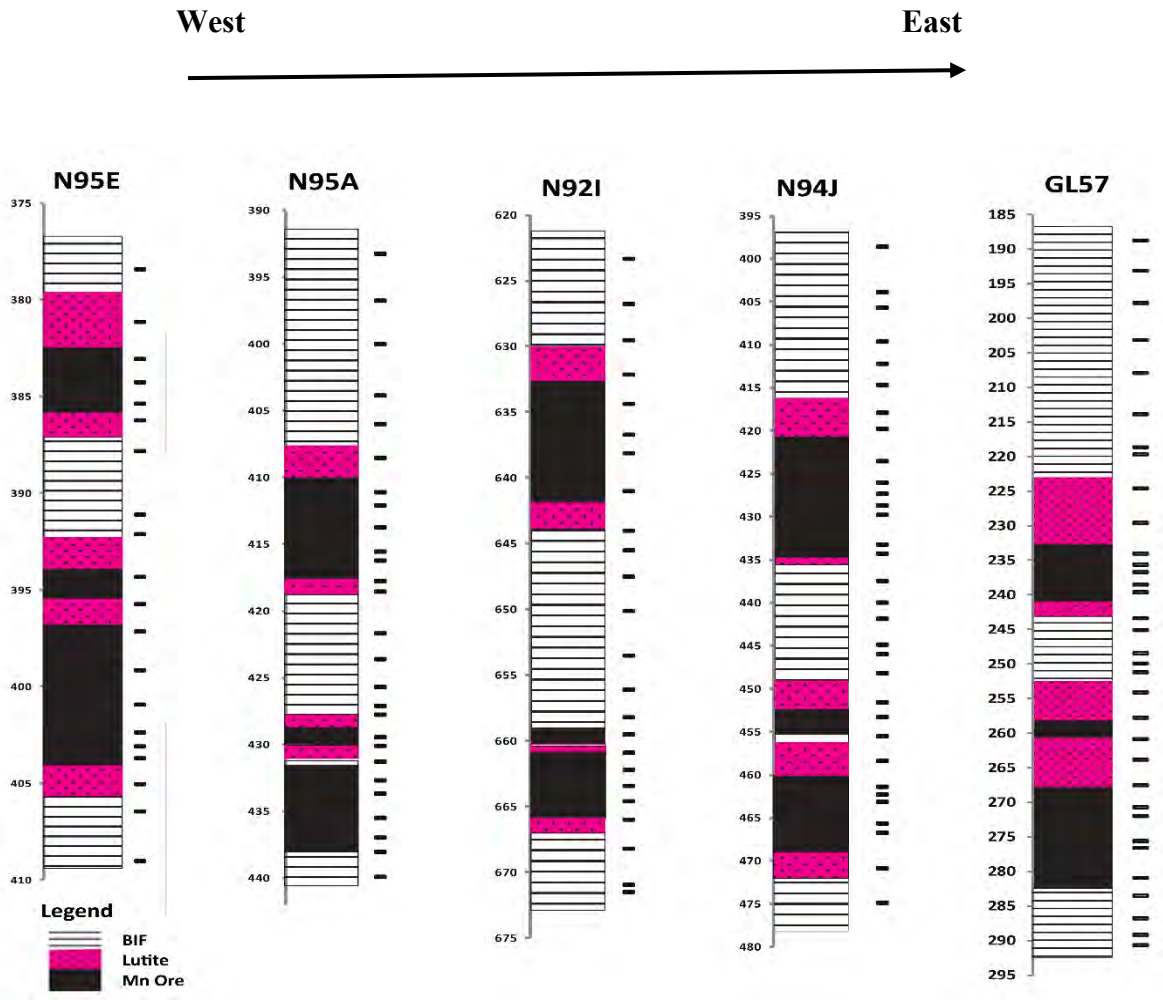

Figure 1. 6: Stratigraphic representation of all drill core intersections showing the three major rock types of the Hotazel Formation. The positions of samples collected are represented by horizontal stripes.

CHAPTER 2. REGIONAL GEOLOGY

2.1. The Transvaal Supergroup

The Transvaal Supergroup in southern Africa was deposited between the late Archean to Paleoproterozoic (2.65 – 2.05Ga) and is well preserved in the Kaapvaal craton (Gutzmer and Beukes, 1996; Moore et al., 2001). It is developed into two major successions known as the Transvaal and the Griqualand West basins situated in the north-eastern and central segments of the Kaapvaal craton respectively (Figure 2.1). These two successions have high lithostratigraphic similarities, especially in the lower parts of the successions, and as such they have both been included under the stratigraphic term "Transvaal Supergroup" (Beukes, 1983; Moore et al., 2001). The Griqualand West basin of the Transvaal Supergroup is developed in the Northern Cape and Northwest provinces in South Africa, and also extends into the southernmost parts of Botswana to the north (Beukes, 1983). The sequence as developed in the Northern Cape Province is the region of focus in this thesis.

The Transvaal Supergroup occurs along the western margin of the Kaapvaal Craton. This region is bordered by a sharp tectonic contact with the Kheis metamorphic province to the west and by the Namaqua-Natal Metamorphic Belt to the southwest (Figure 2.1). The Kheis orogeny event (1180-1280Ma) is the major cause of many large-scale low-angle thrusts onto the western margin of the Kaapvaal craton (Eglington, 2006).

The simplified stratigraphy of the Transvaal Supergroup is shown in figure 2.2. The Griqualand Supergroup is subdivided into the Ghaap and Postmasburg Groups with the lower part of the stratigraphy represented by the Ghaap Group. Siliciclastic rock units (mudstones and wackes), occur with carbonates and lava at the base within the Schmidtstrif Subgroup, and with minor iron-formation at the top where the Koegas Subgroup formed. In between those two Subgroups lies the Ghaap Group which comprises dominantly carbonates rocks of the Campbellrand Subgroup overlain by thick units of iron-formation of the Asbesheuwels subgroup. The latter are further subdivided into the Kuruman and Griquatown Formations (Moore et al., 2001).

The top Group of the Transvaal Supergroup is the Postmasburg Group and is approximately 1 km thick. The Makganyene Formation comprises of a unit of glacial diamictite which forms the basal part of the Postmasburg Group (Tsikos et al., 2003). A thick succession of continental flood-type basaltic andesites of the Ongeluk Formation overlies the Makganyene

diamictites. The Ongeluk Formation contains volcaniclastic and ferruginous ("jasper") breccia deposits in its uppermost part, on which rests the Hotazel Formation (Beukes, 1983; Moore et al., 2001). The Hotazel Formation comprises a chemo-sedimentary succession of iron-formations interbedded with three layers of manganese-rich sedimentary rock, which together with the overlying Mooidraai carbonates represents the youngest episode of chemical sedimentation in the Transvaal Supergroup.

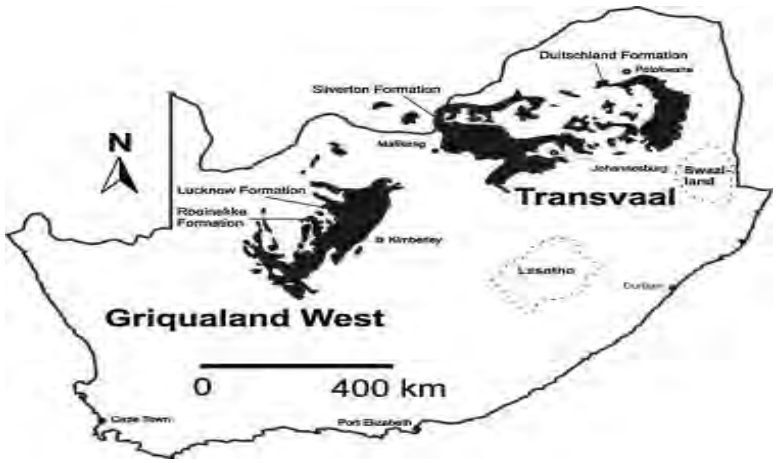

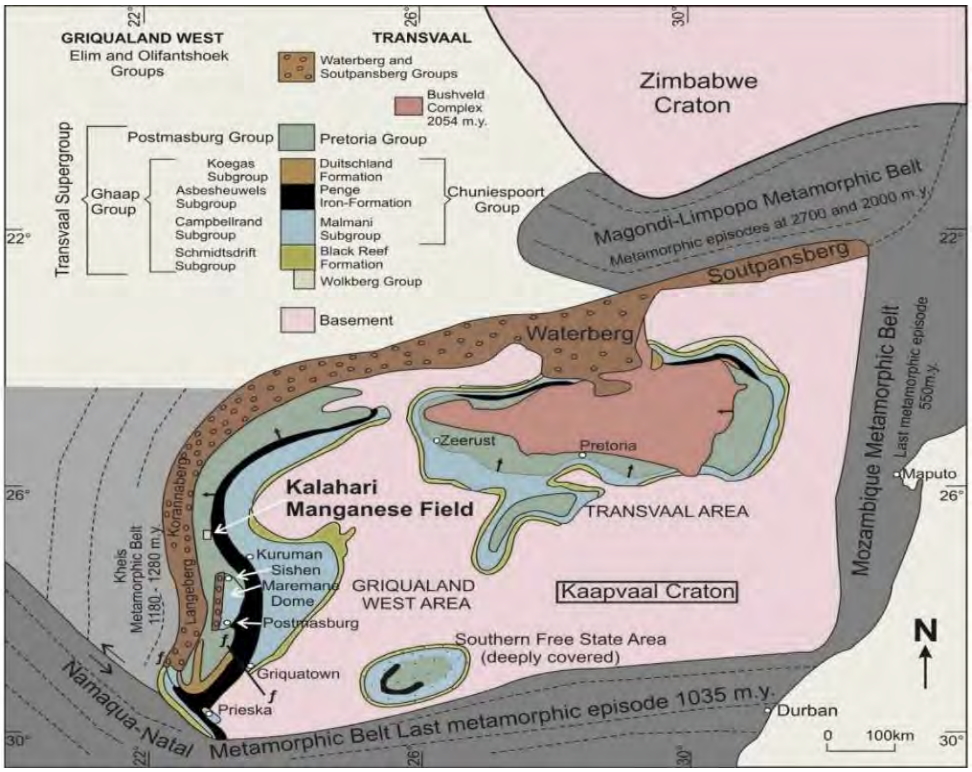

Figure 2. 1: (Above): Simplified map of South Africa showing the distribution of the erosional relic of the Transvaal Supergroup. (Below): Geological map illustrating the distribution of tectonic terranes associated with the Transvaal Supergroup. This map also shows the Kaapvaal and Zimbabwe Craton (Modified after Cairncross and Beukes, 2013)

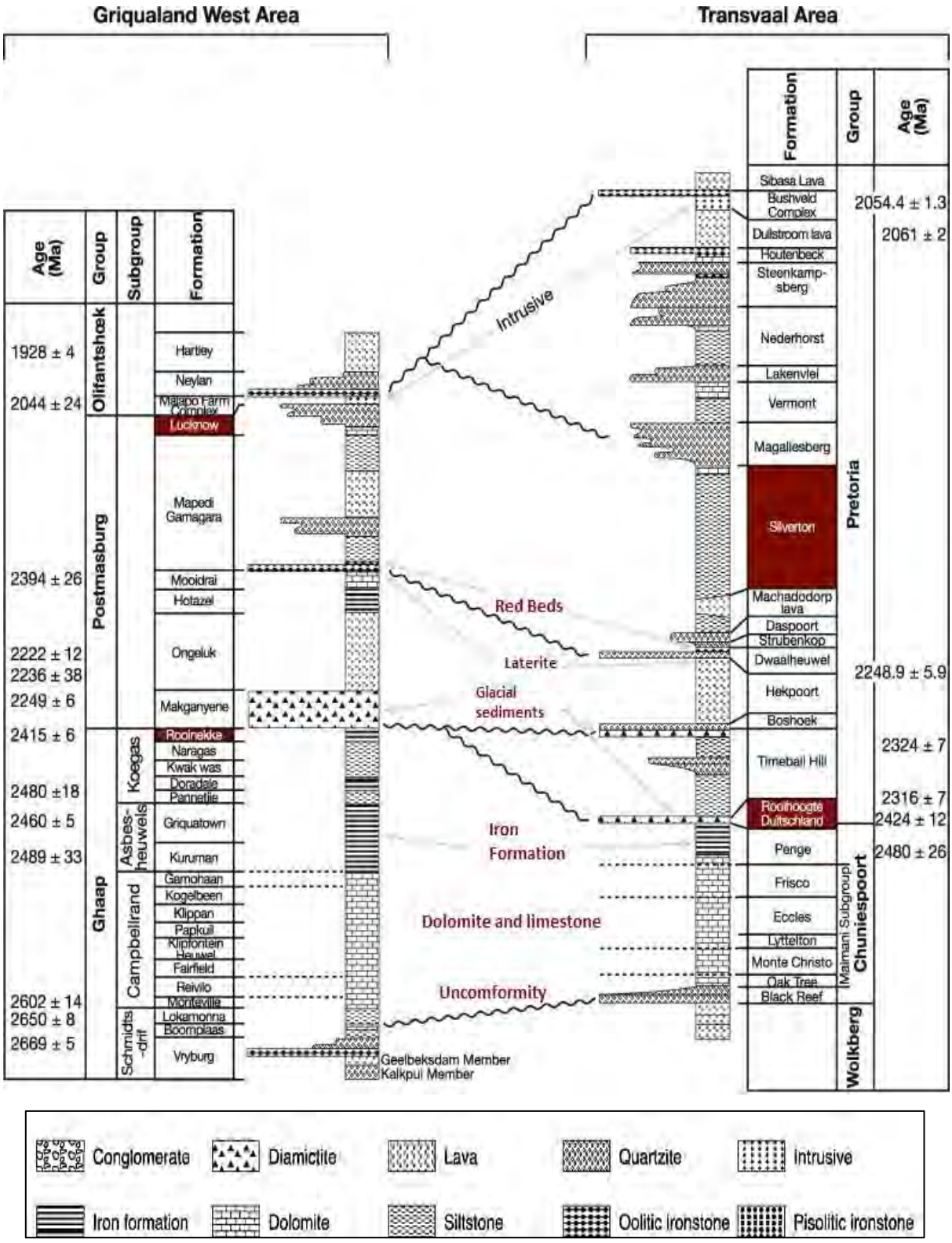

Figure 2. 2: Stratigraphic successions showing the lithological units in the Griqualand West and Transvaal areas of the Transvaal Supergroup (modified after Coetzee, 2001; Blignaut, 2017).

2.2. The Hotazel Formation

The Hotazel Formation develops almost exclusively in the KMF, which represents one of its five erosional relics. In the KMF, Cenozoic sands and calcretes of the Kalahari Formation, except for certain areas where exploitation has been taking place, cover the Hotazel Formation. The Hotazel Formation is conformably underlain by pillow basalts, andesitic lava and hyaloclastite of the Ongeluk Formation, and it grades into carbonate rocks of the overlying Mooidraai Formation. There appears to have been no significant time gap inferred between the age of the chemical sediments of the Hotazel Formation and that of the volcanic rocks of the Ongeluk Formation (Schier et al., 2020). The stratigraphy of the Hotazel Formation and adjacent lithologic units point to the conclusion that these rocks must have been deposited in a relatively shallow marine sedimentary environment (Gutzmer and Beukes, 1996).

The classic stratigraphic configuration of the Hotazel Formation is three cycles of iron formation interbedded with Mn ore beds (upper, middle and lower). The transitions between the two rock types for each cycle is usually gradational and consists of very fine-grained, carbonate-rich hematite rock described in the literature as hematite lutite (Kleyenstuber 1984; Tsikos et al., 2003). The three Mn ore beds have been interpreted as the centers of three chemical sedimentary cycles forming the Hotazel lithostratigraphic (Figure 2.3).

The causes for this most striking and important characteristic of the rocks of the Hotazel Formation – namely the cyclicity of the sedimentary Mn-Fe rich ore beds – are not conclusively proven or constrained. It is thought that their development must have been the result of periodic changes in Eh-pH conditions at the paleoenvironment of deposition, which were probably modulated as a result of tectonically or even climatically driven transgression-regression cycles (Beukes, 1983; Tsikos and Moore, 1997; Schneiderhan et al., 2006).

Over many years, the lowermost manganese unit has been the major focus of mining activity due to its substantial thickness and Mn content. However, relative thicknesses of the Mn beds vary greatly (Tsikos et al., 2003), while the grades of manganese ore become highest in the hydrothermally affected northernmost KMD where Wessels-type ore occurs. Therefore, the column of Figure 2.3 is only indicative of the regional lithostratigraphy of the Hotazel Formation and applies mainly to the southernmost part of the KMD where the low-grade Mamatwan Mn mine is situated.

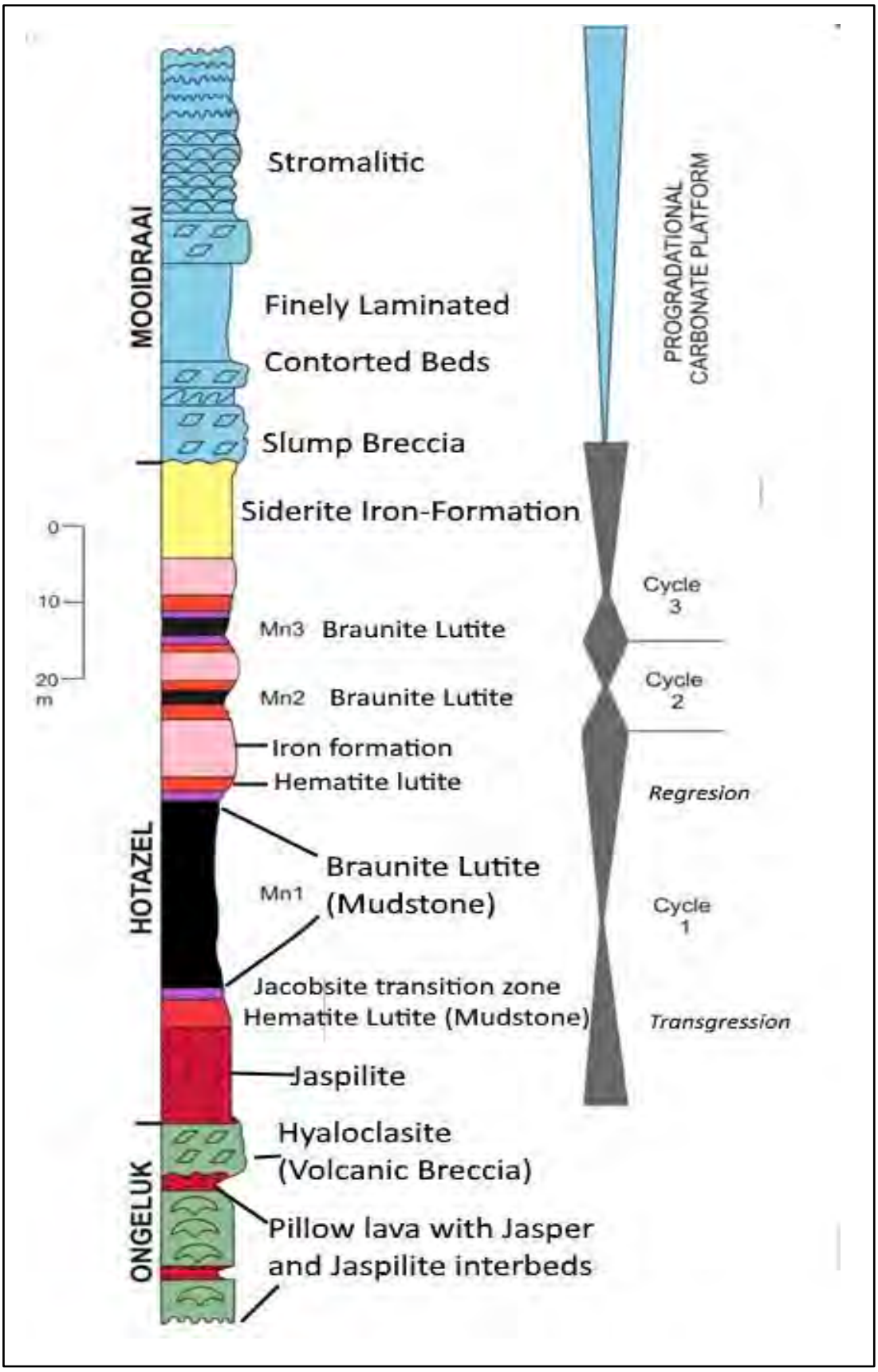

Figure 2. 3: Stratigraphic profile of the Hotazel Formation showing the three Mn ore beds and alternating BIF layers. The overlying Moodraai Formation and underlying Ongeluk Formation is also shown modified after Cairncross and Beukes, 2013; Blignaut, 2017)

CHAPTER 3. PETROGRAPHY

3.1. Introduction

Previous petrographic studies on the rocks of the Hotazel Formation concentrated mainly on individual lithological units, especially the lower Mn ore body, due to its high economic value. Some authors (Tsikos, 1999; Tsikos and Moore, 1997) focussed only on the Banded Iron Formation (hereafter referred to also as BIF) hosting the Mn ore layers. As stated earlier, this work will focus on the entire Hotazel Formation, hence the main aim of this chapter is to describe and illustrate the bulk petrographic and mineralogical characteristics of the rock types observed, as a backbone to the detailed geochemistry that follows. Naturally more attention will be given to the Mn ores due to their mineralogical and textural variations that have been discussed by many authors (Cairncross et al., 2000; Gutzmer and Beukes, 1996), but this chapter will also investigate and briefly characterise the mineralogy of the BIFs and the hematite lutite. Cairncross and Beukes (2013) stated that more than 140 mineral species have been identified within the Wessel-type ores, which also characterise the mine area dealt with in this thesis. This mineralogical diversity is not encountered here, and relates more to the variable effects of alteration by hydrothermal fluids moving on highly localised scales through structures such as faults, fractures, thrust planes, or even along the Mapedi/Gamagara unconformity (Gutzmer and Beukes, 1995, 1996; Kleyenstüber, 1984; Tsikos et al., 2003).

In this chapter, observations and results of representative samples from each of the main three lithologies in the Hotazel formation are presented using the optical microscope for petrographic description, Scanning Electron Microscope (SEM) and powder X-ray Diffraction (XRD) analysis. The BIFs will be described holistically and not in the context of each drillcore. On the other hand, the two Mn ore bodies will be described more systematically in connection with the five drill cores and with emphasis on the mineralogical and textural variation present in both the upper and lower ore bodies vertically (i.e. within a given drillcore) and laterally.

In terms of macroscopic characteristics of the ores, there is often clear textural variation between the different types. As mentioned also in the introduction earlier, one of the key distinguishing features is the presence or absence of carbonate laminations and so-called ovoids, that is, oval-shaped micro-features abundantly observed in the low-grade ores of the

Mamatwan type, which constitutes the likely protolith to the high-grade equivalents. This suggests that primary textures may or may not be preserved during high-grade ore formation.

3.2. **Banded Iron Formation**

Macroscopically, throughout the five boreholes, the BIFs vary primarily in terms of colour and style of banding.

1) Fe-enriched BIF. This occurs prominently at the stratigraphic top of two (i.e. N92I, GL57) of the five boreholes. These are typically dark red to brown in colour, massive, with faint banding, and dominated by fine-grained crystalline hematite. Visible pore spaces (vugs) are seen here which may inform processes of mineral (silicate or carbonate) dissolution during their development. Similar BIF is seen also immediately below the upper Mn bed and above and below the lower Mn bed. The almost mono-minerallic hematitic appearance of this BIF permits the use of the term “massive hematite”, as coined by Tsikos (1999).

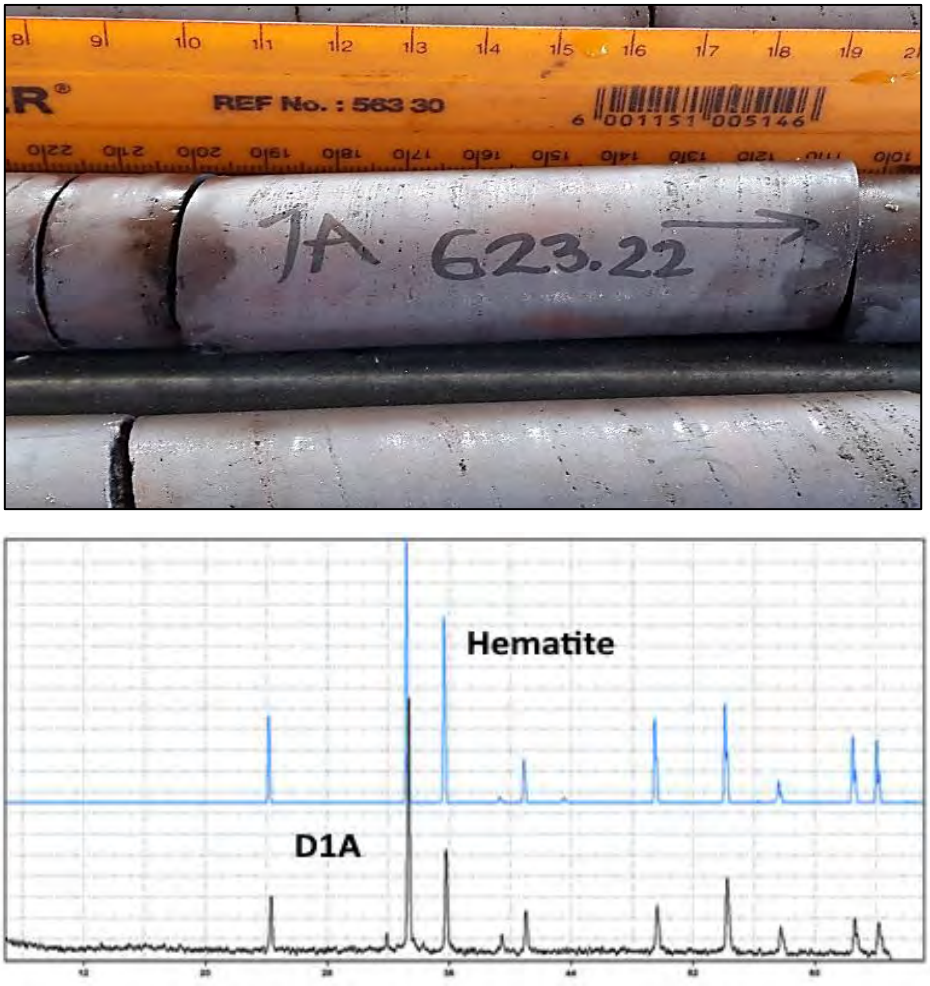

Figure 3. 1. Image and XRD results of BIF seen at the top of the stratigraphy of borehole N92I. XRD shows only hematite in the the massive ore. Sample D1A at 623.22 m

2) BIF with well-banded hematite and chert-rich layers (Fig. 3.2). This is the BIF that characteristically dominates essentially all drillcores. The microbands can vary in thickness from 2mm up to 6mm, alternating between chert and microcrystalline hematite. These iron-formations have little or no carbonate minerals but when they do, they occur as minor siderite/ankerite or calcite. The chert layers comprise of fined-grained microcrystalline quartz with smaller interspersed grains or inclusions of hematite, locally intergrown with minor minute carbonate grains. The hematite bands consist of hematite microcrystals that are usually fine-grained but occasionally also form granules and irregularly clustered masses. Although the thickness of bands can vary across samples, there is not much variation in the actual grain size of quartz or hematite across the stratigraphy.

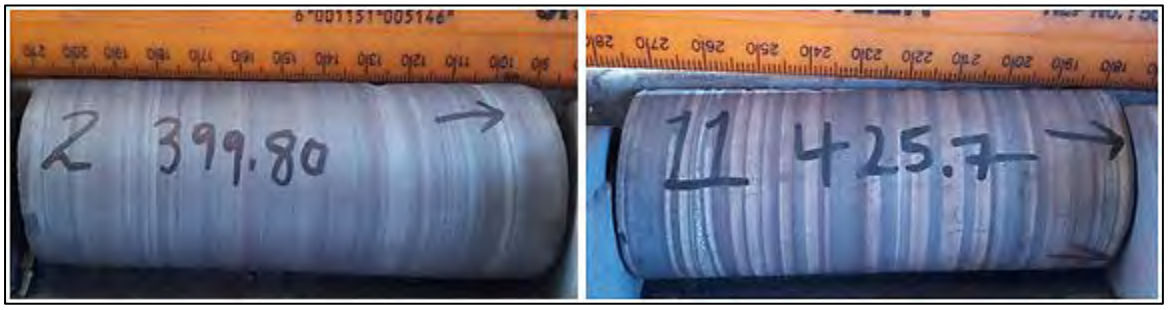

Figure 3. 2. Image of chert-hematite BIFs from borehole N95E. Depths of sampling is shown.

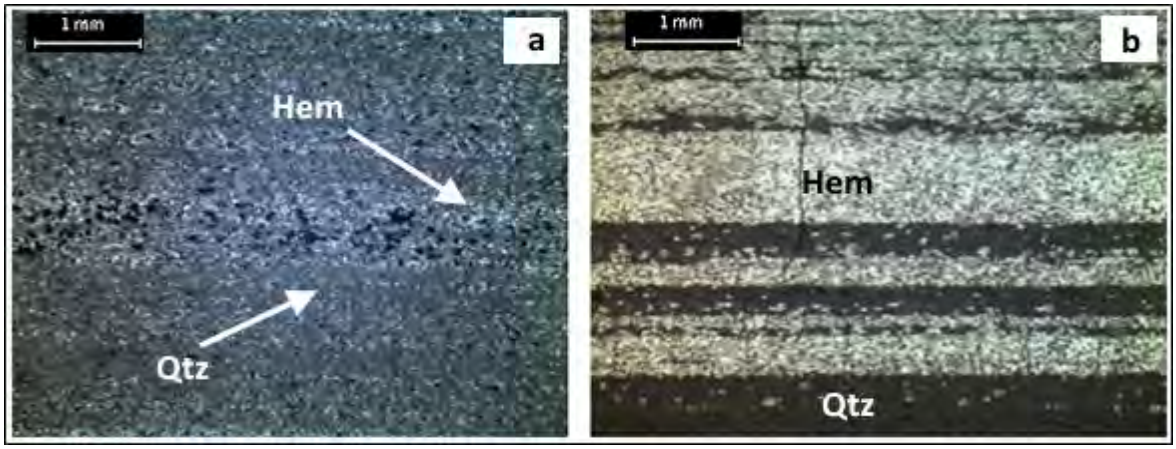

Figure 3. 3 A) Reflected light image of crudely banded fine-grained quartz and hematite in BIF from drillcore N95A, sample T2. B) Reflected light image of thicker, well-defined bands of quartz and microcrystalline hematite in BIF of sample T11 from drillcore N95A.

3) Alkali-rich BIF. This is seen in some drillcore sections below the upper manganese ore layer, between the middle and lower ore layers and locally below the lower ore layer too. They are characterised by cloudy or yellowish-grey bands (~2-5 mm) dominated by the mineral aegirine. Aegirine is a sodic, Fe(III) pyroxene which has been reported before by Tsikos and Moore (2005). The aegirine-rich bands alternate with hematite-rich ones and contain little to no quartz. Band thickness varies from mm-thick aegirine-dominated laminae alternating with microcrystalline massive hematite bands, or in thicker bands occurring in subordinate amounts along with laminated quartz-hematite assemblages. When coarse enough, the aegirine shows distinct pleochroic behaviour from green to brown-green. Colour zonation indicating possible compositional variation is also present in large grains where the rim appears darker than the core. Where abundant, the presence of aegirine in the samples is confirmed by XRD analysis as shown in the appendix.

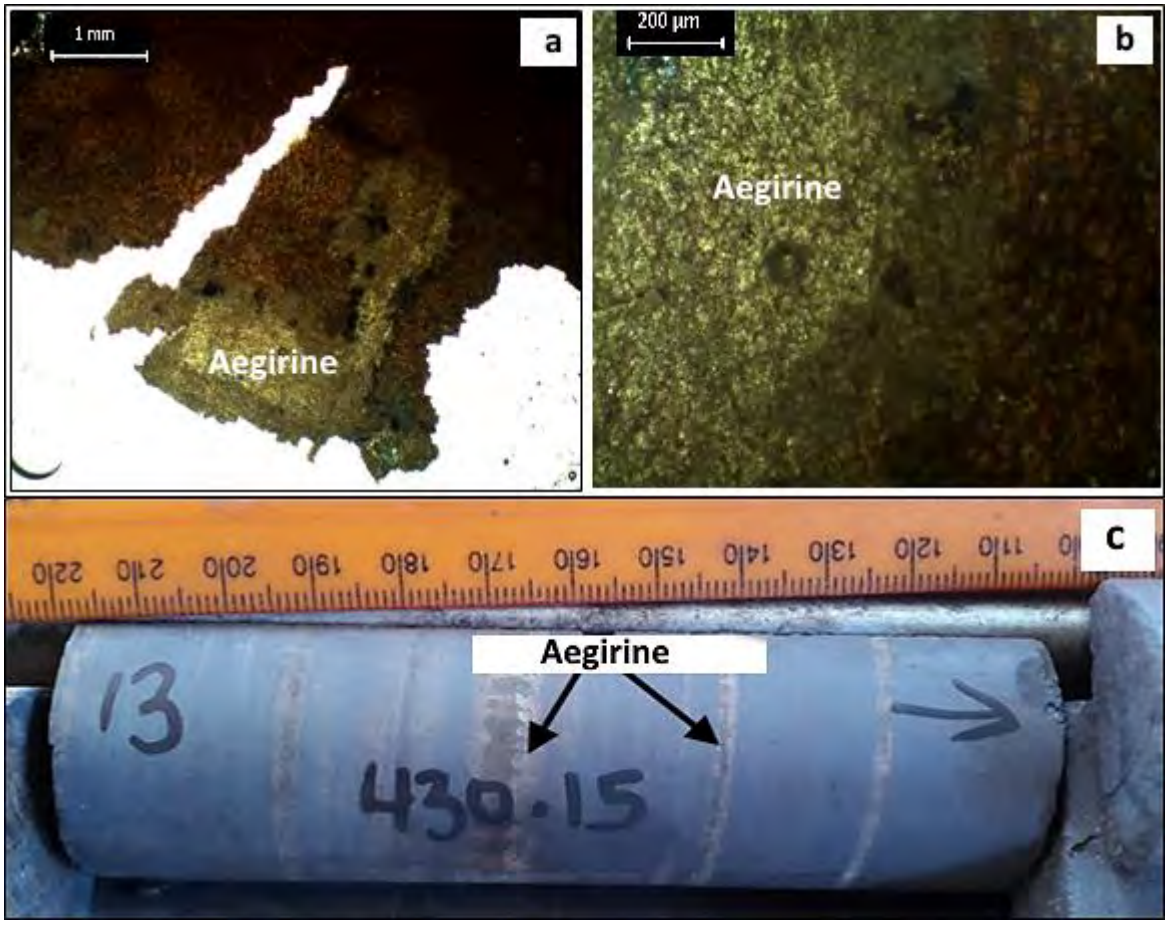

Figure 3. 4. Low (A) and high (B) magnification of relatively coarse-grained aegirine occuring in BIFs of sample T13 from N95A. C) Image of the BIF with bands of aegirine ranging from 2-5 mm.

3.3. Mn Ore mineralogy

3.3.1. Drillcore N95E

Macroscopically, the upper Mn ore body in this drillcore shows a laminated appearance and is black but with a reddish tint suggesting the possible presence of increased hematite in the ore. The lower Mn ore body is also black but lacking a reddish tint, more massive, containing fine grains of silicate and carbonate (white) minerals.

Figure 3. 5. Image of samples from the upper (left) and lower (right) Mn ore bodies of N95E. Depths of sampling are shown.

Microscopically, there are subtle textural variations between the upper and lower ore bodies. The upper ore body shows a more massive, finer-grained texture while the lower ore body shows evidence of re-crystallisation effects, and thus has relatively larger grain (>100 μm) sizes. The top layer consists predominantly of braunite with hausmannite and the subordinate presence of hematite, andradite and minor barite. The lower ore body consists predominantly of coarse-grained (>250 μm) hausmannite with marokite, braunite II, and lesser calcite and barite.

Hausmannite and braunite in the upper ore body occur generally as anhedral masses intergrown with fine-grained andradite. Hausmannite in the lower ore body occurs as more subhedral, coarser grains along with braunite II, marokite and calcite. Hausmannite is the more dominant Mn mineral in the lower ore layer indicating a hausmannite-rich end-member of Wessels-type ore, with increased Ca hosted in marokite and calcite. Apparent replacement textures as complex intergrowths appear to develop between the hausmannite and the marokite, with calcite included mainly in the latter. Regarding the upper Mn ore layer, it is comparatively braunite/hausmannite-rich with associated Fe-rich mineralogy (hematite and andradite). There is therefore an apparent difference in Fe and Ca contents from the bulk mineralogy between the two ore layers. Finally, minor barite is present within both ore

bodies. In the top layer, it occurs as fine-grained anhedral grains interstitial to hausmannite and andradite, while in the lower layer it occurs as fine anhedral inclusions within coarse hausmannite.

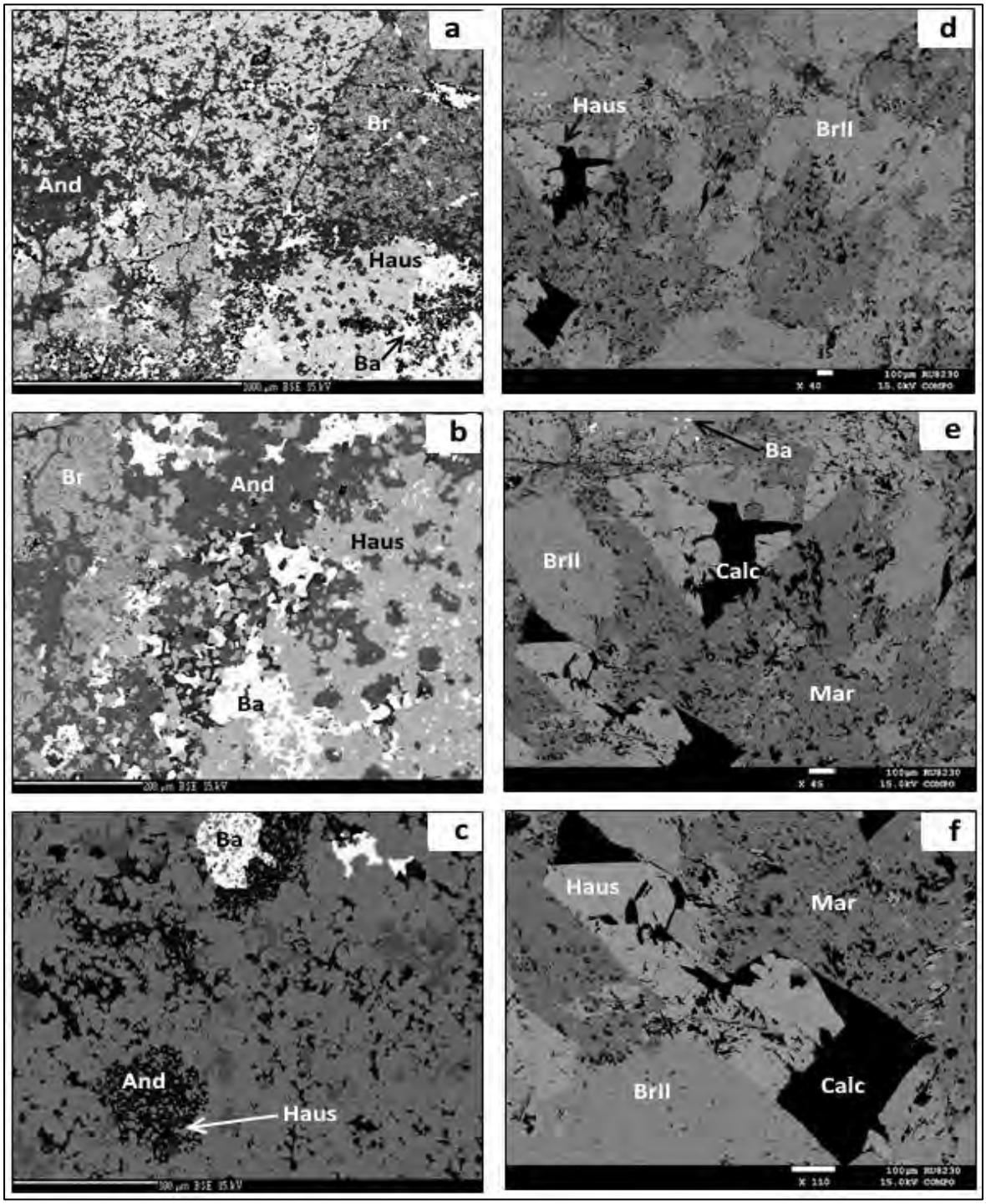

Figure 3. 6. Mineralogical and textural associations of the top (a-c) and lower ore bodies (d-f) of N95E. BSE images showing (a) braunite and hausmannite with andradite and barite (b) high magnification image of hausmannite intergrown by andradite and interstitial barite (c) higher magnification image of andradite with hausmannite (d) hausmannite and braunite II (e) hausmannite grains with interstitial barite and (f) marokite intergrown with hausmannite.

3.3.2. Drillcore N95A

Macroscopically, manganese ore samples from drillcore N95A are dark grey to black with minor secondary carbonates infilling pore spaces, fractures, along bedding planes and within the ore matrix. The upper ore layer displays generally a far more vuggy appearance by comparison to the lower layer which appears massive and compact without any signs of secondary porosity

Figure 3. 7. Image of samples from the upper (left) and lower (right) Mn ore bodies of N95A.

Microscopically, there are no major mineralogical variations between the upper and lower Mn ore layers as they are both dominated by the mineral braunite. The upper ore layer consists predominantly of coarse braunite grains in banded domains in association with hematite and patches of andradite. The lower Mn ore layer consists predominantly of a structureless, massive matrix of medium- to fine-grained braunite with fine inclusions and intergrowths of andradite and calcite. Hausmannite is a minor mineral constituent in the lower ore body occurring as fine-grained assemblages in ovoid-like and vein-like structures associated with andradite and calcite.

With regard to the textural appearance of andradite, in the top Mn ore body it is fined-grained, anhedral, and occurs along the contact of the braunite and hematite bands while in the lower ore layer it appears to form as a replacement mineral occurring with hausmannite in apparent oval-shaped structures. It is therefore possible that, in this instance at least, the andraditic assemblage may have formed from replacement processes of pre-existing carbonate ovoids, thus sourcing its Ca from the latter.

In summarizing, both ore layers in drill core N95A are dominated by braunite. Geochemically, however, the upper ore layer is expected to be more iron-rich due to the distinct presence of hematite, while the lower ore layer would be relatively less iron-rich but more calcic due to the presence of calcite together with andradite.

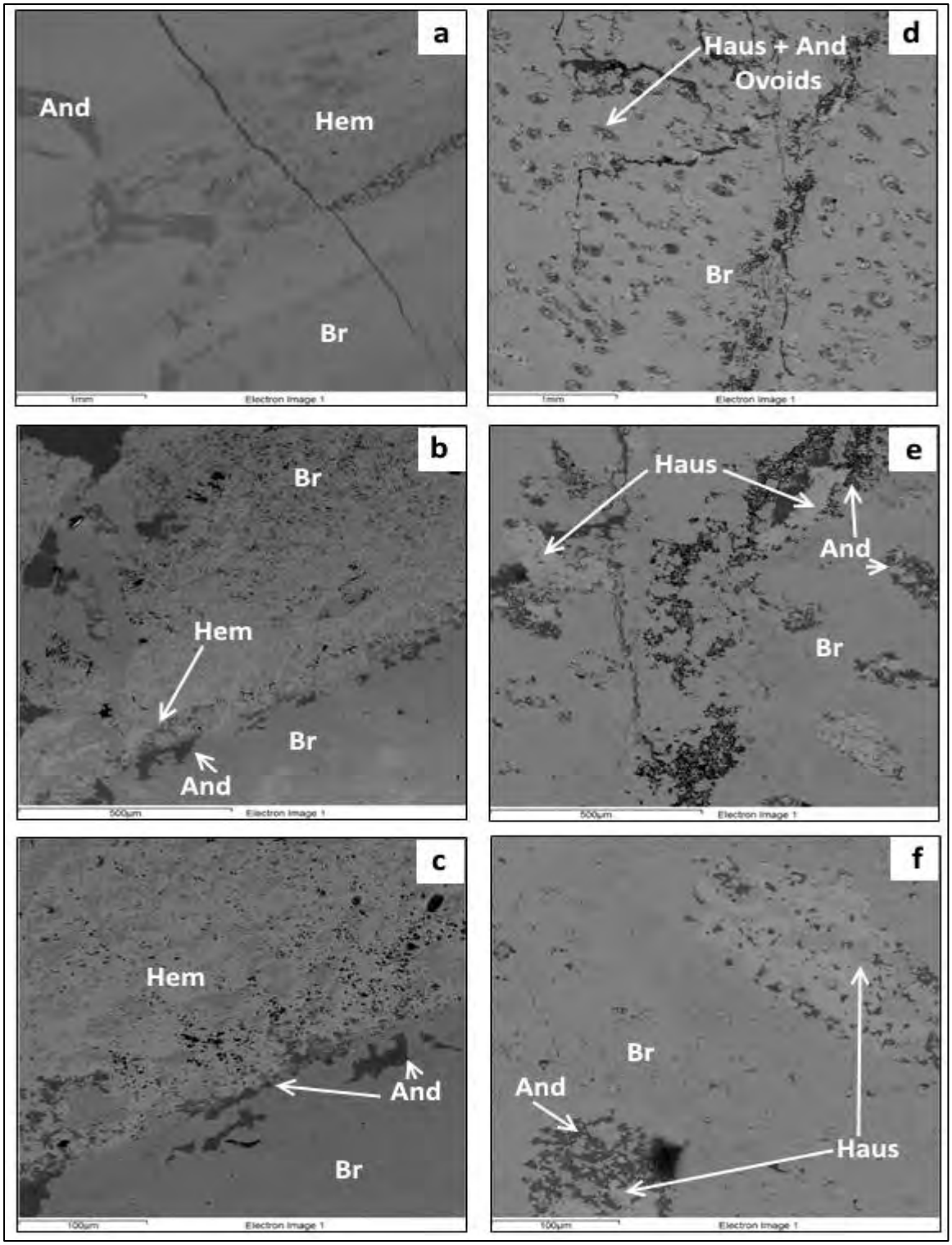

Figure 3. 8. Mineralogical and textural associations of the top (a-c) and lower ore bodies (d-f) of N95A. BSE images showing (a) braunite matrix with andradite and hematite (b) braunite grains occurring in vein-like structures and as overgrowths with andradite (c) anhedral andradite grains apparently replacing braunite and hematite (d) braunite matrix with andradite and hausmannite (e) hausmannite grains occurring with andradite and calcite (f) andradite and hausmannite apparently replacing an assemblage of braunite, hematite and calcite.

3.3.3. Drillcore N92I

Macroscopically, the top Mn ore layer in drillcore N92I is dark grey to black in colour with apparent laminations and fine carbonate grains in an otherwise massive type ore. The lower ore layer is also dark grey to black and likewise with carbonate grains apparently developing in pore spaces and along bedding planes visible within a massive to laminated matrix.

Figure 3. 9. Image of samples from the upper (left) and lower (right) Mn ore bodies of N92I.

Mineralogically, the top ore layer consists predominantly of braunite II and hausmannite with lesser occurrences of andradite, calcite and minor marokite and manganite. The lower ore layer consists predominantly of braunite and hausmannite with minor andradite and calcite. Braunite II thus makes up the matrix of the top ore layer, with laminated textures that are defined by fine-grained carbonate grains occurring along planes of layering. The andradite seems to be developing as reaction (replacement?) textures at the expense of hausmannite, calcite and manganite. Hausmannite generally occurs as fine- to coarse-grained aggregates, along grains of braunite II, and in intergrowths with andradite in both ore bodies.

Andradite occurs in both ore layers in minor abundances, typically as fined grained intergrowt.hs with hausmannite and hematite. As stated earlier, patches of andradite grains appear to form through a reaction of braunite with hausmannite and hematite. The hematite itself is minor but laths of hematite are seen at microscopic level occurring within grains of hausmannite in the top Mn orebody. The upper ore layer therefore shows at least some signs of increased iron content which is comparable to what has been observed in previous drillcore intersections.

Marokite and manganite occur in lesser abundances in the top ore body but were identifiable through the use of XRD analysis (see APPENDIX). In this respect, some similarity can be drawn between the mineralogy in this drillcore and that of drillcore N95E in an earlier section.

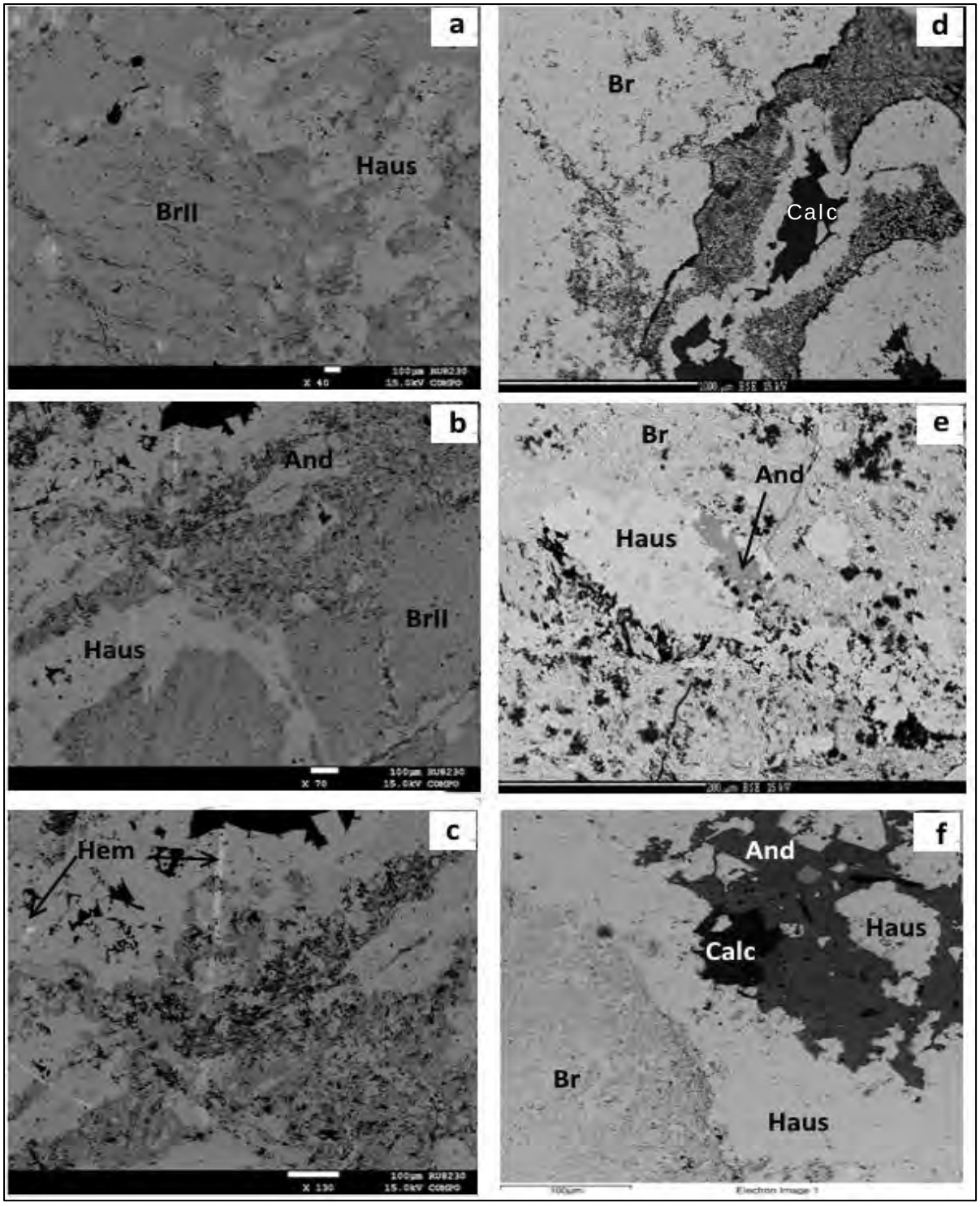

Figure 3. 10. Mineralogical and textural associations of the top (a-c) and lower ore layers (d-f) of N92I. BSE images showing (a) matrix of predominantly braunite II occurring with hausmannite (b) braunite II with laminated structures defined by carbonates and hausmannite concentration along braunite II-rich domains (c) hematite laths enclosed in hausmannite grains (d) braunite matrix containing calcite and andradite (e) hausmannite grains apparently replaced by braunite and andradite (f) hausmannitee intergrowt.hs with calcite and andradite.

3.3.4. Drillcore N94J

Macroscopically, the samples from the top Mn ore layer of N92J are dark grey to black in colour with abundant pore spaces and occasional carbonate veins in otherwise massive ore. The lower ore body is also dark grey to black and appears more carbonate-rich in the form of pore and vug-fills within a massive manganiferous matrix.

Figure 3. 11. Image of samples from the upper (left) and lower (right) Mn ore layers of N94J.

Microscopically, there are only minor textural and mineralogical variations between the top and lower Mn ore layers in this drillcore. According to unpublished bulk analyses of the ores from this drillcore made available to the author at the time of selection by the mining company (ASSMANG), this drill core contains some of the highest grade ore in the Nchwaning area with reference to both ore layers. This is reflected in the bulk mineralogy as both orebodies consist predominantly of hausmannite. The top ore layer has a relatively simple mineral assemblage of hausmannite, calcite and minor barite, while the lower ore layer has a comparable mineral assemblage of hausmannite with lesser braunite and calcite.

In the top ore layer, hausmannite essentially occurs as a coarse-grained massive matrix, but finer-grained domains in association with calcite and barite, or even hausmannite-bearing calcite veins, are also seen. In the lower ore body, hausmannite similarly occurs as a coarse-grained matrix mineral containing subordinate braunite and calcite. The braunite in the lower ore layer occurs mainly as subhedral to euhedral, coarse-grained aggregates with hausmannite and associated minor calcite. Calcite occurs in both ore bodies as coarse, often subhedral grains in a hausmannite matrix, and as carbonate infill in veins and pore spaces.

Finally, barite occurs in the top layer as a minor to trace mineral component interstitially with hausmannite and calcite. It is important to note that this drill core shows the least evidence of iron addition/metasomatism compared to the other upper layers of ore from the Nchwaning area, due to the obvious absence of Fe-rich mineral constituents such as hematite and andradite.

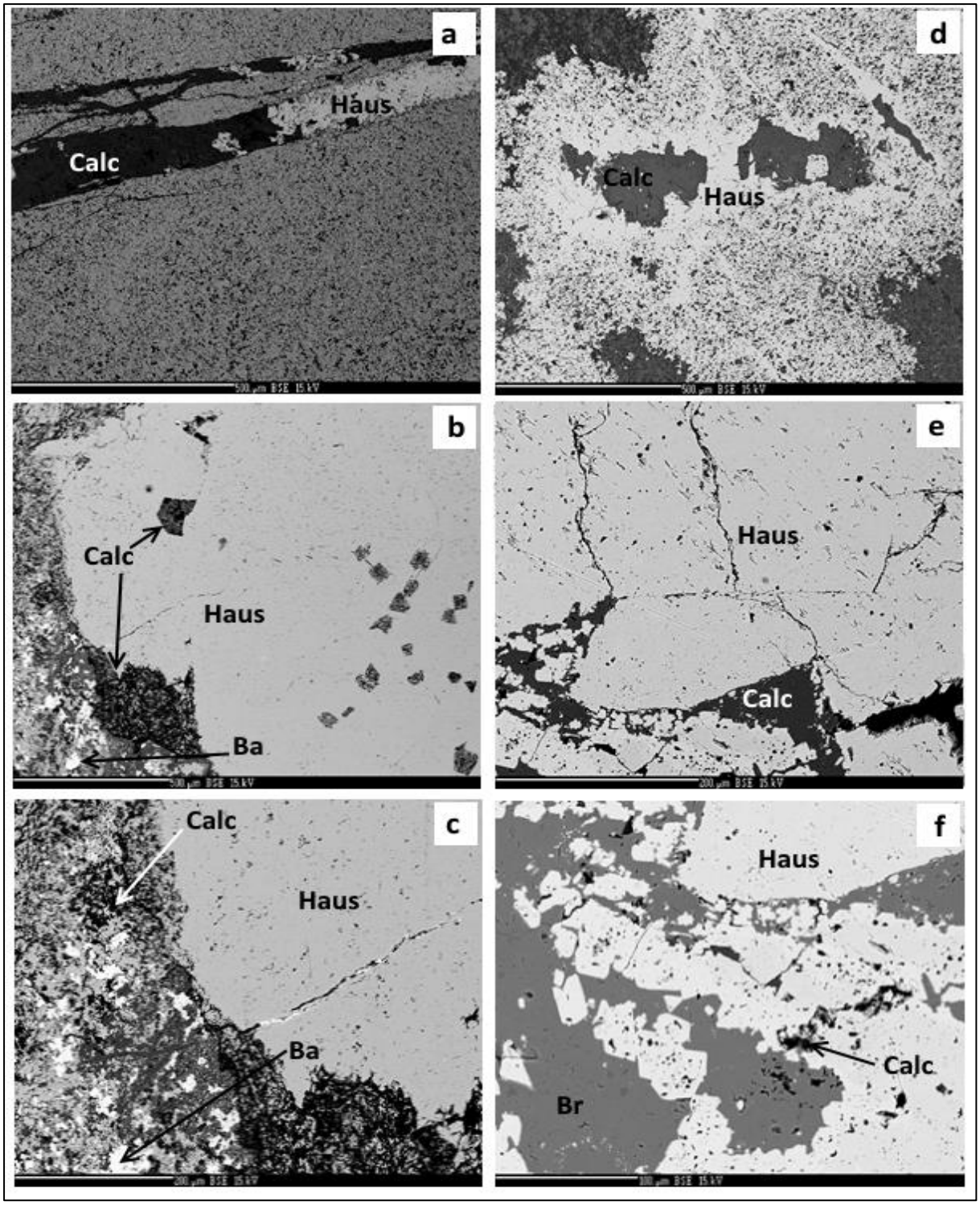

Figure 3. 12. Mineralogical and textural associations of the upper (a-c) and lower ore bodies (d-f) of N94J. BSE images showing (a) hausmannite grains occurring in vein-like structure with calcite (b) matrix of predominantly coarse-grained hausmannite occurring with calcite and specs of barite (c) higher magnification image of the replacement of hausmannite (d) euhedral calcite grains in matrix of hausmannite (e) higher magnification of the replacement texture in image (d) (f) higher magnification of image (e) showing of hausmannite overgrown by braunite and calcite.

3.3.5. Drillcore GL57

As described earlier, GL57 is a core from the low-grade Gloria Mn mine, but it distinguishes itself in that it has high-grade Wessels-type ore in the top ore layer and low-grade Mamatwan-type ore in the lower ore layer. Macroscopically, samples from the top ore layer are dark grey to black in colour and massive, with faintly visible laminations. On the other hand, the lower ore layer is light to dark grey with abundant white ovoids and laminations in a matrix of very fine-grained massive manganese ore, akin to typical Mamatwan-type ore.

Figure 3. 13. Image of samples from the upper (left) and lower (right) Mn ore bodies of GL57.

Microscopically, the top ore layer is markedly different to the low-grade lower ore layer in terms of mineral textures, compositions, mineral proportions and grain sizes. The top ore layer consists predominantly of hausmannite that is coarse-grained, subhedral to anhedral and in association with carbonate. Braunite is also present within this ore in lesser abundances and is generally finer-grained and interstitial to the larger hausmannite grains. The carbonate occurs in apparent vein-like features and are predominantly made up of calcite, but dolomite is also present as anhedral to subhedral intergrowths within calcite grains.

The lower ore layer consists predominantly of a fine-grained groundmass of braunite and carbonate laminae and ovoids (calcite and kutnahorite), with minor barite and hausmannite. At low magnification, the samples show ovoids of lenticular calcite grains at the core and braunite grains along the rims associated with fine-grained kutnahorite. The hausmannite can be seen in the BSE images but the kutnohorite is not easily identifiable, but its presence is confirmed through XRD results shown in the APPENDIX. In BSE images, calcite occurs mainly as dark grey, fine grains dominating the matrix of the samples and forming the cores of the ovoids. Braunite, on the other hand, occurs as the lighter, fine-grained mineral in the groundmass and along the ovoid rims. Kutnahorite occurs also mainly along ovoid rims whereas barite also occurs interstitially along braunite and calcite laminations.

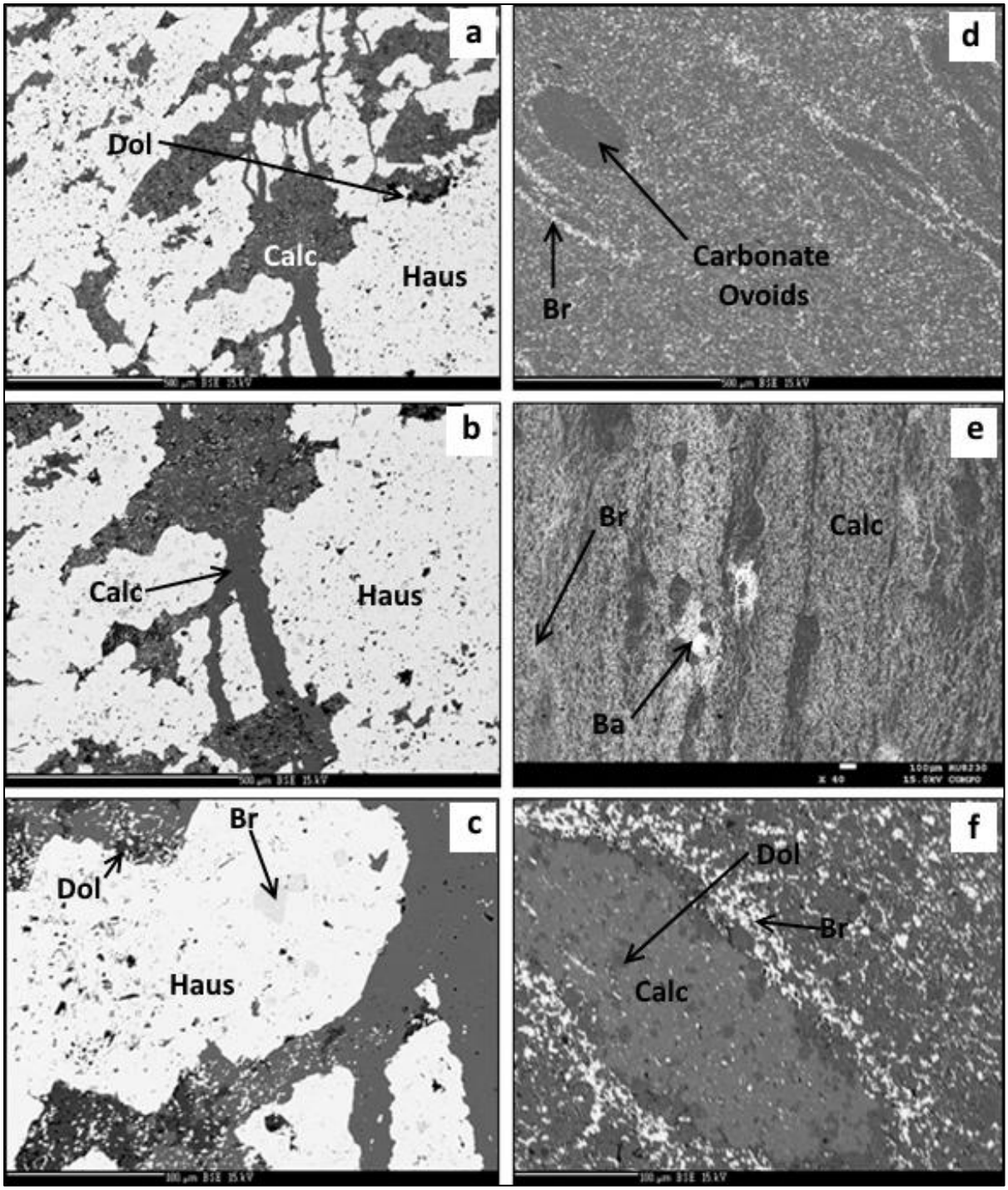

Figure 3. 14. Mineralogical and textural associations of the upper (a-c) and lower ore layers (d-f) of GL57. BSE images showing (a) low and (b) high magnification of predominantly hausmannite matrix occurring with calcite veins and fine grains of dolomite (c) Hausmannite grains with fine-grained braunite (d) primary textures of low-grade braunite-rich ores with lenticular calcite grains (e) similar textures with barite grains occurring in association with calcite and braunite (f) high-magnification of ovoids with calcite grains in the core and fine-grained braunite at the rim. Kutnahorite occurs within the core and along the rim of the ovoids.

3.4. Summary

Table 1 presents a summary of the mineralogical assemblages of the BIF and Mn ore bodies in each of the five drill cores used in this study. The mineral phases included here have been identified using a combination of optical microscopy, qualitative SEM analysis and XRD results shown in the APPENDIX, where modal abundances were sufficiently high for detection.

Table 1. Mineralogical composition of the BIF and Mn ore bodies from all of the drill cores determined by SEM, XRD and petrographic analysis. (XXXX – dominant mineral phase, >50%; XXX-major mineral phase, 20-50%; XX-minor mineral phase, 5-20%; X-trivial, <5%)

Banded Iron Formation	N95E	N95A	N92I	N94J	GL57
Aegirine	XX	X	-	-	-
Hematite	XXXX	XXX	XXXX	XXX	XXX
Quartz	XX	XXX	XX	XXX	XXX
Upper Mn Ore Body					
Andradite	XX	XX	XX	-	-
Barite	X	X	-	XX	-
Braunite	XXX	XXXX	-	-	X
Braunite II	-	-	XXX	-	-
Calcite	X	-	X	XX	X
Dolomite	-	-	-	-	X
Hausmannite	XXX	-	XX	XXXX	XXXX
Hematite	XX	XX	X	-	-
Manganite	-	-	X	-	-
Marokite	-	-	X	-	-
Lower Mn Ore Body					
Andradite	-	XX	XX	-	-
Barite	X	X	-	-	X
Braunite	-	XXX	XXX	XX	XXX
Braunite II	XX	X	-	-	-
Calcite	XX	XX	XX	XX	XXX
Dolomite	-	X	-	-	X
Hausmannite	XXX	X	XXX	XXXX	X
Kutnahorite	-	-	-	-	X
Hematite	-	-	-	-	-
Manganite	-	-	-	-	-
Marokite	XX	-	-	-	-

% = abundance by Volume

The BIFs in the study area are dominantly hematite- and chert-rich with variable relative modal abundances between the two minerals depending on sample size and sampling philosophy, as the rocks are intrinsically banded and thus heterogeneous. An important characteristic in the examined subfacies of BIF is the massive hematite occurences which suggest that major leaching of the original BIF protolith has occurred to produce such compositionally extreme materials. These massive hematite samples are seen usually at the top of the stratigraphy of drill cores in close contact with the overlying Hotazel-Mapedi/Gamagara unconformity, but can also be seen deeper in the stratigraphy. Aegirine-rich BIF and lutites are seen below and above the Mn ore bodies exactly as described previousy by Tsikos & Moore (2005), but these ocurrences were only observed in selected drill cores (N95E and N95A) from the west of the study area at Nchwaning.

Macroscopically, the Mn ore samples look all texturally similar with the exception of the lower ore layer of drillcore GL57. The Mn ores have a banded/layered to massive appearance; when layered or banded, these range from less than 1mm to approximately 1cm in thickness. Colours usually grade from grey or reddish in colour depending primarily on iron (as hematite) content, while some samples have domains of carbonate occurring roughly along layering. These multi-scale laminations are usually less visible in ore that is more carbonate-poor and Mn-rich, in broad agreement with previous petrographic studies (Gutzmer and Beukes, 1996, 1997).

Microscopically, the Mn ore beds in all five drill cores show mineralogical and textural variations both laterally and vertically (i.e., across the two Mn ore beds within a drillcore). The top Mn ore body generally shows textures indicative of possible replacement reactions, as well as a relatively higher Fe content by comparison to the lower Mn ore layers, which themselves appear to be relatively more Ca-rich (in carbonate and locally in marokite). Dolomite is a mineral only seen in appreciable abundance in the higher-grade upper layer of drill core GL57 from the Gloria area,

Generally, on the basis of mineralogy alone, the lower ore bodies only appear to be of higher-grade in two drillcores (N95E and N92I) with respect to Mn, than the top ore layers. In other situations, drill cores have similar mineralogy (N95A and N94J) and thus expectedly similar Mn grades in both ore layers, while in the case of drillcore GL57, the lower ore body is Mamatwan-type ore and thus of substantially lower Mn abundance than the top ore layer in

the same drillcore. The less common Mn minerals marokite and manganite were only observed in drill cores that are associated with high contents of Fe in the top ore layer.

From the above, it becomes apparent that there is a great diversity in mineralogy and textures of the individual Mn ore layer intersections laterally and even within a single drill core. Considering that the protolith ores of the Mamatwan type have consistently a higher grade lower ore layer than the top ore layer, it would mean that fluid-induced enrichment processes away from vertical faults according to the model by Beukes *et al*. (1995) and Gutzmer and Beukes (1995) cannot readily explain the erratic spatial distribution observed in Mn contents and mineralogical compositions. There is already a strong indication, therefore, that alteration must have occurred at multiple stages and potentially involving more than one structural features in the KMF.

CHAPTER 4. BULK-ROCK GEOCHEMISTRY

4.1. Introduction

The assessment of whole rock geochemical data for major, trace and rare-earth elements in the Hotazel Formation, is the focus of this chapter. Samples from all five drill cores described earlier were analysed for whole-rock geochemical compositions using combined XRF (major) and LA-ICP-MS (trace element) analyses performed at the University of Stellenbosch (see APPENDIX for methodology and tabulated data). The samples represent the Hotazel Formation across both the BIF and Mn ore layers alike. All geochemical results are presented and evaluated in this chapter using a variety of plots and diagrams, with the purpose of understanding lateral and vertical geochemical relationships across the Nchwaning and Gloria areas, in order to elucidate the controls thereof.

As indicated earlier, the context for the critical treatment and cross-comparison of the results of this study lies in the PhD study by Dr X. Mhlanga of Rhodes University (Mhlanga, 2020), which dealt with the Hotazel Formation at Gloria mine in comprehensive and high-resolution detail for both BIFs and Mn ores across the entire sequence as it is develop there (full raw data used from that thesis are also included in the APPENDIX). The Gloria mine exploits low-grade, Mamatwan-type carbonate-rich Mn ore and forms the ideal protolith for comparisons with high-grade ore equivalents in the geographically adjacent Nchwaning mine. This is further supported by the similar relative thickness relationships in the broader area of the Gloria-Nchwaning-Wessels mines in the northern KMD. The Gloria data have therefore formed an invaluable benchmark for the evaluation and interpretation of the gochemical results presented in the sections that follow.

4.2. Comparative Geochemistry

Results of selected major and trace elements are graphically illustrated in Figures 4.1 - 4.15 to show geochemical variations across stratigraphy for all five boreholes and for the presumed protolith intersection of the Hotazel Formation from Gloria mine. Stratigraphic variation plots for all boreholes are shown using three (3) elemental groupings namely major elements, transition metals and “alkalis” (alkali + alkali earths). Elements that show very low and largely invariant concentrations (below detection limit for most samples) such as high field strength elements (HFSEs), have been omitted from further

consideration. Although Zn is a transition metal, it has been grouped with Pb and the alkalis because it appears to show better correlation with some of them (e.g. Ba) that might be important to note. In every instance, corresponding profiles are also shown for drillcore GL136 of Mhlanga (2020) to enable direct comparisons.

4.2.1. Drillcore N95E

Geochemical profiles for MnO, Fe_2O_3, CaO, MgO and SiO_2 across the Mn ore layers of drillcore N95E are illustrated in Figure 4.1. Although lower in sample resolution, there are a number of features that appear to be conservatively preserved in the profiles of N95E by comparison to the signals of protolith section GL136: the most striking is the maxima in Mn as recorded in the three Mn beds (i.e. including the thin Mn "marker" between the two main Mn ore beds). Comparable maxima are also seen to correspond with the peaks in Mn, although the distribution of CaO values appears asymmetric with peaks near the top Mn-BIF contact in both ore-beds. In terms of bulk Fe content, the rocks appear to be especially rich at the topmost BIF section. In the same samples, total Si contents are rather low, and values only approach those of a classic BIF (*i.e.* 30-45 wt.% SiO_2) in a couple of samples from the middle and upper BIF sections.

In terms of alkali profiles (Fig. 4. 2), there is a striking similarity in the profiles of Ba, Sr, Pb and Zn in terms of overall geometry, suggesting a likely strong mineralogical control for these elements. It is suggested that the main mineral controlling these behaviours is barite, whereby Ba is being substituted in the mineral structure by the other elements in a divalent state. From a quantitative point of view, it also appears as though the higher alkali values are recorded in the top half of the stratigraphic section where Na contents also appear to be correspondingly higher with high aegirine in the BIF. This suggests a broadly homogeneous input of alkalis into the rocks (e.g. bulk rock Ba concentration exceeds 10000 ppm in the upper Mn ore layer by comparison to the protilith which records a maximum Ba concentration of ~1000 ppm).

Finally, transition metals show little stratigraphic variability (Fig. 4.3). Maxima in Co abundance appears to coincide with Mn-rich beds and adjacent lutites in a conservative fashion from the protolith. Elevated Cu appears to concur with high Co but only in the upper Mn bed. The remaining elements show invariant behaviour and only peak at the topmost and very hematite-rich sample near the overlying unconformity with the Mapedi/Gamagara strata.

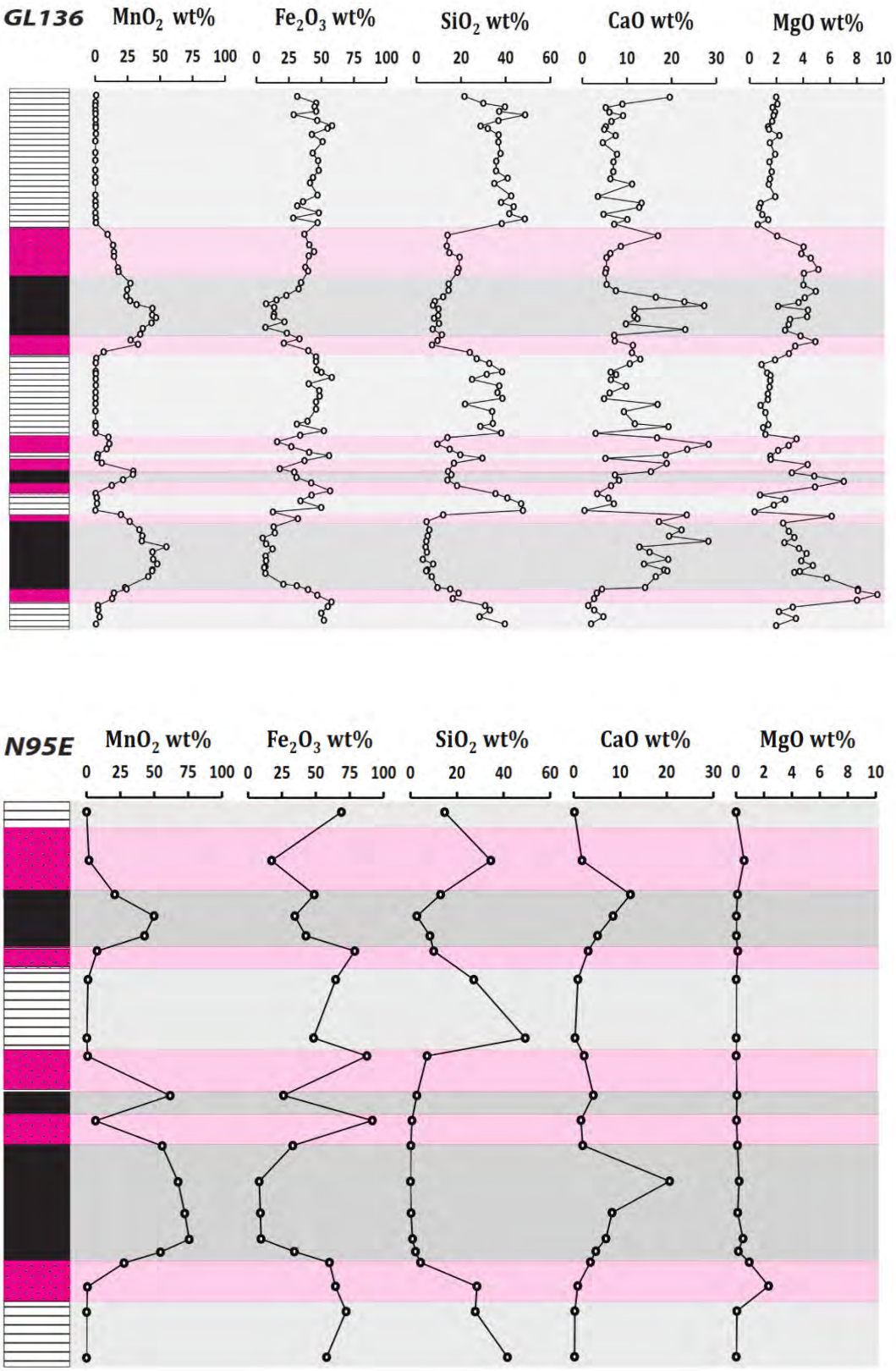

Figure 4. 1: Comparative variation plots of selected major elements for the statigraphic profiles of drillcores N95E and the protolith (GL136). Stratigraphic columns are not to scale, but shows relative thickness for the lithological units.

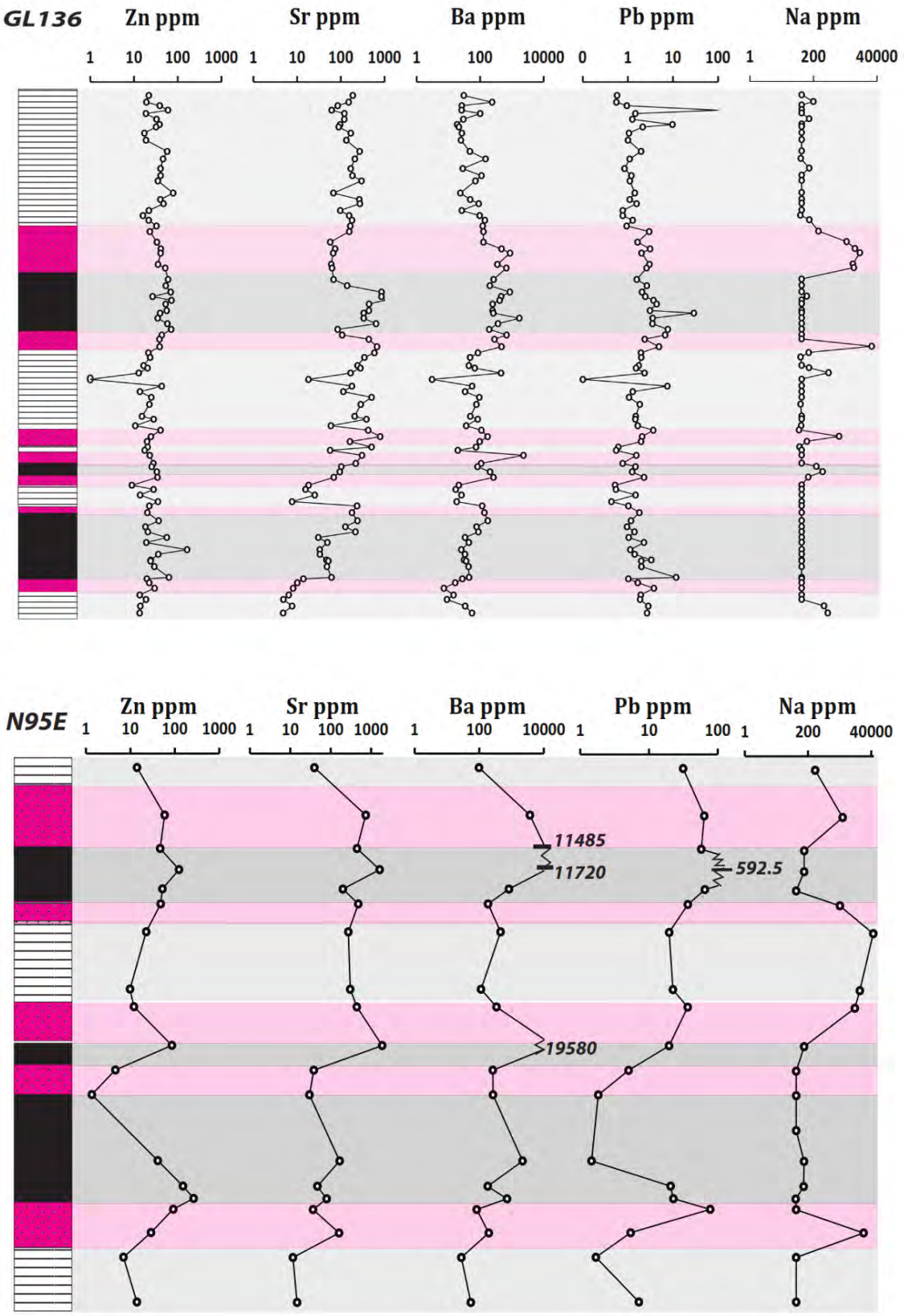

Figure 4. 2: Comparative variation plots of selected alkali elements for the statigraphic profiles of drillcores N95E and the protolith (GL136). Stratigraphic columns are not to scale, but shows relative thickness for the lithological units.

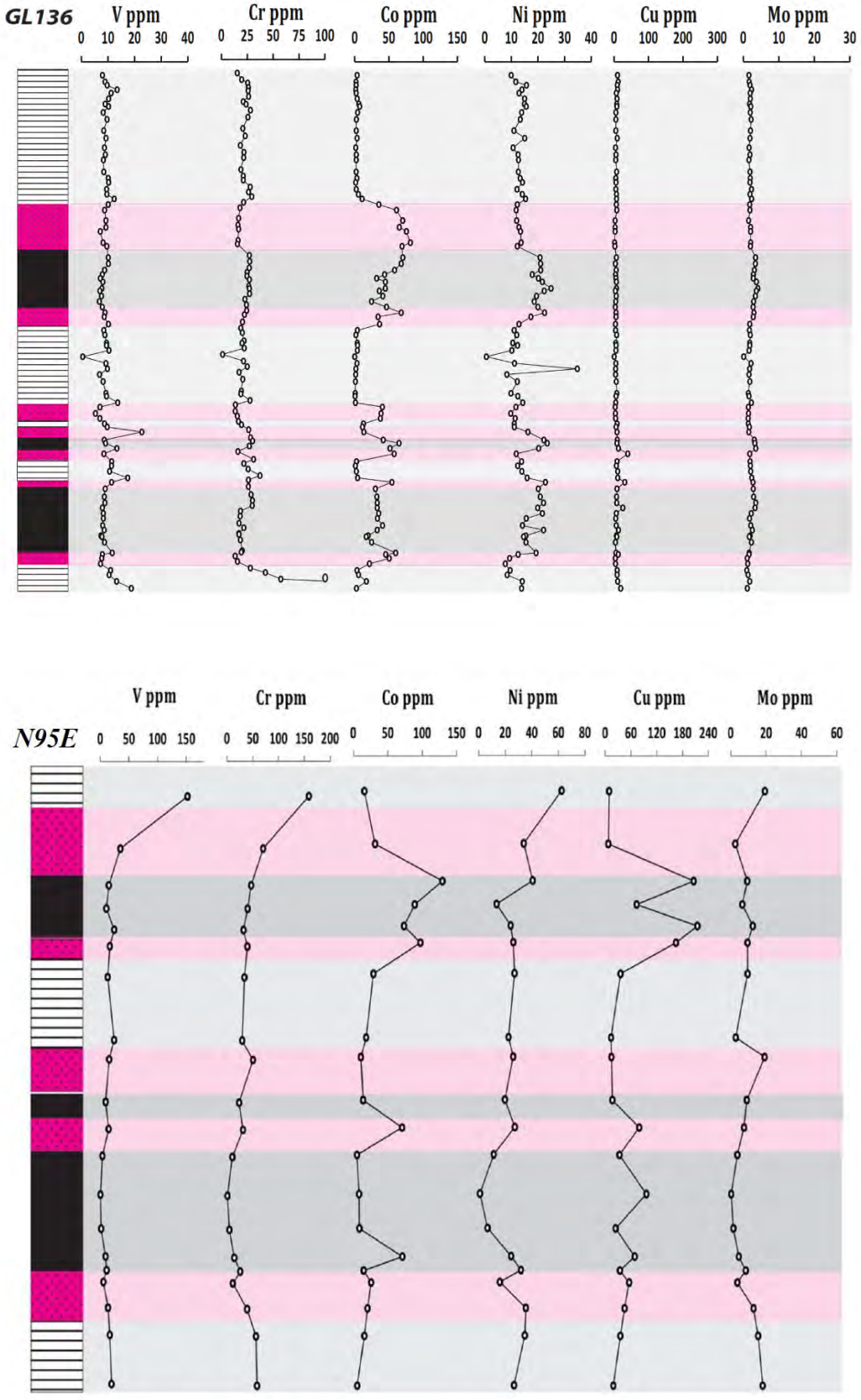

Figure 4. 3: Comparative variation plots of selected transitional elements for the statigraphic profiles of drillcores N95E and the protolith (GL136). Stratigraphic columns are not to scale, but shows relative thickness for the lithological units.

4.2.2. Drillcore N95A

Major element geochemical profiles for bulk MnO, Fe_2O_3 and SiO_2 concentrations across drillcore N95A (Fig. 4. 4), show a very similar geometry to the ones from protolith drillcore GL136. This suggests that all three of these profiles record a broadly conservative behaviour in relation to the protolith, almost as though they have not changed at all except for the loss of carbonate from the rock and resultant relative enrichment of each of them on a percentage basis. With regard to CaO and MgO, concentrations in drillcore N95A are very low for the largest part of the Hotazel stratigraphy compared to the corresponding protolith. This confirms the almost complete loss of carbonate in the ore as one cause of enrichment of the remaining immobile major elements. The slightly higher values of Ca in the upper Mn ore layer reflect the ore content in andradite, but also part of the contained braunite probably containing Ca in its structure (i.e. as braunite II). The corresponding MgO concentrations in the same ore layer are very low, precluding occurrence of Ca with Mg in dolomitic carbonate. However, high CaO and correspondingly high MgO with a very similar profile geometry are seen at the lowermost part of the N95A section, specifically the lower part of the lower Mn layer and underlying iron formation. This suggests the presence of dolomitic carbonate in the rocks, which appears similar to dolomitic-facies IF seen elsewhere in the Nchwaning area (Tsikos et al., 2003) developing with depth from the Olifantshoek-Hotazel unconformable contact.

Alkali profiles (Fig. 4. 5) show some interesting relationships that both agree and disagree in part with what is seen in the previous drillcore N95E. Specifically, the bulk rock Ba, Sr, Zn and Pb profiles all appear similar, but their peaks appear to be confined to the core of the Mn layers whereas the interlayered BIFs record very low values. This suggests a more selective distribution of barite in the Mn ore beds which would account for all four elements. The corresponding Na profile is very insightful by comparison, because it shows minima in Na abundance in the Mn ores but peaks in the hematite lutites. This is similar to the report of Tsikos and Moore (2005) which explains high aegirine concentrations in the transitional hematite lutites as the result of host-rock control, and specifically the low abundance of Si in the Mn ores and high in the lutite transitions and BIF.

Finally, transition metals in drillcore N95A (Fig. 4. 6) show little variability across stratigraphy, with the exception of Cu and Co. Both these elements appear to peak and correlate directly with each-other, suggesting possibly a localised “nugget” effect in the ore due to the presence of a possible Cu-Co accessory (sulphide?) mineral.

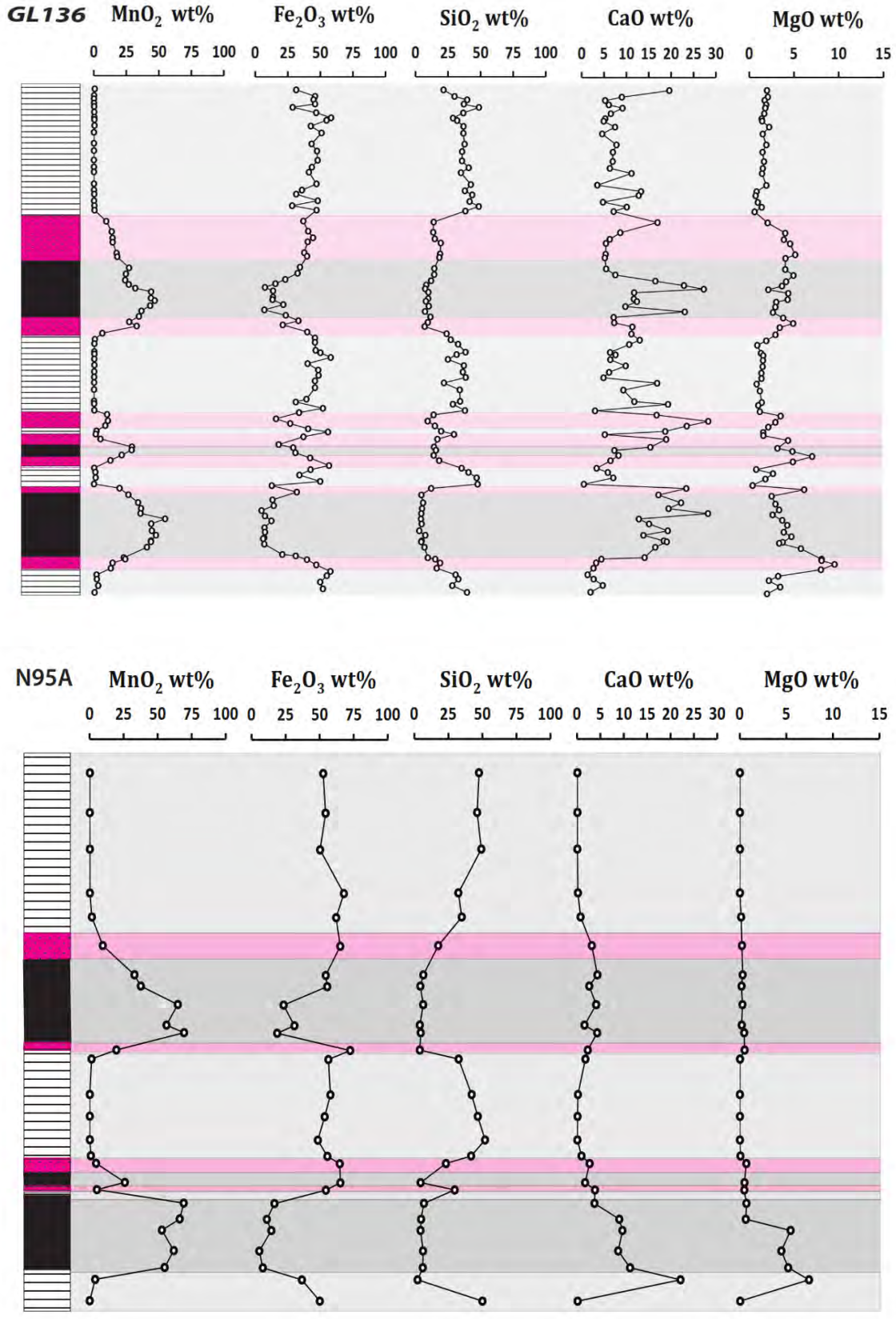

Figure 4. 4: Comparative variation plots of selected major elements for the statigraphic profiles of drillcores N95A and the protolith (GL136). Stratigraphic columns are not to scale, but shows relative thickness for the lithological units.

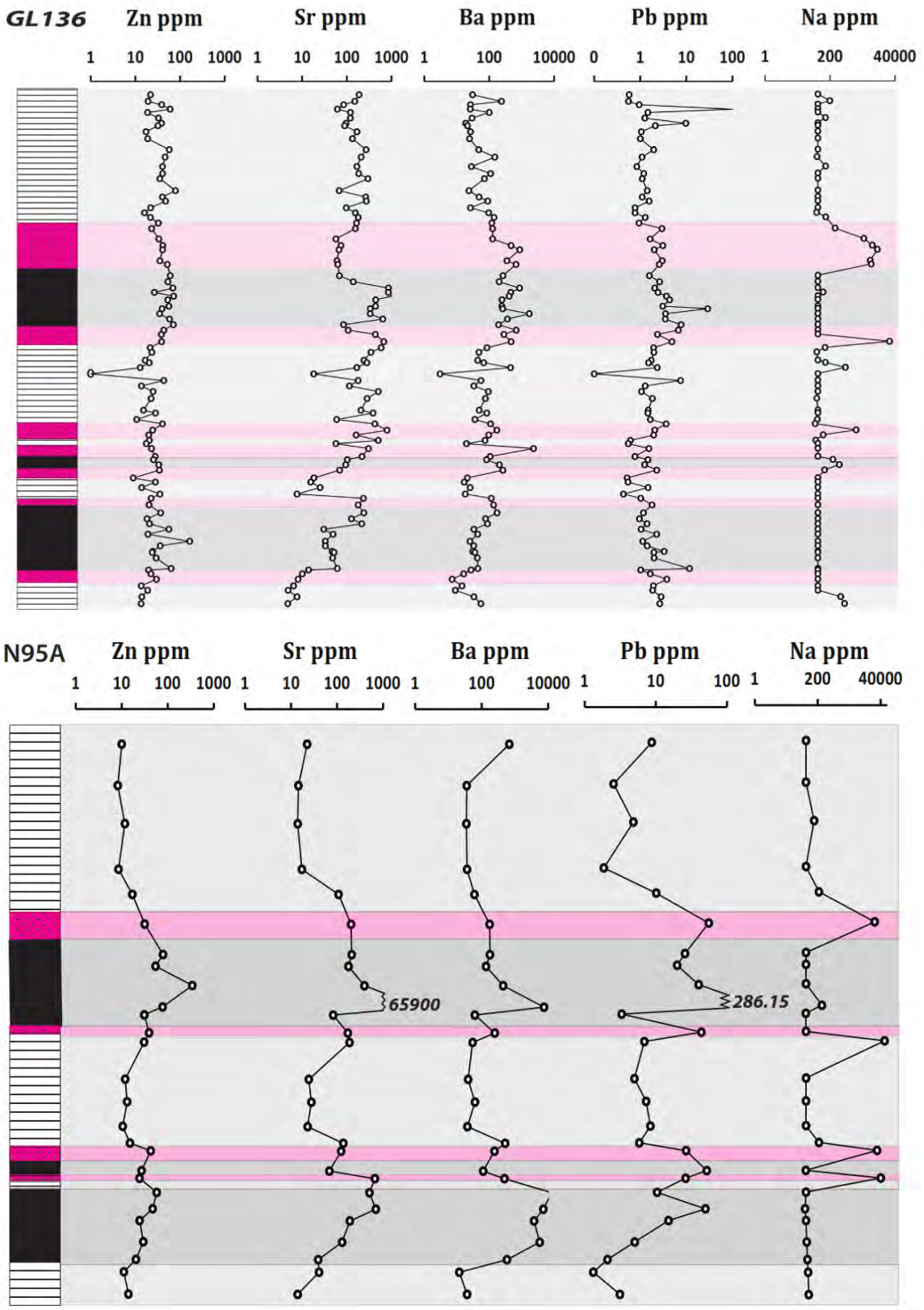

Figure 4. 5: Comparative variation plots of selected alkali elements for the statigraphic profiles of drillcores N95A and the protolith (GL136). Stratigraphic columns are not to scale, but shows relative thickness for the lithological units.

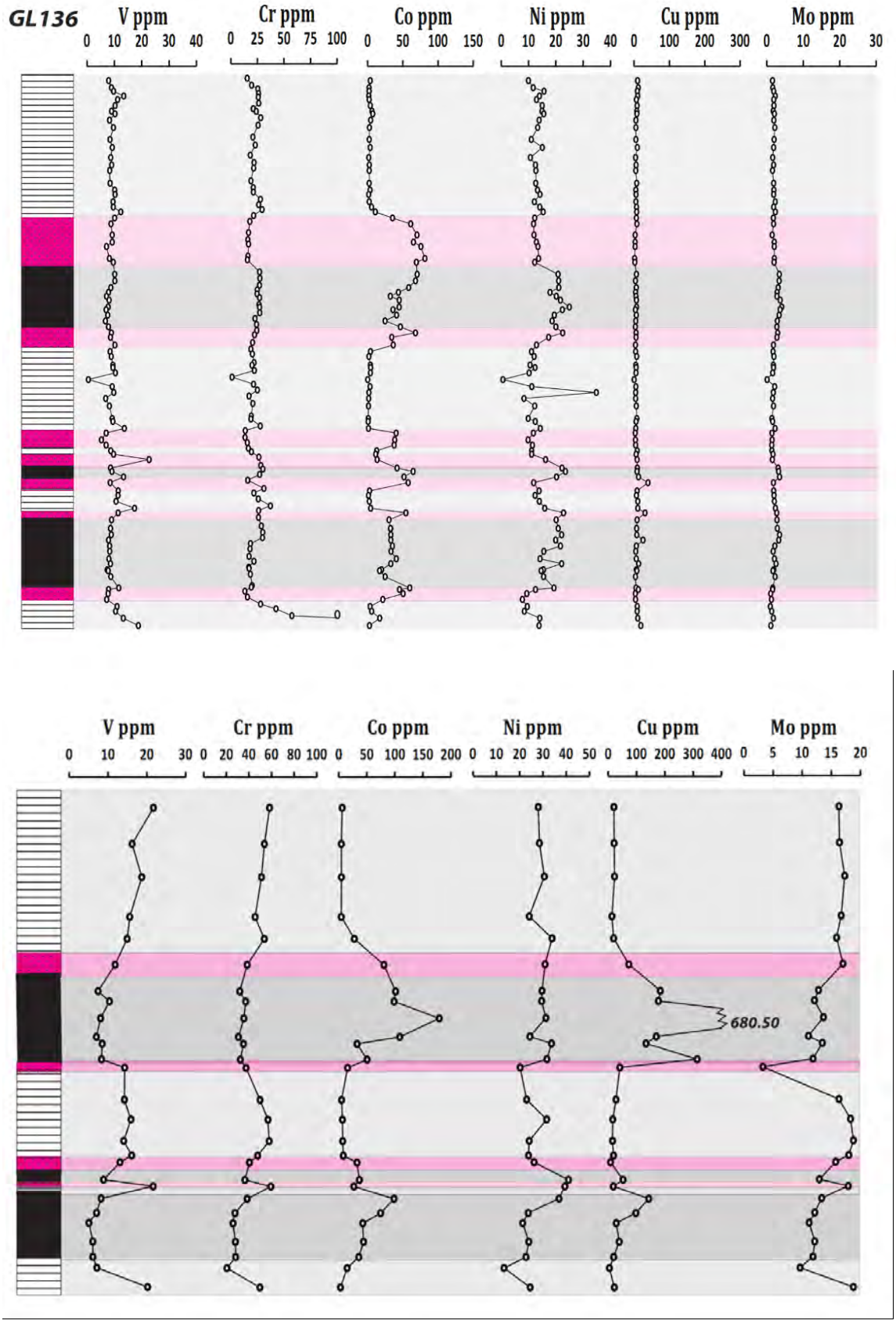

Figure 4. 6: Comparative variation plots of selected transitional elements for the statigraphic profiles of drillcores N95A and the protolith (GL136). Stratigraphic columns are not to scale, but shows relative thickness for the lithological units.

4.2.3. Drillcore N92I

Similarly with drillcore N95A in the previous section, geochemical profiles of drillcore N92I show somewhat comparable geometry across most part of the Hotazel stratigraphy with that of the protolith drillcore GL136 (Fig. 4. 7). Higher values of total Mn concentration are recorded in the lower Mn ore layer of N92I in comparison to the upper Mn ore layer, and this is mainly a function of the relative dominance of hausmannite over braunite in the lower ore bed. CaO and MgO profiles record very low concentrations, with the peaks in Ca seen in the Mn ore beds due to the presence of andradite, braunite II, secondary calcite and minor marokite. MgO, by contrast, is very low and invariant throughout the stratigraphy.

With regard to the bulk Fe profile of intersection N92I, it is important to highlight three notable features (Fig. 4. 7): the first one concerns the BIF section at the top of the stratigraphy, which contains classic massive hematite as seen in the previous chapter. This is a typical section of highly ferruginous BIF that has lost all of its primary carbonate and silica content through a leaching process and corresponds to the massive hematite reported by Tsikos (1999) from similar sections of the Hotazel stratigraphy in the same geographical area. The second feature is the clearly antithetic Fe-Si behaviour in the remaining BIF of the stratigraphy, which reflects the relative interplay of modal hematite against quartz. Finally, notable is also the higher Fe (relative to Mn) content in the upper Mn ore bed by comparison to the lower one, which is due to the presence of hematite and andradite in the former and complete absence of hematite in the latter.

In terms of alkali concentrations and stratigraphic behaviour (Fig. 4.8) , drillcore N92I shows again all profiles (except for Na), peaking in the Mn layers with very comparable geometry. Highest values are seen in the lower Mn ore bed than in the upper one. By comparison to the other elements, Na is very low and invariant across the entire stratigraphic section.

Finally, the transition metals (Fig. 4. 9) show relatively inconsistent behaviour across the stratigraphy with “spikes” in concentration occurring throughout the sampled borehole intersection. There are similarities in the distribution of spikes especially in the uppermost and most ferruginous part of the section. In the rest of the stratigraphy, the other notable feature concerns peaks in concentrations for Co, Cu, Ni and Mo, which appear to coincide with the peaks in Mn concentration for the lower Mn ore bed and also in those for Pb and Zn in the “alkali” profiles.

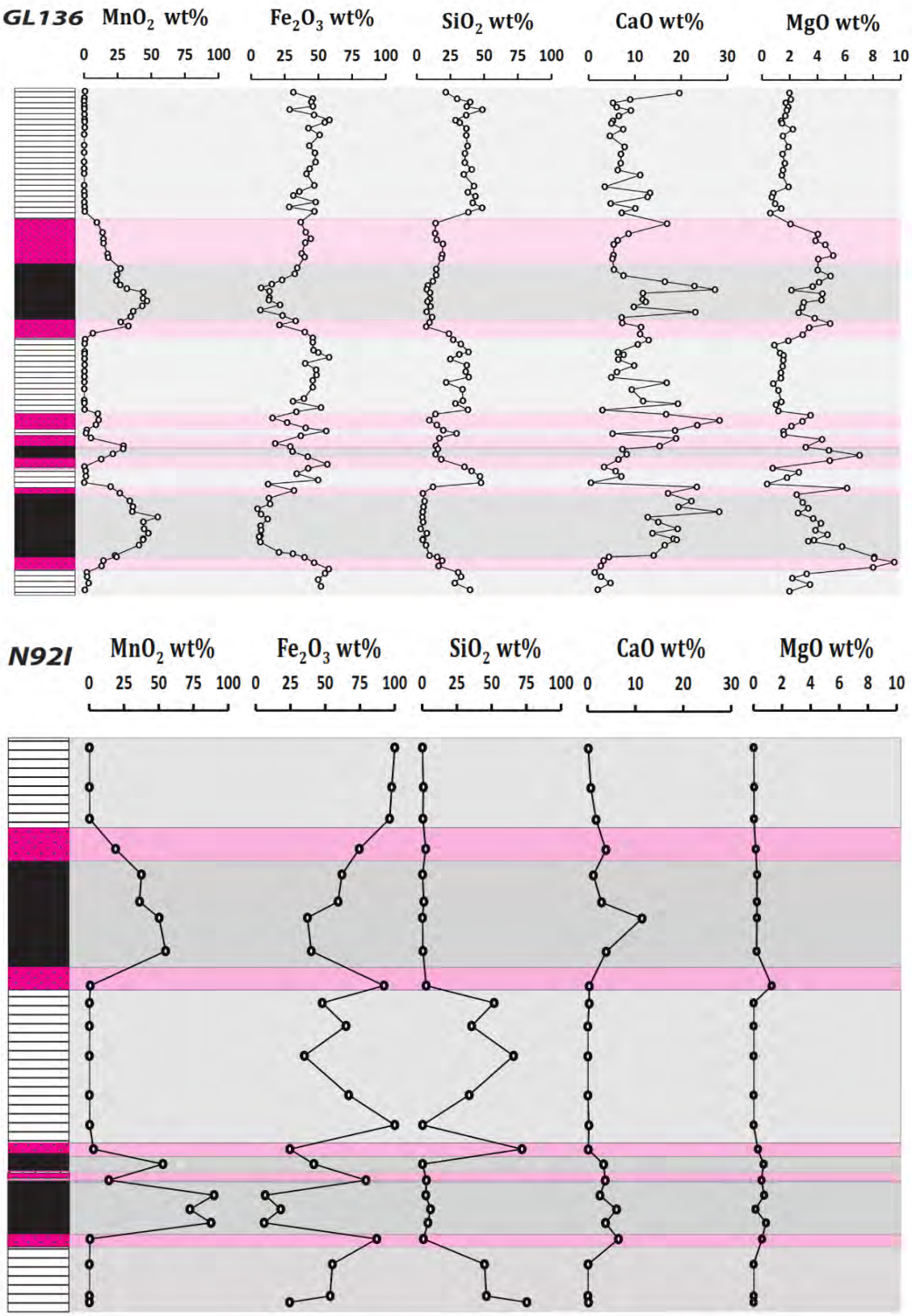

Figure 4. 7: Comparative variation plots of selected major elements for the statigraphic profiles of drillcores N92I and the protolith (GL136). Stratigraphic columns are not to scale, but shows relative thickness for the lithological units.

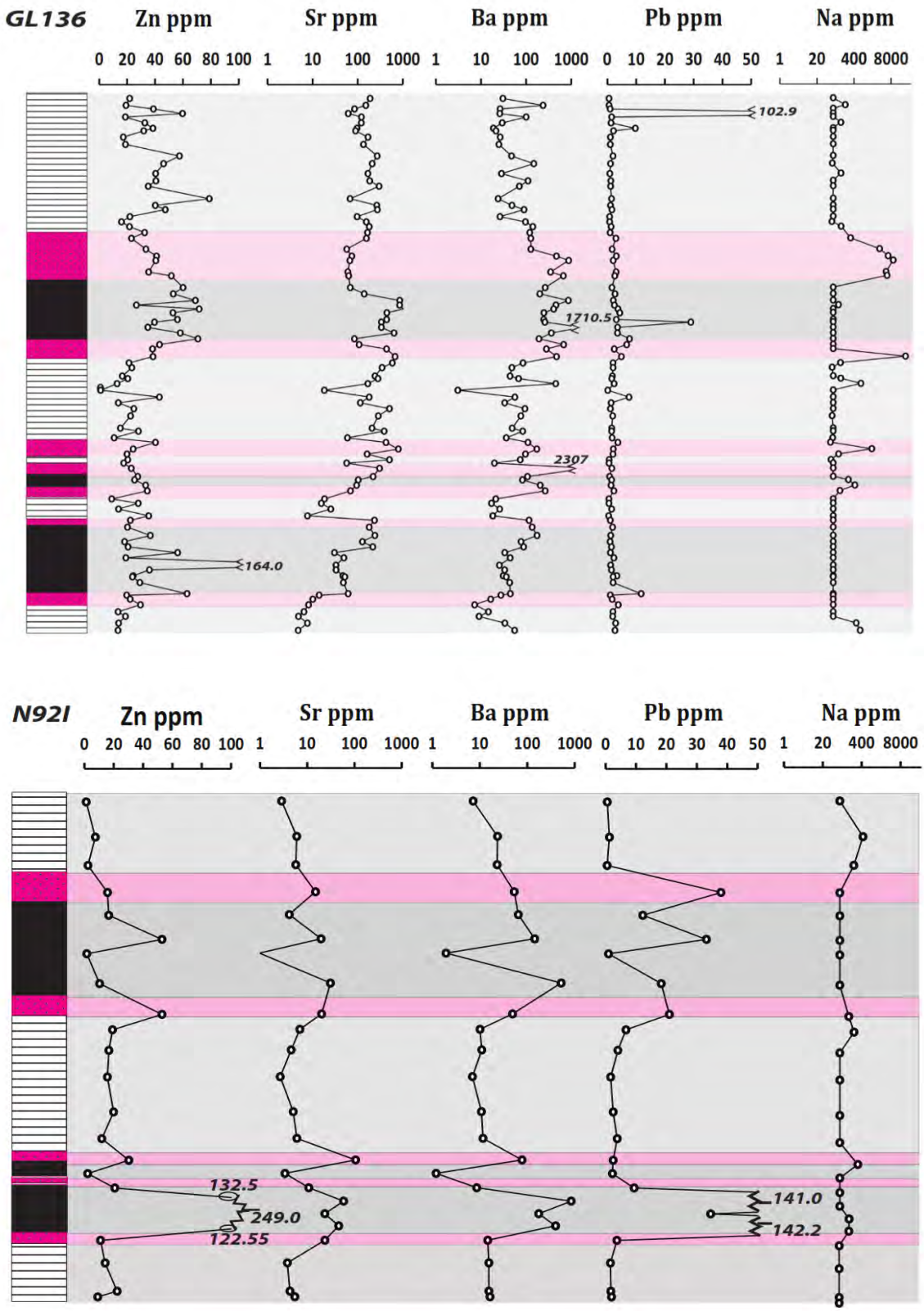

Figure 4. 8: Comparative variation plots of selected akali elements for the statigraphic profiles of drillcores N92I and the protolith (GL136). Stratigraphic columns are not to scale, but shows relative thickness for the lithological units.

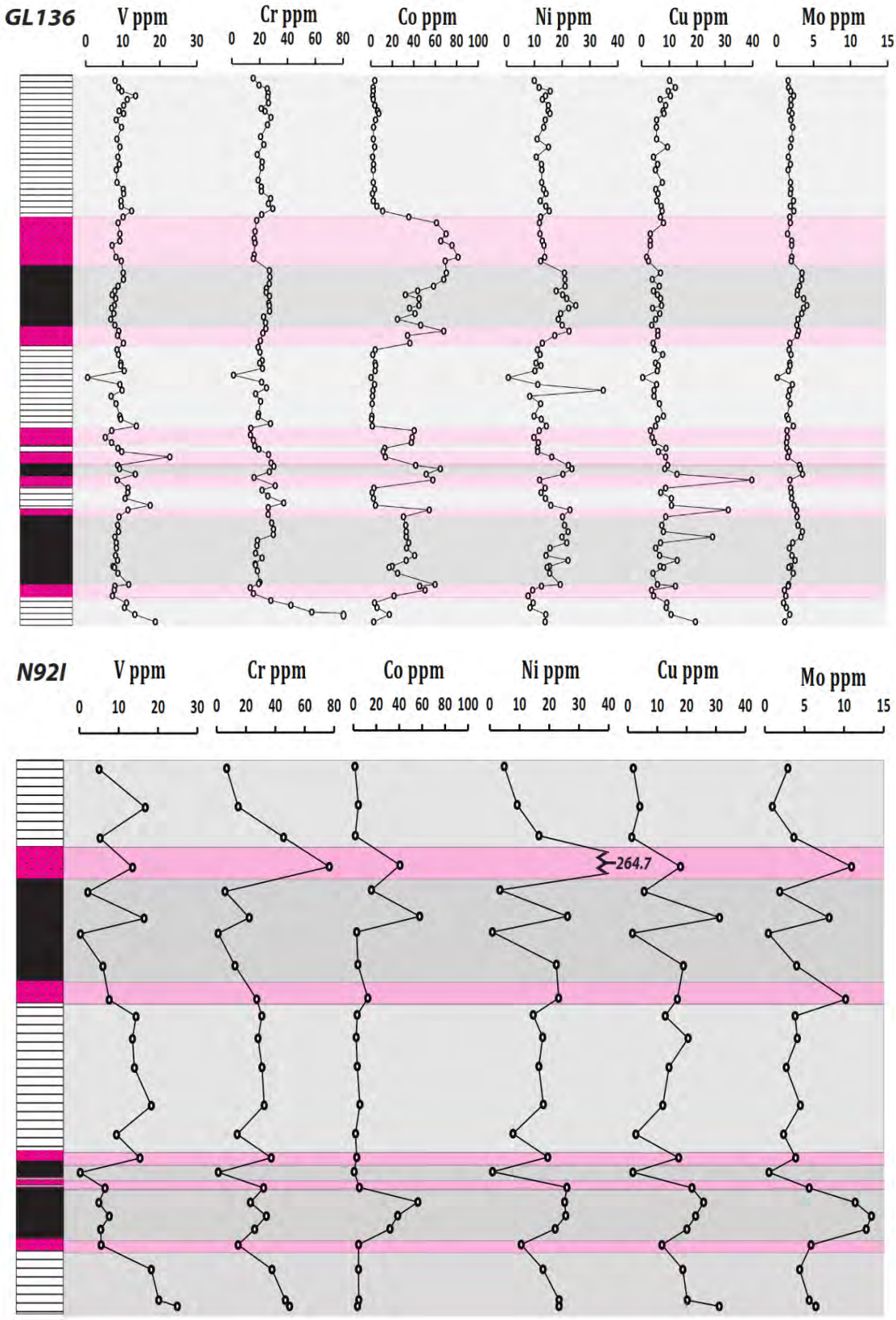

Figure 4. 9: Comparative variation plots of selected transitional elements for the statigraphic profiles of drillcores N92I and the protolith (GL136). Stratigraphic columns are not to scale, but shows relative thickness for the lithological units.

4.2.4. Drillcore N94J

The major element geochemical profiles for borehole intersection N95J (Fig. 4. 10) display a very comparable relationship for the three key element oxides, namely MnO_2, Fe_2O_3 and SiO_2, in the context of the presumed protolith. All three of these species show a geometry that mimics very closely that of the protolith section GL136, suggesting that they were largely conservative in their behaviour, just like what is seen it drillcore N95A earlier. By contrast, the element oxides that show almost complete loss across the stratigraphy are those of CaO and MgO. With the exception of a few samples in transitional hematite lutites where both seem to peak (due to the expected localised presence of dolomitic carbonate), in the rest of the stratigraphy their contents are vanishingly low. This observation agrees with the general consensus for the origin of Wessels type ores in general, which predict that enrichment in Fe and Mn in the Hotazel sequence must be related largely to the loss of the carbonate fraction of the protolith during the alteration process. However, in addition to carbonate, loss of silica must also have been severe especially in the Mn ore layers. This has resulted in a dominantly hausmannite-rich ore assemblages which also carry, for the same reason, the highest Mn metal grades out of all five intersections sampled and studied in this thesis. However, loss of Si was not very pronounced in the BIF, as the relative abundances of Fe and Si in the corresponding samples suggest.

In the case of the alkali profiles (Fig. 4. 11), here the similarity among all elements plotted is very strong once again, like it is in the other drillcore sections already shown. The main difference perhaps relates to the behaviour of Pb, which shows a decoupled distribution compared to all others when it comes to the top ore bed. Specifically, the Pb concentration in the upper Mn bed seems to be in the hematite lutite transitions above and below the maximum manganese abundances, whereas all other “alkali” elements peak along with peak manganese concentrations in the centre of the Mn ore beds. By contrast, the Pb seems to behave in a more consistent way with the other elements in the lower ore bed. Na, contrary to all other elements, shows very low values with insignificant peaks in the hematite lutite transitions similar to those it displays in the protolith section GL136.

Finally, the transition metals show a relatively erratic behaviour across the intersection N94J (Fig. 4. 12), with corresponding spikey peaks in most cases occurring throughout the section. The profile for Co shows the characteristic maxima in the Mn ore beds similarly to the protolith intersection, but there is also a notable peak in Cu values in the upper Mn ore bed, which is not replicated in the lower Mn ore bed.

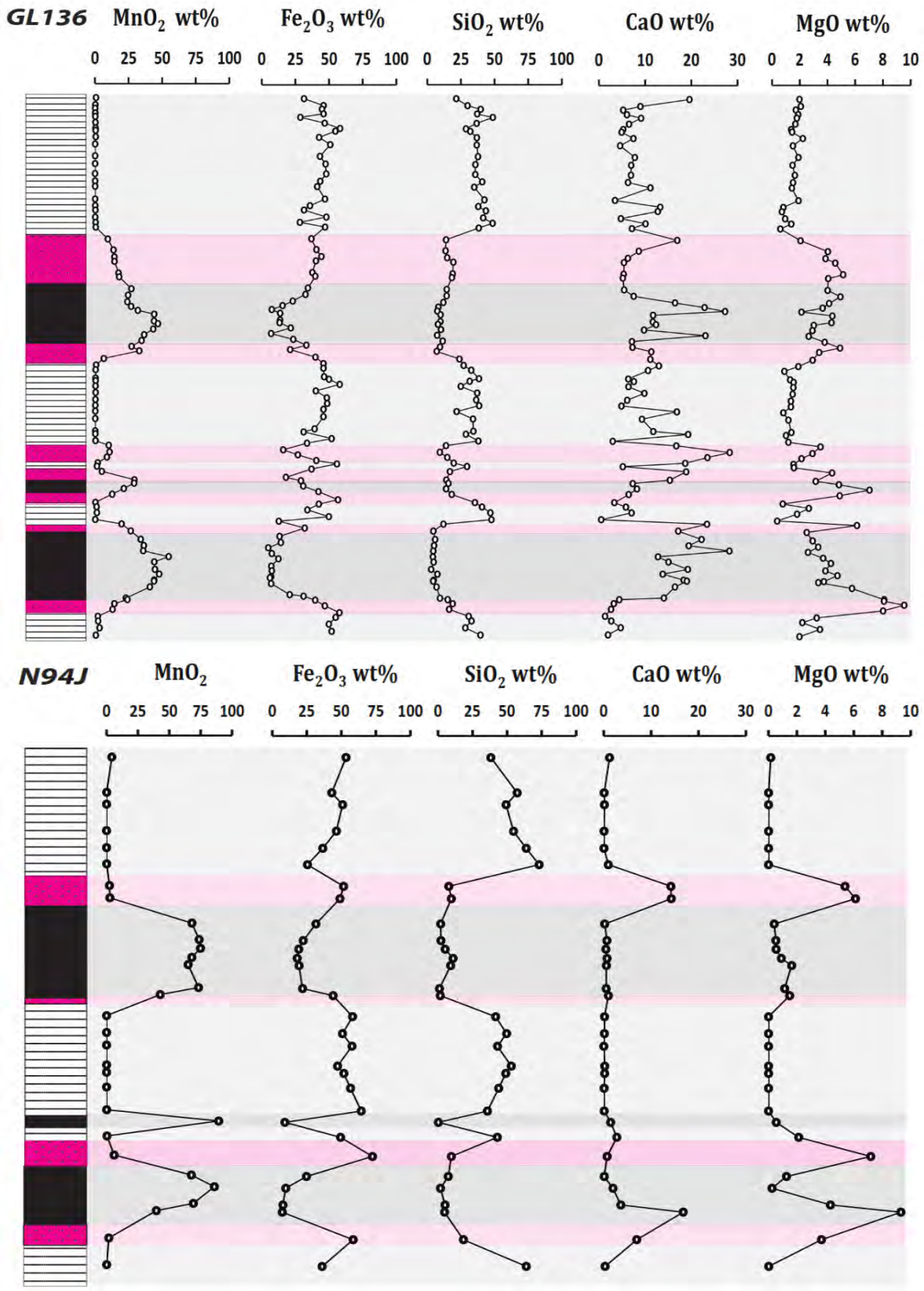

Figure 4. 10: Comparative variation plots of selected major element oxides for the statigraphic profiles of drillcores N94J and the protolith (GL136). Stratigraphic columns are not to scale, but shows relative thickness for the lithological units.

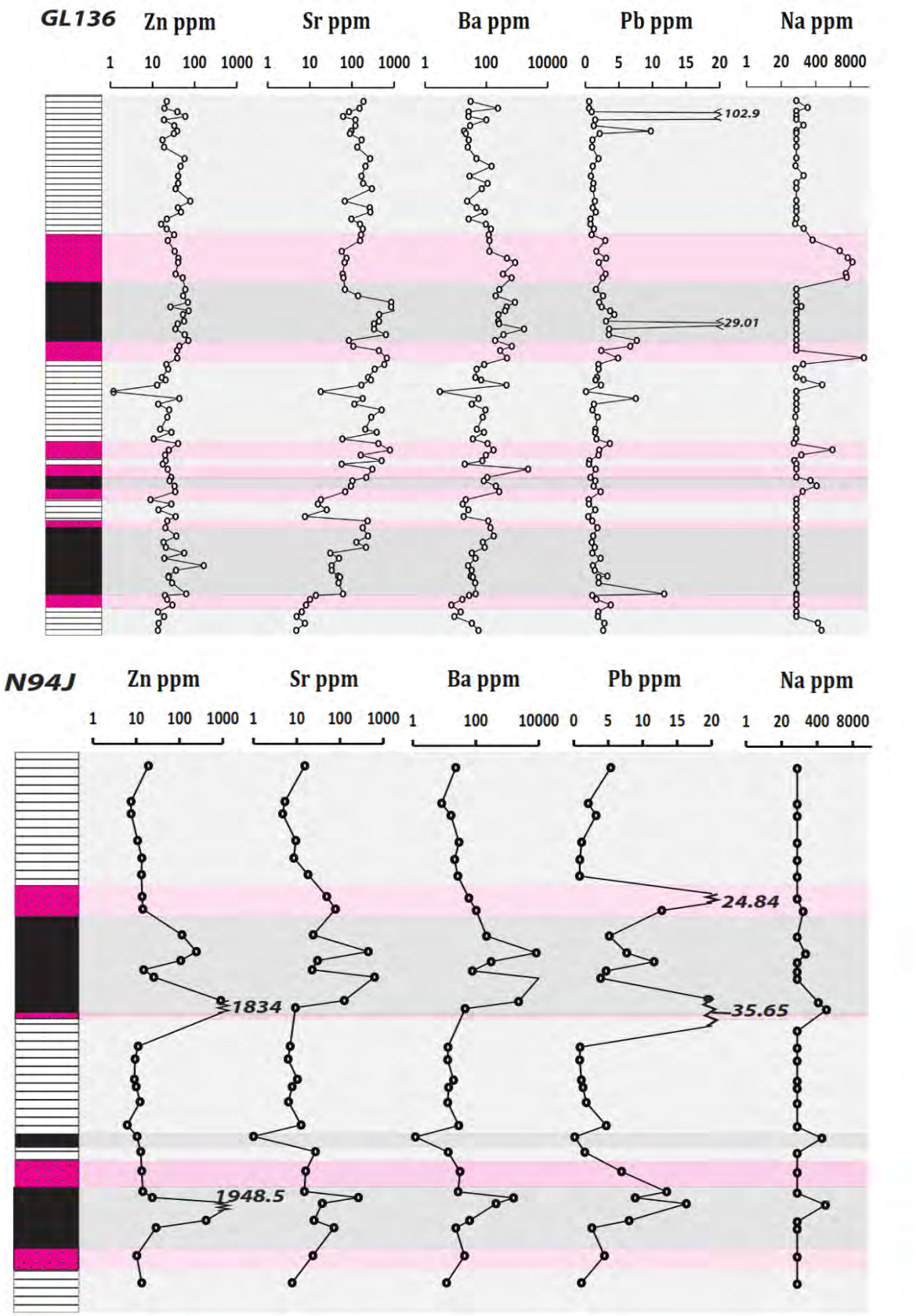

Figure 4. 11: Comparative variation plots of selected akali elements for the statigraphic profiles of drillcores N94J and the protolith (GL136). Stratigraphic columns are not to scale, but shows relative thickness for the lithological units.

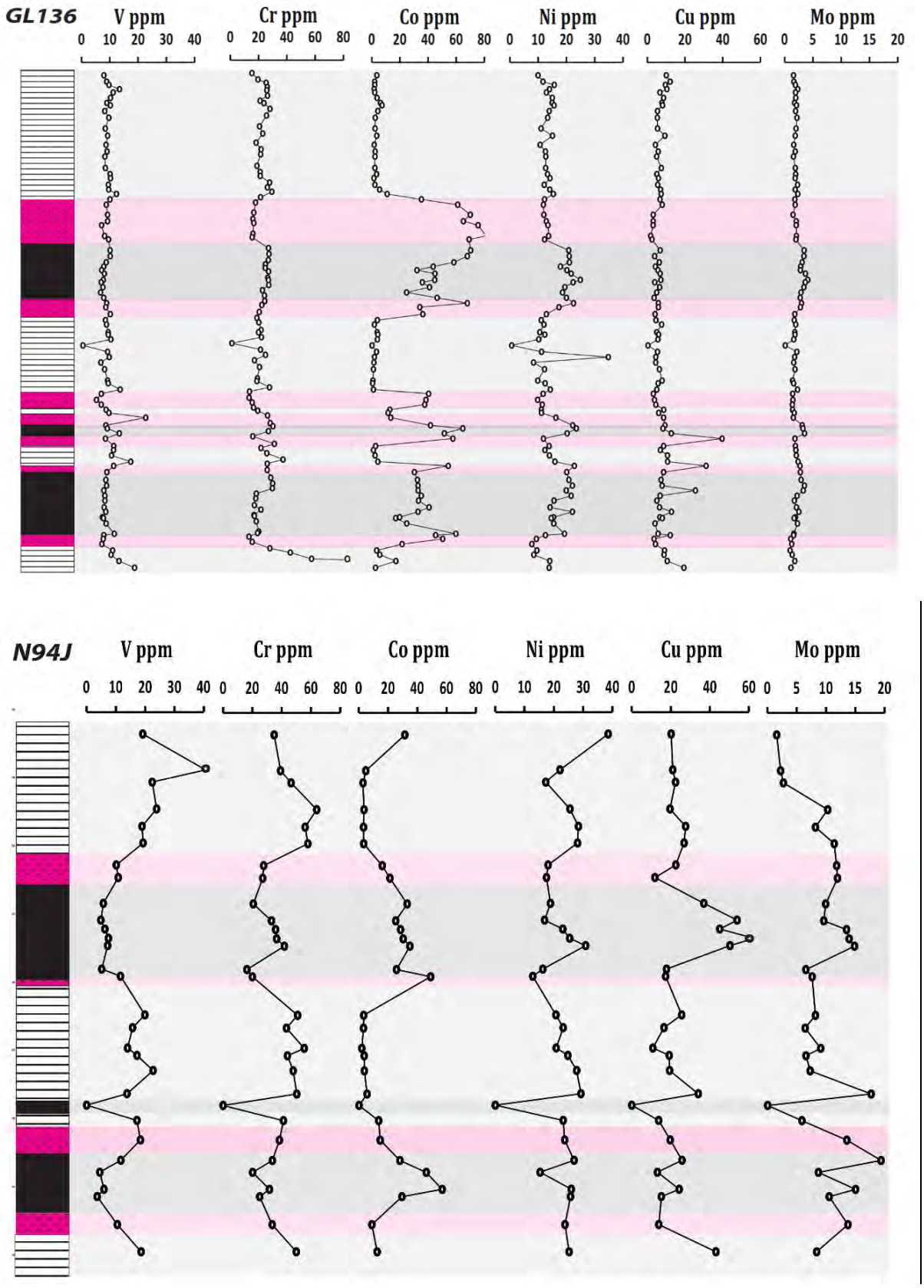

Figure 4. 12: Comparative variation plots of selected transitional elements for the statigraphic profiles of drillcores N94J and the protolith (GL136). Stratigraphic columns are not to scale, but shows relative thickness for the lithological units.

4.2.5. Drillcore GL57

Geochemical profiles of the major elements MnO, Fe_2O_3, and SiO_2 in drillcore GL57 (Fig. 4. 13) show similar geometry to the ones from the protolith core intersection for most of the samples across drillcore GL57. However, there are also some important differences that relate to the unusual circumstances of the presence of high-grade ore ("Wessels-type") in the upper ore bed coexisting with low-grade, "Mαmatwan-type" ore in the lower ore bed, as also suggested through the mineralogy of this drillcore section shown earlier.

The differences mentioned above translate to the clearly higher abundance of Mn in the upper Mn ore bed by comparison to the lower Mn ore bed. This appears to be mainly a function of the lower Si and Fe abundance in the top ore bed, which confirms that the ore here is mainly hausmannitic in composition with low associated hematite content. The carbonate fraction of the upper ore bed is relatively high, but this is mainly due to the presence of secondary dolomite which is reflected very well in the excellent relationship between the CaO and MgO profiles in that part of the section. Such a relationship does not develop in the Mamatwan-type ore in general and in the lower Mn ore bed of GL57, where the carbonate present is far more calcic and typical of the Mn calcite and kutnahorite assemblages that typify Mamatwan-type ore. The BIF that envelops the top Mn ore bed shows one key characteristic, which is the clearly antithetic relationship between the bulk Fe and Si profiles and very low carbonate abundances, suggesting that it is also altered like the Mn ore bed it encloses. In this drillcore also like in earlier ones from the Nchwaning area, highest Fe concentrations in the BIF appear to occur at the stratigraphic topmost part of the intersections.

In terms of trace element behaviour, concentrations of alkalis and associated metals (Fig. 4. 14) show little stratigraphic variability or relative enrichment like that seen in results of the previous borehole intersections presented It is only in the upper Mn bed where occasional spikes in Zn, Pb and Ba are recorded, and these are not very significant in terms of the absolute concentrations for those metals. Likewise, there is little to be said about the transition metal stratigraphic behaviours (Fig. 4. 15), except for the following three points: firstly, the Co profile displays the characteristic maximum in the lower Mn ore bed, but a similar maximum in the Mn-enriched upper ore bed is not seen. Secondly, the elements Ni, V and Cr appear to show highest values at the top of the BIF section where the Fe enrichment is also the highest. And finally, Mo shows a curious behaviour that in it attains the highest concentrations in the BIF sections and the lowest in the Mn ore beds, which is a feature not really seen in the other drillcores.

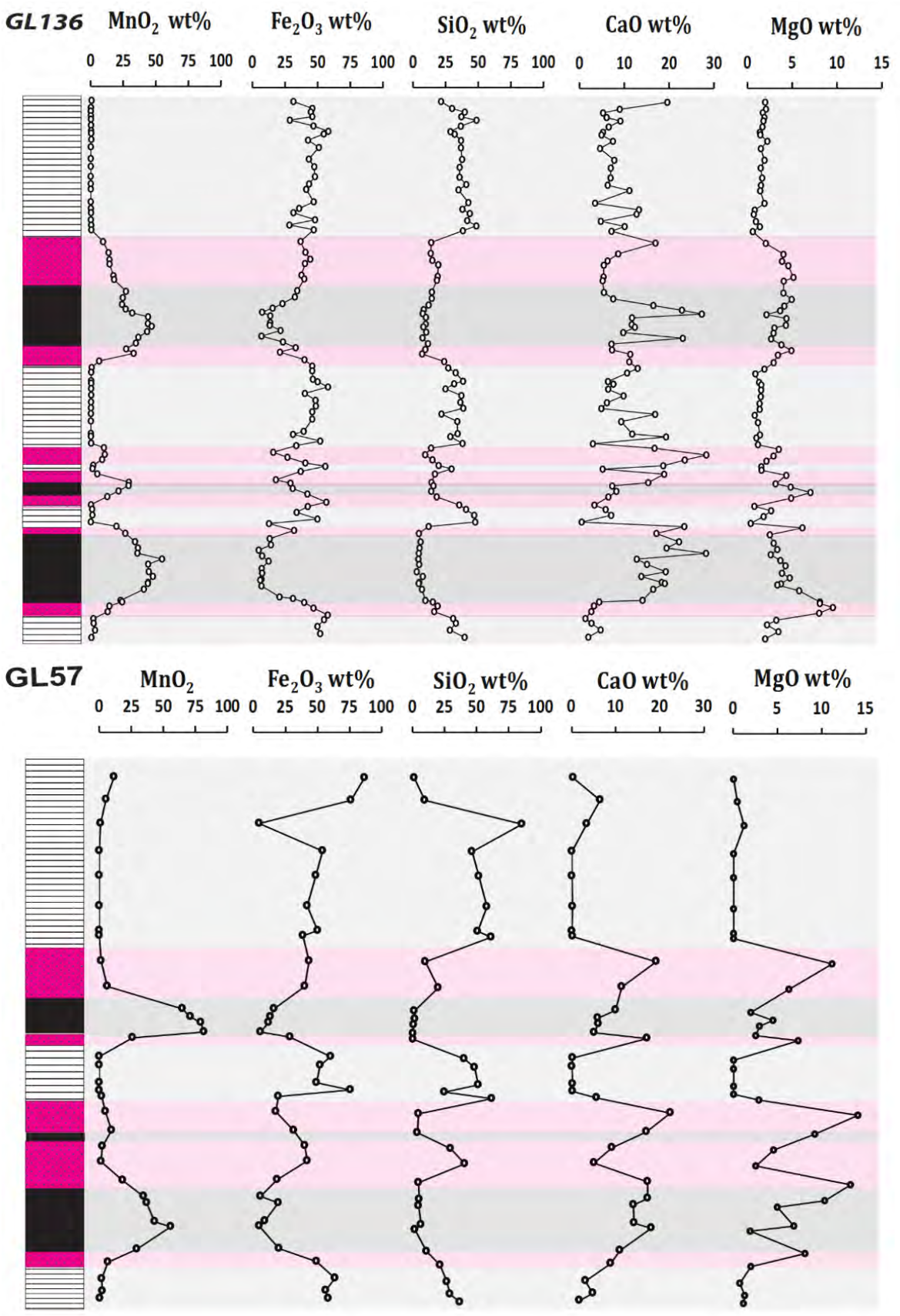

Figure 4. 13: Comparative variation plots of selected major element oxides for the statigraphic profiles of drillcores GL57 and the protolith (GL136). Stratigraphic columns are not to scale, but shows relative thickness for the lithological units.

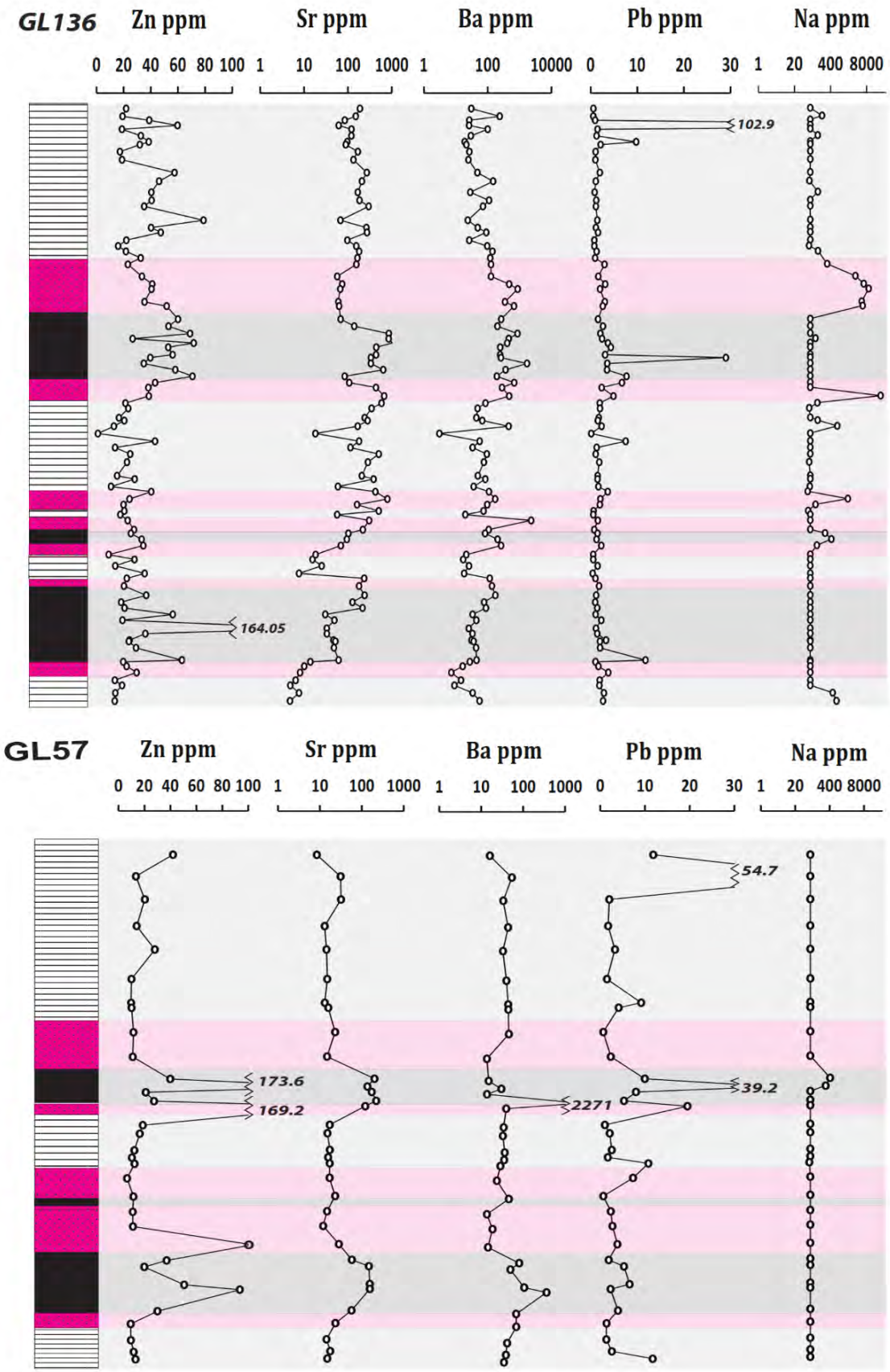

Figure 4. 14: Comparative variation plots of selected transitional elements for the statigraphic profiles of drillcores GL57 and the protolith (GL136). Stratigraphic columns are not to scale, but shows relative thickness for the lithological units.

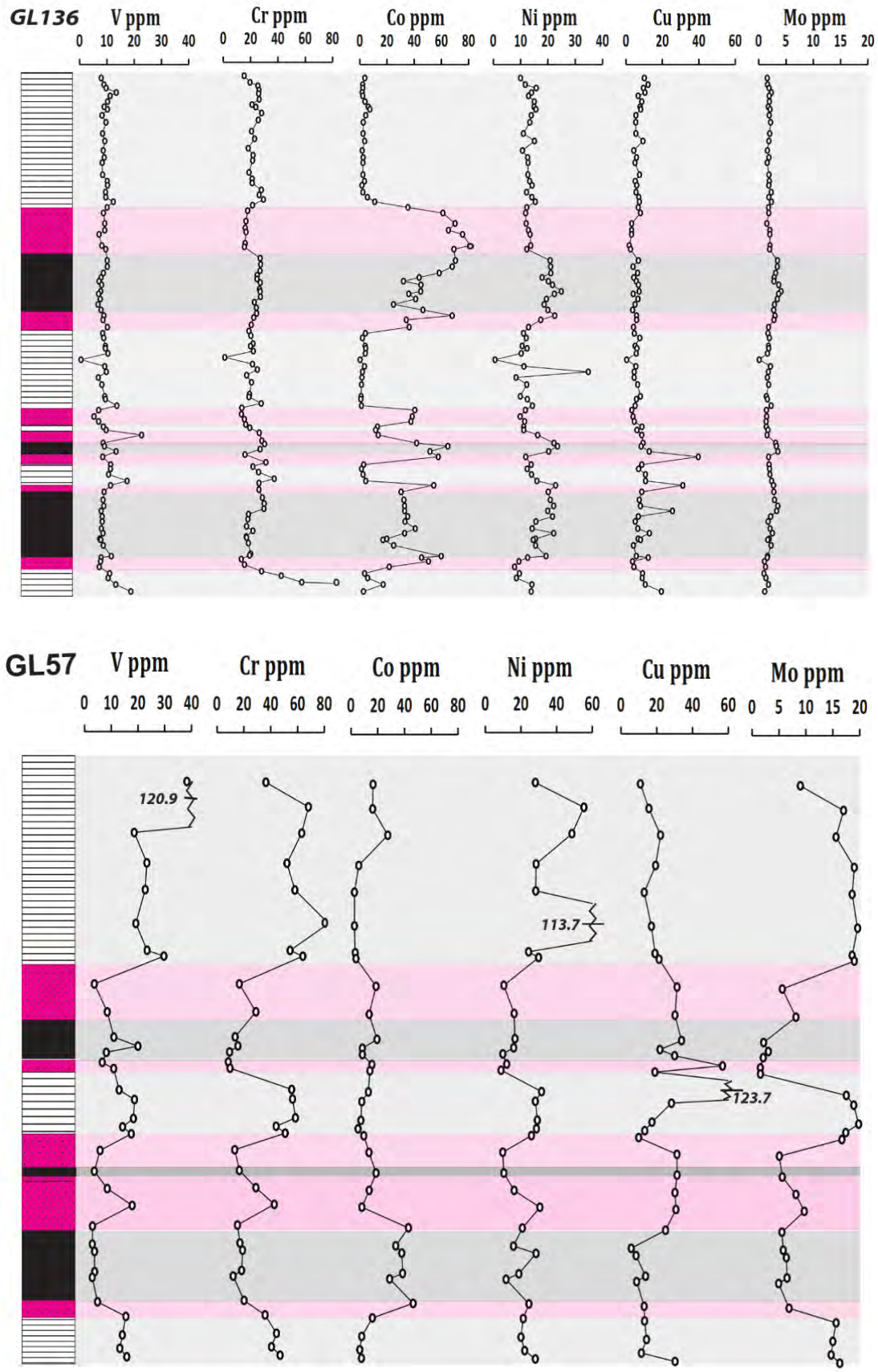

Figure 4. 15: Comparative variation plots of selected transitional elements for the statigraphic profiles of drillcores GL57 and the protolith (GL136). Stratigraphic columns are not to scale, but shows relative thickness for the lithological units.

4.3. Comparative mass balance considerations

4.3.1. Major Elements

Figure 4.16 below provides a simple summary of major element comparative considerations for each Mn ore bed for each of the five drillcores examined. It specifically shows average major element information in terms of relative enrichments and depletions for each drillcore, taking as common protolith for all five of them the average compositional characteristics for drillcore GL136. The exercise is applied for the five key element oxides, namely SiO_2, Fe_2O_3, CaO, MgO, and MnO_2.

The main outcome of the above-mentioned diagrams of Fig. 4. 16, concerns the relative net enrichment in both bulk metal oxides of Fe_2O_3 and MnO_2 as compared to the clear depletions in SiO_2, CaO and MgO, in almost all instances (except for the upper ore bed in GL57 where MgO appears to be enriched relative to the protolith due to the presence of secondary dolomite). The common reference in each diagram is the 1:1 line of constant mass for the protolith abundances. It is more than clear that the relative enrichments in Mn from one drillcore to the next and from one ore bed to the next, is highly variable. There is also no consistent correspondence between the relative degree of Mn enrichment between the two ore beds in any given drillcore. There is also no consistent behaviour of any of the other chemical species between the two groups of ore beds (upper vs, lower). Arguably the only element oxide that shows a consistent behaviour is that of Fe, whereby the upper ore layer shows substantial Fe enrichments compared to the protolith but also compared to the lower Mn ore bed too, where only one drillcore (N95E) shows marginal enrichment in Fe compared to the protolith.

4.3.2. Trace Elements

The diagrams in Figures 4.17, 4.18, and 4.19 show in a bit more detail the concentration ranges and averages of selected trace elements for both the top and lower ore bodies in all 5 selected drill cores for this study, as they compare to those of the original protolith (i.e. intersection GL136). The data are plotted in such a way as to permit a comparison between each of the two ore beds within a drillcore (horizontally across) but also for the same ore bed (upper or lower) among different drillcores (vertically across). For convenience, the elements chosen for plotting have been subdivided into three groups, namely V, Cr, Ni and Co; Cu, Mo and Sr; and Pb, Ba and Zn. The objective of this plotting exercise will be mainly to distinguish which elements appear to show net enrichment in the ores of magnitudes that

suggest significant addition by fluids, against those that show largely residual enrichment which may not be larger than an order of magnitude from the original protolith. This consideration is based on the possibility that the alteration process was accompanied by major loss of mass, which in itself can lead to substantial residual enrichment of elements that behaved as immobile during fluid-rock interaction. For example, a mass loss of 50% in a rock during alteration would lead to doubling of the abundances of immobile elements. In the case of the Wessels alteration event in the KMF, a mass loss of approximately 20-25% is believed to have been achieved, based on previous studies (Tsikos et al., 2003)

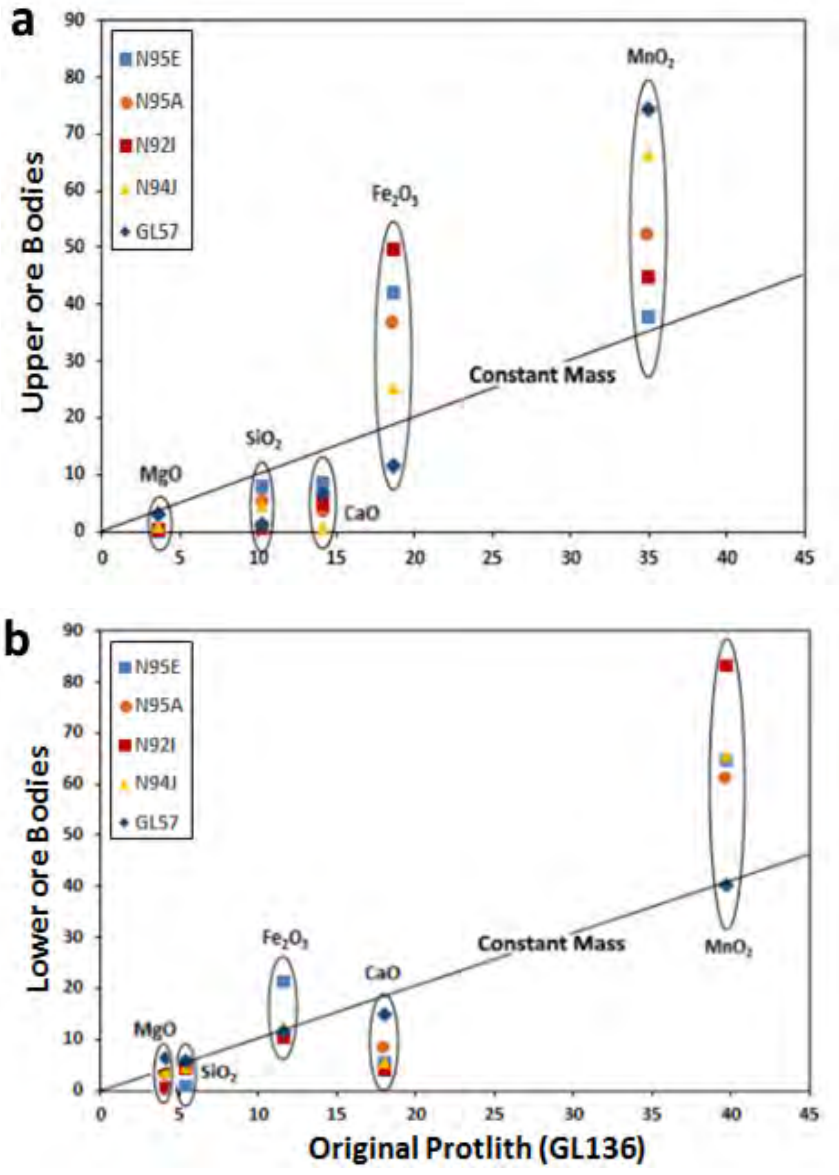

Figure 4. 166. Graphs showing variation in the distribution of major element oxides for the five drill cores for the top ("a") and bottom ("b") ore beds against the assumed protolith composition (MTO, x-axis).

Concerning the elements V, Ni, Co and Cr (Fig. 4.17), they display a conservative behaviour, either by virtue of not increasing much compared to the protolith, or by increasing by less that an order of magnitude. These elements can therefore be regarded as largely conservative to the alteration process. The only additional notable feature is the far higher ranges and deviation of elemental concentrations in the upper ore bed as compared to the lower one.

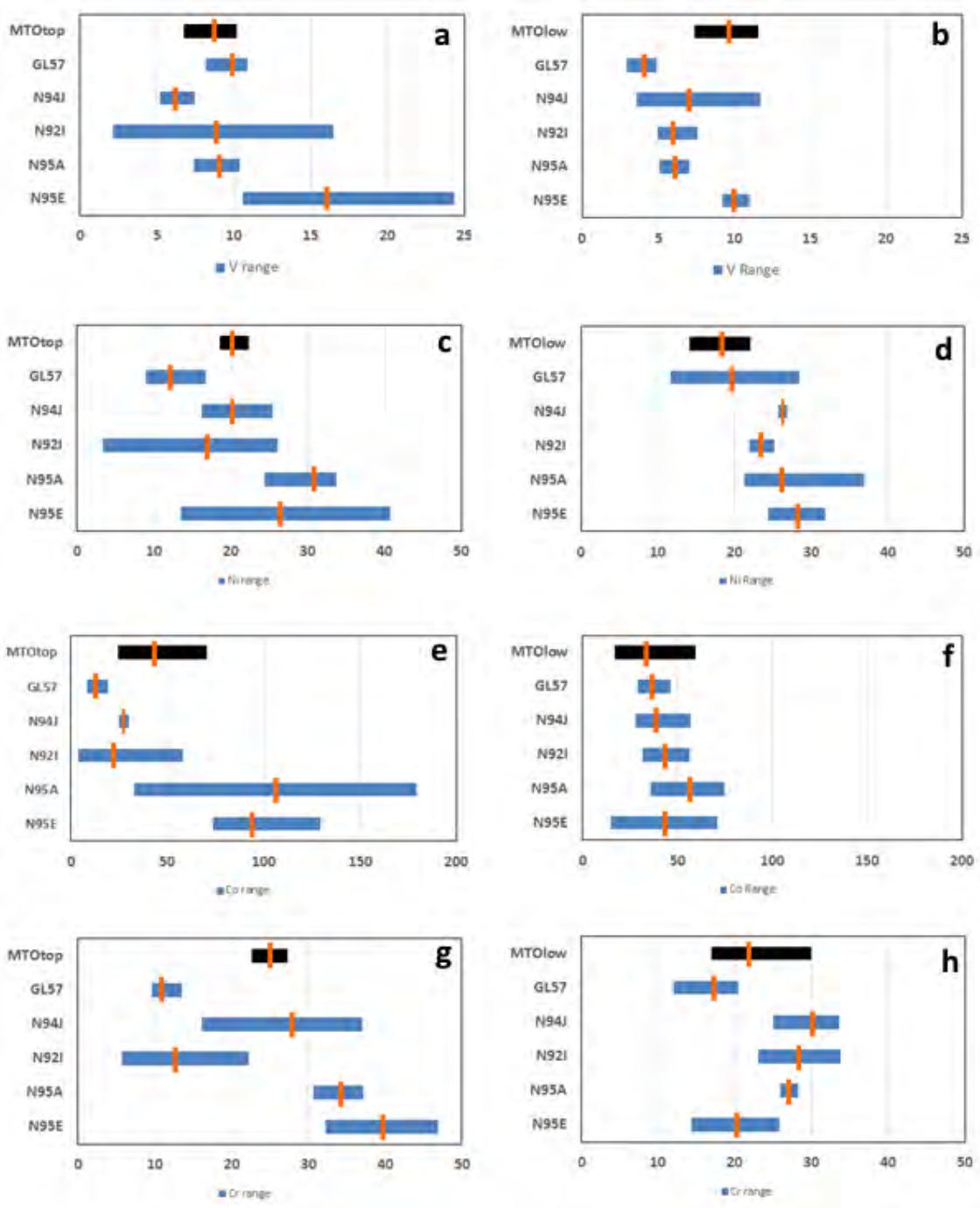

Figure 4. 177. Graphs showing variation in the distribution of selected trace elements between the five drill cores for the top (left) and bottom (right) ore layer against the assumed protolith (MTO). Selected trace elements include V, Ni, Co and Cr. The bars represent min-max and the orange line the average. N.B. All values on the x-axis are ppms

With respect to Cu, Mo and Sr (Fig. 4.18), here the situation is somewhat more erratic: Cu ranges vary significantly from very tight for some drillcores to highly variable in others. Where the ranges are very variable, averages are orders of magnitudes higher than the protolith in both ore beds, especially the upper one (e.g. cores N95E, N95A), suggesting substantial Cu addition. The same appears to apply also in the case of Mo which shows highly variable ranges in all drillcores for both ore layers, with averages well above those of the protolith ore beds. Finally, whereas Sr appears to show no enrichment in both ore beds, there is at least one high-ranging significant enrichment in the lower ore bed (N95A)

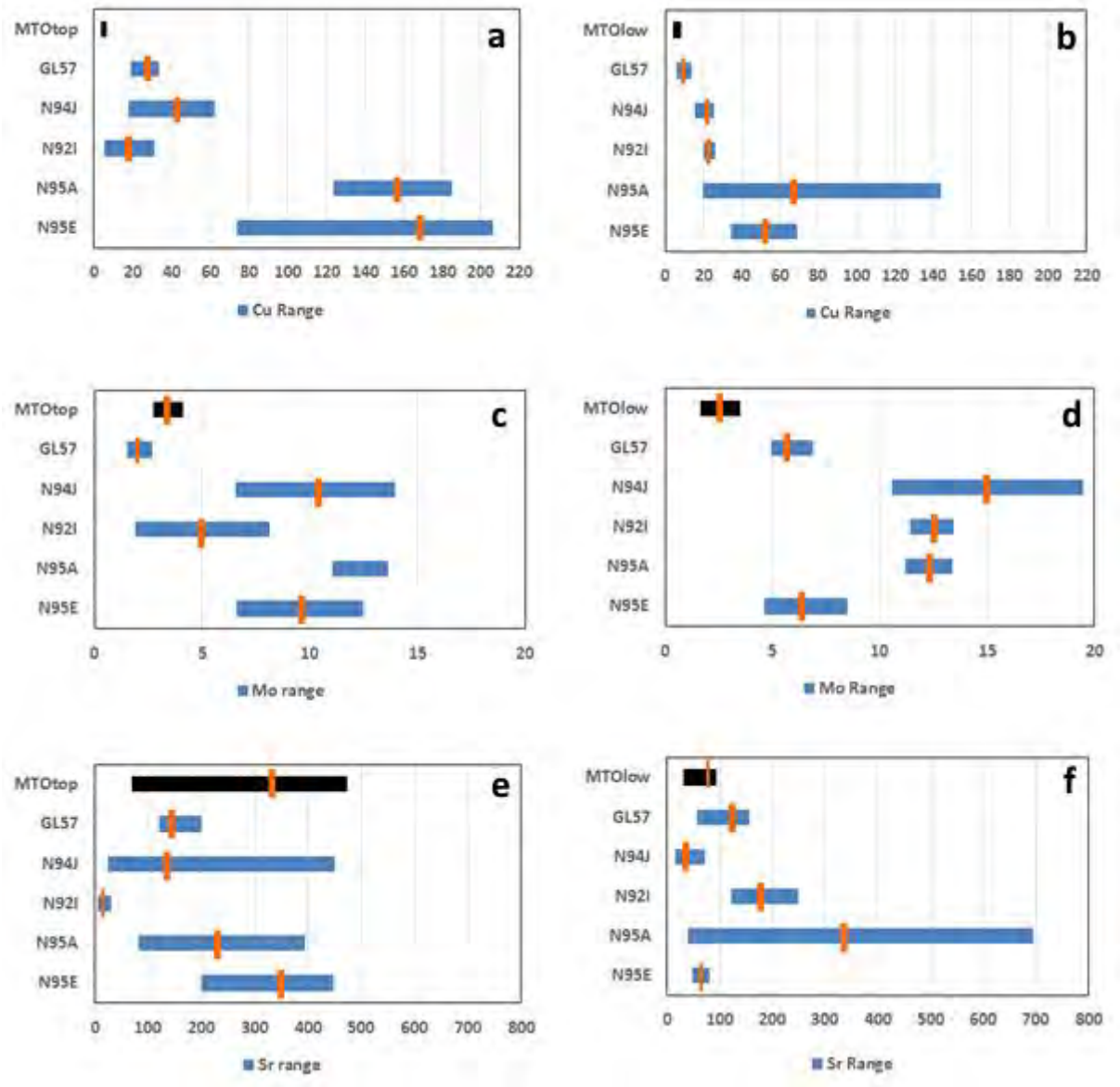

Figure 4. 188. Graphs showing variation in the distribution of selescted trace elements between the five drill cores for the top (left) and bottom (right) ore layer against the assumed protolith (MTO). Selected trace elements include Cu, Mo, and Sr.

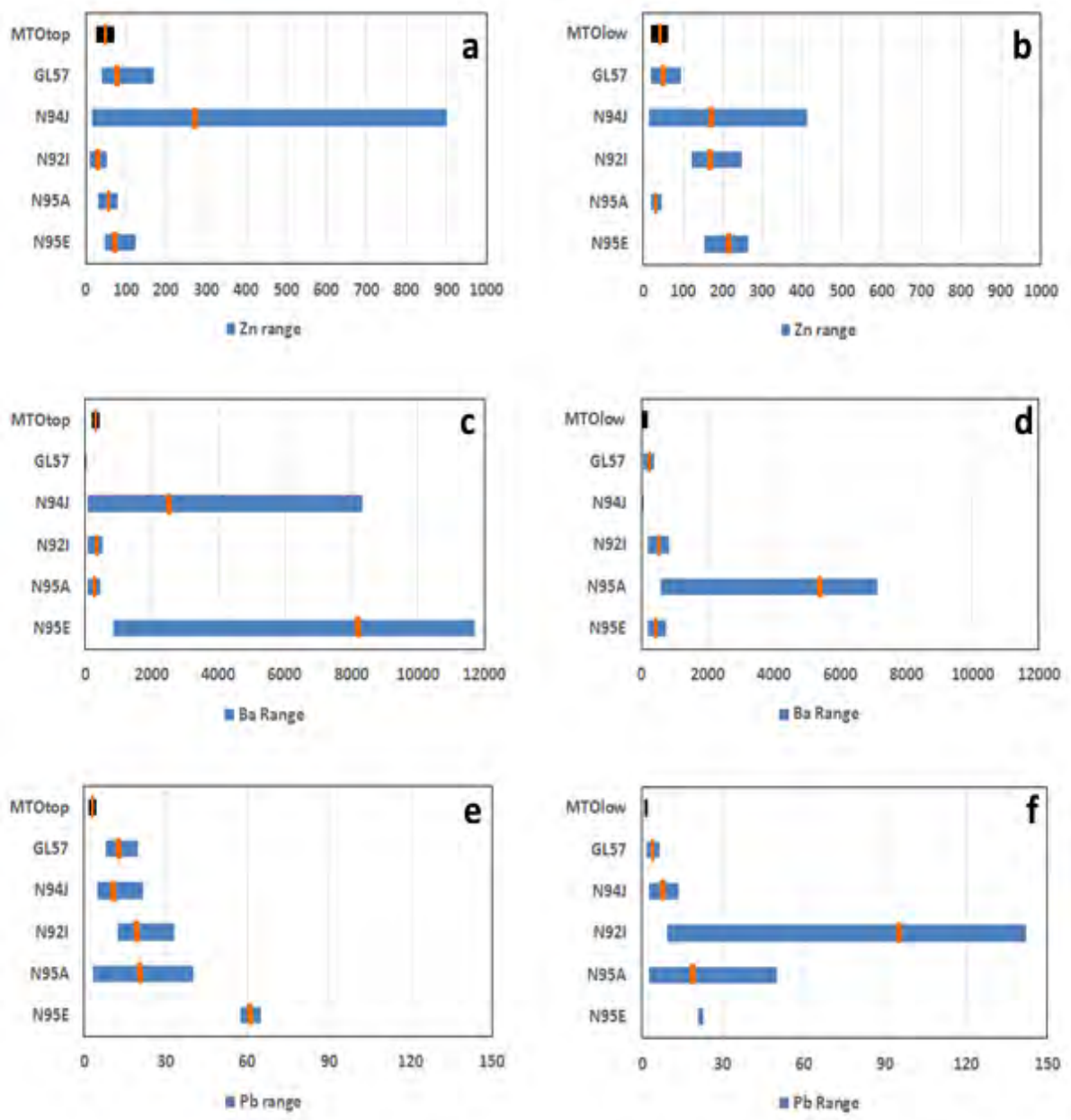

Figure 4. 199. Graphs showing variation in the distribution of selected trace elements between the five drill cores for the top (left) and bottom (right) ore layer against the assumed protolith (MTO). Selected trace elements include Zn, Ba, and Pb.

Finally, the elements Zn, Ba and Pb (Fig. 4. 19) are those that arguably show the clearest enrichment potential. In the case of Zn, concentration ranges in all five drillcores are generally tight for both ore beds, with the exception of drillcore N94J. It is in that drillcore where the net enrichment is also the highest relative to the protolith. Ba behaves similarly, as it has narrow ranges and low relative enrichment in some sections and very high ranges and large enrichment in others. This points to the generally erratic distribution of barite in the rocks with evident concentration "spikes" in some cases and very low values in others.

Finally, Pb shows generally tighter behaviour in terms of concentration ranges except for the lower ore bed in drillcore N92I. In almost every instance, relative enrichments appear to be much higher than those expected conservatively through mass loss during alteration.

4.4. Rare-earth element geochemistry

Rare-earth elements studies is a major tool in ore geology as it provides information on the potential sources responsible for the genesis of ore minerals and the Mn ores of the Hotazel Formation are definitely no exception. Therefore, analyses for the REE were done on samples from all borehole intersections. The first diagram shows the sums of REE (∑REE) for all boreholes plotted against MnO_2 values on a bivariate plot (Fig. 4. 20) to test first-order variability. The plot shows a scattered distribution of data for the two ore bodies in all drill cores, with no specific relationship that can be gleaned as they all fall within a similar range of values. With respect to the protolith, the diagram illustrates that the process of addition or removal of REE during the enrichment process must have been generally minor and largely conservative.

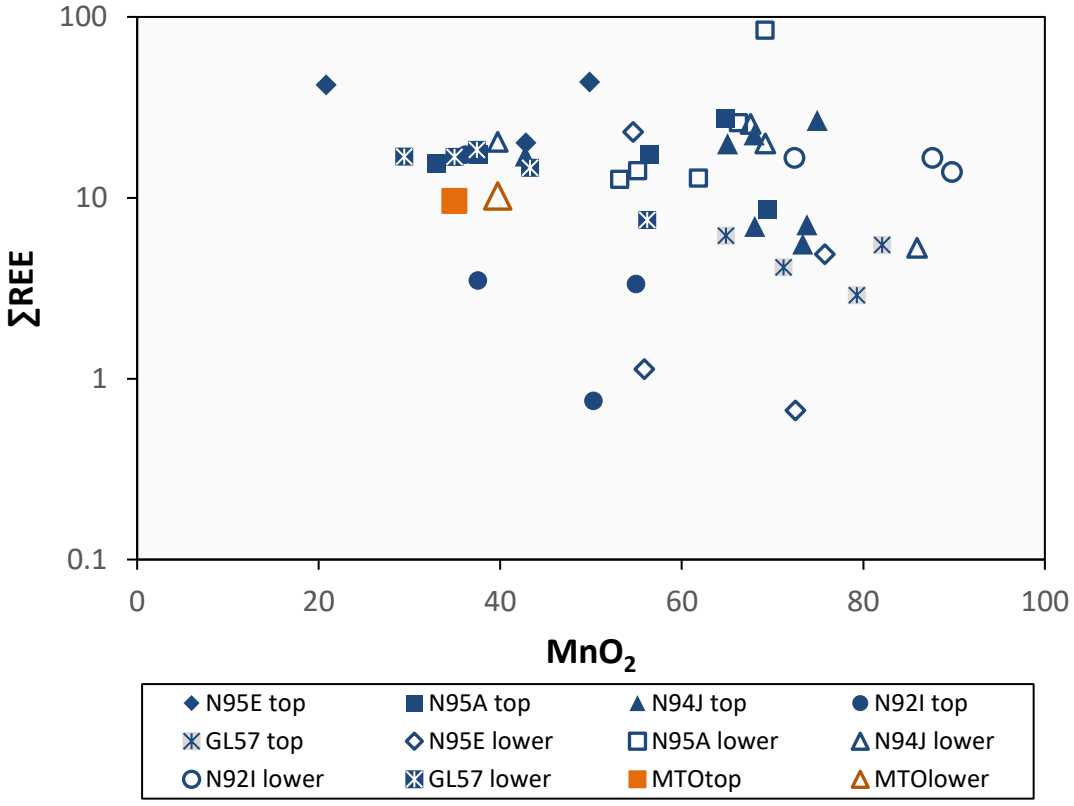

Figure 4. 20. Bivariate plot of Manganese oxides (as MnO_2) versus total REE (∑REE) for the top and lower Mn ore bodies of the five drillcores. The average values of the two ore bodies in GL136 are plotted for comparison

Table 2. Averages of REE results for selected samples from all of the drill cores. n = number of samples

Core ID.	GL136		N95E		N95A		N92I		N94J		GL57	
Ore Body	Top	Lower	Top	Lower	Top	Lower	Top	Lower	Top	Lower	Top	Lower
n	10	9	3	3	4	4	2	3	5	3	4	4
	Ave.	Ave	Ave.	Ave	Ave.	Ave	Ave.	Ave	Ave.	Ave	Ave.	Ave
La	3.10	3.66	8.65	2.78	4.44	4.70	0.62	4.00	3.97	5.98	1.27	4.06
Ce	3.27	3.23	10.13	2.71	4.58	4.28	0.90	4.35	3.52	4.18	1.58	4.74
Pr	0.45	0.48	1.77	0.63	0.68	0.70	0.13	0.61	0.59	1.00	0.16	0.73
Nd	1.91	2.04	7.76	3.17	3.07	3.02	0.63	2.73	2.59	4.37	0.68	3.18
Sm	0.30	0.31	1.46	0.57	0.58	0.45	0.11	0.43	0.38	0.95	0.14	0.62
Eu	0.09	0.08	0.90	0.22	0.18	0.31	0.04	0.15	0.20	0.29	0.07	0.19
Gd	0.47	0.41	1.28	0.74	0.67	0.64	0.21	0.81	0.58	1.47	0.16	0.75
Tb	0.07	0.06	0.19	0.11	0.14	0.10	0.04	0.13	0.08	0.22	0.02	0.11
Dy	0.12	0.13	1.17	0.68	0.93	0.78	0.23	0.80	0.61	1.44	0.20	0.75
Ho	0.52	0.54	0.27	0.16	0.27	0.17	0.05	0.22	0.16	0.35	0.05	0.18
Er	0.40	0.37	0.76	0.42	0.73	0.56	0.19	0.63	0.45	0.88	0.12	0.60
Tm	0.06	0.05	0.10	0.06	0.11	0.08	0.03	0.10	0.06	0.11	0.03	0.09
Yb	0.44	0.35	0.70	0.39	0.72	0.54	0.19	0.64	0.43	0.61	0.16	0.58
Lu	0.07	0.05	0.10	0.07	0.13	0.08	0.03	0.11	0.08	0.11	0.04	0.09
LREE	9.58	10.21	31.94	10.81	14.19	14.09	2.65	13.07	11.83	18.24	4.06	14.27
HREE	1.68	1.55	3.30	1.88	3.03	2.31	0.77	2.63	1.88	3.71	0.61	2.40
∑REE	11.26	11.76	35.24	12.68	17.22	16.40	3.42	15.69	13.71	21.95	4.67	16.67
$(Eu/Eu^*)_{SN}$	1.08	0.98	2.88	1.88	1.37	2.70	1.14	1.18	3.03	1.12	2.05	1.27
$(Ce/Ce^*)_{SN}$	0.62	0.54	0.68	0.46	0.73	0.56	0.74	0.65	0.74	0.39	0.78	0.64
$(Pr/Pr^*)_{SN}$	1.04	1.08	1.08	1.11	1.00	1.07	0.99	1.03	1.04	1.26	0.92	1.08
La/Lu*	41.97	70.71	83.41	39.89	33.50	60.37	18.75	36.88	47.27	56.80	31.68	45.78

The REE values for all ore bodies are graphically represented in classic spidergram plots in Figures 4.21 and 4.22. The data have all been normalized against the Post-Archean Australian Shale (PAAS; Taylor and McLennan, 1985), which is most often used for chemical sedimentary rocks such as the ones used in this study (Bau and Dulski, 1996; Chetty, 2008; Chetty and Gutzmer, 2012). The two layers of Mn ore are shown separately to appreciate the variability that might have been recorded in each due to the enrichment process.

REE diagrams, for sedimentary rocks, can be evaluated on the basis of a number of parameters, among the most common being the degree of positive or negative anomalies in the redox-sensitive Eu and Ce and the overall trend/slope of the spidergrams which would reflect relative depletions and/or enrichment in the light-REE (La-Sm) relative to heavy-REE (Gd-Lu). In general, BIFs and associated Mn ore layers of the Hotazel Formation display consistent positive-sloping REE patterns against PAAS, with slightly negative to no Ce anomalies, positive La anomalies and variable Eu anomalies. The slope of the REE patterns of the Hotazel rocks is very similar to that of seawater, suggesting that the latter was the main source of REE in the Hotazel Formation and for BIFs in the Griqualand West Basin (Tsikos and Moore, 1997; Schier et al., 2020). Moreover, the suggestion has been made that the overall hydrothermal alteration of the Hotazel strata was conservative in terms of net REE enrichment, i.e. no external addition is deemed necessary (Chetty, 2008; Chetty and Gutzmer, 2012).

The REE plots shown in Fig. 4. 21 and 4. 22 reveal a vary erratic behaviour of REE from one ore bed to the next, and from one drillcore to the next. Relative to the protolith signature (drillcore GL136), a given set of REE data from a given ore bed may reveal close similarities in terms of the overall slopes of the data (e.g. both ore beds of drillcore N95A) or significant differences (upper ore bed of N92I or lower ore bed of N94J). Similar discrepancies apply with respect to positive Eu anomalies which may appear highly pronounced in samples from some ore beds (upper ore bed of N95E or lower ore bed of N95A), although it is important to note that the same does not apply to positive Ce anomalies which are all but absent from the dataset presented in this thesis. Finally, it is important to stress that the REE abundances appear to be generally higher than those of the protolith, but exceptions do occur to that rule as well. Finally, comparisons of REE behaviour between the ore beds in any given drillcore suggest a general similarity, although in certain instances (e.g. drillcore N94J), the variability in REE behaviour may be strikingly dissimilar between samples from the same ore bed as well as between the two ore beds.

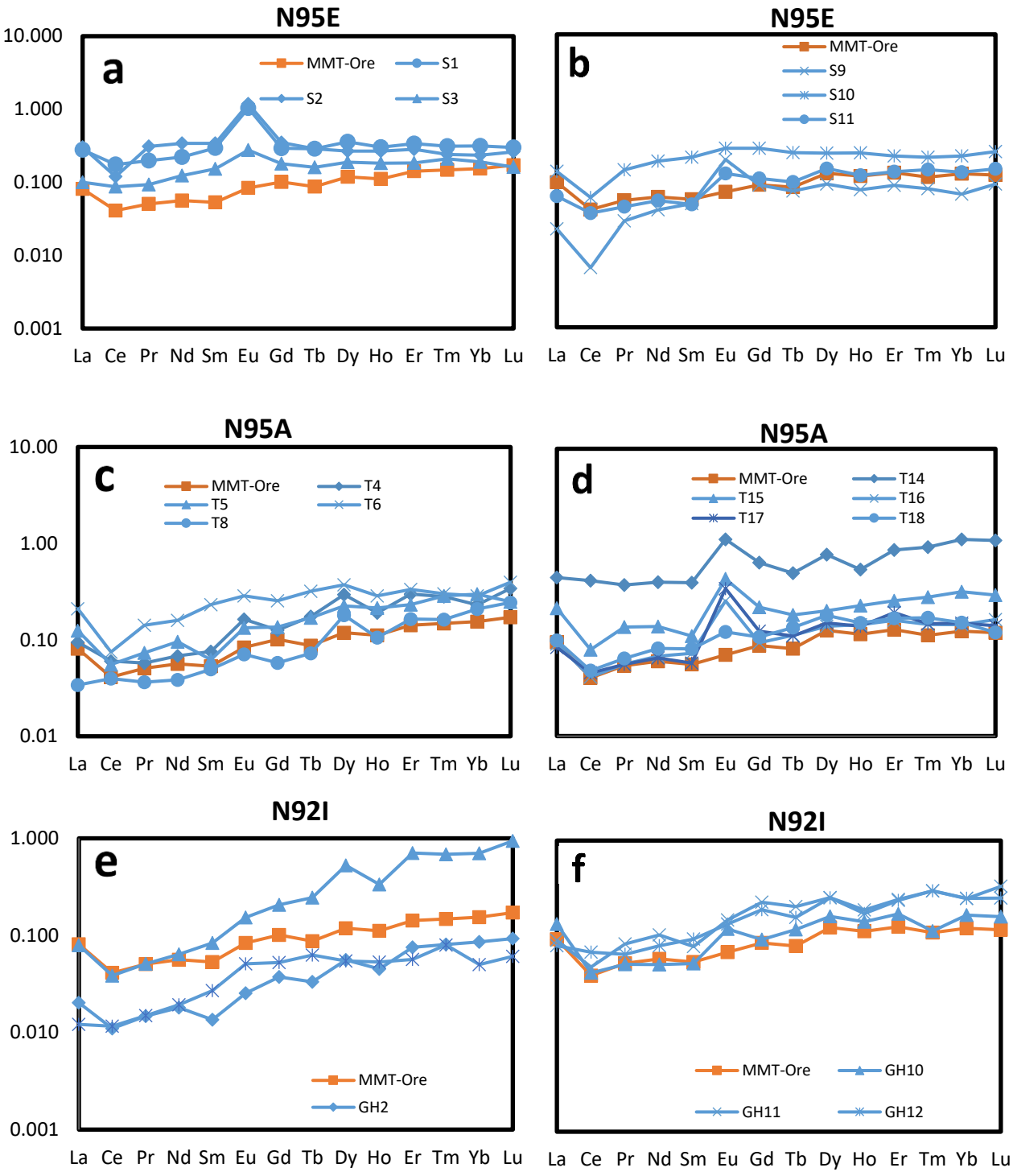

Figure 4. 21. PAAS-normalised, REE plots for samples from the top (left) and lower (right) ore bodies of drillcores N95A, N95E, and N92I. Each graph includes for comparison the pattern for the average values of the corresponding manganese ore bodies of protolith section GL136.

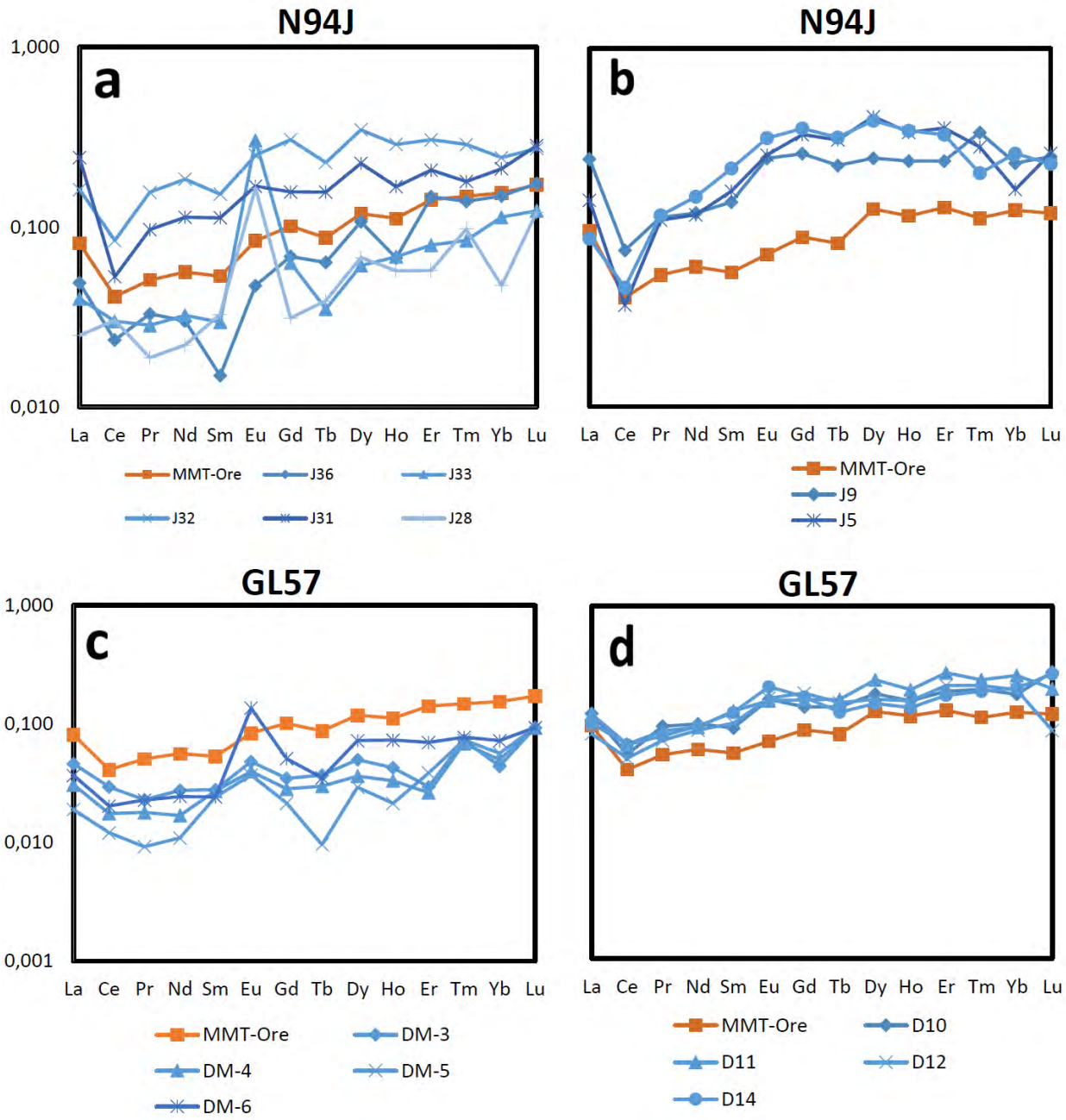

Figure 4. 22. PASS-normalised, REE geochemical patterns for samples from the top (left) and lower (right) ore bodies of drillcores N94J and GL57. Each graph includes the pattern for the average values of the respective ore bodies of protolith intersection GL136, for comparison

4.5. Summary

The key results illustrated and presented in the foregoing sections can be summarised in the following bullet points:

- Banded iron formations in all drill cores from the Nchwaning area are dominated by Fe_2O_3 and SiO_2. These can vary in concentration from very high Fe_2O_3 (≥90 wt.%) in massive hematite ores seen in a few of the drill cores to high SiO_2 (≥40 wt.%) concentrations in more classic BIF-type samples.
- There is generally an antithetic relationship between MnO_2 and the other major oxides within the Mn ore beds. This represents the so called closure effect in geochemical data.
- There is consistently a higher concentration of Fe in the top ore bed of all drillcores compared to the protolith; this relationship is not replicated in the lower ore bed where Fe contents are either very close to the protolith ones or even lower than the latter. It follows that the bulk Mn content of the upper ore bed is expected to be generally lower and more ferruginous than that of the lower Mn bed.
- With regard to trace elements, there is a relative enrichment observed in the various ore beds that appears to be largely conservative with respect to the protolith, i.e. it owes its origin to passive enrichment through mass loss during alteration. Among the trace elements that appear to satisfy that condition are Ni, Cr, V, and Co.
- By contrast, the trace elements Mo, Cu, Zn, Pb, and Ba, make up a subgroup that appear to show comparable behaviour and are considered as having been added metasomatically to the altered ores by the fluid/s involved. Nevertheless, the degree of enrichment is highlty variable from the upper ore bed to the lower one across drillcores, and points to more localised rather than pervasive enrichments in each of those elements.
- Finally, REE plots for the Mn ore beds across all drillcores, exhibit a distinct positive slope with relative depletion in LREE relative to HREE, similar to that of the original Mamatwan protolith. In some drillcores, the similarity between the diagrams for the protolith and the altered ores is very close, while in others there are striking differences. The same applies with respect to the behaviour of Eu anomalies. Otherwise, the general consensus is that the altered Mn ore beds are relatively and conservatively enriched in REE, by comparison to the protolith.

CHAPTER 5. SYNTHESIS

5.1. Introduction

Previous research conducted on the Hotazel Formation and its origins, has been focused mainly on the mineralogical and geochemical characteristics of the iron-formations or the Mn ore bodies separately (e.g. Gutzmer & Beukes, 1995, 1996; Tsikos et al., 2003). In this study, an attempt is made to understand these characteristics for the entire Formation considering all lithological subfacies (BIF, Mn ore, transitional lutites) altogether in a more holistic fashion. Geochemically and mineralogically, the results of this study have revealed significant variation across all lithofacies: the iron-formations show similarities for most of the samples both geochemically and mineralogically, but some variability has been identified vertically and laterally in the different boreholes. The Mn ore bodies, on the other hand, show much more substantial chemical and mineralogical nuance both vertically in a single drill core and laterally from one borehole to another.

The previous two chapters in this research work have illustrated in quite some detail the aforementioned variabilities. These have been attributed and can be utilized to test different models that consider a variety of structures as the medium for fluid passage leading to the alteration of the pre-existing sediments of the Hotazel Formation. One major aim of this study was to see investigate the relative roles of faults, unconformity, sub-outcrops, dykes and/or thrust planes in the enrichment of the ores. In this section, a discussion is presented that intertwines the results presented for the five selected boreholes with proposed alteration models, while giving due consideration to all possible structural players in the hydrothermal alteration process.

5.2. Alteration Models

The two farms in this study are situated in the northernmost part of the KMF, and, as discussed earlier, host high-grade Wessel-type Mn ores. The area is characterised by evidence for multiple thrust sheets, while the succession of the Hotazel Formation is capped by a shale quartzite package of rock of the lower Olifantsh oek Group, thus defining an unconformable contact. A selection of models have been comprehensively discussed over the years to account for the processes involved in the alteration and upgrade of the manganese ore in the

northernmost part of the KMF (Beukes et al., 1995; Gutzmer and Beukes, 1995,1996; Tsikos et al., 2003; Chetty and Gutzmer, 2012; Gutzmer et al., 2012). This section will discuss the ore-forming models and how they relate to the major structures we see in this study area, through the lens of this study and its results.

The classic ore-forming model proposed previously by Gutzmer and Beukes (1995), argued that the hydrothermal process that led to the progressive alteration and upgrade of the Mn ores required the use of normal high-angle faults as feeder conduits for fluids circulation. This model, which is referred to as the fault-controlled model, notes that the degree to which the rocks were altered decreases as the fluids move away from the faults laterally, in a skarn-like zonal fashion. This would have left low-grade unaltered manganese ore further from the fluid source at the center of two faulted blocks, while high-grade altered ore would occupy the space more adjacent to the faults.

It has been demonstrated that the process of enrichment due to the fluid-rock interaction involved the dissolution of carbonates and the leaching of silica from the protolith manganese ores. This was also obvious and became confirmed through the results of this study. This loss of the carbonate components (Ca, Mg and CO_2) of the primary ores would have resulted in abundant secondary porosity that involved volume loss and subsequently compaction of the ore bodies to approximately two-thirds of the original thickness (see also Tsikos et al., 2003). Gutzmer and Beukes (1995) based this model on mineralogical and textural variation of the Mn ores recorded with increasing distance away from the faults. Chetty (2008) further concurred with the interpretation of the Gutzmer and Beukes (1995) model in that the mineralogical assemblage in the Mn ore beds would have remained virtually constant with depth, but mineralogical and textural characteristics vary significantly with distance laterally from the fault as illustrated in Figure 5.1.

Tsikos (1999) and Tsikos *et al*. (2003) however, proposed a model that described the alteration process in the northernmost part of the KMF at least partly as a result of unconformity-related fluid-rock interaction processes. This model claims that, to some extent at least, the alteration of the Hotazel Formation and secondary enrichment of the ores were due to low-temperature fluid processes induced by descending meteoric-sourced fluids (Tsikos, 1999). Tsikos (1999), maintains that the process of alteration may have occurred at either pre- or syn-Olifantshoek times (>1.9Ga) following the gentle tilting of strata towards the west. This fluid would have moved downwards to as far as 60 m stratigraphic depth, with

the relatively more paleo-elevated areas enduring a larger effect of fluid leaching of the carbonate and chert material from the original rocks.

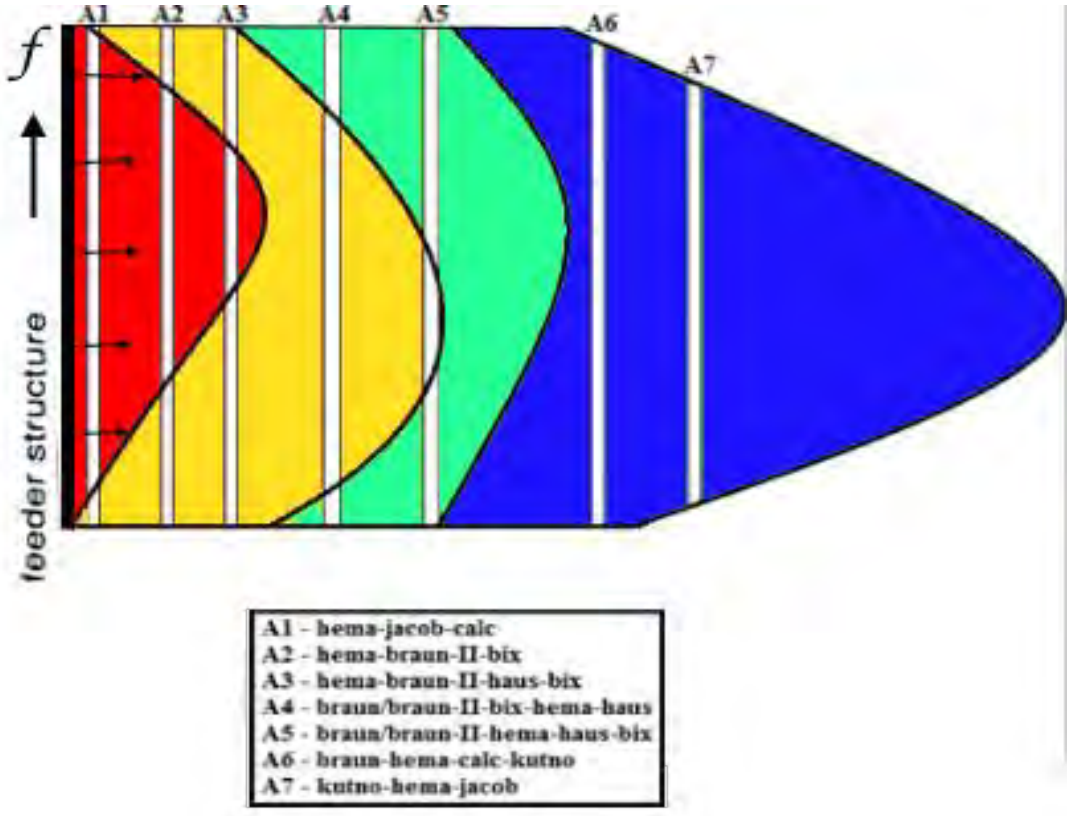

Figure 5. 1. Schematic diagram illustrating the changes in mineralogical assemblages with distance from faults associated with hydrothermal activities. The fault (*f*) acts as a feeder channel for fluids that interacts with the original rocks creating advanced hydrothermal fronts (represented by different colours) laterally away from the fault (modified after Chetty, 2008).

Tsikos (1999) further argues that the downward movement of fluids along the unconformity contact as well as other lithological contacts sub-parallel to that, would have led to the development of zonation with an overall vertical component, as illustrated in Figure 5. 2. In this zonal pattern as gleaned only from the BIF geochemistry and mineralogy, massive hematite prevails in the top of the stratigraphy due to the intense leaching process associated with the immediately overlying unconformity contact. The continuous leaching of carbonate material downward in the stratigraphy would be a dominant effect causing remobilisation of Ca, Mg, Sr, Ba (+/- some soluble Fe and Mn), and residual enrichment in Si, most Fe and other relatively immobile trace metals (Ni, V, Cr, Pb, and Th) in the BIF immediately underlying massive hematite (Tsikos 1999). Down-dipping movement of solutes would have began to cause partial re-precipitation at deeper levels with secondary dolomitic subfacies

developing in association with partially leached BIF. Even deeper, the rocks would have remained largely unaffected (Fig. 5. 2).

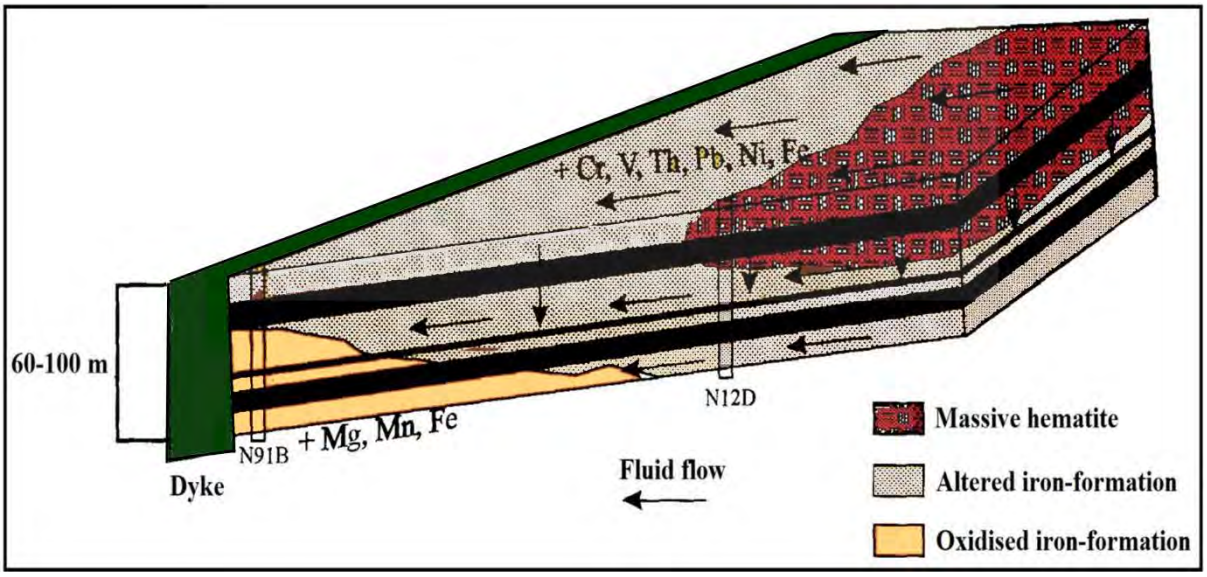

Figure 5. 2. Conceptual schematic diagram (not to scale) modified after Tsikos (1999) that illustrates the development of altered and oxidised iron-formation as a result of low-temperature fluid-rock interaction processes associated with descending low-temperature fluids at and parallel to the unconformity. The most paleo-elevated parts of the sequence would have suffered intense alteration and development of residual, massive hematite (Tsikos, 1999).

5.3. Alteration process as recorded in the different Mn ore layers

The mineralogy and geochemistry sections of this thesis showed how variable the ores are in the northern part of the KMF where the Nchwaning and Gloria mines are located. This subchapter aims to go into finer detail with the purpose of discussing the possible significance of lateral and vertical geochemical variations in the five borehole intersections studied. The major elements of consideration that are used are the rock-forming oxides MnO_2, SiO_2, CaO, and Fe_2O_3, by comparison with the geochemistry of the assumed protolith (GL136). Diagrams are first plotted that display the average of ratios of the three oxides SiO_2, CaO and Fe_2O_3 as percentages against MnO_2, and are then used to examine the degree of major geochemical change that has occurred across all boreholes laterally and vertically, i.e., between two ore bodies of the same borehole.

In addition, a comparative exercise of mass balance reconstructions is done by re-creating "enriched" intersections of the two Mn ore bodies from the protolith drillcore GL136, including also the overlying BIF in each instance. This exercise involves a mathematical

process that essentially assumes passive enrichment of the protolith intersection through hypothetical wholesale removal of all major elements associated with a process of decarbonation, namely CO_2 and the alkali earths Ca and Mg. This is done simply by subtracting the concentrations of CaO, MgO and LOI (assuming that LOI is effectively the total CO_2 present in the rock) and recalculating the bulk geochemical data of GL136 to 100% assuming zero $CaCO_3$ and $MgCO_3$. The calculated weight percent (wt.%) of the mass loss that corresponds to this reduction in mass is then removed as a corresponding stratigraphic thickness of the lithological units, assuming no major density changes have occurred.

The above exercise is admittedly oversimplistic, as it assumes a constant thickness laterally for both ore beds for effective comparisons. It is done for both ore bodies to compare with each of the five boreholes selected in this thesis, in order to generate further clarity on the degree of apparent compaction and therefore mass loss that was experienced by each high-grade ore bed and overlying BIF, and how that actually relates to the actual chemical mass balance as gleaned from the geochemical results in each borehole case.

Table 3. Data used in the comparative mass balance exercise. Volume lost is total carbonate (CaO, MgO and CO_2) lost due to the enrichement process.

Units	Original thickness	Volume lost	Volume remained	Reduced thickness	N95E	N95A	N92I	N94J	GL57
Top BIF	24.0	17.7	82.3	19.8	2.5	16.7	7.6	19.2	36.5
Lutite	9.80	21.8	78.2	7.66	4.5	3.1	3.4	6.8	9.8
Top Mn	10.5	36.5	63.5	6.67	4.0	7.0	7.9	11.0	7.8
BIF + Lutite	5.80	19.2	80.8	4.69	1.8	1.6	1.0	4.4	6.0
Lower Mn	13.0	42.7	57.3	7.45	7.0	7.5	4.2	7.0	13.1
Lower BIF	3.90	9.43	90.6	3.53	3.7	3.4	5.0	5.2	8.5

The representative Mamatwan-type protolith for the two ore bodies (MTO) is always from intersection GL136 at Gloria mine (Mhlanga, 2020). Here, the top ore body is 10.5 meters thick and its percentage major element oxide ratios plot at 71%, 77% and 58% MnO_2 over CaO, SiO_2 and Fe_2O_3 respectively. The lower ore body is 13 meters thick and its percentage major element oxide ratios plot at 70%, 88% and 77% MnO_2 over CaO, SiO_2 and Fe_2O_3 Respectively. At first glance, the ensuing ratio diagrams (Figs. 5. 3, 5. 5) show a large range in the distribution of the calculated ratios, especially for the top ore body compared to the lower one. There is also a general enrichment, relative to MTO, in MnO_2 over CaO and SiO_2

for all samples in both ore bodies at different scales (except for core GL57). Below follows a more detailed account for each ore bed.

5.3.1. Upper Mn ore layers

Textural information from earlier chapters show that the top Mn ore bed does not record much variation texturally, as the degree of alteration appears to be advanced resulting in generally very massive textures of ore. Geochemically, borehole N95E located in the northernmost part of Nchwaning farm has the highest average percentages of Ca and Si, hence shows the least enrichment in MnO_2 relative to CaO and SiO_2 in the top ore body. This drill core also has the thinnest section of the top ore body and is the closest to the Mapedi/Gamagara unconformity. Drillcores N94J and GL57 have the highest enrichment of Mn in the top ore body. However, N94J is enriched in Mn relative to Ca, due to little or no Ca content available in this ore body, while GL57 is enriched in MnO_2 in large part due to a major apparent loss in its Si and Fe content relative to the protolith. Drillcores N95E, N92I and GL57 all have massive hematite ore in the top BIF but N95E has ferruginised ore while GL57 does not. This variation can be attributed to differing distance of the ore beds from the Mapedi/Gamagara unconformity, which is previously said to have been a major contributing feature in the alteration of the ores and adjacent BIF (Tsikos et al., 2003).

Gutzmer and Beukes (1997) explains that alteration to Wessels-type ore involving intense removal of carbonates from the Mn ore bed would lead to porosity and subsequent compaction due to the overlying lithostatic overburden. Using this concept, one would expect that high-grade ores with little or no carbonate material preserved in them would have experienced higher compaction and thickness reduction than the low-grade ores. Drill core N95E, characterised by low-grade ferruginised ore with high carbonates content, indeed appears to show the highest reduction in thickness, but drill core N94J which is characterised by high-grade ore with low carbonate contents, shows no such apparent reduction in thickness. This could be related to primary lateral differences in the original stratigraphic thickness between the two drill cores or due to more intense alteration and mass loss/compaction experienced in drill core N95E that is in much closer proximity to the unconformity above it. It should be also added though that the thickness of the top ore bodies of all other three (3) remaining drill cores correlates well with the calculated reduced thickness of the hypothetically “enriched” GL136 top ore body (Fig. 5.4).

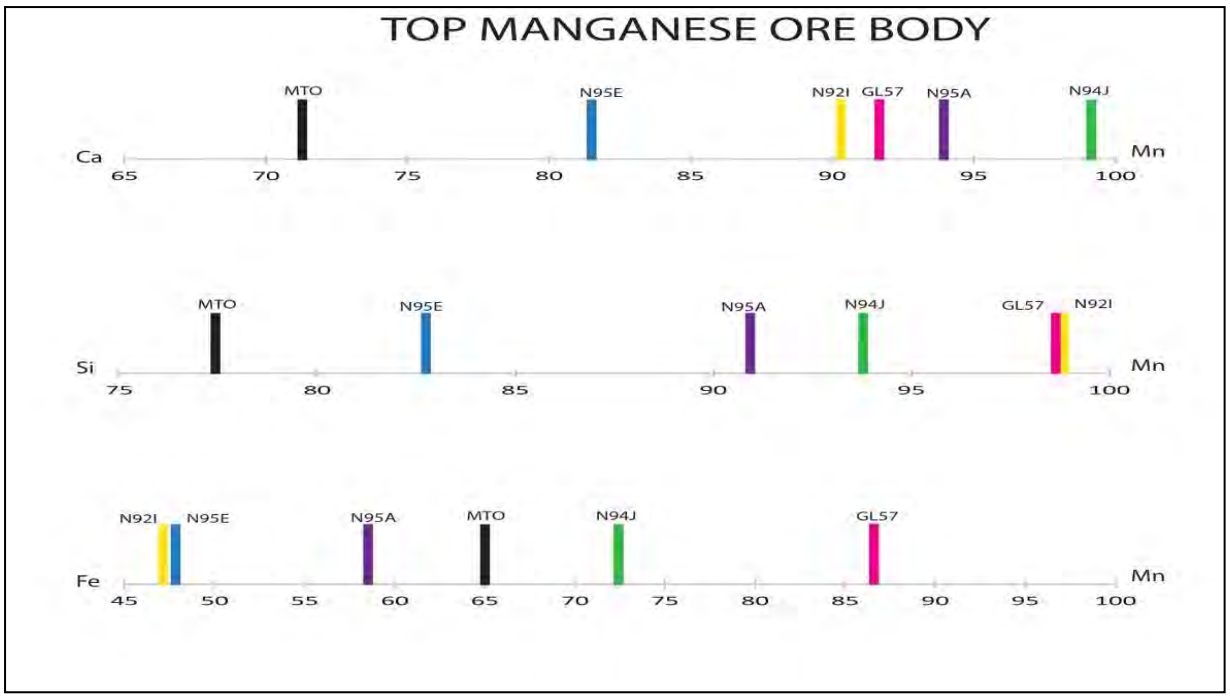

Figure 5. 3. Diagram showing variation in elemental ratios as percentages for the top Mn ore body of the five drill cores used in this study relative to the assumed protolith.

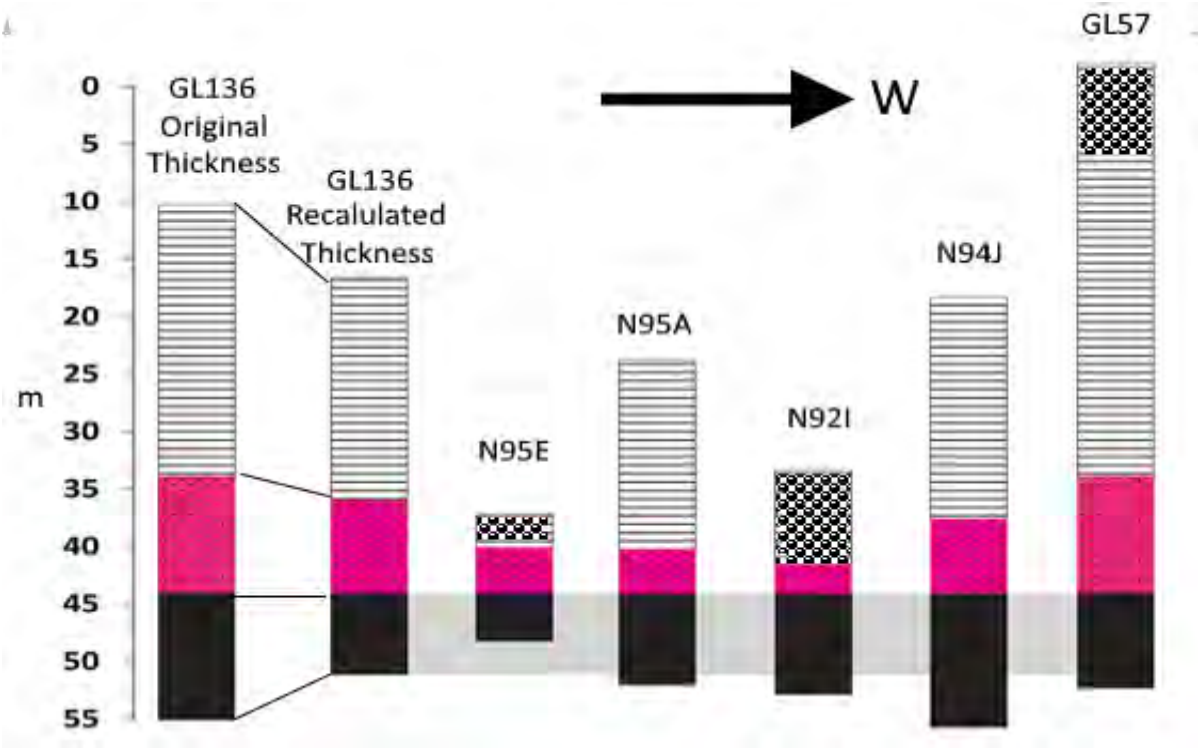

Figure 5. 4. Simplified stratigraphic profile showing the original and recalculated thickness of the protolith. This diagram illustrates a comparative mass loss due to alteration of the top Mn ore bodies, which was done by the removal of the total carbonates, relative to the altered ores of the five drill cores used in this study.

5.3.2. Lower Mn ore layers

The lower ore bodies of the five drill cores show lower degrees of ferruginisation and contain generally more hausmannite-rich ore than the top ore bodies. This is, of course, not the same for drillcore GL57 which contains low-grade Mamatwan-type lower ore body similar to the protolith; hence, it plots very close to the protolith on the comparative elemental percentage ratio diagrams. This is also supported by the texture preservation in that ore bed dominated by braunite and calcite/kutnahorite laminae and ovoids. Crucially, the alteration process affecting the intersection of drillcore GL57 does not at all correlate with the fault-controlled model of Beukes *et al*. (1995) and Gutzmer and Beukes (1995). Simply speaking, on the very narrow width scale of a single borehole, it is very surprising to observe Wessels-type ore higher in the stratigraphy (top ore bed) while lower down in the lower ore body the effects of Wessels-type alteration are non-existent. This pattern of alteration change is much more consistent with top-down alteration effects (Tsikos et al., 2003), rather than with laterally expanding alteration against near-vertical fluid-flow pathways (Gutzmer and Beukes, 1995).

Contrary to GL57, drillcore N92I is located proximally with the major graben structure, has the lowest CaO and Fe_2O_3 abundances in the lower ore body and it shows significantly high enrichment in MnO_2 relative to both element oxides (Fig. 5. 5). It can be said that due to the evidently high degree of removal of Ca and Si during alteration, the lower orebody here has the highest concentration of manganese in large part due to residual enrichment. With regard to the lower ore bodies of N95A and N92J (both from the southern portion of Nchwaning farm), these have similar elemental ratios although N95A seems to have a bit higher carbonate content than N94J. Drillcores N95E and N92I both contain highly altered, ferruginised BIFs and lutite above the top ore body, as well as in samples closer to the lower ore body. These are result of deeper infiltration of hydrothermal fluids in a bedding-parallel fashion as a consequence of dynamic leaching of carbonate and silica and self-propagation of the reacting fluids along gradients.

As expected in terms of thickness variations, the lower ore body of GL57 characterised by low-grade Mamatwan-type ore with inherently high carbonate content, shows no apparent reduction. By contrast, drill core N92I, characterised by high-grade ores with low carbonate contents, shows the highest relative reduction in thickness compared to the artificially enriched protolith (Fig. 5. 6). The thickness of the lower ore bodies of all other three (3) drill cores correlates well with that of the assumed “enriched and thinned” GL136 lower ore body.

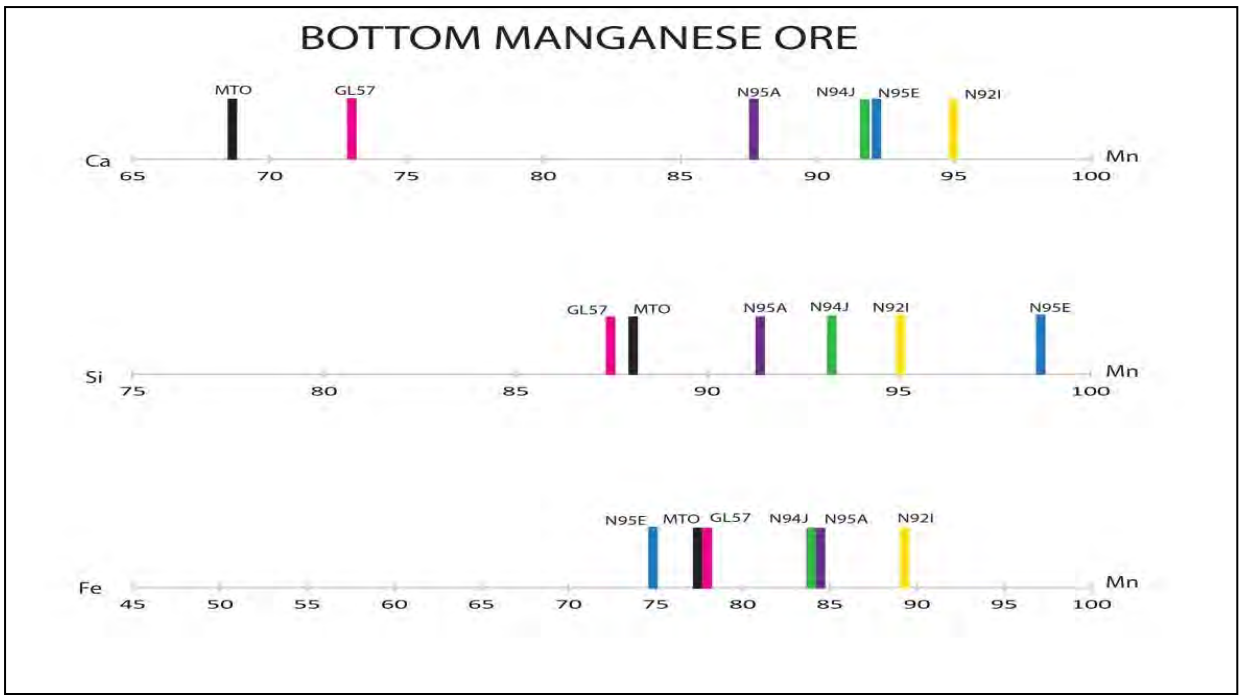

Figure 5. 5. Diagram showing variation in elemental ratios as percentages for the lower Mn ore body of the five drill cores used in this study relative to the assumed protolith.

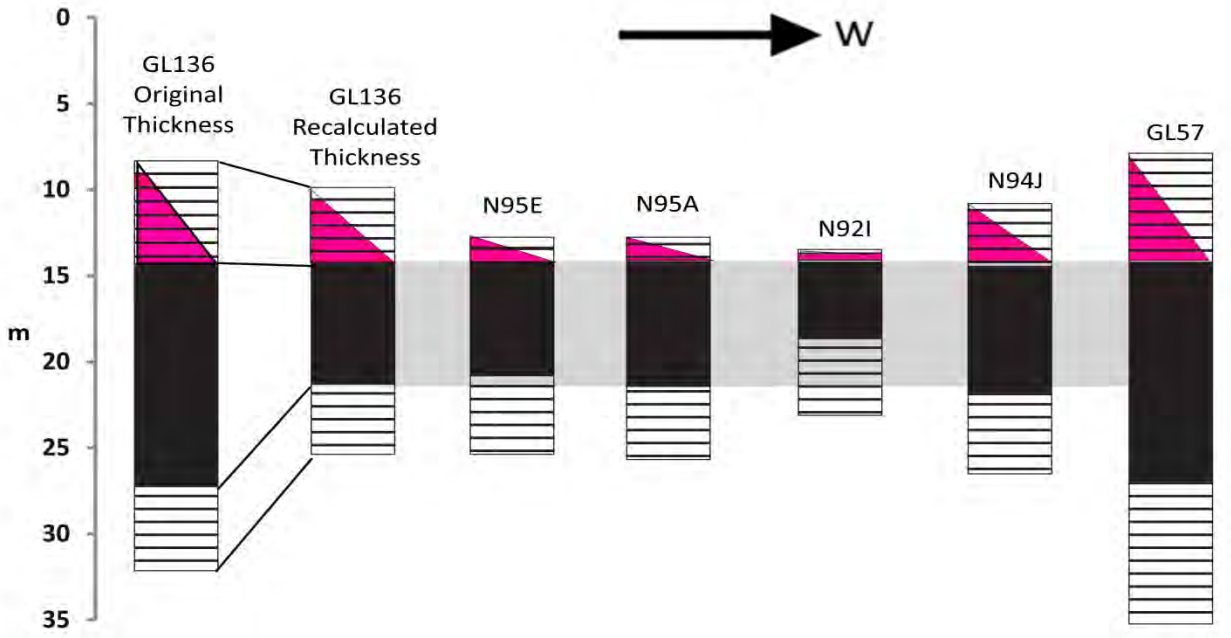

Figure 5. 6. Simplified stratigraphic profile showing the original and recalculated thickness of the protolith. This diagram illustrates a comparative mass loss due to alteration of the lower Mn ore bodies, which was done by the removal of the total carbonates, relative to the altered ores of the five drill cores used in this study.

5.4. Summary of alteration process across different drillcores

Drillcore N95E is the only one that shows the Mapedi/Gamagara shale resting just above the top Mn ore body and is also close to a fault structure. The section of BIF at the very top of the intersected section can actually be regarded as ferruginised shale due to its high Al content (up to 25 wt.% Al_2O_3). The top Mn ore body is thus lying about 5m below the overlying unconformity and the ore appears highly ferruginised with very low Mn/Fe ratios. The mineral assemblage here includes hausmannite-braunite-andradite-barite plus abundant hematite. It is evident therefore, that there must have been intense Fe addition and reduction in thickness of the Mn ore bed due to the decarbonation by fluids from the unconformity. Relative to the protolith, the significant addition of Fe is accompanied by similar additions in trace elements such as Pb, Cu, Ba, Co, Mo, and Zn. Consequently the net enrichment in Mn is low (avg. 38 wt.% MnO_2) relative to the assumed protolith. All these characteristics noted above are indicative of intense alteration due to the infiltration of fluids from the overlying unconformity, as argued previously by Tsikos et al. (2003).

Downwards within the stratigraphy of N95E, there are still signals of intense Fe enrichment in both the BIFs and lutite below the upper Mn ore bed, down to about 20 meters within the succession. The lower ore body rests about 22 m from the unconformity and the ore here is mainly (except for samples closer the to contact with the BIF) characterised by low Fe content hence a higher Mn/Fe ratio. The ore of this lower Mn ore bed is much higher grade (ave. 65 wt.% MnO_2) consisting of hausmannite, braunite II, calcite, marokite and minor barite abundances. Relative to the protolith, there is an apparent high loss of Si and significant loss of Ca due to intense leaching of the primary protolith ore. This alteration process must also have led to the enrichment of Pb, Cu, Ba, Co, Mo, and Zn within the ore. Below the lower Mn ore bed one also sees a notable gain in Fe content in both the lutite and the BIF samples. The enrichment of the ores in the lower ore body of this drill core may mainly be due to alteration by fault-related hydrothermal fluids penetrating laterally away from the fault conduits, with possible lesser effect of alteration from top-down fluid-flow. The latter would be supported by the overall thickness of this drill core being only 32m while, according to Tsikos (1999), unconformity-driven fluids have impacted the succession as deep as 60 m below the unconformity contact. This is also the reason for the relative ferruginisation of the rocks in this stratigraphy with depth. The dykes situated closer to this

drill core could have acted as fluid barrier to both lateral and/or down-dip fluid circulation from above.

Drillcore N95A located in the south-western region of the study area is not associated/lies further away from the major N-S graben structure, but minor E-W-trending faults are present nearby. The distance from the top ore body is more than 18 m to the unconformity contact above. The BIFs overlying this ore body are normal BIFs with a balanced concentration of Fe and Si at the upper section of the core, and a relatively small increase in Fe and decrease in Si with depth. The ores are high grade (ave. 64 wt.% MnO_2) with relatively high Mn/Fe ratios and show replacement of earlier textures. The minerals present in this ore body is predominantly braunite with minor abundances of andradite and hematite, and according to Gutzmer and Beukes (1995), this is characteristic of ore further away from the fault planes. Relative to the protolith, the ores of the top Mn ore body show significant loss of Ca, Mg and Si with a minor gain of Fe. Concurrently, there is a significant gain in Pb, Cu, Co and Mo and little to no change in the concentration of Zn, Ba and Ni relative to the assumed protolith.

The BIF layers below the top ore body until the top of the lower ore body show no obvious geochemical/mineralogical variation, similar to the ones at the top of the section, as they all appear to have a bimodal composition of hematite and chert. The distance from the top of the stratigraphy to the top of the lower Mn ore body is about 38 m, and both ore bodies are quite similar in thickness. The Mn ore of the lower Mn bed is also high-grade with similar average MnO_2 concentration (63 wt.%) as the top ore body but the lower ore body has a significantly higher Mn/Fe due to the low Fe content of these ores. Relative to the protolith, there is an evident and significant loss of Si, Ca and Mg and a minor loss of Fe due to alteration by fluids. This alteration process also led to the gain of Pb, Ba, Cu, Sr, Mo and Co relative to the unaltered ores. The lack of evident ferruginisation in the BIFs at the top of the sequence and overall similarity in assemblages across the studied succession, suggests a relatively more homogeneous alteration effect with no sign of differential top-down overprints.

Drillcore N92I is located proximally to the major graben fault at the centre of the Nchwaning farm and is consequently at a greater present depth than the rest of the other drill cores. This drill core is about 52m thick and the distance from the top of the section (Gamagara/Mapedi unconfofrmity) to the top Mn ore body is about 10m. Massive hematite dominates the BIF above the top ore body. The latter is also highly ferruginised with a low Mn/Fe on average and the highest concentration of Fe_2O_3 (ave. 50 wt.%) among the 5 drill cores. The mineral

assemblage within these ores is braunite II-hausmannite-andradite with traces of marokite and manganite. Relative to the protolith, this ore body has the highest gain of Fe and the highest loss of Si among the five drill cores. These characteristics are indicative of intense alteration and Fe addition due to the infiltration of fluids which again may have derived mainly from fluid flow along the overlying unconformity.

Similar to drillcore N95E, drill core N92I also contains ferruginised BIFs and transitional lutite downwards in the stratigraphy before reaching the lower ore body at about 40m from the top of the section. The lower ore body is significantly thinner (4m) than the top ore body (10m), and the intense alteration effects that led to such compaction could be responsible for the formation of high-grade ore occurring just about 18 m below the top Mn ore bed. This ore is characterised by very low Fe_2O_3 content and a high MnO_2 content hence a very high Mn/Fe ratio. This high-grade ore has thus comparatively much higher Mn content (avg. 84 wt. % MnO_2) relative to the top ore body (avg. 45 wt.% MnO_2). Relative to the protolith, this ore body has evidently experienced the highest loss of Fe and Ca with a somewhat smaller to no loss of Si. The minerals identified within this ore body were predominantly hausmannite, braunite, calcite, andradite and minor hematite which corresponds to the mineral assemblage of the hausmannite ore as discussed by Gutzmer and Beukes (1997). Significant gain of Pb, Ba, Cu, Mo and Zn and loss of Mg and Sr within this ore body are also seen relative to the presumed protolith.

The two ore bodies encountered in drill core N92I occur at almost equal distance from the major N-S faults that formed the graben structure. However, they vary significantly in mineral assemblages and textural characteristics. It is plausible, based on the evidence available, that enrichment was the combined effect of fluid flow from the upper contact but also laterally away from adjacent faults, with the former accounting mainly for the effects witnessed in the upper stratigraphic portions.

Drillcore N94J is situated within the south-easterly region of the study area; it is associated with a major fault structure and lies about 200m away from the easternmost EW-trending dyke. This section is the thickest drill core section from the Nchwaning farm included in this study and the distance from the top of the BIF in contact with the overlying shales until the top Mn ore bed is 25m. The 18 m of BIF overlying this section are normal altered BIFs with a balanced concentration of Fe_2O_3 and SiO_2. The top Mn ore bed is 11m thick and contains high-grade Mn ores (ave. 67 wt.% MnO_2) with a high Mn/Fe ratio and Mn/Ca ratio. Relative

to the protolith, this ore body shows the highest apparent loss of Ca among all 5 drill cores and a significantly high loss of Si, Fe and Mg. There is, concurrently, a significant gain in Pb, Cu, Ba, Zn, and Mo, while Co, V, and Sr are among the trace elements that appear partly lost during the process of alteration of the assumed protolith. The mineral assemblage of this upper ore is hausmannite-calcite-barite and corresponds to the type of ore expected to be at intermediate distances away from faults, as described by Gutzmer and Beukes (1995, 1997).

Downward the stratigraphy is a thick (15m) layer of BIFs that is dominated entirely by hematite and chert. The distance to the lower Mn ore body from the top of the intersection is 62 m and the ore bed is about 7m thick. Similar to the top ore body of the drill core, the ore of the lower ore body is high grade with high average MnO_2 concentration (70 wt.%) and a high Mn/Fe ratio. Relative to the protolith, there is likewise a significantly high apparent loss in Si, Ca, Fe and Mg due to alteration of the unaltered ores by fluid-rock interaction. Accompanying trace element enrichments include those for Pb, Cu, Zn, and Mo relative to the assumed protolith. The mineral assemblage of this ore is also an intermediate one in the context of distance from faults as per the model of Gutzmer and Beukes (1995, 1997).

This drill core shows minimal effects of ferruginisation throughout the stratigraphy evident by its high Mn/Fe ratio in the Mn ore beds and the absence of massive hematite ores or Fe-enriched BIFs in general. On that evidence alone, fluid-flow associated with the overlying unconformity would not have played a major role here in the alteration process. This is further supported by the fact that both ore bodies are similar mineralogically and compositionally, and therefore probably owe their origin mainly to one fluid process.

Drillcore GL57 is located in the northwest section of the Gloria farm and lies the most easterly relative to the drill cores from the Nchwaning area. This section is more than 100m thick and the distance from the top of the section (Gamagara/Mapedi u/c) to the top Mn ore bed is about 40m. There are samples of massive hematite present at the very top of the section which grades into normal BIF that is characterised by balanced proportions of hematite and chert. The top Mn ore body is 8m thick, and it hosts high-grade ore with high MnO_2 concentration (ave. 74 wt.%) and high Mn/Fe ratio due to the relatively low Fe content. It also has a low concentration of SiO_2 and thus a significantly high Mn/Si ratio. The mineral assemblage of these ores is hausmannite-dolomite-braunite, which compares well with assemblages of intermediate distance from faults as described by Chetty (2008) and Gutzmer and Beukes (1995). However, the presence of massive hematite ore at the top of the

stratigraphy also points to the possibility of fluids from the unconformity playing a role in the alteration of the top Mn ore bed. Relative to the protolith, this ore body has the highest loss of Fe and Si among all five drill cores and also a significant loss of Ca but corresponding apparent gain in Mg. There is also an evident enrichment in Cu, Pb and Zn, while other trace elements record little to no major change in abundance (e.g. Ba, Ni, Co, Mo, and Zr).

Further down the stratigraphy, the BIF is compositionally similar to that described above while the hematite lutite transitions have classically high concentrations of Fe, Ca and Si. There is a general increase in carbonates content with depth below the top ore body, due to an apparent decrease in fluid-rock interaction effects and alteration deeper into the succession. The lower Mn ore bed is much thicker (15m) than the top ore body and has a relatively low MnO_2 concentration (ave. 35 wt.%). It maintains a mineralogy and textural appearance that compares directly to the low-grade Mamatwan-type ore, as evident by the presence of carbonate ovoids and laminae in a braunite matrix. This ore body is thus very similar to the protolith without any evidence of chemical mass change, and a composition that should reflect the core of a faulted block of Hotazel Fm enduring no alteration laterally away from faults. However, the presence of Wessels-type ore at the top of the section suggests that a top-down model of fluid-alteration can be applicable here, while there is no obvious reason to consider any effect from far afield fault-controlled fluid-flow.

5.5. Geological controls on alteration in the Northern KMD

A number of authors have attributed the alteration of the rocks of the Hotazel Formation to specific geological features (structural and sedimentary) that occurr in the Northern portion of the KMD and relate to both pre- and post-Olifantshoek times. The important ones that are possible contributors to the alteration of the ores from the Nchwaning and Gloria areas are:

1. Pre-Olifantshoek NE-SW-trending dykes that crosscut the KMD mainly in the Nchwaning area;
2. The pre-Olifantshoek Mapedi/Gamagara erosional unconformity that separates the Mapedi/Gamagara Formation from the underlying Mn-BIF Hotazel Formation;
3. Major N-S and minor E-W-striking faults forming post-deposition of the Olifantshoek sediments; and,
4. Thrust faults along the northwestern part of the KMD.

Alterations involving the N-S and E-W-striking normal faults above have been considered as the major structural features responsible for the alteration of the Hotazel Formation and subsequent enrichment of the ores by Gutzmer and Beukes (1995, 1996, 1997) based on petrological and geochemical studies performed on the lower ore body only. According to these studies, different mineral assemblages have been suggested to have been the result of hydrothermal fluids that infiltrated the rocks of the Hotazel Formation through faults, leading to varying degrees of alteration with distance from them. Later, Tsikos (1999) and Tsikos et al. (2003) proposed that the model involving only faults as major structures responsible for the alteration of these ore does not explain many other observations, which include the presence of different types of apparently altered iron-formation encountered across stratigraphy. Tsikos *et al*. (2003) posit that the Mapedi/Gamagara unconformity must have been a significant and important structure responsible for the alteration process especially in the upper part of the stratigraphy of the Hotazel Formation where the unconformity intersects BIF and Mn sections of the Hotazel Formation. The fluid-rock interaction involving low-temperature fluids of possible meteoric origin along the unconformity, would have occurred vertically leaving massive hematite and ferruginised ores at the top of the stratigraphy and more oxidised/less leached rocks in the lower stratigraphy.

Thrust faults seen in the western part of the Northern KMD are significant structural features for the alteration of ores in the Hotazel Formation (Kleyenstüber, 1984, 1985). Thrusting in the KMD is thought to be associated with the Kheis orogenic event dated at 1.8 – 1.9 Ga as documented by the presence of major thrust faults in the Black Rock mine area. Kleyenstüber (1985) noted that movement of hydrothermal fluids through normal faults must have also been affected by the thrust faults too. Thrust structures can also act as aquifers along which tectonically-driven, ascending fluids from deeply buried adjacent regions may pass. Such ascending fluids are generally in the form of evolved saline brines derived from the process of basin dewatering in buried sedimentary sequences (Tsikos, 1999).

A series of sub-parallel, NE-SW-trending dykes are also present in the area and are postulated to have intruded before the N-S-trending faults. This is based on geological relationships, as the NE-SW-trending andesitic dykes appear to be truncated by the erosional Mapedi/Gamagara unconformity, which suggests that they must have intruded before 1.9 Ga. The dykes could have acted as fluid barriers during hydrothermal fluid-flows that postdate their intrusion (Tsikos, 1999). Retardation of fluid circulation would have been a function of

the original fluid-direction and therefore the overall geometry of fluid-flow in relation to the three-dimensional geometry of fluid-flow conduits and the dykes themselves.

An important feature attributed to the alteration of the Hotazel formation in association with the unconformity is the presence of massive hematite ore at the top of the section in the BIF layers that is then followed deeper down by ferruginisation of the Mn ores beneath the BIFs. This relationship is thought to be a result of the interaction of low-temperature fluids with the underlying Hotazel Formation, which caused intense removal of silica and carbonates from the primary rocks with subsequent oxidative ferruginisation of the rocks. Based on the age of metasomatic sugilite assemblages associated with the alteration of the lower ore body at 1.0 Ga (Gnos *et al*., 2003), the fluids implicated in alteration of the Hotazel rocks would have circulated much later than the deposition of the Mapedi/Gamagara beds (dated approximately at 1.9 Ga). This implies that the fluids may have exploited either the faults and/or the unconformity and thrust contacts as suitable fluid pathways.

It is important to note here that fluid movement along a fault would result in a more laterally pronounced alteration gradient and hence should depict evidence of lateral zonal variation in mineralogy and chemistry. Gutzmer and Beukes (1995, 1996, 1997) showed in their papers that such variations in the Mn ore bodies of the Northern KMD occur laterally with distance away from fault structures. Chetty (2008) also showed that the lower Mn ore body exhibits mineralogical and textural variations laterally while the mineralogical assemblages remain virtually constant with depth. She further uses two ore body intersections from different drill cores on either side of a fault with different mineralogy and textures, to argue that it is only plausible to have such variation in the degree of alteration between closely spaced cores when considering fluids movement along the N-S fault rather than via downward movement of fluids originating from along the unconformity.

Drillcores N95A and N94 both show similar geochemical and mineralogical characteristics between both ore bodies and such enrichment is consistent to have been due to alteration associated with fluid movement along a fault structure. N95A is located in the SW of Nchwaning farm, a distance away from major faults, and has braunite-rich ores in both ore bodies, although the top ore body is more Fe-rich than the lower one. Drillcore N94J is located in the southeast of the Nchwaning area, closer to a fault and has hausmannite-rich ores in both ore bodies with the top ore body being more Fe-rich and Ca-poor compared to the lower ore body. Although the difference in Fe concentration could be due to the chemistry

of the original “protolith” intersection which also has higher Fe content in the top ore body than the lower ore body before the alteration process, the degree of enrichment in Fe suggests net Fe addition which cannot be accounted for purely through residual enrichment effects.

Other relatively more recent studies (Blignaut, 2017; Tsikos, 1999; Tsikos et al., 2003) have highlighted instead the vertical variation with drill cores from the Northern KMD where there are significant mineralogical and textural variations between the two ore bodies in a given intersection that are only a few meters apart. Tsikos (1999) has argued that the fault- and unconformity-controlled fluid models need not be mutually exclusive, and that although faulting may have played a role in the alteration process at some stage in the geological history, it cannot be the sole or most important mechanism affecting the rocks of the Hotazel Formation. Massive hematite layers are present in the top BIFs of N92I and GL57, which can be far more easily attributed to fluid-flow at the unconformity. Drillcore N95E shows effects of ferruginisation in the upper parts of the intersection with characteristically ferruginised Mn ore in the top ore bed. However, the ferruginisation due to alteration by unconformity-driven fluids does not seem to extend to the Mn ores and the BIF below the top ore body. Regarding the other cores (N95A and N94J) located in the southwest and southeast respectively of the Nchwaning area, they show no signs of intense ferruginisation textures both macroscopically and microscopically throughout the drill cores, and they possibly were not affected as much by fluid flow associated with the unconformity.

The effect of dykes is not well shown in this study, as most of the drill cores do not show sufficiently proximal association with the dykes intersecting the area. Dykes are said to have played a role in the post-depositional alteration history of the Hotazel formation. The geometry of the dykes in relation to the westerly dip direction of the Hotazel strata and the abundant N-S faults, suggests that fluid flow sub-parallel to bedding would encounter the dykes as barriers, whether in an ascending or descending fashion. Tsikos (1999) stated that an apparent “shadow effect” at the dykes whereby dissimilar ore grades appear immediately on either side of the dykes, suggests that alteration effects must have been affected by the dykes in a passive yet profound way. Drillcore. N95E is probably one of the closest to any dyke structure and shows intense alteration of the lower Mn ore as well as ferruginisation of the BIFs and lutite above it. It is possible that there is a combination of alteration effects in that drillcore that may have been impacted by the presence of the dyke as a fluid barrier.

Thrust faults were also mentioned by Kleyenstüber (1985) and Tsikos (1999) as potentially important structures in the alteration processes of the Northern KMD. The noticeable existence of the mineral aegirine in certain parts of the Hotazel stratigraphy, in combination with the complex metasomatic mineral occurrences seen locally across the northernmost KMD, suggests the fluid process of a strongly alkaline metasomatic-hydrothermal signature have affected the rocks. It remains unknown whether the strong alkali character of many of the mineral assemblages observed in the northern KMD and in this study, relates to the Wessels alteration event or has acted more as an overprinting feature. The formation of the mineral aegirine is supported by precursor material containing already binary mixtures of hematite and quartz, which would have derived from an earlier alteration event at the expense of primary BIF (Tsikos, 1999). The presence of aegirine in this study is limited to samples from the drill cores in the western part of the Nchwaning area which is also where the thrust faults are prominently developed. Therefore, it is plausible that there is a link between Na-metasomatism and thrust faulting, which most likely contributed to the alteration process of the ores in this area in some way, at least locally. Large-scale fluid-flow systems associated with thrust faults like the one seen in the KMD, are believed to be responsible for world-class ore districts like the MVT class of Zn-Pb-Ba deposits associated with orogenically driven fluid flow across space and geological time (Robb, 2005).

The results of this study have shown that brine-related, alkali- and associated metal metasomatism in the Hotazel rocks is a feature that is probably not as localised as originally thought. Although the intensity of metasomatic change varies from one drillcore to the next and in some cases involves largely chemical redistribution from the Hotazel protolith (e.g. REE; Chetty and Gutzmer, 2012, see also Fig. 5. 7.) a common denominator in almost all drillcore sections studied here is that the elements Pb, Zn, Cu and Ba are the key chemical species that show striking, albeit localised in many cases, net enrichment across all sections studied (Fig. 5. 7.). It is therefore possible that the main Wessels alteration event is in fact a broadly west-to-east alkali-metasomatic process with variable effect on the rocks across the region, which probably relates at least to some degree on the exact structures that constituted the main fluid pathways for brine fluid-flow.

Such a metasomatic effect may have overprinted in space and/or time, earlier alteration processes associated with fluid-flow at the unconformity contact, which would itself had involved down-dip E-W oxidation and low-temperature decarbonation of the rocks as ground preparation to the resultant metal enrichment process. In other words, two fluid-flow and

alteration events may have affected the rocks at the juncture represented today by the geographical area of the northernmost KMD. Although this study cannot provide any firmer constraints as to the relative timing and importance of these processes, it has hopefully at least taken a small step closer towards eventually elucidating their relative and cumulative impact.

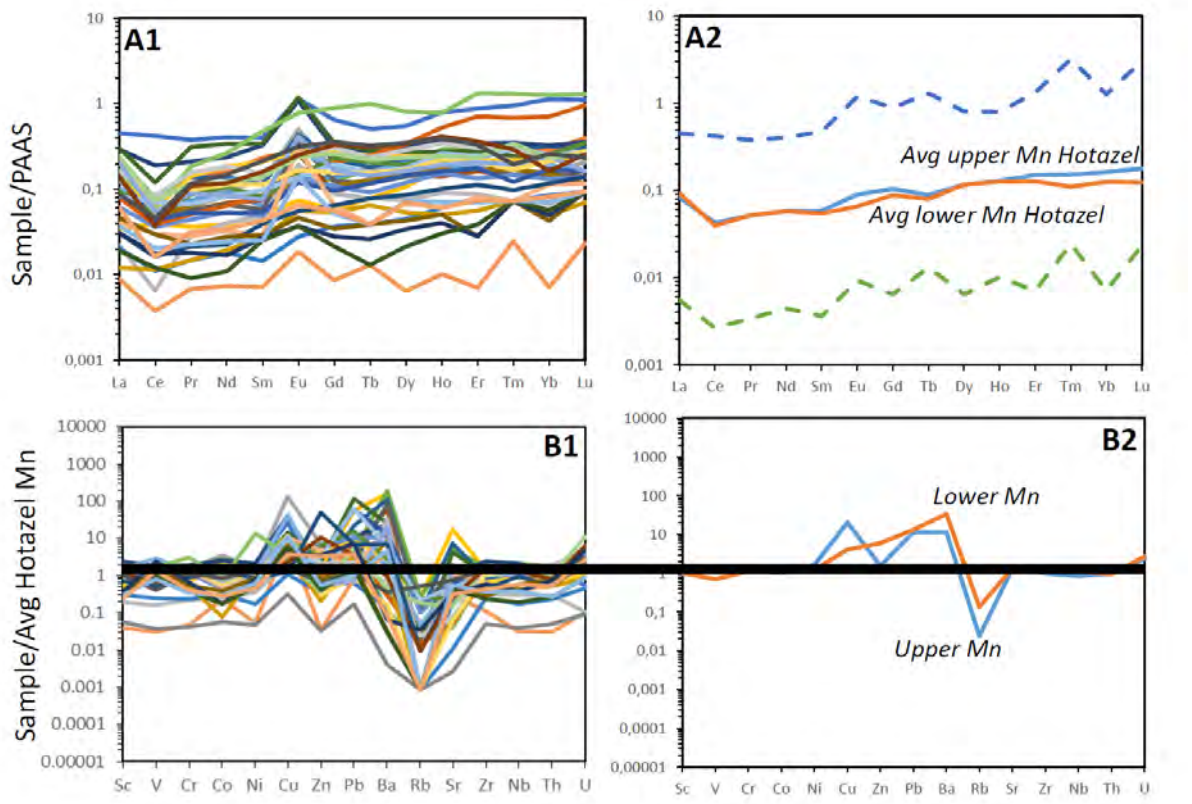

Figure 5. 7. Spidergrams illustrating the behaviour of REE (plots A1 & A2) and remaining trace elements (B1, B2) during hydrothermal alteration producing Wessels-type high-grade Mn ore. Although highly variable, REE patterns for both altered Mn ore beds as studied here, occupy a field of values showing both relative enrichment and depletions by comparison to the protolith signatures (A2). The fact that the protolith spidergams appear to occupy the middle point in the range of values recorded by the altered samples studied here, agrees broadly with the conservative REE behaviour during alteration as predicted by Chetty ad Gutzmer (2012). The protolith-normalised spidergrams for trace elements (except REE) for all Mn samples analysed in this study (B1) suggest that the only elements that show clear net enrichment during alteration are Zn, Pb, Cu and Ba. The thick black band across diagrams B1 and B2 indicates the range of values that would represent conservative enrichment due to mass loss during Wessels-type alteration against the assumed protolith. The latter is represented by the Gloria mine data for the upper and lower Mn ore beds of Mhlanga (2020).

5.6. Summary and Conclusions

The results of this study have contributed to the idea that multiple alteration events must have led to the alteration and enrichment of the Hotazel Fe-Mn Formation. To achieve that objective, the focus was placed, for the first time, on the entire succession of the Hotazel formation that includes the Mn ore beds and interlayered BIF, although understandably more emphasis was placed on data from the ore beds themselves.

The results from individual drillcores painted a rather mixed picture of alteration effects. Some drillcores are characterized by intense ferruginisation in their upper sections, which has been interpreted previously but also here as well, as an alteration effect of oxidation, leaching and largely passive enrichment in metals due to fluid-flow at the unconformity contact separating the Hotazel Formation and overlying Olifantshoek beds. Other drillcores towards the western Nchwaning area seem to record alkali metasomatic effects with clear and in most cases relatively localised enrichments in the elements Na, Ba, Zn, Pb and Cu. This is a geochemical signal that appears to be pervasive and may represent the fingerprint of the Wessels alteration event at about 1.0Ga. Finally, in some drillcores the alkali imprint is not so intense while the geochemistry of the Hotazel rocks appears to be comparable across the stratigraphy for both Mn (upper and lower ore beds) and Fe-rich lithofacies, suggesting operation of a single fluid event. In short, on the basis of only the five selected drillcores, it becomes obvious that the view of the alteration process in the northernmost KMD remains rather hazy and unclear.

It has become evident nonetheless, that specific mineralogical assemblages can be tentatively attributed to the structures present as possible fluid- passageways. Although two major structural features have been discussed as the dominating contributors to the alteration events, namely vertical faults and unconformity contacts, we cannot ignore evidence that suggests that other major structures in the Northern KMD may have played an important role. The aegirine-rich drill cores in the western part of the Nchwaning area, for example, appear to be spatially associated with thrust faults as plausible fluid conduits. This suggests that at some point in the alteration history of the ores, Na-rich metasomatic brines might have infiltrated the rocks *via* thrust planes, as manifested in the common enrichments of the rocks in Ba, Cu, Pb and Zn. These brines may well have been the major alteration driver for the Wessels alteration event *sensu stricto*, but it is also likely that the rocks had already been altered by

that time *via* earlier oxidative and leaching processes related to unconformity-driven flow of low-temperature fluids.

The confluence of the above two fluid events has ultimately led to the present picture of the northernmost KMD, which remains complex and continues to await full resolution. The results of this study certainly make it very hard to conclude that the alteration of the Hotazel formation occurred primarily through one alteration model or another. They have also highlighted once again, however, that the alteration and subsequent enrichment of the Hotazel Mn ores occurred through more than one fluid-events that utilized – or were at least influenced by – several geological features as either fluid conduits or barriers.

REFERENCES

Bau, M. and Dulski, P. (1996), "Distribution of yttrium and rare-earth elements in the Penge and Kuruman iron-formations, Transvaal Supergroup, South Africa", *Precambrian Research*, Vol. 79 No. 1–2, pp. 37–55.

Beukes, N.J. (1983), "Palaeoenvironmental setting of iron-formations in the depositional basin of the Transvaal Supergroup, South Africa.", in Trendall, A.F. and Morris, R.C. (Eds.), *Iron-Formation: Facts and Problems*, Elsevier Science, Amsterdam, pp. 131–209.

Beukes, N.J., Burger, A.M. and Gutzmer, J. (1995), "Fault-controlled hydrothermal alteration of Palaeoproterozoic manganese ore in Wessels Mine, Kalahari manganese field", *Sourth African Journal of Geology*, Vol. 98, pp. 430–451.

Blignaut, L.C. (2017), "A Petrographical and Geochemical Analysis of the Upper and Lower Manganese Ore Bodies from the Kalahari Manganese Deposit , Northern Cape , South Africa – Controls on Hydrothermal Metasomatism and Metal Upgrading". Ph.D thesis (unpubl.) University of Johannesburg, 248 pp.

Boardman, L.G. (1941), "The Black Rock Manganese Deposit in the South-Eastern Kalahari", *Transactions of the Geological Society of South Africa*, Vol. 44, pp. 51–60.

Cairncross, B. and Beukes, N.J. (2013), *The Kalahari Manganese Field, The Adventure Continues*, Struik Nature, Random House Struik (Pty) Ltd.

Cairncross, B., Tsikos, H. and Harris, C. (2000), "Prehnite from the Kalahari manganese field, South Africa, and its possible implications", *South African Journal of Geology*, Vol. 103 No. 3–4, pp. 231–236.

Chetty, D. (2008), "A geometallurgical evaluation of the ores of the northern Kalahari Manganese Deposit , South Africa", Ph.D. thesis (unpbl.), University of Johannesburg, 271 pp.

Chetty, D. and Gutzmer, J. (2012), "REE redistribution during hydrothermal alteration of ores of the Kalahari Manganese Deposit", *Ore Geology Reviews*, Vol. 47, pp. 126–135.

Coetzee, L.L. (2001), "Genetic stratigraphy of the Palaeoproterozoic Pretoria Group in the Western Transvaal", M. Sc Dissertation (unpbl). Rand Afrikaans University. 212 pp.

de Villiers, J.E. (1983), “The Manganese Deposits of Griqualand West , South Africa : Some Mineralogical Aspects”, *Geology*, Vol. 78, pp. 1108–1118.

de Villiers, J.P.R. (1970), “The geology and mineralogy of the Kalahari Manganese Field north of Sishen, Cape Province”, *Geological Survey of Southern Africa*, Memoir 59, Pretoria, p. 84.

Dulski, P. (1994), “Interferences of oxide, hydroxide and chloride analyte species in the determination of rare earth elements in geological samples by inductively coupled plasma-mass spectrometry”, *Fresenius’ Journal of Analytical Chemistry*, Vol. 350 No. 4–5, pp. 194–203.

Eglington, B.M. (2006), “Evolution of the Namaqua-Natal Belt, southern Africa - A geochronological and isotope geochemical review”, *Journal of African Earth Sciences*, Vol. 46 No. 1–2. pp. 93–111.

Frankel, J.J. (1958), “Manganese ores from the Kuruman District, Cape Province, South Africa”, *Economic Geology*, Vol. 53, pp. 577–597.

Gnos, E., Armbruster, T. and Villa, I.M. (2003), “Norrishite, $K(Mn_{23}+Li)Si_4O_{10}(O)(_2)$, an oxymica associated with sugilite from the Wessels Mine, South Africa: Crystal chemistry and Ar-40-Ar-39 dating”, *American Mineralogist*, Vol. 88 No. 1, pp. 189–194.

Grant, A. (1986), “The isocon diagram - a simple solution to Gresens’ equation for metasomatic alteration”, *Economic Geology*, Vol. 81, pp. 1976–1982.

Gutzmer, J. (1996), “Genesis and alteration of the Kalahari and Postmasburg manganese deposits, Griqualand West, South Africa”, *Unpublished PhD, Rand Afrikaans University*, p. 266.

Gutzmer, J. and Beukes, N.. (1995), “Fault-Controlled metasomatic alteration of Early Proterozoic sedimentary manganese ores in the Kalahari Manganese Fields, South Africa”, *Economic Geology*, Vol. 90, pp. 823–844.

Gutzmer, J. and Beukes, N.J. (1996), “Mineral paragenesis of the Kalahari managanese field, South Africa”, *Ore Geology Reviews*, Vol. 11 No. 6, pp. 405–428.

Gutzmer, J. and Beukes, N.J. (1997), “Effects of mass transfer, compaction and secondary porosity on hydrothermal upgrading of Paleoproterozoic sedimentary manganese ore in

the Kalahari manganese field, South Africa", *Mineralium Deposita*, Vol. 32 No. 3, pp. 250–256.

Gutzmer, J. and Beukes, N.J. (1998), *High-Grade Manganese Ores in the Kalahari Manganese Field: Characterisation and Dating of Ore-Forming Events.*, Unpbl. Report, Geology Department, Rand Afrikaans University.

Gutzmer, J., Du Plooy, A.P. and Beukes, N.J. (2012), "Timing of supergene enrichment of low-grade sedimentary manganese ores in the Kalahari Manganese Field, South Africa", *Ore Geology Reviews*, Vol. 47, pp. 136–153.

Kirschvink, J.L., Gaidos, E.J., Bertani, L.E., Beukes, N.J., Gutzmer, J., Maepa, L.N. and Steinberger, R.E. (2000), "Paleoproterozoic snowball Earth: Extreme climatic and geochemical global change and its biological consequences", *Proceedings of the National Academy of Sciences*, Vol. 97 No. 4, pp. 1400–1405.

Kleyenstüber, A.S.E. (1984), "The mineralogy of the manganese-bearing Hotazel Formation of the Proterozoic Transvaal sequence in Griqualand West, South Africa", *Transactions of the Geological Society of South Africas*, Vol. 87, pp. 257–272.

Kleyenstüber, A.S.E. (1985), "A Regional Mineralogical Study of the Manganese-Bearing Voelwater Subgroup in the Northeastern Cape Province". Ph.D thesis, Rand Afrikaans University (unpbl.)

Kleyenstüber, A.S.E. (1993), "Significant characteristics of the manganese ores and some of the minerals occurring in the Proterozoic Kalahari Manganese Field, South Africa", *Resource Geology*, Special Issue No. 17, pp. 2–11.

Klinkhammer, G.P., Elderfield, H., Edmond, J.M. and Mitra, A. (1994), "Geochemical implications of rare earth elements patterns in hydrothermal fluids from mid-ocean ridges", *Geochimica et Cosmochima Acta*, Vol. 58 No. 23, pp. 5105–5113.

Mhlanga, X.R., (2020) "A reappraisal of the origin of the Hotazel iron-manganese Formation in an evolving early Earth system, through the application of mineral-specific geochemistry, speciation techniques and stable isotope systematics". Unpublished PhD thesis, Rhodes University, 161 pp.

Moore, J.M., Tsikos, H. and Polteau, S. (2001), "Deconstructing the Transvaal Supergroup, South Africa: implications for Palaeoproterozoic palaeoclimate models", *Journal of*

African Earth Sciences, Vol. 33 No. 3–4, pp. 437–444.

Motilaodi, K.D. (2018), "Mineral-chemical variation in high-grade ores of the Kalahari Manganese Field, and implications for geometallurgy″, MSc Dissertation (unpbl). Rhodes University. 120 pp.

Ostwald, J. (1992), “Mineralogy, paragenesis and genesis of the braunite deposits of the Mary Valley Manganese Belt, Queensland, Australia”, *Mineralium Deposita*, Vol. 27, pp. 326–335.

Du Plooy, A.P. (2002), "Geochemistry and Mineralogy of Supergene Altered Manganese Ore below the Kalahari Unconformity in the Kalahari Manganese Field, Northern Cape, Province, South Africa". MSc thesis, Rand Afrikaans University (unpbl).

Puchner, R.A. (2002), "The Geology and Rock Mass Quality of the Cenozoic Kalahari Group , Nchwaning Mine Northern Cape". MSc thesis, University of Natal (unpbl).

Rogers, A.W. (1907), “Geological Survey of parts of Vryburg, Kuruman, Hay and Gordonia.”, *Annual Report of the Geological Commission of the Cape of Good Hope*, pp. 11–122.

Schier K., Bau M., Smith, A.J.B., Beukes, N.J., Coetzee, L.L., and Viehmann, S. (2020) Chemical evolution of seawater in the Transvaal Ocean between 2426 Ma (Ongeluk Large Igneous Province) and 2413 Ma ago (Kalahari Manganese Field). *Gondwana Research,* Vol. 88, pp 373-388

Schneiderhan, E.A., Gutzmer, J., Strauss, H., Mezger, K. and Beukes, N.J. (2006), “The chemostratigraphy of a Paleoproterozoic MnF-BIF succession - The Voëlwater Subgroup of the Transvaal Supergroup in Griqualand West, South Africa”, *South African Journal of Geology*, Vol. 109 No. 1–2, pp. 63–80.

Taylor, S.R. and McLennan, S.M. (1985), "The Continental Crust: Its Composition and Evolution″. Blackwell, Oxford.

Thomas, R.J., Agenbacht, A.L.D., Cornell, D.H. and Moore, J.M. (1994), “The Kibaran of southern Africa: Tectonic evolution and metallogeny”, *Ore Geology Reviews*, Vol. 9 No. 2, pp. 131–160.

Tsikos, H. (1999), "Petrographic and Geochemical Constraints on the Origin and Post-Depositional History of the Hotazel Iron-Manganese Deposits, Kalahari Manganese

Field. South Africa". *Rhodes University PhD Thesis*, 286 pp

Tsikos, H., Beukes, N.J., Moore, J.M. and Harris, C. (2003), "Deposition, Diagenesis, and Secondary Enrichment of Metals in the Paleoproterozoic Hotazel Iron Formation, Kalahari Manganese Field, South Africa", *Economic Geology*, Vol. 98 No. 7, pp. 1449–1462.

Tsikos, H. and Moore, J.M. (1997), "Petrography and geochemistry of the Paleoproterozoic Hotazel iron-formation, Kalahari manganese field, South Africa: Implications for Precambrian manganese metallogenesis", *Economic Geology*, Vol. 92 No. 1, pp. 87–97.

Tsikos, H. and Moore, J.M. (2005), "Sodic metasomatism in the Palaeoproterozoic Hotazel iron-formation, Transvaal Supergroup, South Africa: Implications for fluid-rock interaction in the Kalahari manganese field", *Geofluids*, Vol. 5 No. 4, pp. 264–271.

Appendices

Appendix I. Elemental ratio Maps

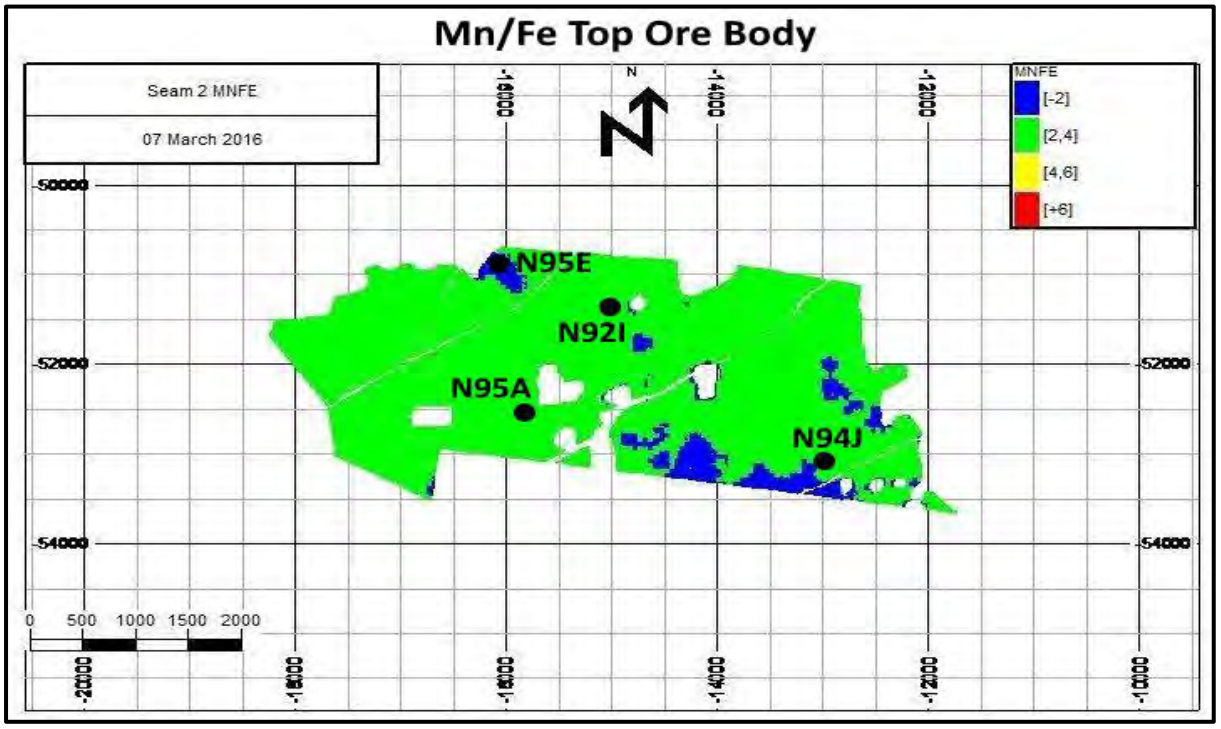

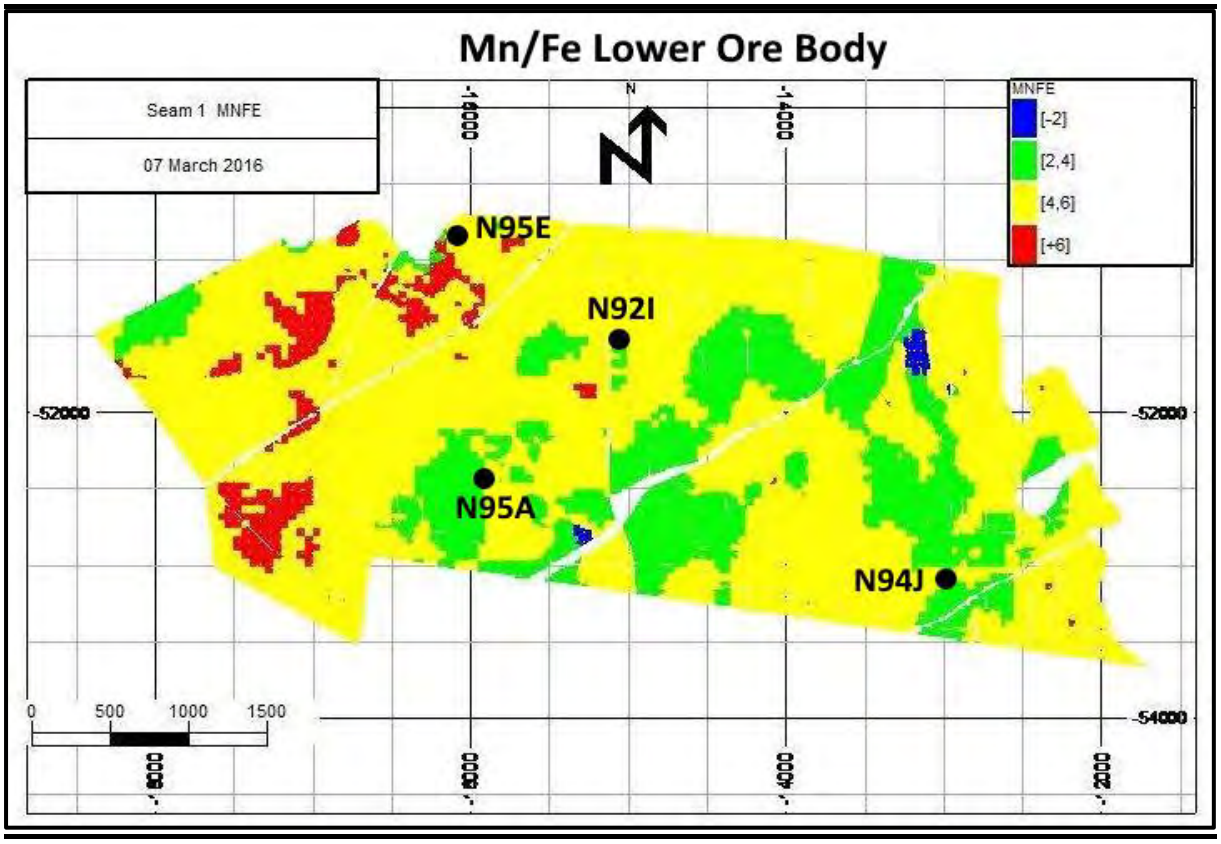

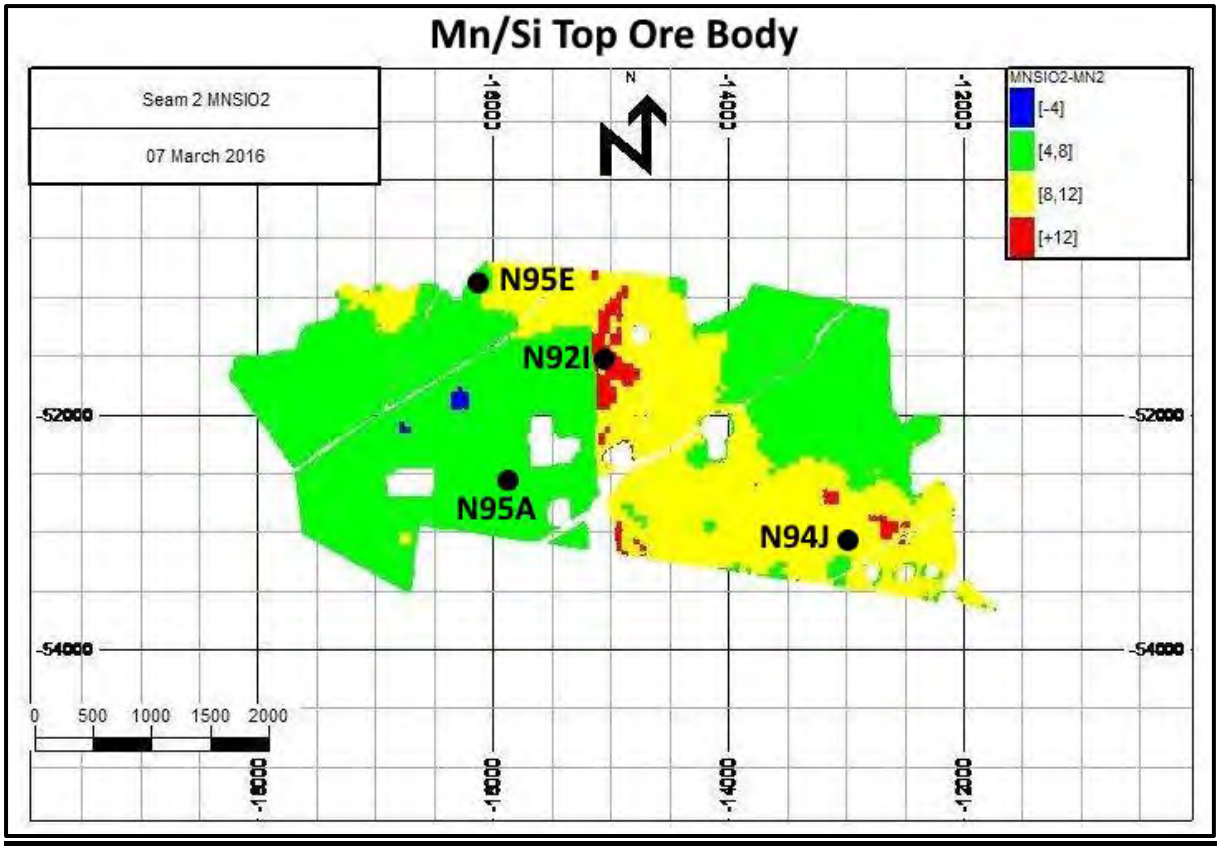
Mn/Si Top Ore Body
Seam 2 MNSIO2
07 March 2016
N
MNSIO2-MN2
[-4]
[4,8]
[8,12]
[+12]
N95E
N92I
N95A
N94J
-52000
-54000
0 500 1000 1500 2000

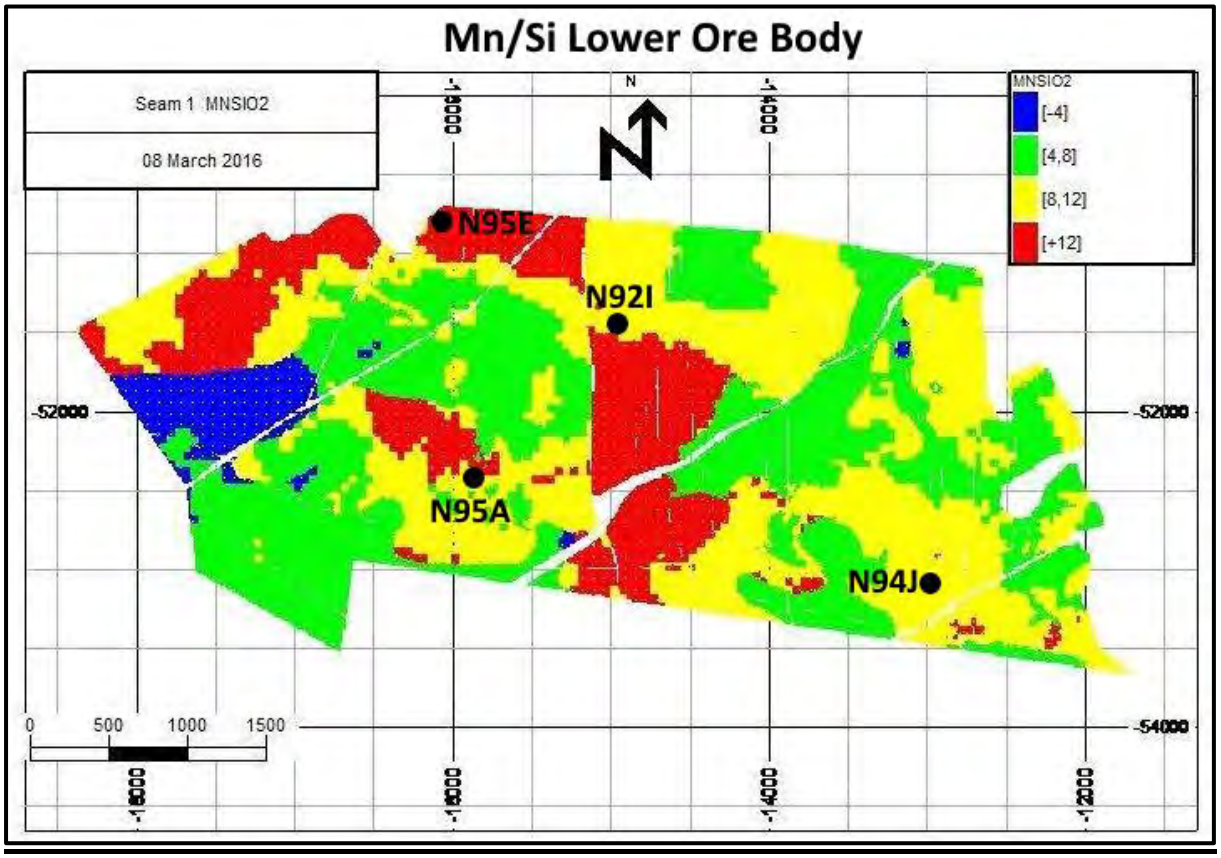
Mn/Si Lower Ore Body
Seam 1 MNSIO2
08 March 2016
N
MNSIO2
[-4]
[4,8]
[8,12]
[+12]
N95E
N92I
N95A
N94J
-52000
-54000
0 500 1000 1500

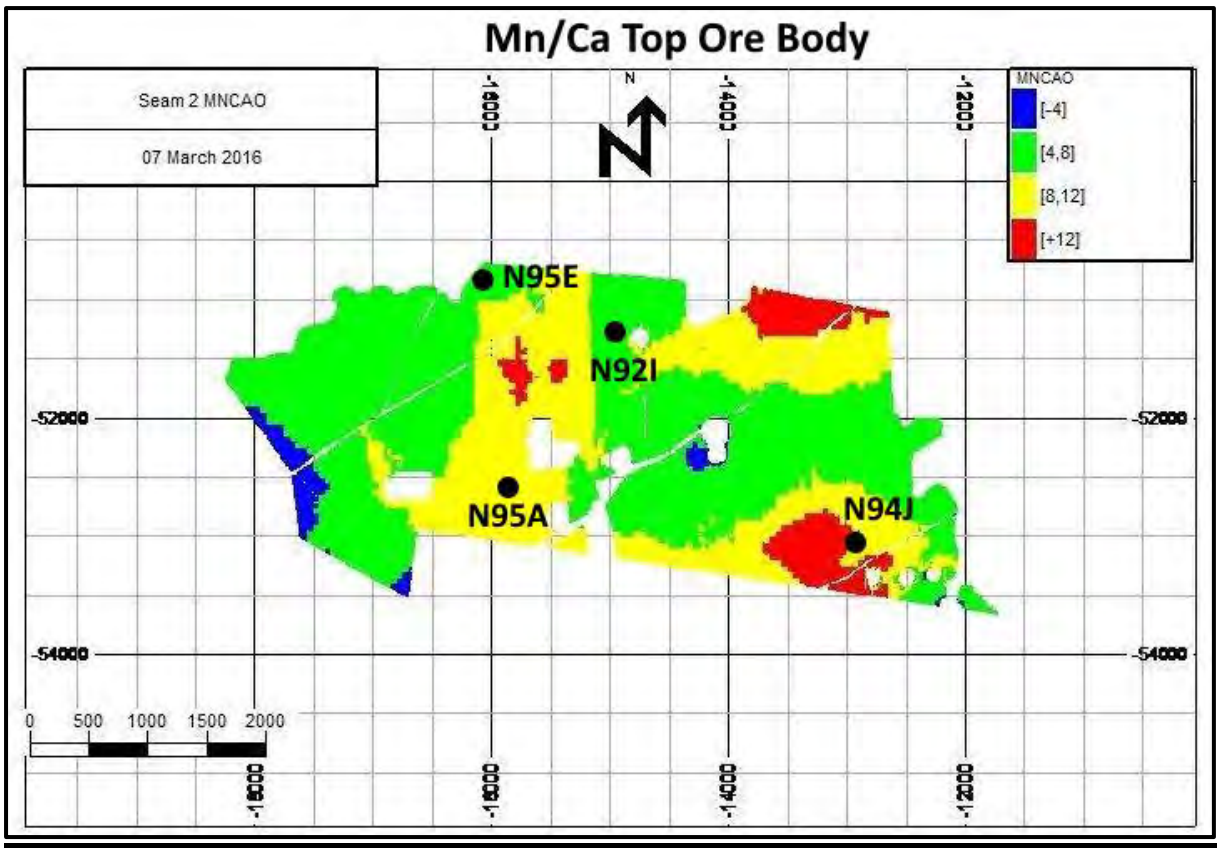
Mn/Ca Top Ore Body
Seam 2 MNCAO
07 March 2016
N
MNCAO
[-4]
[4,8]
[8,12]
[+12]
N95E
N92I
N95A
N94J
-52000
-54000
0 500 1000 1500 2000
-16000
-14000
-12000

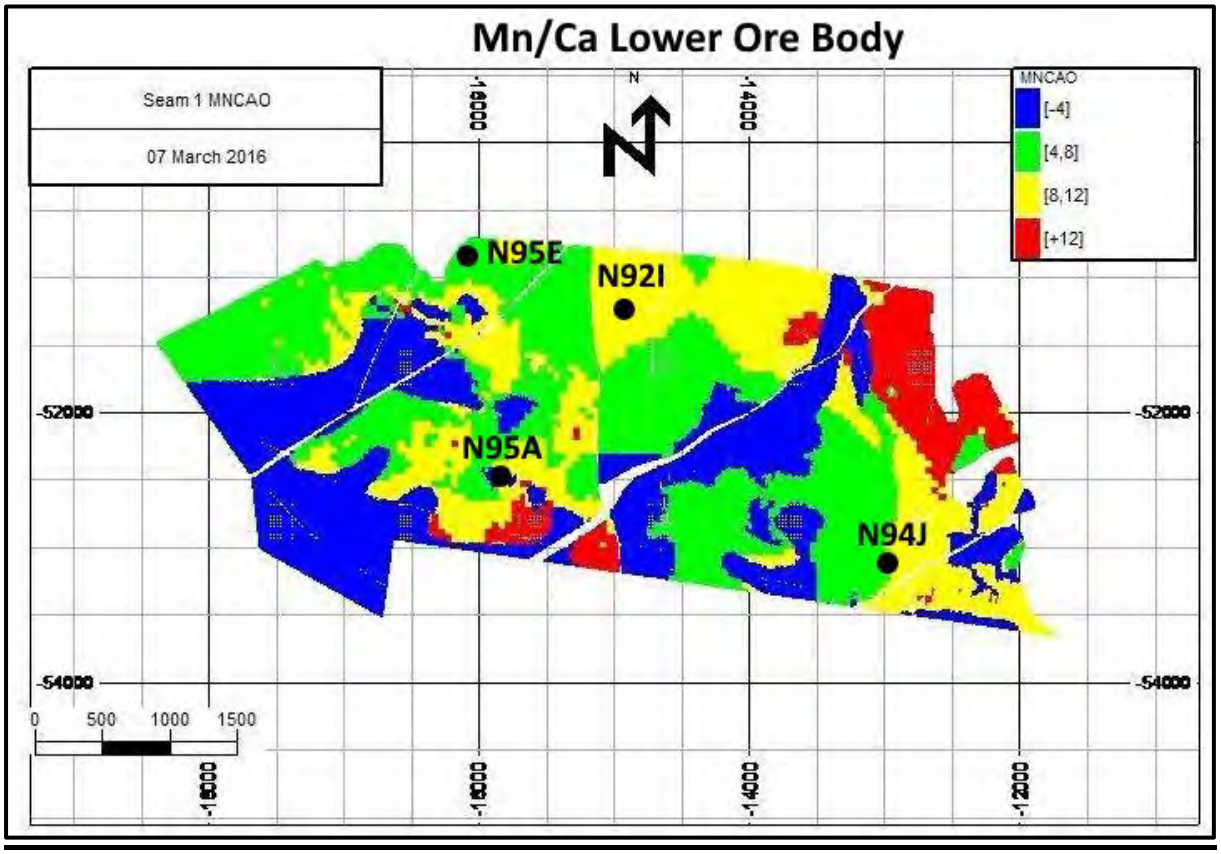
Mn/Ca Lower Ore Body
Seam 1 MNCAO
07 March 2016
N
MNCAO
[-4]
[4,8]
[8,12]
[+12]
N95E
N92I
N95A
N94J
-52000
-54000
0 500 1000 1500
-16000
-14000
-12000

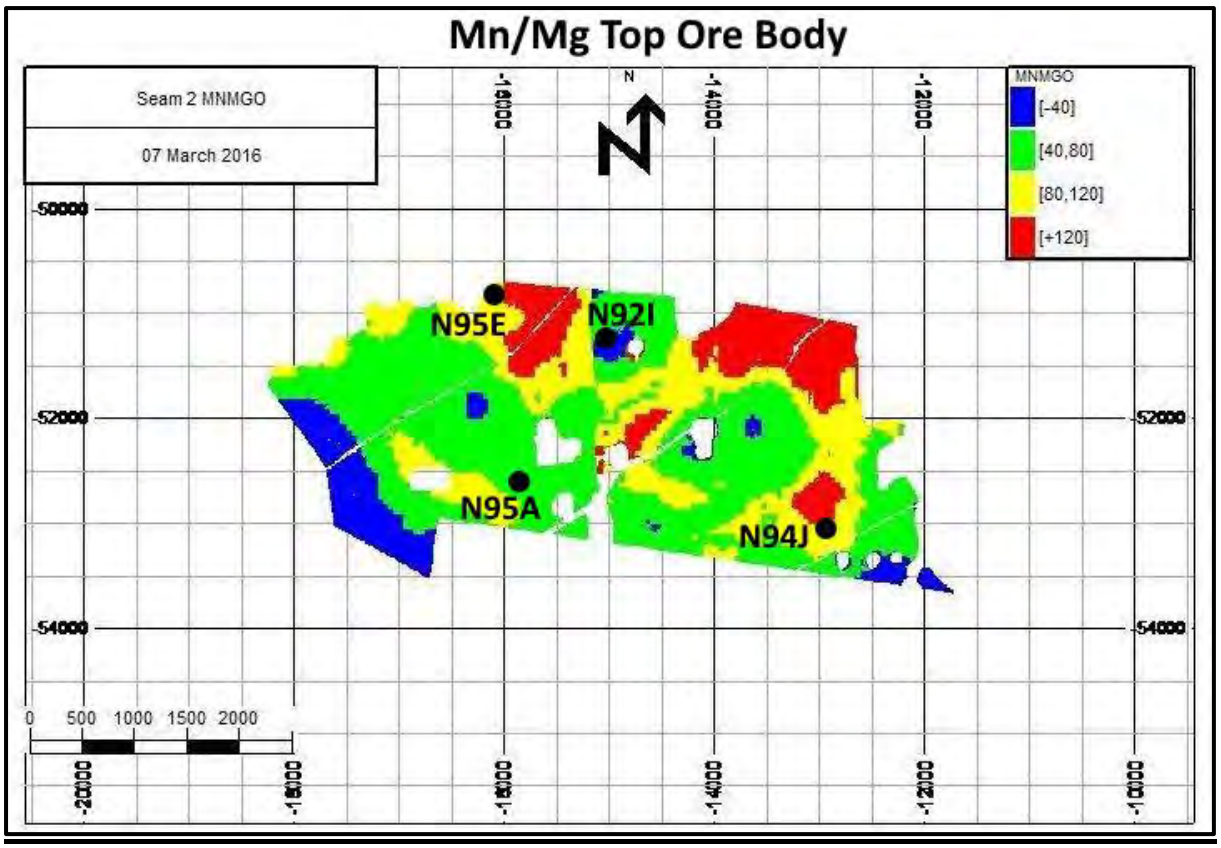
Mn/Mg Top Ore Body
Seam 2 MNMGO
07 March 2016
N
MNMGO
[-40]
[40,80]
[80,120]
[+120]
N95E
N92I
N95A
N94J
-50000
-52000
-54000
0 500 1000 1500 2000

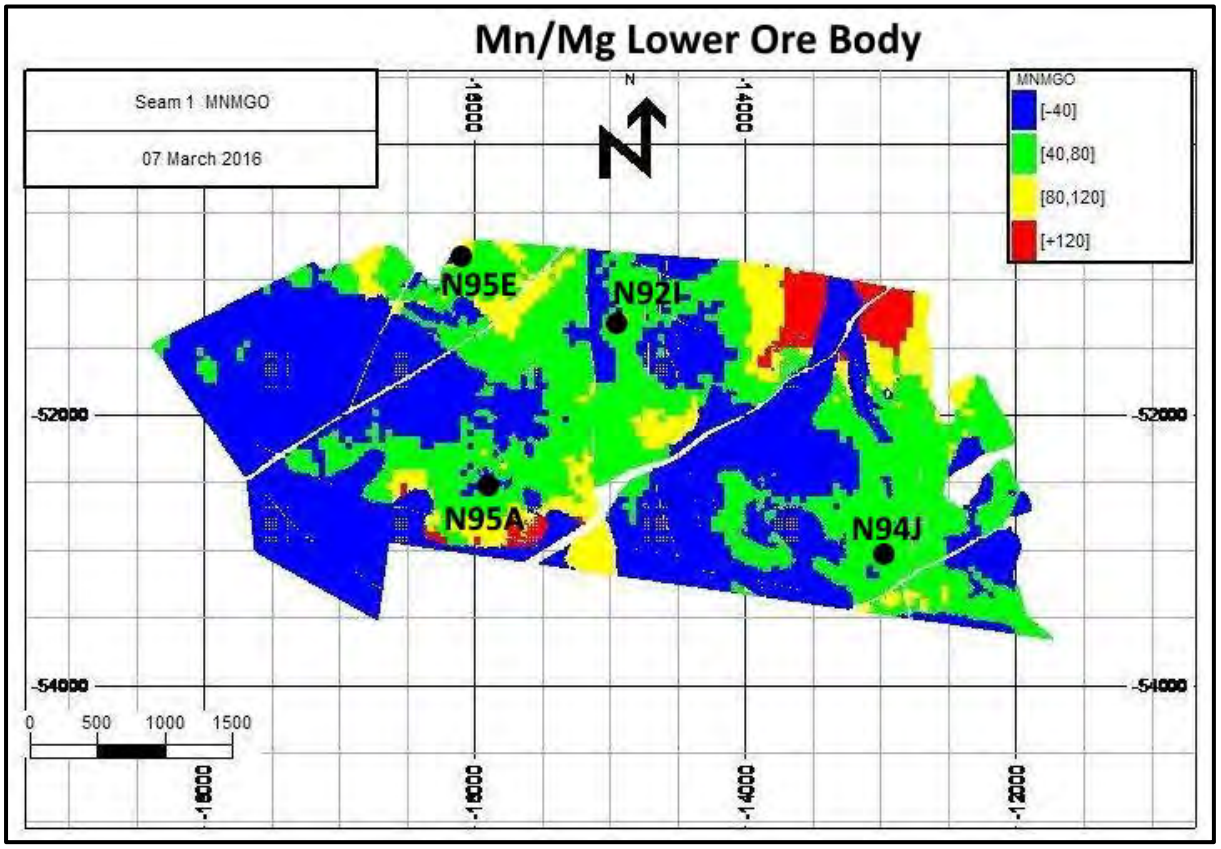
Mn/Mg Lower Ore Body
Seam 1 MNMGO
07 March 2016
N
MNMGO
[-40]
[40,80]
[80,120]
[+120]
N95E
N92L
N95A
N94J
-52000
-54000
0 500 1000 1500

Appendix II : XRD results for different rock types

Banded Iron Formations (BIFs)

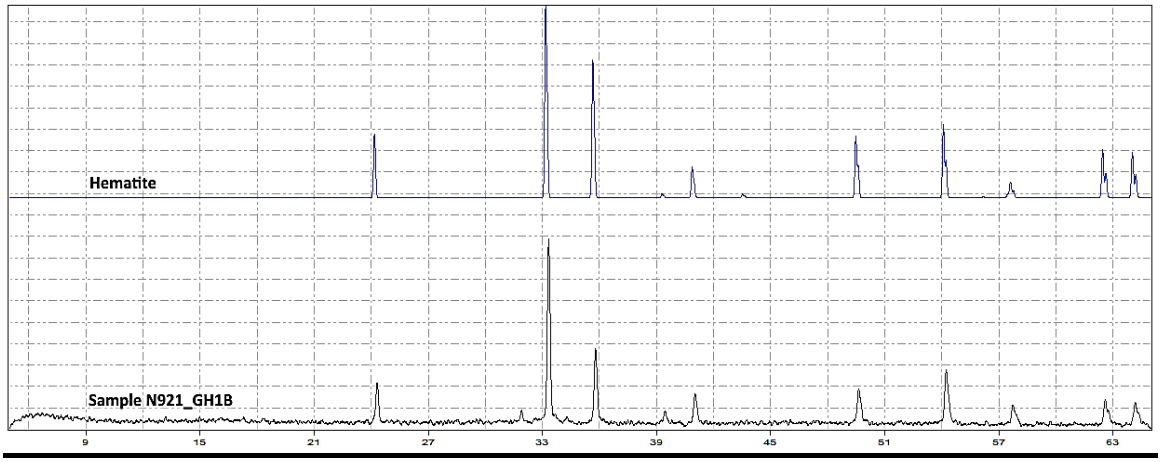

Appendix 2. 1. XRD showing Ferruginised BIF with only hematite.

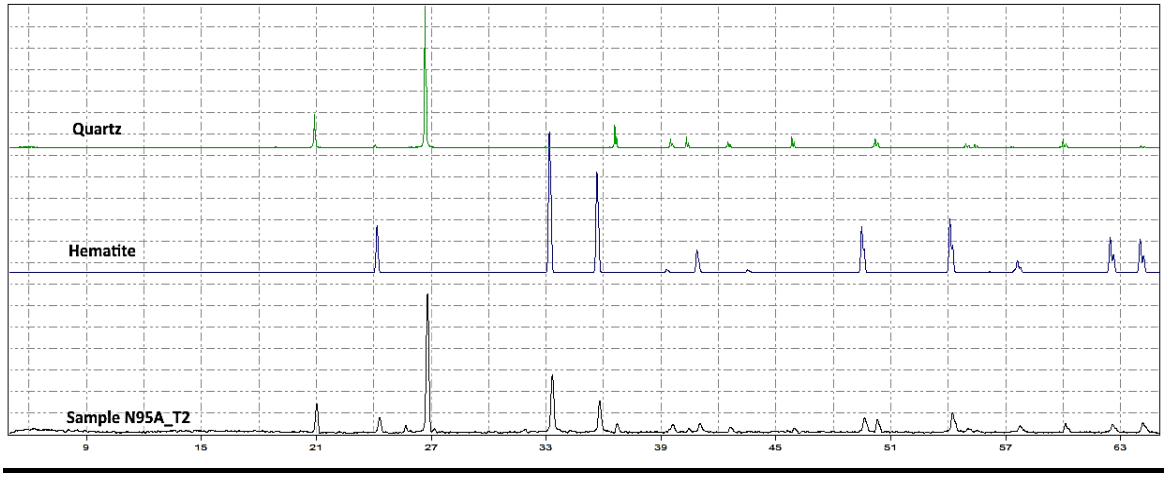

Appendix 2. 2. XRD plot showing normal altered BIF with hematite and quartz.

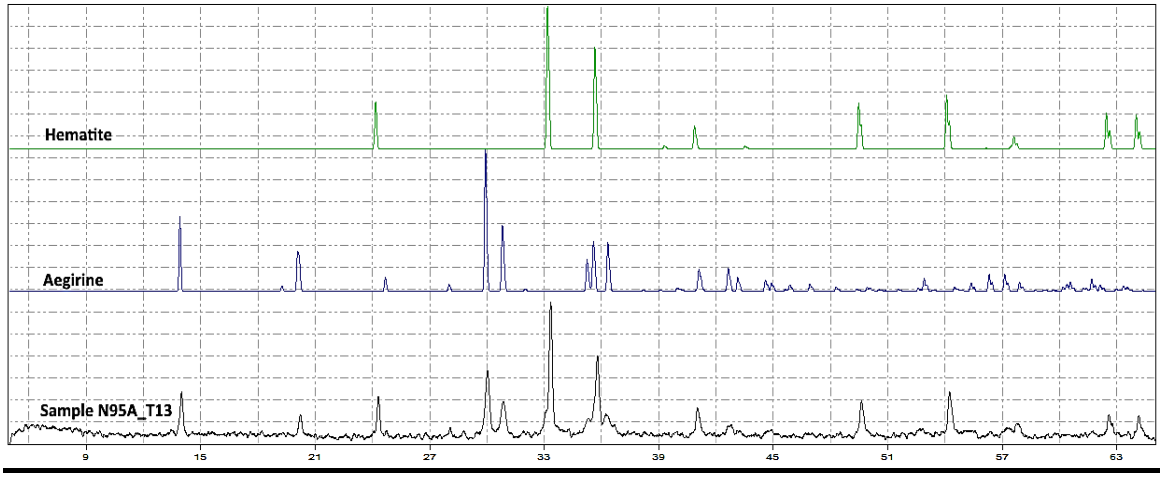

Appendix 2. 3. XRD plot showing BIF samples associated with aegirine.

Hematite Lutite

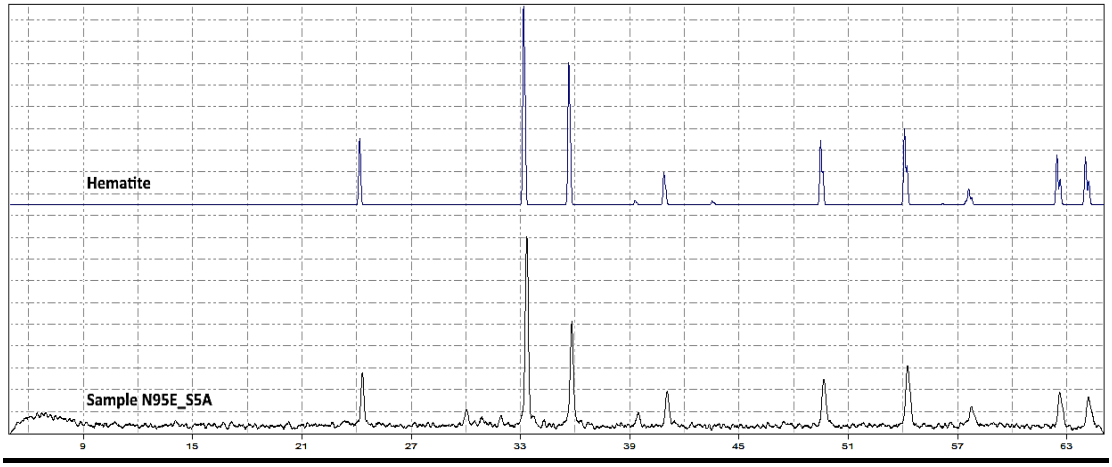

Appendix 2. 4. XRD plot showing altered lutite sample with only hematite present.

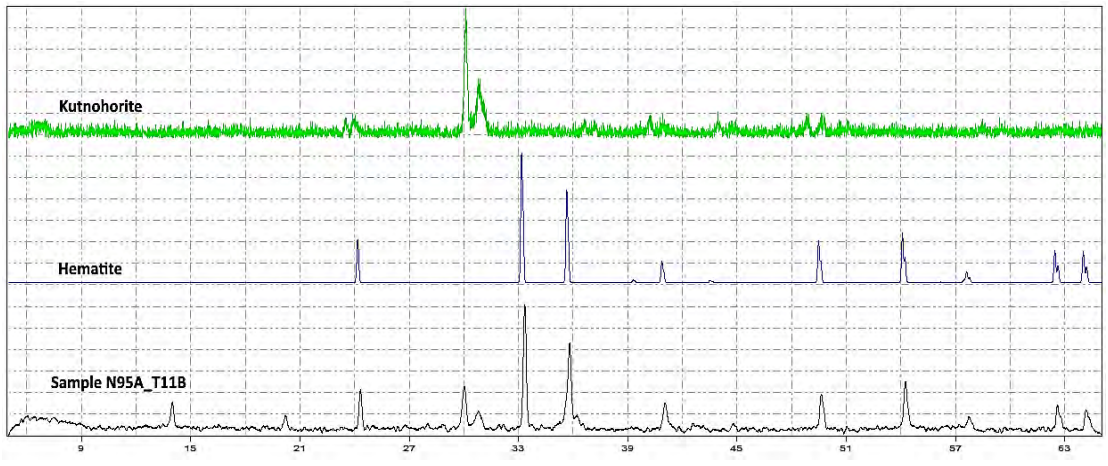

Appendix 2. 5. XRD plot of lutite sample with hematite and kutnahorite present.

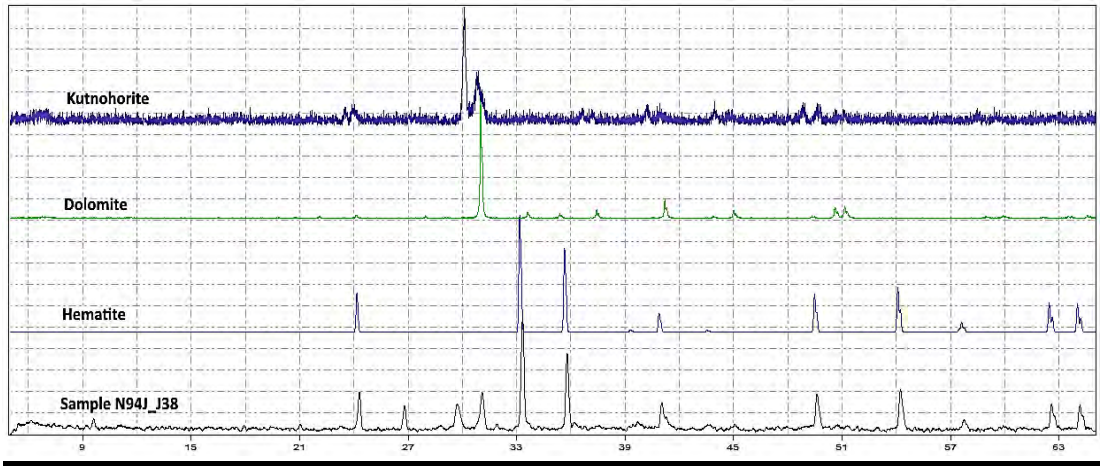

Appendix 2. 6. XRD plot of lutite sample with hematite, dolomite and kutnahorite present.

Mn Ores

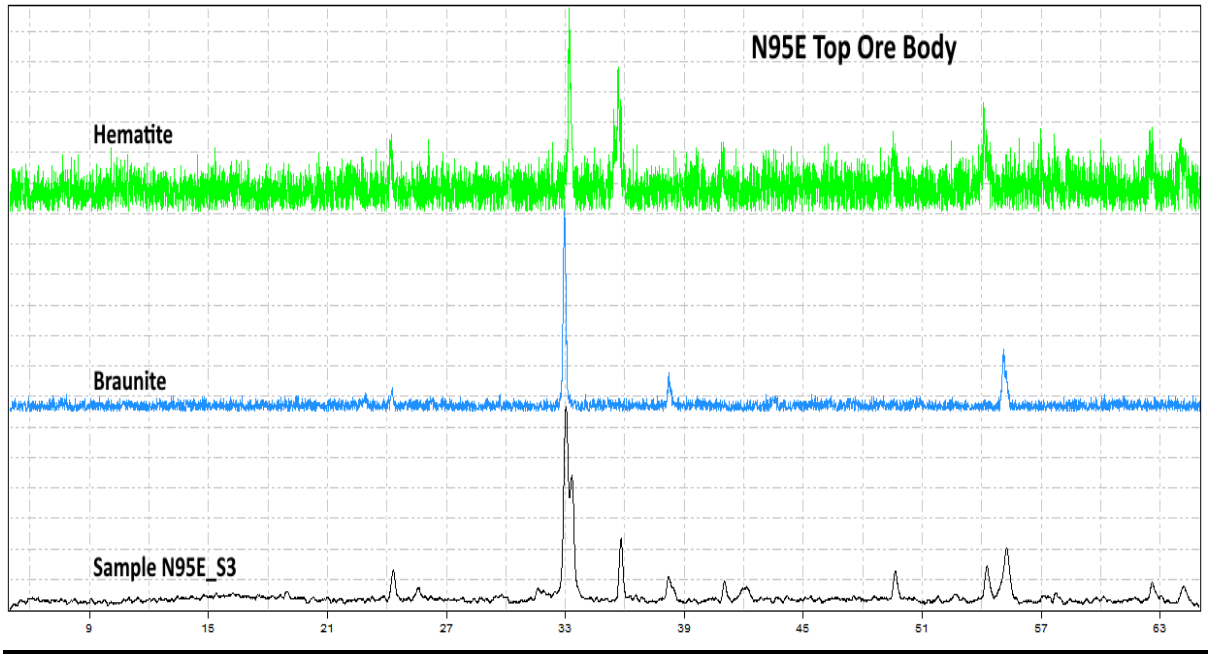

Appendix 2. 7. XRD plot of a sample from the top Mn ore body of N95E showing braunite and hematite peaks.

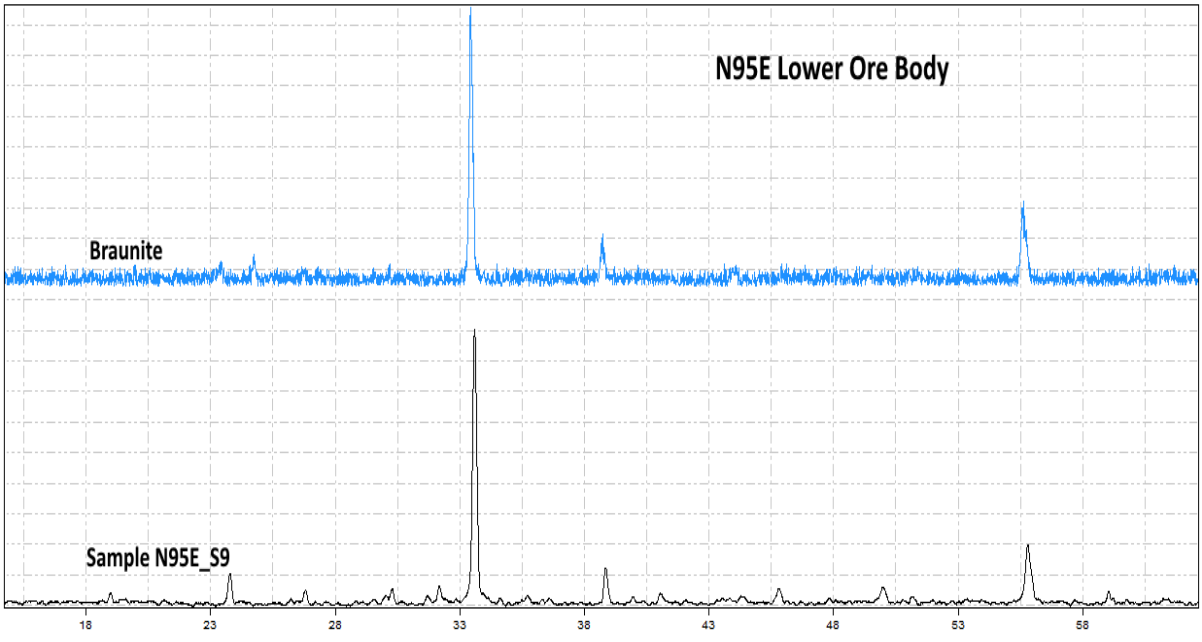

Appendix 2. 8. XRD plot of a sample from the lower Mn ore body of N95E showing braunite peak.

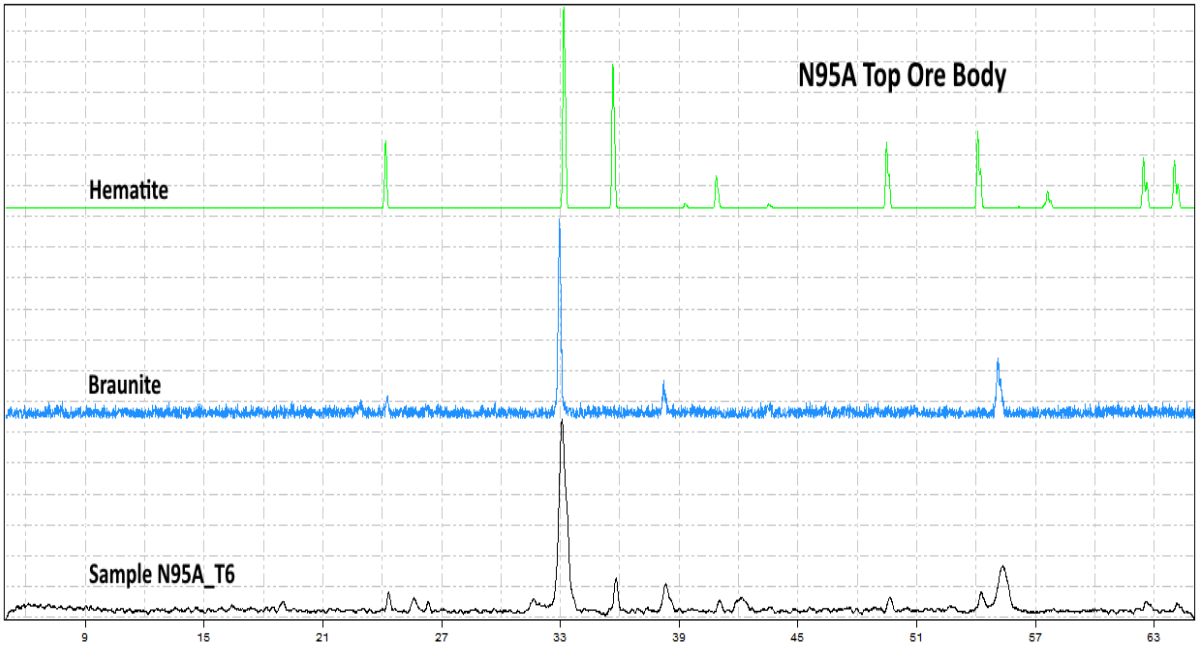

Appendix 2. 9. XRD plot of a sample from the top Mn ore body of N95A showing braunite and hematite peaks.

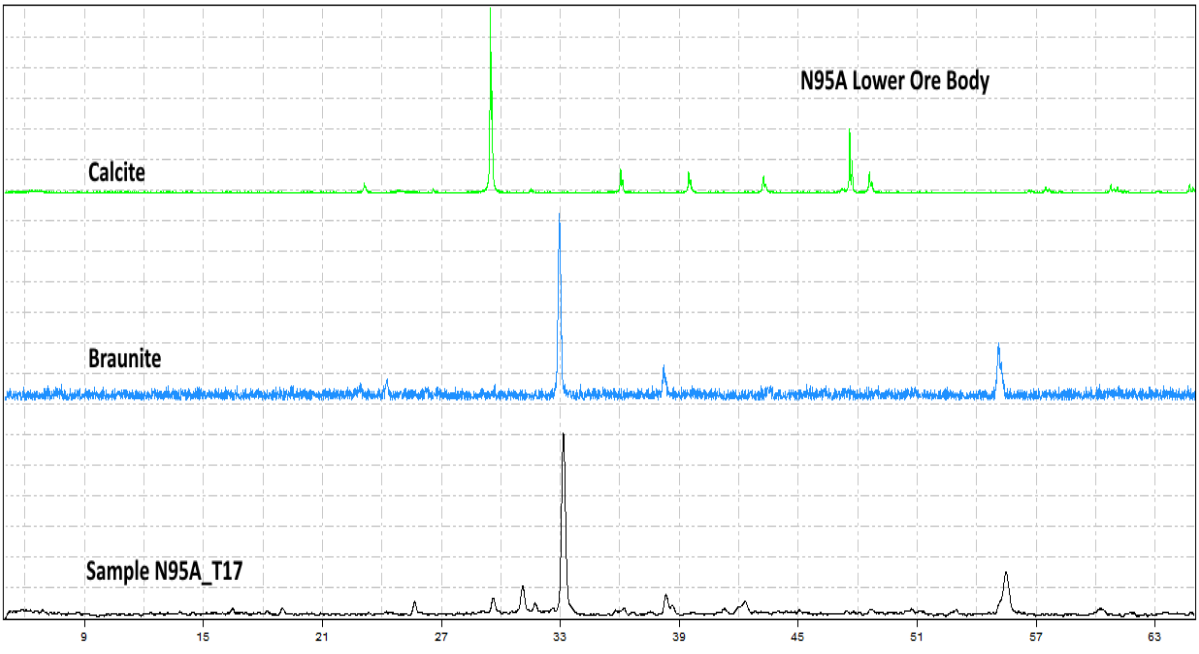

Appendix 2. 10. XRD plot of a sample from the lower Mn ore body of N95A showing braunite and calcite peaks.

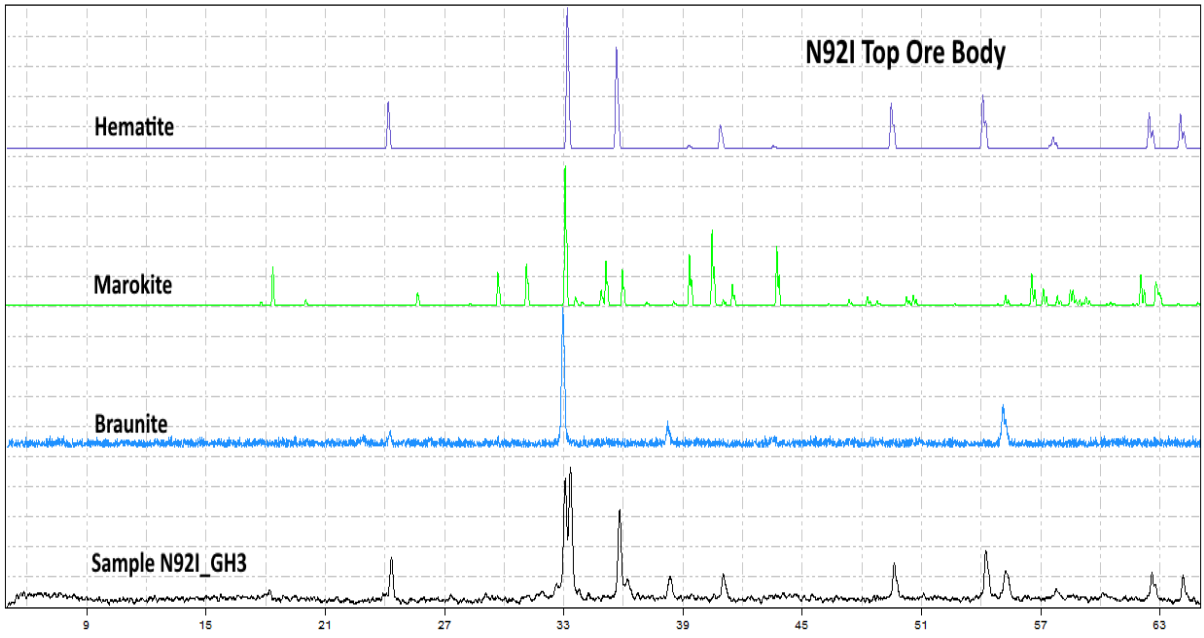

Appendix 2. 11. XRD plot of a sample from the top Mn ore body of N92I showing braunite, marokite and hematite peaks.

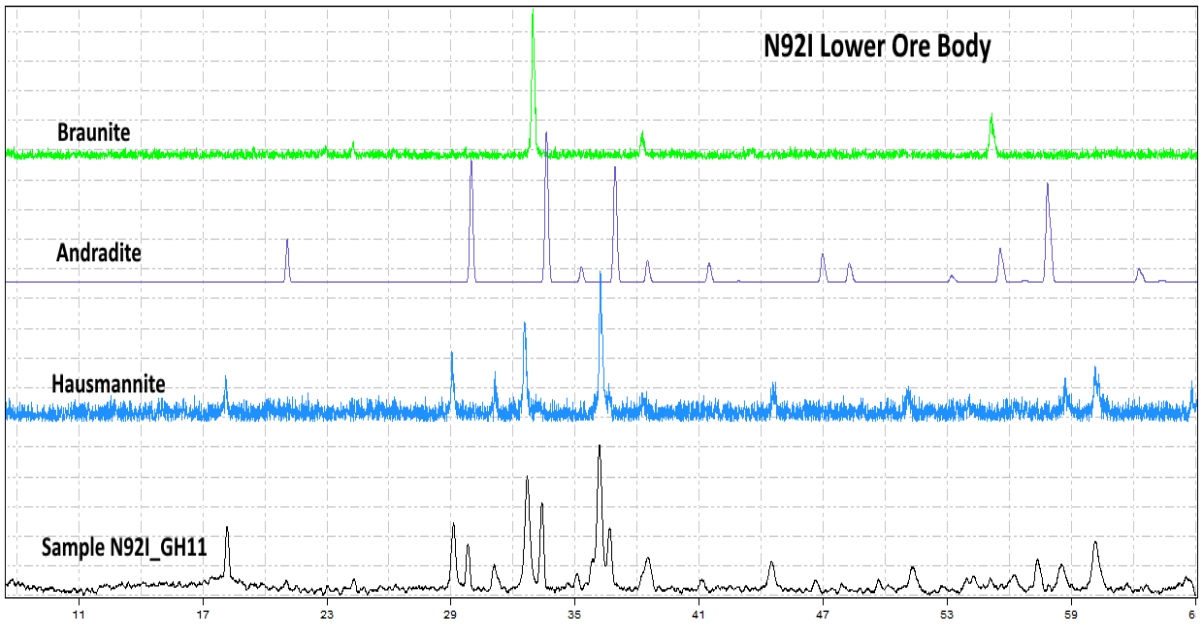

Appendix 2. 12. XRD plot of a sample from the lower Mn ore body of N92I showing hausmannite, andradite and braunite peaks.

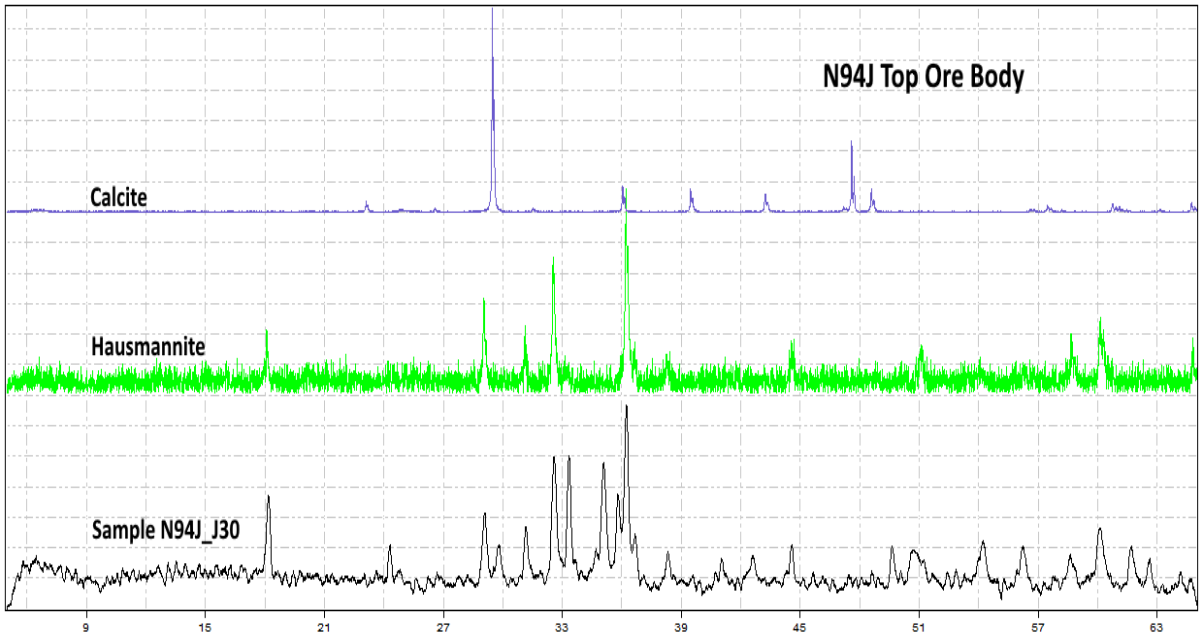

Appendix 2. 13. XRD plot of a sample from the top Mn ore body of N94J showing hausmannite and calcite peaks.

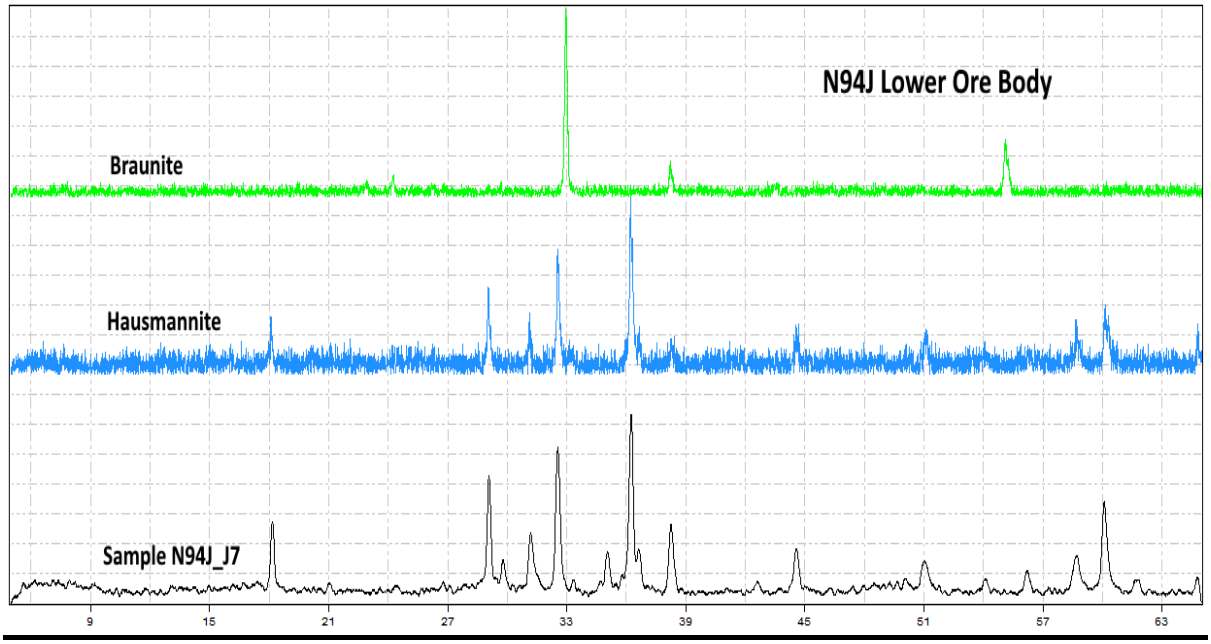

Appendix 2. 14. XRD plot of a sample from the lower Mn ore body of N94J showing hausmannite and braunite peaks.

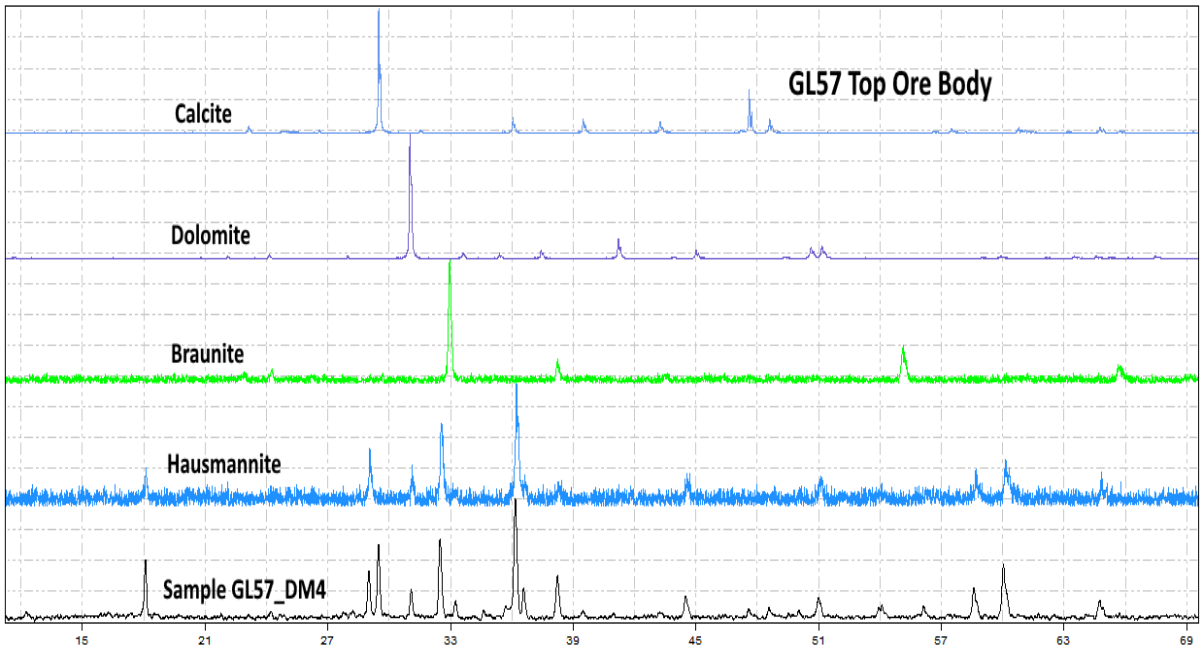
GL57 Top Ore Body
Calcite
Dolomite
Braunite
Hausmannite
Sample GL57_DM4
15
21
27
33
39
45
51
57
63
69

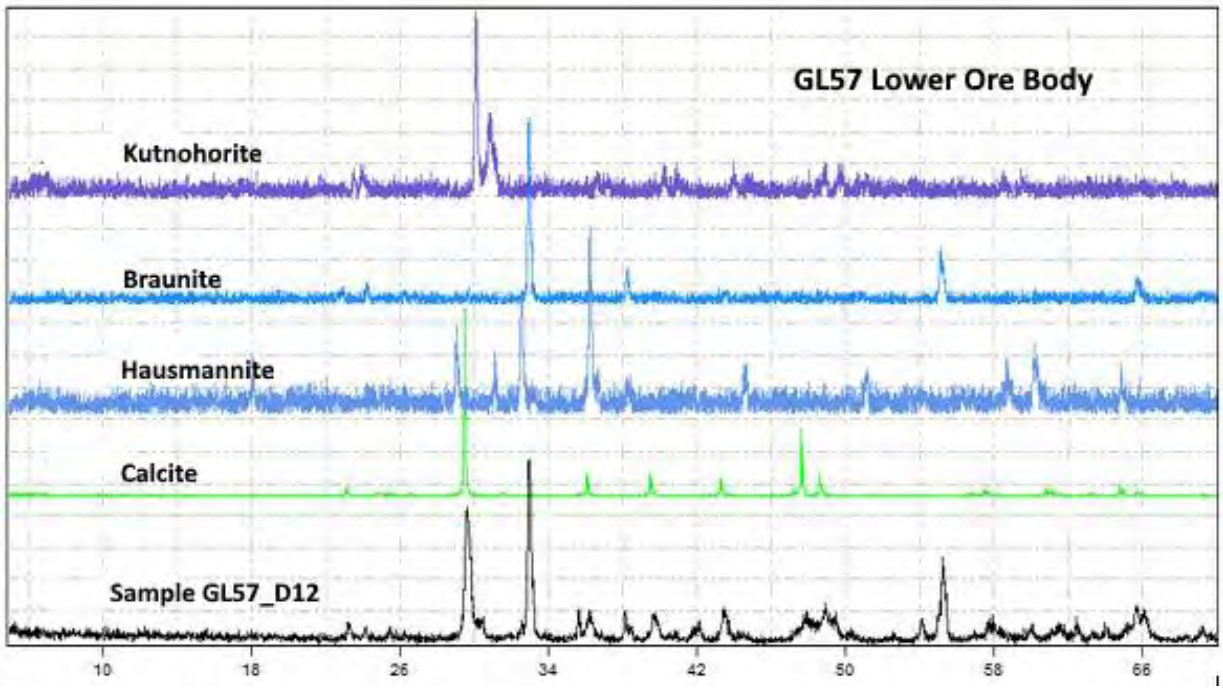
GL57 Lower Ore Body
Kutnohorite
Braunite
Hausmannite
Calcite
Sample GL57_D12
10
18
26
34
42
50
58
66

Appendix III: XRF results

Major elements Geochemistry full results (values in wt.%)

N95A													
	Sample name	**Fe_2O_3**	**MnO_2**	**TiO_2**	**CaO**	**K_2O**	**P_2O_5**	**SiO_2**	**Al_2O_3**	**MgO**	**Na_2O**	**LOI**	**Sum Of Conc.**
		(wt.%)	(wt.%)	(wt.%)	(wt.%)	(wt.%)	(wt.%)	(wt.%)	(wt.%)	(wt.%)	(wt.%)	(wt.%)	(wt.%)
393.00	**T1A**	52.59	0.25	bdl	0.06	bdl	0.04	47.50	0.14	0.01	0.01	0.09	100.69
396.54	**T1**	54.35	0.16	0.01	0.08	bdl	0.07	46.15	0.12	0.01	0.01	0.06	101.02
399.80	**T2**	50.30	0.24	0.01	0.07	bdl	0.06	49.15	0.16	0.01	0.02	0.84	100.86
403.70	**T3**	67.80	0.26	0.01	0.19	bdl	0.12	32.33	0.17	0.01	0.01	0.06	100.96
405.85	**T3A**	62.12	1.63	0.02	0.76	0.02	0.07	34.84	0.18	0.14	0.03	0.71	100.52
408.40	**T3B**	65.11	9.76	0.02	3.18	0.01	0.14	17.55	0.39	0.23	3.26	0.68	100.32
411.00	**T4**	54.45	32.95	0.02	4.35	0.01	0.11	6.62	0.33	0.31	0.01	1.38	100.53
412.00	**T5**	55.52	37.58	0.01	2.60	0.01	0.03	4.39	0.18	0.19	0.01	0.66	101.18
413.65	**T6**	23.53	64.76	0.02	4.09	bdl	0.02	6.47	0.15	0.28	0.01	1.95	101.29
415.48	**T7**	31.46	56.45	0.03	1.62	0.71	0.02	4.05	0.16	0.21	0.04	4.39	99.14
416.16	**T8**	18.85	69.40	bdl	4.32	bdl	0.11	4.69	0.59	0.47	0.01	1.37	99.80

417.70	**T9**	72.40	19.67	0.02	2.29	bdl	0.02	4.00	0.36	0.51	0.01	0.01	99.29
418.50	**T9A**	56.44	1.48	0.01	1.79	0.01	0.13	32.52	0.45	0.02	7.55	0.06	100.45
421.66	**T10**	57.92	0.16	0.01	0.19	0.02	0.11	42.10	0.22	0.01	0.01	0.05	100.80
423.60	**T10A**	53.69	0.13	0.01	0.10	0.01	0.06	46.60	0.20	0.01	0.01	0.04	100.86
425.70	**T11**	48.67	0.13	0.01	0.07	bdl	0.05	51.92	0.15	0.01	0.01	0.04	101.06
427.13	**T11A**	55.68	0.97	0.01	0.97	0.03	0.11	41.70	0.16	0.07	0.03	0.74	100.48
427.80	**T11B**	64.77	4.75	0.01	2.69	bdl	0.01	23.16	0.23	0.70	3.99	0.18	100.49
429.50	**T12**	65.18	25.87	0.03	1.73	bdl	0.04	4.63	0.30	0.50	0.01	1.31	99.60
430.15	**T13**	54.57	5.40	0.02	3.84	0.02	0.01	29.59	0.22	0.48	5.44	0.24	99.82
431.35	**T14**	16.78	69.14	0.04	3.73	bdl	0.07	6.99	0.30	0.71	0.01	2.11	99.88
432.76	**T15**	11.22	66.21	0.02	9.04	bdl	0.06	4.93	0.33	0.64	0.01	6.71	99.17
433.76	**T16**	14.50	53.14	0.01	9.71	bdl	0.05	4.54	0.31	5.45	0.01	12.48	100.20
435.58	**T17**	5.69	61.80	0.02	8.82	bdl	0.04	6.39	0.28	4.46	0.01	11.99	99.49
437.08	**T18**	8.22	55.13	0.02	11.34	bdl	0.05	6.18	0.26	5.20	0.01	14.77	101.17
438.15	**T19**	36.97	4.13	0.01	22.12	bdl	0.05	2.39	0.21	7.43	0.01	25.93	99.26
440.05	**T20**	50.12	0.10	bdl	0.13	bdl	0.06	50.01	0.13	0.04	0.01	0.03	100.62

N95E

Depth	Sample name	Fe_2O_3	MnO_2	TiO_2	CaO	K_2O	P_2O_5	SiO_2	Al_2O_3	MgO	Na_2O	LOI	Sum Of Conc.
		(wt.%)	(wt.%)	(wt.%)	(wt.%)	(wt.%)	(wt.%)	(wt.%)	(wt.%)	(wt.%)	(wt.%)	(wt.%)	(wt.%)
378.8	**S1A**	68.86	0.09	0.82	0.16	3.10	0.10	14.69	10.70	0.00	0.05	1.68	100.24
381.5	**S1b**	17.39	1.84	0.55	1.78	7.15	0.08	34.56	28.64	0.57	0.49	5.98	99.04
383.4	**S1**	48.81	20.82	bdl	12.20	bdl	0.06	12.93	2.71	0.10	0.02	1.89	99.54
384.6	**S2**	34.49	49.84	0.04	8.44	bdl	0.04	2.77	0.50	0.02	0.02	3.17	99.33
385.7	**S3**	42.68	42.81	0.02	5.13	bdl	0.06	8.35	0.56	0.02	0.01	0.91	100.55
386.6	**S3A**	78.73	7.86	0.02	3.10	0.01	0.08	9.99	0.48	0.12	0.39	0.07	100.85
388.1	**S4**	64.62	1.09	bdl	0.90	0.01	0.17	27.22	0.25	0.01	6.36	0.13	100.77
391.4	**S5**	48.31	0.23	bdl	0.28	0.01	0.14	49.34	0.11	0.01	2.06	0.05	100.53
392.4	**S5A**	87.71	0.81	0.02	2.23	0.01	0.49	7.13	0.32	0.00	1.37	0.33	100.41
394.6	**S6**	26.12	61.69	0.04	4.22	bdl	0.06	2.75	0.45	0.06	0.02	3.17	98.58
396.0	**S6A**	91.66	6.64	0.01	1.56	bdl	0.20	0.64	bdl	0.03	0.01	0.75	101.49
397.4	**S7**	33.00	55.86	0.04	1.94	bdl	0.05	0.17	0.17	0.10	0.01	8.16	99.49
399.4	**S8**	8.20	67.61	0.02	20.60	bdl	0.09	0.01	0.12	0.22	0.01	1.37	98.24
401.2	**S9**	11.00	72.52	0.02	8.24	bdl	0.08	0.25	0.14	0.12	0.02	6.72	99.10
402.6	**S10**	9.58	75.76	0.02	6.93	bdl	0.07	0.88	0.32	0.49	0.02	7.08	101.15
403.3	**S11**	34.17	54.63	0.02	4.74	bdl	0.08	2.14	0.26	0.16	0.01	4.12	100.32

403.9	**S12**	60.06	29.50	0.02	3.57	bdl	0.07	4.35	0.29	0.94	0.01	0.97	99.78
405.3	**S12A**	64.44	0.67	0.01	0.87	0.21	0.02	28.55	0.31	2.33	2.84	0.51	100.75
406.7	**S13**	72.32	0.10	0.01	0.24	bdl	0.14	27.86	0.20	0.06	0.01	0.06	101.00
409.2	**S14**	57.98	0.05	0.03	0.18	0.11	0.11	41.68	0.56	0.01	0.01	0.10	100.82

N92I

Depth	Sample name	Fe_2O_3	MnO_2	TiO_2	CaO	K_2O	P_2O_5	SiO_2	Al_2O_3	MgO	Na_2O	LOI	Sum Of Conc.
		(wt.%)	(wt.%)	(wt.%)	(wt.%)	(wt.%)	(wt.%)	(wt.%)	(wt.%)	(wt.%)	(wt.%)	(wt.%)	(wt.%)
623.22	**GH1A**	100.00	0.07	0.02	0.16	0.01	0.12	0.21	0.35	0.01	0.01	0.32	101.28
626.65	**GH1B**	97.85	0.10	0.02	0.69	0.11	0.12	0.90	0.73	0.04	0.06	0.86	101.49
629.4	**GH1C**	96.32	0.20	0.03	1.78	0.07	0.18	0.55	0.53	0.03	0.03	1.61	101.32
632.03	**GH1**	74.45	18.94	0.02	3.83	bdl	0.23	2.59	0.83	0.16	0.01	0.28	101.34
634.25	**GH2**	62.03	37.52	0.02	1.21	bdl	0.13	0.28	0.19	0.25	0.01	-0.51	101.13
636.6	**GH3**	59.21	36.15	0.02	2.92	bdl	0.23	1.26	0.44	0.24	0.01	0.57	101.06
638	**GH4**	37.22	50.24	0.03	11.37	bdl	0.03	0.24	0.49	0.24	0.01	0.39	100.26
640.9	**GH5**	39.96	54.93	0.02	3.87	bdl	0.04	0.63	0.58	0.22	0.01	-0.12	100.14
643.9	**GH5A**	92.25	0.74	0.02	0.34	0.52	0.08	2.89	0.50	1.27	0.02	0.40	99.02
645.4	**GH6**	47.85	0.13	0.01	0.34	0.12	0.05	51.79	0.25	0.01	0.03	0.04	100.62
647.4	**GH6A**	64.93	0.11	0.01	0.04	0.03	0.07	35.62	0.18	0.01	0.01	0.12	101.13
650	**GH7**	34.91	0.08	bdl	0.06	bdl	0.02	65.75	0.11	0.01	0.01	0.01	100.95
653.4	**GH7A**	66.86	0.06	0.02	0.06	bdl	0.03	33.82	0.16	0.01	0.01	0.18	101.20
656	**GH7B**	100.00	0.32	0.03	0.26	0.03	0.01	0.37	0.17	0.01	0.01	0.25	101.45
658.1	**GH7C**	24.54	3.09	bdl	0.15	0.04	0.02	71.85	0.12	0.31	0.04	0.35	100.51
659.4	**GH8**	41.84	52.97	bdl	3.36	bdl	0.16	0.32	bdl	0.70	0.01	1.18	100.53
660.8	**GH9**	79.30	14.09	0.02	3.69	bdl	0.35	3.10	0.19	0.56	0.01	0.01	101.32
662.1	**GH10**	6.77	89.75	0.02	2.59	bdl	0.04	2.68	0.35	0.74	0.01	-0.64	102.32
663.32	**GH11**	17.96	72.40	0.01	6.05	bdl	0.07	6.05	0.32	0.14	0.02	-1.78	101.23
664.5	**GH12**	6.03	87.61	0.01	3.76	bdl	0.09	4.21	0.34	0.87	0.02	-0.27	102.67
665.9	**GH12A**	87.07	0.52	0.01	6.45	bdl	0.02	0.93	0.27	0.60	0.01	5.18	101.04
668.1	**GH12B**	55.11	0.06	0.01	0.10	0.07	0.03	44.89	0.30	0.01	0.01	0.05	100.64
670.85	**GH13**	53.51	0.06	0.02	0.06	0.08	0.03	46.22	0.39	0.01	0.01	0.07	100.46
671.4	**GH14**	24.39	0.09	0.03	0.18	0.12	0.08	75.29	0.39	0.01	0.01	-0.02	100.58

N94J

Depth	Sample name	Fe_2O_3	MnO_2	TiO_2	CaO	K_2O	P_2O_5	SiO_2	Al_2O_3	MgO	Na_2O	LOI	Sum Of Conc.
		(wt.%)	(wt.%)	(wt.%)	(wt.%)	(wt.%)	(wt.%)	(wt.%)	(wt.%)	(wt.%)	(wt.%)	(wt.%)	(wt.%)
398.3	**J46**	53.35	4.21	bdl	1.23	bdl	0.05	38.23	0.16	0.17	0.01	2.76	100.18
403.6	**J45**	43.10	0.06	bdl	0.09	bdl	0.08	57.29	0.18	0.01	0.01	-0.10	100.72
405.4	**J44**	50.92	0.05	0.01	0.15	bdl	0.12	49.25	0.16	0.01	0.01	-0.03	100.65
409.4	**J43**	46.42	0.05	0.01	0.06	0.03	0.04	54.61	0.24	0.01	0.01	-0.18	101.29
412.0	**J42**	36.57	0.05	0.01	0.05	bdl	0.04	63.83	0.14	0.01	0.01	-0.09	100.62
414.5	**J40**	25.48	0.06	bdl	0.97	bdl	0.63	73.20	0.13	0.01	0.01	-0.07	100.42
417.8	**J39**	51.65	2.38	0.02	14.17	bdl	0.09	7.84	0.27	5.38	0.01	18.04	99.85
419.6	**J38**	49.04	2.64	0.01	14.26	bdl	0.10	9.63	0.33	6.12	0.02	17.73	99.87
423.5	**J36**	31.59	68.01	0.01	0.21	bdl	0.07	1.91	0.11	0.41	0.01	-1.31	101.03
426.0	**J33**	22.42	73.76	0.02	0.68	bdl	0.04	2.13	0.32	0.52	0.02	-0.64	99.28
427.3	**J32**	19.19	74.88	0.03	0.46	bdl	0.08	5.17	0.31	0.54	0.01	-0.12	100.55
428.7	**J31**	18.07	67.94	0.02	0.71	bdl	0.06	10.92	0.43	0.91	0.01	1.24	100.32
429.8	**J30**	19.37	65.01	0.02	0.56	bdl	0.12	9.17	0.72	1.63	0.01	2.40	99.01
433.3	**J28**	21.89	73.30	0.02	0.52	bdl	0.05	1.04	0.54	1.14	0.06	1.08	99.64

434.3	**J27**	44.03	42.74	0.01	0.99	bdl	0.03	1.67	0.27	1.49	0.12	9.45	100.80
437.5	**J26**	58.19	0.05	0.01	0.16	0.01	0.11	41.72	0.24	0.01	0.01	0.02	100.53
440.1	**J24**	50.85	0.05	0.01	0.14	bdl	0.09	49.64	0.16	0.01	0.01	-0.04	100.92
442.0	**J22**	57.71	0.04	0.01	0.03	0.02	0.03	43.04	0.17	0.01	0.01	-0.01	101.05
445.0	**J20**	47.27	0.03	bdl	0.21	0.01	0.14	53.05	0.19	0.01	0.01	-0.21	100.71
446.1	**J18**	51.83	0.04	0.01	0.18	0.02	0.13	49.02	0.24	0.01	0.01	-0.11	101.38
448.4	**J16**	56.65	0.05	0.02	0.08	0.01	0.06	43.91	0.30	0.01	0.01	0.02	101.12
451.8	**J14**	64.42	0.11	0.01	0.11	0.02	0.08	35.74	0.21	0.01	0.01	-0.02	100.70
453.5	**J13**	9.11	89.37	0.01	1.46	bdl	0.05	0.24	0.29	0.55	0.08	0.38	101.55
455.8	**J11**	49.44	0.35	0.01	2.77	0.02	0.14	42.90	0.25	2.13	0.01	2.79	100.81
458.7	**J10**	72.54	6.01	0.03	0.72	bdl	0.45	9.61	0.29	7.19	0.01	3.94	100.80
461.7	**J9**	24.80	67.56	0.02	0.10	bdl	0.04	7.41	0.24	1.27	0.01	0.16	101.61
462.6	**J8**	12.79	0.65	0.01	2.55	0.06	0.04	76.56	0.57	1.23	3.51	0.94	98.91
463.5	**J7**	9.75	85.90	0.00	1.95	bdl	0.05	1.76	0.17	0.25	0.11	1.67	101.60
466.0	**J5**	7.72	69.18	0.02	3.62	bdl	0.05	5.08	0.22	4.36	0.01	11.14	101.39
467.1	**J4**	7.26	39.70	0.02	16.76	bdl	0.08	4.70	0.27	9.31	0.01	21.45	99.55
471.3	**J3**	58.55	1.79	0.01	6.97	0.02	0.11	18.40	0.21	3.73	0.01	10.54	100.34
475.3	**J1**	36.12	0.11	0.01	0.30	0.03	0.13	63.87	0.11	0.02	0.01	0.03	100.74

GL57

Depth	Sample name	Fe_2O_3	MnO_2	TiO_2	CaO	K_2O	P_2O_5	SiO_2	Al_2O_3	MgO	Na_2O	LOI	Sum Of Conc.
		(wt.%)	(wt.%)	(wt.%)	(wt.%)	(wt.%)	(wt.%)	(wt.%)	(wt.%)	(wt.%)	(wt.%)	(wt.%)	(wt.%)
188.9	**D1A**	86.54	11.67	0.04	0.28	bdl	0.03	1.32	0.49	0.06	0.01	0.83	101.26
193.3	**D1B**	76.30	5.66	0.05	6.54	bdl	0.03	9.32	2.08	0.45	0.01	0.51	100.94
198.0	**D1C**	4.57	0.97	0.01	3.45	bdl	0.08	85.32	0.45	1.22	0.01	3.94	100.02
203.4	**D1**	53.80	0.06	0.01	0.10	bdl	0.01	46.59	0.22	0.06	0.01	0.07	100.93
208.2	**D2**	48.59	0.07	bdl	0.03	bdl	0.02	51.85	0.15	0.01	0.01	-0.04	100.69
214.2	**D2A**	42.00	0.12	bdl	0.25	0.01	0.02	57.97	0.16	0.01	0.01	0.40	100.95
219.0	**D3**	50.08	0.08	0.01	0.03	bdl	0.03	50.56	0.14	0.01	0.01	0.01	100.95
220.0	**D4**	38.55	0.06	0.01	0.17	0.02	0.11	61.51	0.17	0.01	0.01	-0.12	100.49
225.0	**DM1**	43.25	1.5	0.01	19.23	0.01	0.21	9.86	0.12	11.23	0.01	14.20	99.63
230.0	**DM2**	40.12	6.5	0.01	11.31	0.01	0.09	20.07	0.28	6.35	0.01	13.92	98.67
234.5	**DM3**	15.89	64.85	0.02	9.96	bdl	0.05	1.30	0.41	1.99	0.06	6.79	101.33
236.1	**DM4**	13.04	71.21	0.03	5.90	bdl	0.05	1.62	0.23	4.48	0.04	4.64	101.23
237.2	**DM5**	11.68	79.27	0.02	6.09	bdl	0.03	0.99	0.17	2.98	0.01	-0.07	101.17
239.0	**DM6**	5.57	82.05	0.03	5.09	bdl	0.02	0.58	0.08	2.54	0.01	3.61	99.58
240.1	**DM7**	28.64	26.21	0.02	17.06	bdl	0.10	0.52	0.36	7.38	0.01	19.31	99.59

243.9	**D4A**	60.40	0.06	0.01	0.14	bdl	0.09	40.21	0.06	0.01	0.01	0.05	101.04
245.6	**D5**	51.91	0.05	0.01	0.12	bdl	0.08	48.40	0.18	0.01	0.01	-0.07	100.69
249.1	**D6**	49.13	0.06	0.01	0.18	0.01	0.11	51.21	0.19	0.01	0.01	-0.06	100.86
250.5	**D7**	75.72	0.03	0.01	0.14	0.02	0.08	24.71	0.23	0.01	0.01	0.18	101.13
251.7	**D8**	19.54	1.91	0.01	5.65	0.01	0.10	61.83	0.14	2.92	0.01	8.41	100.53
254.7	**D8A**	19.30	5.18	0.01	22.44	bdl	0.03	4.59	0.08	14.15	0.01	34.90	100.69
258.4	**D9**	31.36	9.85	0.01	16.96	bdl	0.07	3.83	0.26	9.27	0.01	27.53	99.14
261.5	**D9A**	40.03	2.76	0.01	9.16	0.01	0.09	29.50	0.11	4.55	0.01	13.72	99.95
264.5	**D9B**	42.01	1.78	0.01	5.12	0.01	0.24	40.86	0.11	2.53	0.01	7.50	100.19
268.2	**D9C**	18.70	18.35	0.01	17.21	bdl	0.04	4.81	0.19	13.26	0.01	26.59	99.17
271.4	**D10**	6.69	34.95	0.01	17.20	bdl	0.04	5.09	0.25	10.34	0.01	25.42	99.99
272.7	**D11**	19.39	37.43	0.02	14.01	bdl	0.06	4.69	0.39	5.02	0.01	18.85	99.86
276.3	**D12**	8.73	43.28	0.01	14.15	bdl	0.04	6.71	0.21	6.86	0.01	20.10	100.10
277.3	**D13**	4.68	56.16	0.01	18.03	bdl	0.03	1.62	0.12	1.90	0.01	16.70	99.27
281.7	**D14**	20.13	29.42	0.02	10.96	bdl	0.06	10.71	0.29	8.13	0.01	20.65	100.39
284.3	**D15**	49.31	6.79	0.01	8.79	bdl	0.07	21.51	0.14	2.00	0.01	12.05	100.68
287.6	**D16**	63.47	2.00	0.01	3.07	bdl	0.08	26.84	0.24	0.75	0.01	4.46	100.92
290.0	**D17**	56.22	2.48	bdl	4.79	bdl	0.08	29.35	0.16	1.26	0.01	6.35	100.70
291.5	**D18**	58.50	0.59	0.02	1.70	bdl	0.19	36.73	0.70	1.18	0.01	1.14	100.74

GL136

Depth	Sample name	Fe_2O_3	MnO_2	TiO_2	CaO	K_2O	P_2O_5	SiO_2	Al_2O_3	MgO	Na_2O	LOI	Sum Of Conc.
292.48	**89**	31.40	0.83	0.01	19.60	0.01	0.05	21.54	0.28	1.98	bdl	23.45	99.16
293.72	**88**	45.94	0.28	0.01	8.98	0.06	0.11	29.98	0.29	2.08	0.03	11.25	99.00
294.36	**87**	44.77	0.18	0.01	5.25	0.02	0.10	39.67	0.19	1.72	bdl	7.25	99.15
295.19	**86**	45.93	0.21	0.01	6.07	0.04	0.13	37.12	0.25	1.89	bdl	7.43	99.07
295.81	**85**	28.71	0.31	0.01	9.13	0.03	0.09	48.69	0.21	1.79	bdl	10.35	99.32
296.86	**84**	46.80	0.41	0.01	6.51	0.04	0.06	36.73	0.20	1.68	0.02	7.22	99.68
297.83	**83**	58.25	0.47	bdl	5.25	0.02	0.05	28.73	0.20	1.38	bdl	5.26	99.60
298.29	**82**	54.71	0.51	0.01	4.91	0.01	0.08	31.99	0.23	1.44	bdl	5.13	99.02
299.41	**81**	42.65	0.62	bdl	7.45	0.03	0.06	36.81	0.17	2.22	bdl	9.38	99.40
300.71	**80**	50.93	0.17	0.01	4.58	0.04	0.10	36.74	0.19	1.50	bdl	4.76	99.02
302.79	**79**	43.28	0.18	bdl	7.77	0.02	0.07	37.71	0.14	1.90	bdl	7.99	99.07
304.18	**78**	47.38	0.17	bdl	6.98	0.04	0.08	35.79	0.20	1.48	0.01	6.89	99.03
305.95	**77**	47.89	0.11	0.01	6.93	0.03	0.10	35.71	0.19	1.65	0.02	6.45	99.08
307.25	**76**	43.49	0.15	bdl	6.30	0.03	0.07	40.86	0.18	1.51	bdl	6.59	99.18
308.21	**75**	41.20	0.20	bdl	11.15	0.03	0.11	34.92	0.14	1.43	bdl	10.05	99.23
310.45	**74**	47.00	0.16	bdl	3.48	0.03	0.13	42.50	0.15	1.91	bdl	3.69	99.05
311.64	**73**	35.86	0.26	bdl	13.26	0.03	0.17	37.94	0.15	0.81	bdl	10.53	99.02
312.41	**72**	31.39	0.37	bdl	12.74	0.03	0.13	43.58	0.14	0.71	bdl	10.00	99.09
313.67	**71**	47.97	0.26	bdl	4.76	0.03	0.10	41.59	0.15	0.95	bdl	3.53	99.32
314.61	**70**	28.30	0.52	bdl	10.09	0.04	0.06	48.57	0.17	1.39	0.01	9.97	99.13
315.46	**69**	47.06	0.63	0.01	7.15	0.06	0.09	38.23	0.22	0.60	0.02	5.07	99.13
317.55	**67**	36.89	9.63	0.01	16.95	0.06	0.07	13.96	0.27	2.06	0.04	18.65	98.58
319.49	**66**	40.60	13.82	0.01	8.62	0.11	0.07	13.62	0.30	4.03	0.42	16.83	98.44

320.74	**65**	44.31	14.45	0.01	6.27	0.17	0.07	14.79	0.25	3.86	0.85	14.01	99.04
321.52	**64**	40.29	14.56	0.01	5.43	0.29	0.06	19.39	0.25	4.56	1.29	12.47	98.60
323.59	**63**	37.62	17.58	0.01	5.36	0.35	0.10	18.92	0.26	5.13	0.72	13.29	99.32
324.27	**62**	39.79	18.02	0.01	5.18	0.43	0.06	18.33	0.24	4.06	0.78	12.57	99.47
326.37	**61**	34.34	27.14	bdl	5.46	0.20	0.06	14.44	0.14	4.02	bdl	15.09	100.89
327.51	**60**	32.45	24.70	bdl	7.52	0.17	0.05	14.40	0.21	4.94	bdl	16.57	101.00
328.69	**59**	23.02	24.10	0.02	16.47	0.23	0.06	11.97	0.26	4.12	bdl	19.78	100.02
329.52	**58**	15.49	26.90	0.01	22.85	0.08	0.05	8.23	0.28	3.65	0.02	23.13	100.69
330.21	**57**	7.44	31.90	0.01	27.29	0.01	0.04	7.44	0.28	2.13	bdl	23.97	100.51
330.89	**56**	13.64	44.07	bdl	11.73	bdl	0.03	9.88	0.25	4.35	bdl	16.60	100.57
332.09	**55**	13.59	43.97	bdl	11.67	bdl	0.04	9.76	0.29	4.29	bdl	16.58	100.19
332.57	**54**	13.22	46.85	bdl	12.36	bdl	0.03	7.93	0.20	3.01	bdl	16.51	100.11
333.51	**53**	21.52	43.39	bdl	9.77	bdl	0.05	10.14	0.05	2.92	bdl	13.66	101.51
334.52	**52**	6.98	36.64	bdl	23.05	bdl	0.03	7.31	0.19	2.65	bdl	23.72	100.56
335.56	**51**	23.38	34.72	bdl	7.14	0.06	0.05	11.43	0.21	3.79	bdl	20.45	101.23
336.6	**50**	33.13	27.26	bdl	7.27	0.15	0.08	9.46	0.23	4.91	bdl	19.26	101.75
337.38	**49**	21.08	33.02	bdl	11.32	bdl	0.04	7.01	0.14	3.40	bdl	25.66	101.69
338.74	**48**	39.94	6.62	0.01	11.12	0.13	0.06	23.93	0.29	2.93	3.46	10.71	99.20
339.89	**47**	45.85	0.87	0.01	12.97	0.07	0.07	27.02	0.29	1.90	0.02	10.04	99.11
340.73	**46**	45.87	0.54	0.01	10.63	0.03	0.09	32.66	0.17	0.89	0.01	8.32	99.22
342.24	**45**	46.33	0.48	bdl	6.35	0.02	0.08	38.40	0.19	1.31	bdl	6.03	99.19
342.69	**44**	49.97	0.50	0.01	7.57	0.04	0.08	31.55	0.28	1.55	0.02	7.48	99.05
343.61	**43**	57.92	0.46	0.02	6.40	0.22	0.13	24.93	0.79	1.54	0.09	6.21	98.70
344.78	**42**	40.20	0.51	bdl	9.83	0.02	0.04	37.11	0.18	1.49	bdl	9.92	99.30
346.01	**41**	48.37	0.39	0.01	6.13	0.02	0.08	36.34	0.20	1.36	bdl	6.26	99.16
347.04	**40**	48.61	0.33	0.01	4.87	0.01	0.09	38.53	0.16	1.36	bdl	5.23	99.21
348.08	**39**	45.84	0.31	bdl	16.87	0.03	0.09	21.80	0.16	0.82	bdl	13.19	99.11
349.39	**38**	45.86	0.22	bdl	9.31	0.01	0.10	33.95	0.15	1.18	0.01	8.32	99.11
351.58	**37**	39.28	0.27	bdl	11.78	0.01	0.12	34.24	0.19	1.40	bdl	11.11	98.39

352.11	**36**	31.14	0.33	0.01	19.30	0.02	0.09	28.68	0.23	1.01	bdl	18.24	99.03
353.32	**35**	51.95	0.43	0.01	2.98	0.03	0.08	37.98	0.26	1.18	0.01	4.07	98.98
354.13	**34**	33.59	10.22	bdl	16.75	0.02	0.05	13.90	0.20	3.50	0.01	19.30	97.55
355.32	**33**	15.99	10.86	0.01	28.30	0.07	0.04	9.32	0.22	2.92	0.23	26.71	94.66
356.23	**32**	26.81	8.91	0.01	23.50	0.05	0.05	14.92	0.23	2.13	0.02	22.63	99.24
357.24	**31**	40.59	2.13	bdl	18.69	0.04	0.06	19.68	0.21	1.55	0.01	16.24	99.19
357.84	**30**	55.87	1.50	0.01	5.16	0.04	0.08	29.57	0.17	1.57	bdl	4.55	98.53
358.76	**29**	37.00	5.18	0.03	18.88	0.10	0.06	16.81	0.77	4.33	bdl	15.44	98.62
360.25	**28**	17.99	29.35	0.01	15.35	bdl	0.05	14.21	0.13	3.15	bdl	20.14	100.38
360.85	**27**	29.10	29.16	0.01	7.32	bdl	0.06	15.66	0.18	4.82	0.03	14.50	100.83
361.81	**26**	30.83	21.49	0.01	8.23	bdl	0.07	13.94	0.13	7.03	0.06	17.68	99.46
362.81	**25**	42.14	12.80	0.01	6.44	0.01	0.08	18.21	0.22	4.88	0.02	13.66	98.47
364.26	**24**	56.61	0.40	0.01	3.35	bdl	0.13	35.43	0.27	0.78	bdl	1.89	98.86
365.04	**23**	42.39	1.21	0.01	5.82	bdl	0.16	40.73	0.18	2.65	bdl	6.05	99.20
366.07	**22**	33.93	1.48	bdl	7.06	0.02	0.19	46.89	0.22	1.81	bdl	7.41	99.01
367.29	**21**	49.88	0.20	0.01	0.48	bdl	0.25	47.71	0.26	0.37	bdl	-1.43	97.73
368.09	**20**	12.65	19.87	0.01	23.38	bdl	0.05	12.01	0.21	6.13	bdl	24.71	99.01
369.32	**19**	31.89	26.66	0.02	17.15	bdl	0.06	4.54	0.15	2.50	bdl	17.88	100.85
370.81	**18**	13.22	34.10	0.02	22.23	bdl	0.04	5.80	0.32	2.93	bdl	20.59	99.24
371.92	**17**	14.21	36.35	0.02	19.43	bdl	0.04	5.03	0.26	3.33	bdl	20.55	99.22
372.86	**16**	4.79	35.96	0.01	28.24	bdl	0.04	4.47	0.38	2.60	bdl	24.20	100.69
373.89	**15**	7.45	54.81	0.02	12.79	bdl	0.03	4.18	0.26	3.69	bdl	16.80	100.03
374.82	**14**	12.41	44.17	0.02	15.05	bdl	0.04	4.73	0.18	4.25	bdl	18.50	99.35
376.14	**13**	7.10	44.65	0.02	19.25	bdl	0.04	2.87	0.21	3.85	bdl	21.65	99.64
376.98	**12**	7.44	47.82	0.02	13.81	0.02	0.03	7.50	0.20	4.72	bdl	17.45	99.01
378.04	**11**	6.97	44.00	0.01	18.34	bdl	0.03	4.84	0.16	3.74	bdl	20.97	99.06
378.22	**10**	6.06	43.98	0.02	19.04	bdl	0.03	4.38	0.19	3.34	bdl	22.26	99.30
379.26	**9**	6.98	40.89	0.01	16.46	0.02	0.03	6.88	0.18	5.77	bdl	21.86	99.08
381.24	**8**	20.73	23.07	0.02	14.05	bdl	0.06	9.48	0.38	8.09	bdl	24.72	100.60

381.51	**7**	31.03	24.21	0.01	4.39	bdl	0.06	15.17	0.11	8.08	bdl	18.53	101.58
382.23	**6**	39.71	14.45	bdl	3.23	bdl	0.07	18.90	0.22	9.53	bdl	13.48	99.58
383.24	**5**	46.85	13.11	bdl	2.63	bdl	0.08	16.27	0.10	8.01	bdl	11.52	98.57
384.48	**4**	57.72	2.17	bdl	1.31	0.02	0.09	30.77	0.23	3.22	bdl	3.53	99.06
385.31	**3**	54.93	2.36	bdl	2.67	0.01	0.08	32.90	0.15	2.19	bdl	3.62	98.91
386.52	**2**	49.85	3.46	0.03	4.72	0.15	0.08	28.27	0.51	3.46	0.06	8.25	98.84
387.81	**1**	51.90	0.68	0.03	1.95	0.17	0.21	39.59	0.66	1.98	0.09	1.86	99.11

Trace elements Geochemistry full results (values in ppm)

N95A

Values in ppm	Sc	V	Cr	Co	Ni	Cu	Zn	Rb	Sr	Y	Zr	Nb	Mo	Cs	Ba	Hf	Ta	Pb	Th	U
T1A	5.9	21.7	58.3	6.1	28.0	20.3	10.0	0.54	22.4	4.2	5.2	0.35	16.3	0.12	678.0	bdl	bdl	8.8	0.19	0.11
T1	4.5	16.2	53.7	4.7	28.5	21.3	8.2	0.18	14.5	4.6	4.0	0.26	16.4	0.12	35.6	bdl	0.02	2.6	0.19	bdl
T2	4.8	18.7	51.1	4.7	30.6	22.7	11.7	0.34	13.9	2.9	5.0	0.45	17.3	0.12	34.7	bdl	0.02	4.8	0.24	0.06
T3	4.7	15.6	45.5	4.5	24.1	13.5	8.5	0.26	17.2	5.7	4.8	0.39	16.7	0.09	36.4	0.04	bdl	1.9	0.23	0.05
T3A	4.6	14.9	53.6	27.9	33.9	19.4	17.0	2.61	107.8	10.3	6.6	0.49	15.9	0.80	60.6	0.08	bdl	10.1	0.54	0.12
T3B	3.7	11.8	38.5	80.6	30.9	72.9	31.6	0.48	201.3	26.2	8.2	0.58	17.0	0.19	173.5	0.16	0.05	55.4	0.56	0.29
T4	2.9	7.4	32.0	101.3	29.6	184.3	79.2	0.48	207.2	12.3	6.7	0.45	12.8	0.19	177.5	0.09	0.03	25.7	0.42	0.19
T5	1.7	10.4	37.2	98.7	29.5	177.4	54.3	0.37	177.6	11.5	5.8	0.59	12.1	0.10	135.6	0.07	0.02	19.9	0.41	0.13
T6	2.5	8.1	35.6	179.2	31.3	680.5	342.5	0.15	393.1	13.1	7.1	0.76	13.7	bdl	442.5	0.17	0.05	40.0	0.79	0.24
T7	2.0	7.0	30.7	108.7	24.4	169.7	77.4	3.12	6590.0	7.7	7.3	0.59	11.1	bdl	7470.0	0.14	0.03	286.2	0.50	0.21
T8	2.3	8.5	35.2	32.6	33.7	133.7	30.9	bdl	82.4	8.3	7.0	0.51	13.5	bdl	62.5	0.13	0.02	3.3	0.48	0.06
T9	2.5	8.3	32.5	50.7	31.7	314.5	39.4	0.31	171.3	16.3	7.6	0.58	11.9	bdl	248.4	0.11	0.03	43.7	0.64	0.23
T9A	4.5	14.3	37.5	15.7	20.2	41.2	30.7	0.92	186.6	11.7	7.2	0.44	3.2	0.09	53.4	0.14	0.02	6.9	0.43	0.25
T10	4.6	14.2	49.8	5.0	23.0	27.7	11.9	0.32	24.3	6.6	5.4	0.53	16.3	0.12	39.1	0.07	0.03	5.0	0.46	0.07
T10A	4.8	15.9	56.9	6.6	31.6	16.3	13.1	0.47	27.6	5.1	6.3	0.50	18.3	0.08	62.8	0.04	0.03	7.3	0.32	0.05
T11	4.6	14.0	57.9	7.1	24.1	15.4	10.5	0.36	22.9	5.6	5.6	0.39	18.8	0.10	37.4	0.06	0.01	8.4	0.19	0.07
T11A	4.2	16.1	47.7	8.1	23.8	19.3	15.1	0.82	137.0	22.9	7.4	0.73	18.0	0.17	509.0	0.07	0.04	5.9	0.47	0.05
T11B	3.4	13.1	40.5	32.6	26.2	8.7	42.7	0.83	122.4	12.0	6.4	0.67	15.8	0.23	242.0	0.14	0.02	26.6	0.46	0.29
T12	2.4	8.9	36.5	36.8	41.0	52.4	27.0	0.53	68.1	12.9	6.7	0.48	13.0	0.07	111.0	0.09	0.05	52.0	0.53	0.24
T13	3.2	21.6	59.4	26.8	39.4	18.4	24.4	0.96	662.0	3.4	7.8	0.54	17.9	0.09	483.0	0.11	0.04	26.2	0.44	0.06
T14	3.4	8.2	38.5	98.8	36.9	143.7	57.7	0.28	505.3	30.7	6.0	0.71	13.4	bdl	12825.0	0.15	0.05	10.4	0.59	0.30
T15	2.0	7.0	27.7	74.6	23.7	97.9	46.9	0.10	694.5	13.5	3.0	0.39	12.2	bdl	7115.0	0.06	0.02	49.8	0.32	0.23
T16	1.8	5.1	26.0	42.8	21.3	28.5	24.6	bdl	189.4	9.0	3.6	0.36	11.2	bdl	3757.5	0.02	0.02	15.1	0.29	0.13

T17	1.9	6.1	28.1	44.2	24.0	39.2	29.4	0.14	128.5	6.1	3.7	0.39	12.2	bdl	5555.0	0.63	0.03	5.1	0.38	0.12
T18	2.1	6.1	28.3	35.7	22.7	19.4	20.4	bdl	38.9	7.7	4.4	0.43	11.9	bdl	575.5	0.12	0.02	2.1	0.43	0.14
T19	1.3	7.1	20.6	14.9	13.3	4.5	11.1	0.12	40.4	6.0	3.9	0.26	9.6	bdl	21.3	0.08	0.01	1.3	0.22	0.04
T20	4.1	20.2	49.7	3.1	24.5	22.0	14.0	0.51	13.9	4.8	5.8	0.44	18.8	bdl	36.5	bdl	bdl	3.1	0.15	bdl

N95E

Values in ppm	Sc	V	Cr	Co	Ni	Cu	Zn	Rb	Sr	Y	Zr	Nb	Mo	Cs	Ba	Hf	Ta	Pb	Th	U
S1A	23.4	152.1	158.6	16.0	62.5	9.3	14.1	56.0	39.4	34.8	181.5	8.3	19.4	3.9	98	4.5	0.5	31.3	8.1	2.2
S1b	13.9	35.1	70.1	31.5	34.0	7.5	59.0	125.3	736.2	19.9	132.2	7.1	2.6	38.4	3699	3.8	0.8	63.6	8.2	1.0
S1	4.1	14.9	46.9	129.5	40.7	205.9	46.8	0.2	447.1	11.7	12.6	1.1	9.4	0.1	11485	0.5	0.1	57.5	0.4	0.6
S2	1.7	10.6	40.2	89.2	13.5	73.3	124.2	0.2	1633	8.9	5.7	0.5	6.6	bdl	11720	1.1	0.0	592.5	0.5	0.2
S3	2.5	24.3	32.3	73.6	24.1	214.6	52.7	0.6	200	6.0	9.0	0.7	12.5	0.1	831	0.2	0.0	64.9	0.7	0.5
S3A	3.9	13.0	34.0	29.2	27.1	35.8	48.1	1.1	483	9.7	9.5	0.8	9.6	1.5	187	0.2	0.0	36.7	0.8	0.1
S4	4.19	24.1	29.7	18.5	22.5	13.7	22.7	0.5	274	14.2	5.6	0.3	2.9	0.4	458	0.1	bdl	19.6	0.1	0.1
S5	5.34	15.48	50.5	10.9	26.0	14.6	9.8	0.5	305	8.9	5.2	0.5	19.2	0.1	113	0.1	bdl	22.3	0.3	0.1
S5A	2.53	9.39	23.6	14.2	19.8	16.7	12.0	0.3	443	15.1	8.4	0.4	9.1	0.2	341	0.1	0.0	36.5	0.4	0.1
S6	1.79	14.64	31.2	70.8	27.3	79.3	85.9	0.1	1881	29.4	5.6	0.5	7.5	0.1	19580	0.1	0.0	19.6	0.5	0.2
S6A	0.70	3.80	10.6	5.3	11.3	33.2	4.6	bdl	38.1	3.9	2.1	0.2	3.8	0.0	264	0.1	0.0	5.1	0.1	0.0
S7	0.06	0.26	1.0	8.4	1.0	95.7	1.4	bdl	29.8	0.2	0.4	0.0	0.4	0.0	267	0.0	0.0	1.8	0.0	0.0
S9	0.30	1.43	4.8	8.8	6.7	24.4	41.5	bdl	166.5	3.5	1.1	0.1	1.6	0.0	2195	0.0	0.0	1.5	0.1	0.0
S10	0.92	9.24	14.4	71.3	24.5	68.8	152.4	0.2	46.8	6.6	2.4	0.3	4.6	0.0	183	0.1	0.0	20.6	0.2	0.1
S11	1.27	11.01	25.8	15.0	31.8	34.2	265.0	0.1	79.4	4.0	4.8	0.3	8.5	0.1	723	0.1	0.0	22.6	0.4	0.2
S12	2.135	13.53	39.2	20.6	35.5	45.2	92.3	0.3	36.5	16.2	5.9	0.4	13.0	bdl	84	0.1	0.0	77.6	0.4	0.2
S12A	4.89	16.5	56.3	15.9	34.8	35.2	29.1	1.1	161.3	12.2	8.8	0.7	15.6	0.2	198	0.2	0.0	5.4	0.4	0.1
S13	3.87	19.6	58.4	5.7	26.6	19.1	7.0	bdl	11.6	8.9	bdl	0.4	18.1	bdl	28	bdl	bdl	1.7	0.2	0.1
S14	4.81	24.8	53.4	4.2	24.5	21.5	14.0	3.4	14.7	7.5	7.2	0.6	17.2	0.5	55	0.1	0.0	7.1	0.8	0.3

N92I

	Sc	V	Cr	Co	Ni	Cu	Zn	Rb	Sr	Y	Zr	Nb	Mo	Cs	Ba	Hf	Ta	Pb	Th	U
GH1A	0.6	5.0	6.8	1.4	4.9	1.9	1.2	0.15	2.9	2.03	1.85	0.13	2.9	0.32	7.2	0.03	0.01	0.6	0.13	0.05
GH1B	1.7	16.8	14.7	4.4	9.2	4.1	7.4	2.12	6.0	3.42	4.42	0.25	1.0	0.24	23.6	0.08	0.01	1.2	0.27	0.24
GH1C	0.9	5.3	45.6	1.7	16.6	1.3	2.4	0.71	5.7	3.05	3.73	0.26	3.7	0.07	23.2	0.07	0.01	0.5	0.21	0.06
GH1	2.7	13.5	76.7	40.7	264	18.0	15.8	0.18	14.9	44.9	6.77	0.54	10.9	0.06	53.1	0.14	0.03	38.0	0.45	0.39
GH2	0.5	2.1	5.7	15.7	3.4	5.6	16.6	bdl	4.2	4.32	1.27	0.09	1.9	0.01	64.6	0.01	0.00	12.2	0.09	0.05
GH3	2.0	16.5	22.2	57.9	26.2	31.2	52.9	0.18	19.7	56.8	6.51	0.53	8.1	bdl	143	0.06	0.03	33.2	0.44	0.15
GH4	0.1	0.3	1.0	2.8	0.9	1.6	1.6	bdl	1.0	0.28	0.25	0.02	0.4	0.00	1.9	0.00	0.00	0.9	0.02	0.00
GH5	0.8	6.0	12.5	4.0	22.4	18.9	10.4	bdl	30.9	2.01	3.18	0.22	4.0	bdl	518.	0.04	0.01	18.3	0.20	0.09
GH5A	1.7	7.6	27.3	12.6	23.2	16.9	52.9	28.3	20.2	4.31	4.04	0.37	10.2	3.7	49.1	0.09	0.01	21.0	0.24	0.04
GH6	4.3	14.4	30.8	3.3	14.6	12.7	19.2	0.61	7.0	4.53	5.81	0.41	3.8	143.	10.1	0.04	bdl	6.7	0.30	0.08
GH6A	3.8	13.5	28.2	2.5	17.8	20.5	16.7	0.46	4.6	5.19	3.95	0.51	4.1	26.0	11.0	bdl	bdl	4.0	0.24	0.12
GH7	4.8	14.0	30.9	3.4	16.5	14.0	15.7	0.68	2.7	2.04	5.31	0.43	2.7	2.16	7.0	bdl	bdl	1.7	0.27	0.01
GH7A	4.3	18.3	32.4	5.7	18.0	11.9	19.9	0.18	5.0	4.94	10.1	0.88	4.5	0.29	10.8	0.10	0.03	2.5	0.73	0.35
GH7B	0.9	9.4	14.0	1.9	7.8	2.7	11.9	0.15	6.0	5.82	6.13	0.42	2.4	30.3	11.7	0.08	0.04	3.8	0.45	0.34

GH7C	4.3	15.4	37.2	2.9	19.5	17.3	30.3	0.90	105	4.54	2.99	0.21	3.9	33.1	77.8	bdl	bdl	2.5	0.16	0.12
GH8	0.1	0.2	1.2	0.7	0.9	1.7	2.2	bdl	3.4	0.19	0.13	0.01	0.5	0.00	1.2	0.00	0.00	2.3	0.01	0.00
GH9	1.6	6.5	32.0	5.2	25.9	21.8	20.7	0.86	10.8	6.32	48.9	0.35	5.6	0.10	8.6	0.28	0.12	9.4	0.47	0.40
GH10	1.5	5.0	23.1	56.3	25.2	25.8	132	0.18	58.8	7.29	6.70	0.40	11.4	0.07	840	0.35	0.03	141	0.39	0.19
GH11	2.1	7.6	33.9	38.7	25.6	23.1	249	0.25	23.5	14.3	6.61	0.44	13.5	0.09	174	0.15	0.03	34.6	0.36	0.12
GH12	1.4	5.4	25.9	32.0	22.0	20.1	122	0.22	46.5	9.43	3.60	0.36	12.8	0.11	393	1.52	0.04	142	0.38	0.37
GH12 A	0.9	5.5	14.7	4.5	10.6	11.6	11.0	0.11	23.6	4.50	4.39	0.29	5.8	0.06	14.7	0.07	0.01	3.7	0.23	0.06
GH12 B	4.4	18.3	37.7	4.5	17.9	18.7	14.1	2.66	3.8	5.15	4.94	0.29	4.4	4.04	15.5	bdl	bdl	1.6	0.23	0.15
GH13	4.4	20.2	46.8	4.8	23.3	20.2	22.3	3.28	4.3	7.37	7.81	0.56	5.6	0.70	15.5	0.25	0.03	1.7	0.41	0.29
GH14	5.9	24.9	49.7	3.7	23.3	31.1	9.1	2.15	5.5	8.49	5.74	0.40	6.4	104	16.4	bdl	0.01	2.0	0.21	0.23

N94J

	Sc	V	Cr	Co	Ni	Cu	Zn	Rb	Sr	Y	Zr	Nb	Mo	Cs	Ba	Hf	Ta	Pb	Th	U
J46	4.5	19.2	34.9	31.4	38.6	20.2	19.2	0.36	15.4	59.9	4.7	0.25	1.6	bdl	23.2	0.07	0.02	5.37	0.19	0.42
J45	6.0	40.6	39.2	4.8	22.1	21.0	7.6	0.30	5.3	5.0	5.3	0.30	2.3	bdl	8.2	0.08	0.02	2.09	0.20	0.09
J44	5.4	22.4	46.4	2.9	17.2	22.4	7.6	1.03	4.7	8.0	8.7	0.34	2.7	bdl	16.3	0.09	0.03	3.23	0.30	0.21
J43	4.6	23.9	63.9	3.6	25.5	19.6	10.8	1.03	9.5	8.4	10.2	0.57	10.3	3.7	29.2	0.12	0.03	1.14	0.33	0.22
J42	4.5	18.9	56.0	3.2	28.4	27.6	13.5	0.30	8.6	4.6	4.2	0.42	8.2	5.0	21.2	0.08	bdl	0.88	0.14	0.16
J40	4.8	19.3	57.9	3.3	28.1	26.8	13.2	0.32	18.2	8.2	3.6	0.34	11.4	3.3	26.8	bdl	0.00	0.84	0.18	0.15
J39	2.1	10.1	27.7	16.1	18.1	22.6	13.7	0.67	49.3	12.6	7.0	0.52	11.8	0.2	60.3	0.13	0.04	24.8	0.45	0.49
J38	2.7	10.8	27.1	21.3	17.5	11.9	14.2	0.53	78.5	11.7	6.6	0.50	12.0	0.3	103	0.28	0.05	12.7	0.47	0.29
J36	0.8	5.7	20.6	33.1	18.9	36.9	114.	0.22	24.0	4.4	5.1	0.27	10.0	0.1	218	0.07	0.02	5.15	0.25	0.43
J33	1.6	4.9	33.0	25.2	16.9	54.0	245	bdl	449	3.4	3.1	0.19	9.6	0.1	8340	0.06	0.01	7.69	0.23	0.32
J32	2.4	6.3	35.9	28.6	23.1	45.1	107	0.29	30.2	20.6	7.4	0.76	13.5	bdl	306	0.11	0.06	11.6	0.77	0.44
J31	2.4	7.5	36.6	30.4	25.4	62.7	14.9	bdl	22.8	12.5	5.5	0.57	14.0	bdl	77.5	0.29	0.04	4.69	0.55	0.49
J30	2.1	7.2	41.8	35.0	30.9	50.3	25.5	bdl	626	10.5	6.4	0.52	14.9	0.1	**10005**	0.06	0.03	3.90	0.52	0.43
J28	1.0	5.2	16.3	25.8	16.3	17.8	902	bdl	125	2.4	3.7	0.23	6.6	0.0	2285	0.11	0.02	21.6	0.23	0.37
J27	1.3	11.6	20.0	49.1	12.8	17.4	1835	0.21	9.3	4.3	3.8	0.29	7.6	0.0	45.7	0.14	0.01	35.6	0.25	0.41
J24	4.4	19.9	50.9	3.3	20.7	25.6	11.1	0.31	7.0	7.5	5.6	0.45	8.2	3.9	13.0	0.12	0.02	0.91	0.26	0.55
J22	4.0	15.7	43.3	3.2	23.2	16.5	9.4	0.79	6.3	2.9	5.3	0.44	6.4	13.2	12.8	bdl	0.02	0.85	0.34	0.87
J20	4.7	14.0	55.4	2.1	20.8	10.8	9.1	0.49	10.4	4.0	5.7	0.38	9.1	15.4	19.5	0.06	bdl	1.10	0.22	0.66
J18	4.7	17.2	44.0	3.7	24.8	19.2	10.0	0.65	7.8	10.0	6.1	0.39	6.6	26.6	13.6	0.05	bdl	1.33	0.37	0.35
J16	6.2	22.7	47.9	3.8	27.8	19.4	12.3	0.90	6.4	29.0	8.6	0.76	7.3	1.7	12.8	0.10	0.05	1.80	0.68	0.50
J14	4.8	13.8	50.3	5.7	29.3	34.1	6.2	0.85	12.6	7.0	6.8	0.49	17.7	0.2	28.7	0.06	bdl	4.71	0.28	0.23
J13	0.0	0.0	0.0	0.2	0.0	0.0	10.4	0.01	1.0	0.0	bdl	bdl	0.0	bdl	0.1	bdl	bdl	0.06	bdl	bdl
J11	3.7	17.2	41.2	13.6	23.2	13.8	12.7	1.14	27.1	11.0	7.0	0.50	5.9	9.2	13.2	0.12	0.02	1.60	0.49	0.17
J10	3.4	18.4	38.5	14.6	23.7	19.7	13.4	0.36	16.1	21.8	12.8	1.01	13.6	0.2	31.5	0.48	0.09	6.93	1.14	0.86

J9	2.3	11.7	33.7	28.1	26.9	25.8	14.2	0.19	15.0	8.1	6.3	0.44	19.4	bdl	27.4	0.16	0.03	13.4	0.35	1.07
J8	6.5	38.4	107	9.7	149	45.0	23.6	2.01	266	1.5	5.6	0.68	18.8	0.6	1571	0.43	0.01	8.91	0.51	0.32
J7	1.1	4.5	20.2	46.1	15.3	13.2	1949	bdl	38.8	5.3	1.5	0.31	8.7	0.1	438	0.20	0.01	16.3	0.17	0.23
J5	1.7	5.9	31.7	57.0	26.0	24.3	411.5	bdl	25.2	19.4	5.7	0.43	15.1	0.2	63.6	0.33	0.06	8.03	0.27	0.60
J4	1.6	3.6	25.0	29.5	25.7	15.2	28.7	0.53	72.4	21.7	5.1	0.40	10.6	0.1	23.1	0.12	0.03	2.63	0.45	0.30
J3	3.1	10.5	33.5	8.9	23.8	13.9	10.3	1.81	23.6	14.8	6.8	0.50	13.8	0.2	43.7	0.08	0.02	4.45	0.42	0.43
J1	5.0	18.6	50.0	12.6	25.2	43.1	13.4	0.35	7.8	4.4	4.5	0.31	8.4	35.4	11.8	0.03	bdl	1.11	0.14	0.21

GL57

	Sc	V	Cr	Co	Ni	Cu	Zn	Rb	Sr	Y	Zr	Nb	Mo	Cs	Ba	Hf	Ta	Pb	Th	U
D1A	1.9	38.3	36.4	16.5	28.1	10.8	42.0	0.1	8.5	8.5	6.7	0.8	9.0	<0.022	16.1	0.2	0.07	11.9	1.0	0.4
D1B	6.8	120.9	68.1	16.2	55.3	15.6	13.4	0.2	31.2	57.9	23.9	1.6	17.0	0.2	53.9	0.2	0.13	54.7	2.0	3.9
D1C	10.2	18.6	63.1	27.5	48.6	22.1	20.3	0.5	31.9	35.6	63.0	1.0	15.6	bdl	33.5	bdl	bdl	2.0	1.2	0.4
D1	5.7	23.3	52.1	5.8	28.5	19.3	14.0	bdl	13.0	2.9	5.7	0.4	19.0	0.2	43.8	bdl	bdl	1.8	0.3	1.4
D2	5.9	22.7	58.0	2.6	28.3	13.0	28.0	0.4	14.4	5.7	4.2	0.4	18.6	bdl	33.0	bdl	bdl	3.3	0.2	1.1
D2A	6.0	19.2	83.1	2.6	113.7	17.0	10.0	0.5	15.0	3.3	4.4	0.5	19.6	0.1	39.9	bdl	bdl	1.5	0.2	1.0
D3	6.2	23.4	54.4	3.1	24.3	19.0	9.7	0.5	13.1	16.6	5.6	0.5	18.6	0.1	44.0	0.0	0.01	9.2	0.2	1.4
D4	6.6	29.7	63.9	3.8	29.9	21.3	10.1	0.6	15.9	6.9	4.9	0.4	19.0	0.2	44.4	bdl	0.00	4.1	0.2	0.9
DM-1	2.0	3.7	16.7	18.7	10.5	31.3	11.6	0.2	23.1	8.6	5.5	0.4	5.6	0.1	45.6	0.1	0.03	0.7	0.4	0.2
DM-2	5.5	8.5	29.0	13.6	16.2	30.2	11.0	0.3	14.8	8.5	8.8	0.5	8.2	0.1	13.7	0.4	0.03	2.4	0.4	0.2
DM-3	0.6	11.0	13.5	19.5	16.7	33.8	39.9	bdl	200.5	2.0	1.4	0.3	2.1	bdl	15.1	bdl	bdl	10.0	0.3	0.2
DM-4	0.6	20.0	15.6	8.5	15.9	21.8	173.7	0.4	135.7	1.3	3.0	0.2	3.0	bdl	30.3	bdl	bdl	39.2	0.3	0.5
DM-5	0.5	8.2	9.3	8.6	9.9	30.0	21.0	bdl	172.4	1.2	1.2	0.1	2.1	bdl	13.8	bdl	bdl	8.0	0.1	0.1
DM-6	0.5	6.7	8.4	15.6	12.0	56.8	27.4	bdl	219.8	2.7	1.8	0.2	1.5	bdl	2272.0	0.0	0.02	5.3	0.1	0.1
DM-7	0.4	10.9	9.7	14.1	8.9	18.9	169.2	bdl	120.6	3.5	2.2	0.3	1.5	bdl	39.4	0.0	0.02	19.5	0.2	0.3
D4A	8.0	13.0	55.6	13.0	31.6	123.8	18.7	0.7	17.2	3.2	6.3	0.5	17.5	0.2	34.2	0.7	0.03	1.1	0.2	0.4
D5	4.7	18.7	56.3	8.1	28.1	28.2	16.4	0.3	15.2	2.6	5.8	0.5	18.9	0.0	32.9	0.0	0.00	2.1	0.4	0.3
D6	4.6	18.3	58.4	7.4	29.2	17.3	12.2	0.5	17.3	4.6	4.3	0.4	19.8	bdl	36.4	bdl	0.01	2.6	0.2	0.9
D7	3.2	14.3	44.0	5.2	28.7	13.3	10.3	0.6	15.7	4.8	4.5	0.4	17.4	0.1	35.3	bdl	bdl	1.7	0.3	1.4
D8	7.3	17.5	50.8	9.6	25.9	9.9	12.4	0.6	17.1	5.3	4.7	0.5	16.7	0.1	28.6	bdl	0.03	10.8	0.4	0.4
D8A	1.6	5.8	13.2	13.5	9.8	31.3	6.7	0.4	17.1	18.3	7.3	0.3	5.1	0.1	23.6	0.1	0.03	7.3	0.3	0.4
D9	2.0	3.7	16.7	18.7	10.5	31.3	11.6	0.2	23.1	8.6	5.5	0.4	5.6	0.1	45.6	0.1	0.03	0.7	0.4	0.2
D9A	5.5	8.5	29.0	13.6	16.2	30.2	11.0	0.3	14.8	8.5	8.8	0.5	8.2	0.1	13.7	0.4	0.03	2.4	0.4	0.2
D9B	8.1	17.8	42.7	8.1	30.7	30.7	11.2	1.0	11.9	10.2	6.6	0.4	9.7	0.3	18.6	0.3	0.03	2.7	0.4	0.5
D9C	1.6	3.0	15.2	42.9	20.8	24.9	103.3	0.2	28.4	5.6	5.2	0.3	5.5	bdl	14.5	0.2	0.04	3.8	0.4	0.1

D10	1.7	2.9	17.1	33.4	15.8	5.7	37.1	0.2	57.8	6.7	6.1	0.4	5.8	0.1	80.4	0.2	0.05	1.9	0.4	0.2
D11	2.2	3.8	19.1	38.0	28.5	8.4	19.9	0.3	147.5	8.7	8.4	0.6	6.4	0.1	49.8	0.1	0.03	5.3	0.6	0.2
D12	2.0	3.8	18.3	38.6	18.9	13.7	50.7	0.4	154.8	7.4	4.3	0.4	6.5	0.1	105.8	0.1	0.03	6.6	0.4	0.3
D13	0.8	2.9	12.0	28.9	11.7	8.8	93.5	0.1	155.2	3.1	2.0	0.2	4.9	0.1	360.5	0.1	0.01	2.3	0.2	0.0
D14	2.8	4.9	20.2	46.5	24.5	13.0	30.0	0.7	56.8	6.4	5.9	0.5	6.9	0.5	68.0	0.1	0.04	4.0	0.6	0.2
D15	3.3	15.5	35.8	16.0	21.3	13.2	9.4	bdl	23.5	14.0	5.6	0.5	15.6	0.1	68.5	bdl	0.02	1.4	0.3	0.1
D16	3.6	14.2	44.3	8.0	20.0	14.3	9.6	0.6	14.4	10.1	6.2	0.5	15.0	0.2	41.3	bdl	0.01	1.4	0.3	0.1
D17	3.6	13.2	40.6	6.5	22.1	11.4	11.7	0.3	17.7	10.0	5.2	0.4	14.7	0.1	38.8	0.0	0.03	2.6	0.3	0.1
D18	4.2	15.8	47.0	7.8	28.1	30.2	13.1	0.3	15.0	9.4	6.8	1.0	16.3	0.2	34.8	0.2	0.05	11.7	0.8	0.4

REE Geochemistry full results (Values in ppm)

N95A														
Values in p	**La**	**Ce**	**Pr**	**Nd**	**Sm**	**Eu**	**Gd**	**Tb**	**Dy**	**Ho**	**Er**	**Tm**	**Yb**	**Lu**
T1A	1.35	2.21	0.43	1.65	0.30	0.14	0.43	0.05	0.32	0.08	0.32	0.05	0.60	0.10
T1	0.84	1.27	0.27	0.62	0.09	0.03	0.39	bdl	0.45	0.13	0.28	0.05	0.40	0.06
T2	0.90	1.05	0.30	1.56	0.56	0.06	0.37	0.04	0.45	0.06	0.23	0.03	0.14	0.02
T3	3.01	3.46	0.69	2.81	0.60	0.13	0.50	0.10	0.64	0.17	0.34	0.09	0.70	0.06
T3A	10.50	7.34	3.12	13.40	3.23	0.59	2.26	0.43	2.38	0.45	1.47	0.26	1.30	0.29
T3B	8.24	5.22	1.15	5.01	0.74	0.30	1.75	0.23	1.84	0.54	1.54	0.24	1.43	0.27
T4	3.62	4.79	0.51	2.32	0.42	0.18	0.59	0.13	0.89	0.29	0.85	0.12	0.65	0.15
T5	4.77	4.42	0.65	3.25	0.35	0.14	0.64	0.13	1.01	0.22	0.66	0.12	0.84	0.11
T6	8.06	5.96	1.25	5.40	1.29	0.31	1.19	0.25	1.34	0.37	0.95	0.12	0.81	0.17
T7	4.86	3.85	0.84	3.44	0.68	0.54	0.78	0.13	0.78	0.19	0.58	0.07	0.43	0.09
T8	1.30	3.16	0.32	1.31	0.28	0.08	0.27	0.06	0.50	0.18	0.47	0.07	0.59	0.11
T9	7.11	7.76	1.17	5.17	1.00	0.27	1.12	0.20	1.34	0.38	1.15	0.14	1.34	0.17
T9A	3.43	4.79	0.58	1.96	0.46	0.11	0.44	0.14	0.76	0.24	0.78	0.13	0.82	0.15
T10	3.35	4.28	0.53	1.57	0.23	0.08	0.33	0.09	0.56	0.13	0.45	0.10	0.58	0.08
T10A	1.83	2.24	0.25	1.10	0.11	0.05	0.38	0.04	0.34	0.11	0.45	0.06	0.41	0.12
T11	1.71	2.07	0.28	0.68	0.36	0.08	0.29	0.04	0.45	0.11	0.36	0.04	0.51	0.08
T11A	5.87	7.74	0.88	4.73	0.85	0.30	1.68	0.26	2.28	0.57	1.98	0.23	2.23	0.19
T11B	7.41	6.37	1.03	4.21	0.88	0.24	1.19	0.12	0.97	0.23	0.78	0.10	0.62	0.11
T12	7.16	5.58	1.12	5.37	0.61	0.24	1.19	0.14	1.06	0.27	0.80	0.15	0.75	0.13
T13	1.51	1.87	0.19	0.89	0.17	0.04	0.25	0.04	0.15	0.10	0.32	0.03	0.39	0.05
T14	17.30	33.43	3.34	13.70	2.22	1.23	3.01	0.39	2.57	0.78	2.50	0.39	3.19	0.48
T15	8.27	6.36	1.22	4.73	0.62	0.47	1.04	0.14	1.08	0.20	0.74	0.12	0.91	0.13
T16	3.49	3.30	0.50	2.32	0.41	0.28	0.44	0.09	0.68	0.14	0.46	0.06	0.41	0.07
T17	3.23	3.63	0.50	2.23	0.32	0.38	0.58	0.09	0.66	0.15	0.56	0.06	0.43	0.06

T18	3.82	3.84	0.57	2.80	0.45	0.13	0.51	0.10	0.71	0.18	0.49	0.07	0.43	0.05
T19	3.06	3.25	0.39	1.75	0.10	0.08	0.46	0.07	0.35	0.13	0.52	0.08	0.60	0.12
T20	1.28	1.78	0.27	0.71	0.03	0.01	0.00	0.05	0.24	0.09	0.26	0.05	0.34	0.09

N95E

	La	Ce	Pr	Nd	Sm	Eu	Gd	Tb	Dy	Ho	Er	Tm	Yb	Lu
S1A	43.0	100.5	8.08	31.80	6.50	1.72	5.75	0.93	5.82	1.20	3.15	0.50	3.50	0.55
S1b	91.2	195.7	14.62	46.38	5.32	1.14	2.92	0.37	2.19	0.57	1.55	0.23	1.73	0.28
S2	11.51	9.54	2.74	11.54	1.90	1.28	1.63	0.22	1.26	0.27	0.81	0.10	0.67	0.11
S3	3.83	6.93	0.82	4.20	0.85	0.30	0.84	0.12	0.86	0.19	0.52	0.09	0.54	0.07
S3A	3.93	7.16	0.63	2.73	0.59	0.18	0.93	0.11	0.85	0.26	0.79	0.14	0.86	0.17
S4	2.87	5.48	0.62	3.16	0.44	0.22	0.89	0.16	1.36	0.31	0.99	0.19	1.22	0.21
S5	1.81	3.34	0.37	1.56	0.20	0.09	0.58	0.05	0.75	0.20	0.72	0.07	0.92	0.10
S5A	2.62	3.50	0.65	2.84	0.81	0.23	1.09	0.17	1.20	0.36	1.12	0.15	1.12	0.20
S6	20.31	9.99	3.27	15.28	1.96	2.00	3.25	0.39	2.27	0.54	1.47	0.20	1.25	0.19
S6A	1.59	1.92	0.27	1.22	0.38	0.08	0.35	0.04	0.32	0.08	0.27	0.05	0.38	0.06
S7	0.34	0.30	0.06	0.25	0.04	0.02	0.04	0.01	0.03	0.01	0.02	0.00	0.02	0.00
S8	0.17	0.16	0.03	0.12	0.02	0.01	0.04	0.01	0.04	0.01	0.03	0.00	0.03	0.00
S9	0.84	0.52	0.25	1.37	0.27	0.21	0.41	0.06	0.35	0.09	0.25	0.03	0.19	0.04
S10	5.15	4.72	1.25	6.31	1.16	0.30	1.30	0.19	1.13	0.24	0.62	0.09	0.62	0.11
S11	2.37	2.89	0.39	1.83	0.27	0.14	0.51	0.07	0.56	0.15	0.38	0.06	0.37	0.06
S12	5.38	2.93	0.67	2.58	0.60	0.24	1.16	0.23	1.43	0.37	1.23	0.20	0.86	0.16
S12A	3.44	4.70	0.63	2.53	0.25	0.13	0.58	0.11	0.95	0.25	0.75	0.12	0.70	0.16
S13	2.30	3.54	0.50	1.97	0.34	0.10	0.35	0.08	0.71	0.17	0.60	0.12	0.81	0.12
S14	3.27	5.37	0.67	3.11	0.62	0.04	0.71	0.08	0.79	0.18	0.64	0.07	0.82	0.08

N92I

	La	Ce	Pr	Nd	Sm	Eu	Gd	Tb	Dy	Ho	Er	Tm	Yb	Lu
GH1A	0.93	1.20	0.18	0.92	0.17	0.06	0.17	0.03	0.06	0.24	0.19	0.03	0.24	0.04
GH1B	3.77	7.67	1.17	4.68	0.75	0.15	0.37	0.05	0.11	0.55	0.39	0.05	0.51	0.08
GH1C	1.08	1.81	0.22	1.14	0.25	0.09	0.32	0.05	0.11	0.41	0.28	0.05	0.32	0.06
GH1	6.32	4.94	1.63	8.90	2.64	0.84	4.15	0.77	0.77	0.77	3.78	0.54	3.58	0.56
GH2	0.78	0.88	0.13	0.61	0.08	0.03	0.17	0.03	0.06	0.21	0.22	0.03	0.24	0.04
GH3	3.04	3.07	0.45	2.17	0.47	0.17	0.97	0.19	0.52	1.57	2.02	0.28	1.99	0.41
GH4	0.21	0.21	0.03	0.15	0.02	0.01	0.03	0.00	0.01	0.03	0.02	0.00	0.02	0.00
GH5	0.46	0.92	0.13	0.66	0.15	0.06	0.25	0.05	0.05	0.25	0.16	0.03	0.14	0.03
GH5A	2.22	8.15	0.35	1.43	0.19	0.08	0.28	0.05	0.41	0.11	0.32	0.05	0.44	0.07
GH6	3.17	3.30	0.47	1.70	0.04	0.01	bdl	0.03	0.16	0.46	0.32	0.08	0.60	0.04
GH6A	2.41	2.57	0.26	1.26	0.31	0.04	0.45	0.05	0.11	0.68	0.48	0.08	0.48	0.09
GH7	10.10	9.21	1.07	3.27	0.31	0.07	bdl	0.02	0.04	bdl	0.08	0.01	0.14	0.04
GH7A	2.72	3.13	0.42	1.67	0.38	0.06	0.32	0.03	0.09	0.43	0.27	0.08	0.59	0.13
GH7B	3.85	3.40	0.45	2.01	0.37	0.10	0.43	0.08	0.15	0.59	0.43	0.06	0.42	0.09
GH7C	2.10	2.32	0.27	0.91	0.02	bdl	bdl	0.02	0.09	0.28	0.39	0.04	0.36	0.06
GH8	0.11	0.12	0.02	0.06	0.01	0.00	0.01	0.00	0.01	0.00	0.01	0.00	0.02	0.00
GH9	4.55	2.50	0.70	1.78	0.43	0.52	0.47	0.12	0.15	0.42	0.32	0.10	0.44	0.09
GH10	5.26	3.45	0.47	1.79	0.30	0.13	0.45	0.09	0.16	0.68	0.50	0.05	0.48	0.07
GH11	3.59	3.96	0.76	3.61	0.45	0.16	1.08	0.16	0.26	0.90	0.71	0.12	0.71	0.15
GH12	3.14	5.65	0.59	2.79	0.54	0.15	0.91	0.12	0.26	0.83	0.69	0.12	0.72	0.11
GH12A	4.56	4.35	0.53	2.05	0.24	0.06	0.29	0.05	0.27	0.09	0.23	0.04	0.25	0.04
GH12B	2.52	2.98	0.33	1.21	0.40	0.08	0.06	0.08	0.14	0.62	0.32	0.08	0.48	0.07
GH13	2.55	3.24	0.33	1.40	0.21	0.07	0.51	0.08	0.21	0.55	0.65	0.11	0.59	0.13
GH14	3.12	4.97	0.62	2.60	0.54	0.15	0.35	0.08	0.19	0.76	0.63	0.12	0.82	0.09

N94J

Values	La	Ce	Pr	Nd	Sm	Eu	Gd	Tb	Dy	Ho	Er	Tm	Yb	Lu
J46	2.41	2.57	0.33	1.74	0.33	0.14	1.09	0.26	0.90	2.82	2.70	0.38	2.25	0.37
J45	15.88	9.53	0.92	3.54	0.28	0.09	0.34	0.05	0.07	0.25	0.27	0.02	0.24	0.04
J44	2.93	3.25	0.39	1.59	0.18	0.05	0.32	0.05	0.13	0.51	0.43	0.06	0.47	0.09
J43	3.41	3.69	0.50	1.78	0.10	0.10	0.57	0.07	0.16	0.52	0.59	0.08	0.38	0.06
J42	0.60	1.01	0.20	0.78	0.13	0.10	0.25	0.04	0.08	0.39	0.20	0.03	0.39	0.04
J40	1.82	2.44	0.27	2.52	0.78	0.10	0.76	0.12	0.17	0.65	0.56	0.05	0.31	0.03
J39	4.16	4.58	0.71	3.01	0.63	0.22	0.88	0.14	1.09	0.24	0.82	0.11	0.76	0.17
J38	4.60	4.97	0.75	2.99	0.54	0.11	0.75	0.13	0.85	0.27	0.88	0.13	0.79	0.15
J36	1.87	1.88	0.29	1.02	0.08	0.05	0.32	0.05	0.11	0.32	0.42	0.06	0.42	0.08
J33	1.53	2.39	0.25	1.10	0.16	0.33	0.30	0.03	0.06	0.32	0.23	0.03	0.32	0.05
J32	6.17	6.71	1.38	6.26	0.85	0.27	1.43	0.18	0.34	1.35	0.87	0.12	0.69	0.12
J31	9.31	4.22	0.86	3.84	0.63	0.18	0.73	0.12	0.22	0.79	0.59	0.07	0.60	0.12
J30	7.84	4.32	0.79	2.85	0.42	0.45	0.77	0.11	0.19	0.77	0.59	0.08	0.68	0.07
J28	0.96	2.42	0.17	0.75	0.18	0.18	0.15	0.03	0.07	0.27	0.16	0.04	0.13	0.05
J27	5.26	7.56	0.46	1.86	0.15	0.07	0.42	0.06	0.10	0.32	0.29	0.06	0.34	0.05
J24	1.28	2.15	0.27	1.82	0.31	0.11	0.49	0.06	0.17	0.75	0.65	0.10	0.58	0.12
J22	2.67	3.58	0.34	1.48	bdl	0.02	0.36	0.04	0.07	0.29	0.26	0.05	0.35	0.07
J20	1.04	1.45	0.26	1.55	0.25	0.14	0.58	0.04	0.12	0.26	0.20	0.03	0.41	0.07
J18	1.37	2.10	0.35	1.85	0.45	0.12	0.73	0.08	0.28	0.94	0.92	0.14	1.09	0.16
J16	4.99	6.87	0.91	3.25	0.43	0.22	1.39	0.24	0.63	1.98	2.42	0.39	2.63	0.50
J14	2.27	2.68	0.41	1.89	0.32	0.07	0.44	0.07	0.14	0.68	0.43	0.06	0.52	0.10
J13	bdl	bdl	bdl	bdl	bdl	bdl	bdl	bdl	bdl	bdl	bdl	bdl	bdl	bdl
J11	4.33	5.66	0.65	3.14	0.67	0.14	0.83	0.15	1.23	0.21	0.87	0.06	0.80	0.10
J10	7.24	11.16	1.89	9.23	1.91	0.59	3.10	0.43	2.54	0.51	1.56	0.21	1.39	0.20
J9	9.23	5.93	1.01	4.08	0.77	0.26	1.21	0.17	0.24	1.10	0.67	0.14	0.65	0.11
J8	2.21	2.49	0.56	1.50	0.28	0.18	0.27	0.04	0.06	0.32	0.16	0.03	0.04	#DIV/0!

J7	1.17	1.29	0.19	0.76	0.22	0.06	0.30	0.06	0.10	0.40	0.32	0.04	0.33	0.06
J5	5.42	2.93	0.97	3.99	0.89	0.27	1.54	0.24	0.41	1.59	1.03	0.12	0.46	0.11
J4	3.31	3.68	1.03	5.04	1.19	0.34	1.67	0.25	0.39	1.63	0.94	0.08	0.73	0.10
J3	3.79	5.01	0.90	3.22	0.59	0.12	1.13	0.19	1.42	0.33	0.81	0.16	0.83	0.14
J1	2.07	3.32	0.32	2.12	0.24	0.13	0.48	0.11	0.08	0.56	0.40	0.06	0.21	0.06

GL57

Values in ppm	La	Ce	Pr	Nd	Sm	Eu	Gd	Tb	Dy	Ho	Er	Tm	Yb	Lu
D1A	3.17	18.05	0.77	3.77	1.52	0.45	1.81	0.26	1.53	0.30	0.93	0.17	0.91	0.15
D1B	30.70	165.40	7.69	35.90	8.70	2.60	9.30	1.43	9.00	1.73	5.42	0.70	4.50	0.77
D1C	17.30	6.13	3.10	14.40	2.33	0.61	5.10	0.56	3.40	0.80	2.38	0.40	1.11	0.26
D1	0.55	1.02	0.21	0.99	0.47	0.09	0.26	0.04	0.35	0.05	0.09	0.03	0.19	0.03
D2	0.83	2.44	0.42	1.51	0.47	0.14	0.90	0.09	0.69	0.13	0.40	0.09	0.58	0.11
D2A	1.18	1.83	0.27	1.32	0.19	0.06	0.15	0.07	0.27	0.07	0.22	0.03	0.40	bdl
D3	1.05	1.65	0.26	1.19	0.43	0.22	0.86	0.13	1.58	0.30	1.10	0.23	1.01	0.15
D4	1.09	2.36	0.38	1.73	0.55	0.14	1.02	0.10	0.70	0.16	0.32	0.09	0.45	0.09
DM-3	1.77	2.35	0.20	0.94	0.16	0.05	0.16	0.03	0.20	0.05	0.08	0.03	0.12	0.04
DM-4	1.17	1.40	0.16	0.57	0.15	0.04	0.13	0.02	0.16	0.04	0.08	0.03	0.14	0.04
DM-5	0.73	0.96	0.08	0.37	0.14	0.04	0.10	0.01	0.10	0.03	0.11	0.03	0.16	0.04
DM-6	1.41	1.62	0.20	0.83	0.14	0.15	0.24	0.03	0.34	0.07	0.20	0.03	0.20	0.04
DM-7	2.33	1.28	0.28	1.16	0.24	0.07	0.26	0.03	0.33	0.06	0.21	0.03	0.23	0.04
D5	0.90	1.68	0.23	1.02	bdl	0.12	0.50	0.07	0.46	0.07	0.36	0.04	0.37	0.12
D6	1.42	2.57	0.39	1.67	0.15	0.17	0.57	0.06	0.52	0.12	0.37	0.05	0.42	0.06
D7	1.91	2.86	0.32	2.01	0.29	0.11	0.57	0.06	0.57	0.10	0.31	0.07	0.72	0.08
D8	2.05	4.04	0.46	2.22	0.48	0.14	0.52	0.05	0.54	0.09	0.38	0.05	0.56	0.20
D8A	5.05	7.25	1.21	5.24	1.04	0.38	1.35	0.25	1.44	0.36	1.06	0.17	1.12	0.09
D9	4.98	5.74	0.77	3.03	0.54	0.24	0.75	0.10	0.75	0.17	0.53	0.09	0.59	0.13

D9A	2.73	4.44	0.54	2.37	0.45	0.17	0.62	0.10	0.91	0.21	0.66	0.11	0.79	0.14
D9B	8.41	13.32	1.64	6.50	1.19	0.31	1.18	0.21	1.33	0.27	0.84	0.12	0.81	0.06
D9C	3.98	4.30	0.62	2.62	0.34	0.17	0.55	0.08	0.54	0.11	0.33	0.03	0.34	0.08
D10	4.67	4.35	0.84	3.37	0.51	0.17	0.65	0.11	0.73	0.18	0.54	0.08	0.50	0.12
D11	4.60	5.31	0.76	3.16	0.71	0.17	0.74	0.12	0.91	0.23	0.77	0.10	0.73	0.09
D12	3.13	4.04	0.64	2.98	0.56	0.18	0.85	0.12	0.73	0.16	0.60	0.09	0.55	0.04
D13	2.47	1.88	0.28	1.16	0.21	0.09	0.31	0.05	0.35	0.09	0.29	0.04	0.23	0.09
D14	3.85	5.26	0.69	3.23	0.69	0.22	0.79	0.10	0.64	0.15	0.50	0.08	0.57	0.11
D15	69.60	90.50	8.42	29.50	3.93	0.79	3.49	0.22	1.48	0.29	0.86	0.12	0.49	0.11
D16	3.76	5.32	0.64	2.95	0.58	0.10	0.56	0.10	0.95	0.24	0.79	0.10	0.81	0.16
D17	3.12	4.09	0.50	2.82	0.35	0.08	0.33	0.07	0.63	0.13	0.69	0.10	0.78	0.12
D18	6.61	10.00	0.99	4.11	0.71	0.17	0.88	0.09	0.94	0.25	0.70	0.10	0.48	0.14